October 1998

Effects of Grit Roughness and Pitch Oscillations on the S824 Airfoil

Airfoil Performance Report, Revised (12/99)

R. Reuss Ramsay
G. M. Gregorek
The Ohio State University
Columbus, Ohio

National Renewable Energy Laboratory
1617 Cole Boulevard
Golden, Colorado 80401-3393
A national laboratory of the U.S. Department of Energy
Managed by Midwest Research Institute
for the U.S. Department of Energy
under contract No. DE-AC36-83CH10093

Foreword

Airfoils for wind turbines have been selected by comparing data from different wind tunnels, tested under different conditions, making it difficult to make accurate comparisons. Most wind tunnel data sets do not contain airfoil performance in stall commonly experienced by turbines operating in the field. Wind turbines commonly experience extreme roughness for which there is very little data. Finally recent tests have shown that dynamic stall is a common occurrence for most wind turbines operating in yawed, stall or turbulent conditions. Very little dynamic stall data exists for the airfoils of interest to wind turbine designer. In summary, very little airfoil performance data exists which is appropriate for wind turbine design.

Recognizing the need for a wind turbine airfoil performance data base the National Renewable Energy Laboratory (NREL), funded by the US Department of Energy, awarded a contract to Ohio State University (OSU) to conduct a wind tunnel test program. Under this program OSU has tested a series of popular wind turbine airfoils. A standard test matrix has been developed to assure that each airfoil was tested under the same conditions. The test matrix was developed in partnership with industry and is intended to include all of the operating conditions experienced by wind turbines. These conditions include airfoil performance at high angles of attack, rough leading edge (bug simulation), steady and unsteady angles of attack.

Special care has been taken to report as much of the test conditions and raw as practical so that designers can make their own comparisons and focus on details of the data relevant to their design goals. Some of the airfoil coordinates are proprietary to NREL or an industry partner. To protect the information which defines the exact shape of the airfoil the coordinates have not been included in the report. Instructions on how to obtain these coordinates may be obtained by contacting C.P. (Sandy) Butterfield at NREL.

C. P. (Sandy) Butterfield
Wind Technology Division
National Renewable Energy Laboratory
1617 Cole Blvd.
Golden, Colorado, 80401 USA
Internet Address: Sandy_Butterfield@NREL.GOV
Phone 303-384-6902
FAX 303-384-6901

Preface

The Ohio State University Aeronautical and Astronautical Research Laboratory is conducting a series of steady state and unsteady wind tunnel tests on a set of airfoils which have been or will be used for wind turbines. The purpose is to investigate the effect of pitch oscillations and leading edge grit roughness on airfoil performance. The study of pitch oscillation effects can help to understand the behavior of horizontal axis wind turbines in yaw or vertical axis wind turbines under standard conditions. The results of these tests will aid in the development of new airfoil performance codes which account for unsteady behavior and also aid in the design of new airfoils for wind turbines. The application of leading edge grit roughness (LEGR) simulates surface irregularities that occur on wind turbines. These irregularities on the blades are due to the accumulation of insect debris, ice, and/or the aging process and can significantly reduce the output of wind turbines. The experimental results from the application of leading edge grit roughness will help develop airfoils that are less sensitive to roughness.

The present work was made possible by the efforts and financial support of the National Renewable Energy Laboratory who provided major funding and technical monitoring and the U.S. Department of Energy, which is credited for its funding of this document through the National Renewable Energy Laboratory under contract number DE-AC36-83CH10093. The staff of The Ohio State University Aeronautical and Astronautical Research Laboratory appreciate the contributions made by personnel from those organizations. In addition, the authors would like to recognize the efforts of the following graduate and undergraduate student research assistants, Jolanta M. Janiszewska, Fernando Falasca, and Mònica Angelats i Coll.

Summary

An S824 airfoil model was tested in The Ohio State University Aeronautical and Astronautical Research Laboratory 3×5 subsonic wind tunnel under steady state and unsteady conditions. The test defined baseline conditions for steady state angles of attack from -10° to +40° and examined unsteady behavior by oscillating the model about its quarter chord pitch axis for three mean angles, three frequencies, and three amplitudes having different wave forms. For all oscillating cases, Reynolds numbers of 0.75, 1, and 1.25 million were used. In addition, the above conditions were repeated after the application of leading edge grit roughness (LEGR) to determine contamination effects on the airfoil performance.

Typical steady state results of the S824 testing showed a baseline maximum lift coefficient of 0.92 at 12.2° angle of attack for 1 million Reynolds number. The application of LEGR reduced the maximum lift coefficient by 14% and increased the 0.0083 minimum drag coefficient value by 71%. The zero lift pitching moment was nearly zero and occurs at zero degrees angle of attack as would be expected for a symmetric airfoil section.

Data was also obtained for three pitch oscillation amplitudes with different wave forms, ±5.5° sine, ±12.5 arctangent, and ±20° arctangent. The larger amplitude cases consistently gave a higher maximum lift coefficient than the smaller amplitude cases and all sets of unsteady maximum lift coefficients were greater than the steady state values. For the unsteady cases, stall was delayed on the airfoil while the angle of attack was increasing, thereby causing an increase in maximum lift coefficient. A hysteresis behavior was exhibited for all the unsteady test cases. The hysteresis loops were larger for the higher reduced frequencies and for the larger amplitude oscillations. As in the steady case, the effect of LEGR in the unsteady case was to reduce the lift coefficient at high angles of attack. Although, at the highest reduced frequencies and for the largest amplitude oscillations the LEGR maximum lift coefficient was higher than the clean data. In addition, for the LEGR cases, the hysteresis behavior persisted into lower angles of attack than with the clean case.

In general, the unsteady maximum lift coefficient was up to 200% higher than the steady state maximum lift coefficient, and variation in the quarter chord pitching moment coefficient at maximum lift coefficient was from .04 to -.39; whereas the steady state pitching moment coefficient at the steady state maximum lift coefficient was in the range of 0 to 0.015. These findings indicate the importance of considering the unsteady flow behavior occurring in wind turbine operation because use of steady state results could greatly underestimate the loads.

Contents

List of Figures page

List of Tables page

List of Symbols

AOA	Angle of attack
A/C, a.c.	Alternating current
c	Model chord length
C_d	Drag coefficient
C_{dmin}	Minimum drag coefficient
C_{dp}	Pressure drag coefficient
C_{dw}	Wake drag coefficient
C_{du}	Uncorrected drag coefficient
C_l	Lift coefficient
C_{lmax}	Maximum lift coefficient
$C_{l\ dec}$	Lift coefficient at angle of maximum lift, but with angle of attack decreasing
C_{lu}	Uncorrected lift coefficient
C_m, $C_{m\frac{1}{4}}$	Pitching moment coefficient about the quarter chord
$C_{m\ dec}$	Pitching moment coefficient at angle of maximum lift, but with angle of attack decreasing
$C_{m\ inc}$	Pitching moment coefficient at angle of maximum lift, but with angle of attack increasing
C_{mo}	Pitching moment coefficient about the quarter chord, at zero lift
$C_{m\frac{1}{4}u}$	Uncorrected pitching moment coefficient about the quarter chord
C_p	Pressure coefficient, $(p- p_\infty)/q_\infty$
C_{pmin}	Minimum pressure coefficient
f	Frequency
h	Wind tunnel test section height
hp, Hp, HP	Horsepower
Hz	Hertz
k	Grit particle size
k/c	Grit particle size divided by airfoil model chord length
p	Pressure
q	Dynamic pressure
q_u	Uncorrected dynamic pressure
q_w	Dynamic pressure through the model wake
q_∞	Free stream dynamic pressure
Re	Reynolds number
Re_u	Uncorrected Reynolds number
t	Time
U_∞	Corrected free stream velocity
V	Velocity
V_u	Uncorrected velocity
x	Axis parallel to model reference line
y	Axis perpendicular to model reference line

α	Angle of attack
α_{dec}	Decreasing angle of attack
α_{inc}	Increasing angle of attack
α_m	Median angle of attack
α_{mean}	Mean angle of attack
α_u	Uncorrected angle of attack
ϵ	Tunnel solid wall correction scalar
ϵ_{sb}	Solid blockage correction scalar
ϵ_{wb}	Wake blockage correction scalar
Λ	Body-shape factor (0.305 used)
λ	Tip speed ratio
π	3.1416
σ	Tunnel solid wall correction parameter
ω_{red}, $\omega_{reduced}$	Reduced frequency, $\pi fc/U_\infty$

Introduction

Vertical axis wind turbine rotors experience unsteady aerodynamics under normal operating conditions. An understanding of this unsteady behavior is necessary to assist in the design of new rotor airfoils. The rotors will in general experience performance degradation due to surface roughness. These surface irregularities are due to the accumulation of insect debris, ice, and/or the aging process. Wind tunnel studies that examine both the steady and unsteady behavior of airfoils can help define pertinent flow phenomena, and the resultant data can also be used to validate analytical computer codes.

An S824 airfoil model was tested in The Ohio State University Aeronautical and Astronautical Research Laboratory (OSU/AARL) 3×5 subsonic wind tunnel (3×5) under steady flow with stationary model conditions, and with the model undergoing pitch oscillations. In order to study the possible extent of performance loss due to surface roughness, a standard grit pattern (LEGR) was used to simulate leading edge contamination. After baseline cases were completed, the LEGR was applied for both steady state and model pitch oscillation cases. The Reynolds numbers for steady state conditions were 0.75, 1, and 1.25 million, while the angle of attack ranged from -10° to +40°. While the model underwent pitch oscillations, data was acquired at Reynolds numbers of 0.75, 1, and 1.25 million, at frequencies of 0.6, 1.2, and 1.8 Hz. One sine wave forcing function was used having ±5.5° and two arc-tangent wave forcing function were used having ±12.5° and ±20°, at mean angles of attack of 0°, 7.5°, and 15°. For purposes herein, any reference to unsteady conditions means the model was in pitch oscillation.

Experimental Facility

Wind Tunnel

The OSU/AARL 3×5 subsonic wind tunnel (3×5) was used to conduct tests on the S824 airfoil section. Schematics of the top and side views are in figures 1 and 2. This open-circuit tunnel has a velocity range of 0 - 55 m/s (180 ft/sec) produced by a 2.4-meter (8-foot) diameter, six-bladed fan. The fan is belt driven by a 93.2-kw (125-hp) three-phase a.c. motor connected to a variable frequency motor controller. Nominal test section dimensions are 1.0-m (39-inches) high by 1.4-m (55-inches) wide with a 2.4-m (96-inches) length. The 457-mm (18-inches) chord airfoil model was mounted vertically in the test section. A steel tube through the quarter chord of the model was used to attach the model to the tunnel during testing. An angle of attack potentiometer was fastened to the model at the top of the tunnel as shown in figure 2. The steady state angle of attack was adjusted with a worm gear drive attached to the model strut below the tunnel floor.

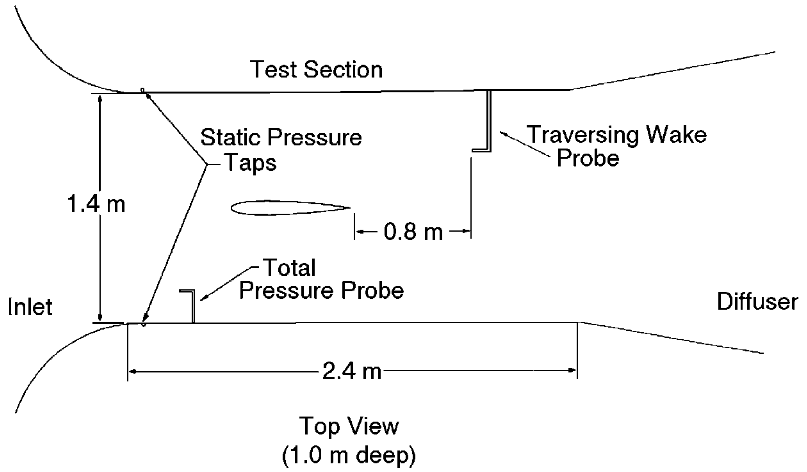

Figure 1. 3×5 Subsonic wind tunnel, top view.

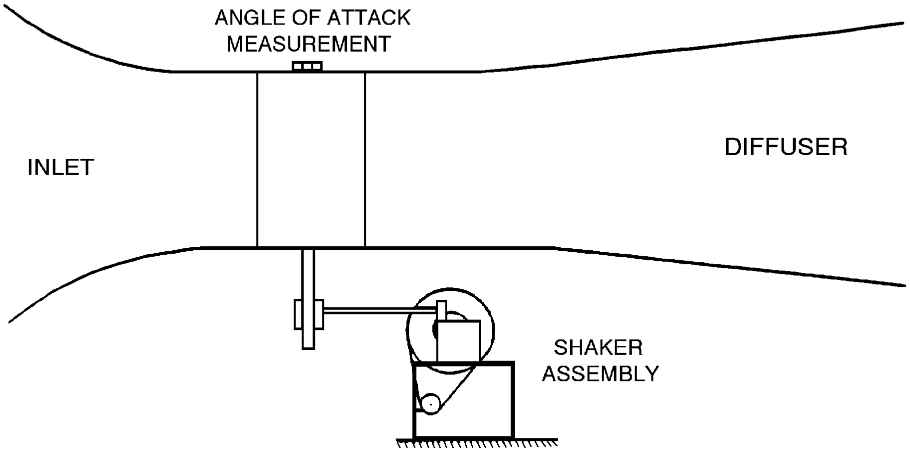

Figure 2. 3×5 Subsonic wind tunnel, side view.

Oscillation System

Portions of the testing required the use of a reliable model pitch oscillation system. The OSU/AARL "shaker" system incorporated a face cam and follower arm attached to the model support tube below the wind tunnel floor, figure 3. The choice of cam governed the type and amplitude of the wave form produced. The sine wave form has an amplitude of ±5.5°; the wave form is defined by the equation

$$\alpha = \alpha_m + A\sin(2\pi ft)$$

where A is the respective amplitude. The arctangent wave form is defined by the following equation

$$\alpha = \alpha_m + \lambda\ A\ atan\left[\frac{\sin(2\pi ft)}{\lambda + \cos(2\pi ft)}\right]$$

again where A is the amplitude having values of 12.5° or 20°. The shaker system was powered by a 5 hp a.c. motor with a variable line frequency controller. The useable oscillating frequency range was 0.1 to 2.0 Hz, with three frequencies used for this test: 0.6, 1.2, and 1.8 Hz.

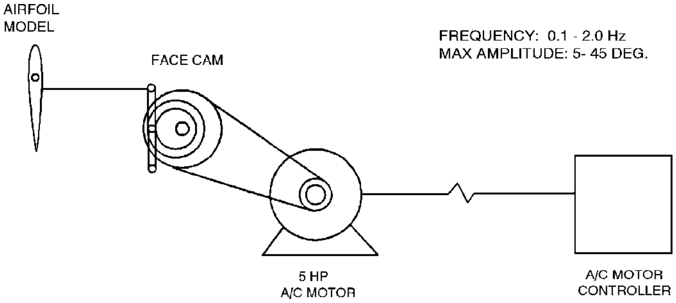

Figure 3. 3×5 Wind tunnel oscillation system.

Model Details

A 457-mm (18-inches) constant chord S824 airfoil model was designed by AARL/OSU personal and manufactured by others. Due to their proprietary nature, model shape and coordinates are not presented. The model trailing edge was thickened to 2.10-mm (0.083-inch) for fabrication purposes. The model was made of a nine layer composite lay up of alternating fiberglass and carbon fiber over ribs. The main load bearing member was a 38-mm (1.5-inches) diameter steel tube which passed through the model quarter chord station. Ribs and end plates were used to transfer loads from the composite skin to the steel tube. The final surface was filled, painted and wet sanded to attain given coordinates within a requested tolerance of ±0.25-mm (±0.01-inches). The completed model was measured at three spanwise locations using a Sheffield-Cordax coordinate measurement machine. Measurements were made in English units and later converted to metric. Figure 4 shows the results of comparing measured-to-desired coordinates by calculating differences normal to the profiled surface at three stations on the model. The "spikes" showing near the trailing edge and at the leading edge are due to the numerical methods and are not real. Although a small portion of the model upper surface near the leading edge was not within tolerance, this model was accepted because the discrepancy was small and over a narrow range.

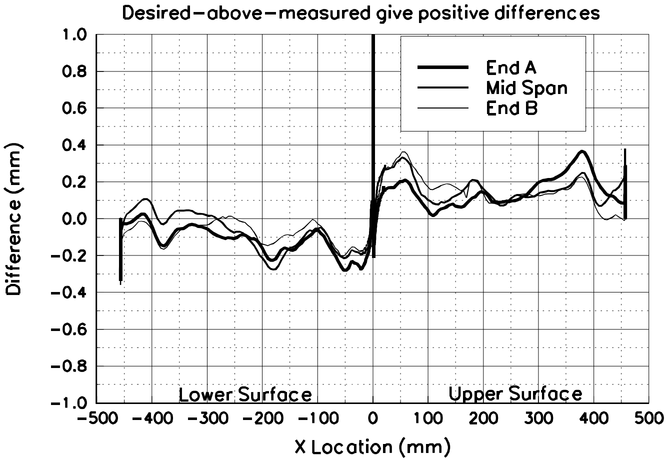

Figure 4. Measured-to-desired model coordinates difference curves.

To minimize pressure response times, which is important for the unsteady testing, the lengths of surface pressure tap lead-out lines had to be as short as possible. Consequently, a compartment was built into the model so pressure scanning modules could be installed inside the model. This compartment was accessed through a panel door fitted flush with the model contour on the lower (pressure) surface.

For test cases involving roughness, a standard roughness pattern developed for the National Renewable Energy Laboratory airfoil test program was employed. The pattern was generated using a molded insect pattern taken from a wind turbine in the field. The particle density was 5 particles per cm^2 (32 particles per square inch) in the middle of the pattern, and thinned to 1.25 particles per cm^2 (8 particles per square inch) at the edge of the pattern. Figure 5 shows the pattern. To make a usable template, the pattern was repeatedly cut into a steel sheet 102-mm (4-inches) wide and 91-cm (3-ft) long with holes just large enough for one grain of grit. Based on average particle size from the field specimen, standard #40 lapidary grit was chosen for the roughness elements, giving $k/c=0.0019$ for a 457-mm (18-inches) chord model.

To use the template, 102-mm (4-inches) wide double-sided tape was applied to one side of the template and grit was poured and brushed from the opposite side. The tape was then removed from the template and transferred to the model. This method allows the same roughness pattern to be replicated for any test.

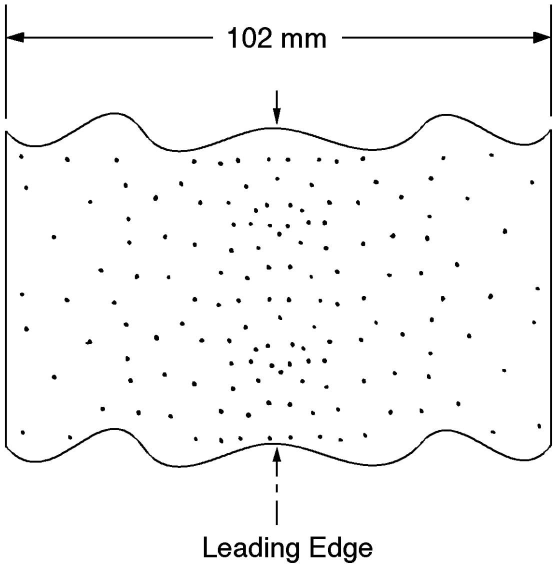

Figure 5. Roughness pattern.

Test Equipment and Procedures

Data Acquisition

Data was acquired and processed from 60 surface pressure taps, four individual tunnel pressure transducers, an angle of attack potentiometer, a wake probe position potentiometer, and a tunnel thermocouple. The data acquisition system included an IBM PC compatible 80486-based computer connected to a Pressure Systems Incorporated (PSI) data scanning system. The PSI system included a 780B Data Acquisition and Control Unit (DACU), 780B Pressure Calibration Unit (PCU), 81-IFC scanning module interface, two 2.5 psid pressure scanning modules (ESPs), one 20" water column range pressure scanning module, and a 30 channel Remotely Addressed Millivolt Module (RAMM-30). Figure 6 shows the data acquisition system schematic.

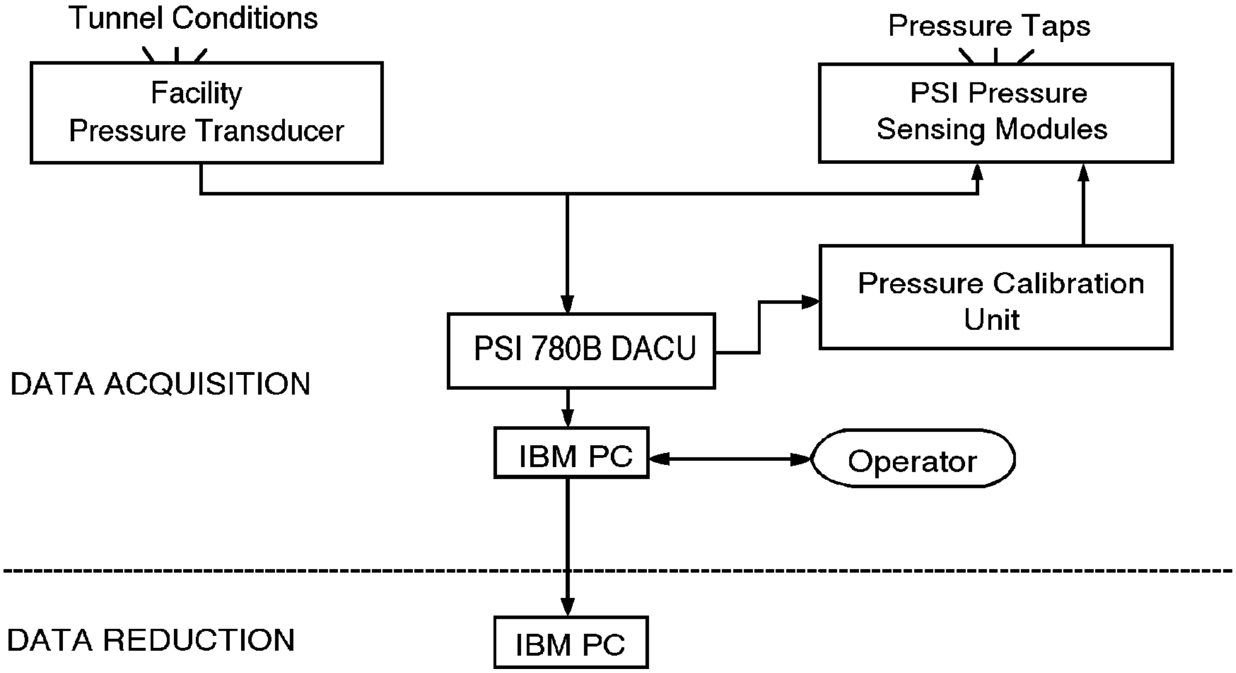

Figure 6. Data acquisition schematic.

Four individual pressure transducers read tunnel total pressure, tunnel north static pressure, tunnel south static pressure, and wake dynamic pressure. Before the test began, these transducers were bench calibrated using a water manometer to determine their sensitivities and offsets. Related values were entered into the data acquisition and reduction program so the transducers could be shunt resistor calibrated before each series of wind tunnel runs.

The rotary angle of attack potentiometer of 0.5% linearity was regularly calibrated during the tunnel pressure transducers shunt calibration. The angle of attack calibration was accomplished by taking voltage readings at known values of set angle of attack. This calibration method gave angle of attack readings within ±0.25° over the entire angle range. The wake probe position potentiometer was a linear potentiometer and it was also regularly calibrated during the shunt calibration of the tunnel pressure transducers.

Calibration of the three ESPs was done simultaneously by using the DACU and PCU. At operator request, the DACU commanded the PCU to apply known regulated pressures to the ESPs and read the output voltages from each integrated pressure sensor. From these values, the DACU calculated the calibration coefficients, and stored them internally until the coefficients were requested by the controlling computer. This calibration was done several times during a run set because the ESPs were installed inside the model and their outputs tended to drift with temperature changes during a test sequence. Frequent on-line calibrations minimized the effect.

For steady state cases, the model was set to angle of attack and the tunnel conditions adjusted. At operator request, pressure measurements from the airfoil surface taps and all other channels of information were acquired and stored by the DACU and subsequently passed to the controlling computer for final processing. The angles of attack were always set in the same progression - from 0° to -10° then from 0° to +40°.

For model oscillating cases, the tunnel conditions were set while the model was stationary at the desired mean angle of attack. The "shaker" was started, the model was allowed to oscillate through at least five cycles to set up the flow field, and then the model surface pressure and tunnel condition data were acquired. Generally, 120 data scans were acquired over three model oscillation cycles. Since surface pressures were scanned sequentially, the data rate was set so the model rotated through less than 0.50° during any data burst. Finally, due to the unsteady and complex nature of the pitch oscillation cases, model wake surveys (for drag) were not conducted.

Data Reduction

The data reduction routine was included as a section of the data acquisition program. This combination of data acquisition and reduction routines allowed data to be reduced on-line during a test. By quickly reducing selected runs, integrity checks could be made to insure the equipment was working properly and to allow timely decisions about the test matrix.

The ambient pressure was manually input into the computer and was updated regularly. This value, as well as the measurements from the tunnel pressure transducers and the tunnel thermocouple, were used to calculate tunnel airspeed. As a continuous check of readings, the tunnel total and static pressures were read by both the tunnel individual pressure transducers and the 20-inch water column ESP.

A typical steady state data point was derived by acquiring 10 data scans of all channels over a 10 second window at each angle of attack and tunnel condition. The reduction portion of the program processed each data scan to coefficient forms C_p, C_l, $C_{m\frac{1}{4}}$, and C_{dp} using the measured surface pressure voltages, calibration coefficients, tap locations and wind tunnel conditions. Then, all scan sets for a given condition were ensemble averaged to provide one data set and that data set was then corrected for the effects of solid tunnel walls. All data was saved in electronic form and selected final data was printed.

Corrections due to solid tunnel sidewalls were applied to the wind tunnel data as found in the text by Pope and Harper (1966). Tunnel conditions were described by the following equations:

$$V = V_u(1+\epsilon)$$

$$q = q_u(1+2\epsilon)$$

$$R_e = R_{e_u}(1+\epsilon)$$

Then airfoil aerodynamic characteristics were corrected by:

$$\alpha = \alpha_u + \frac{57.3\sigma}{2\pi}\left(C_{l_u} + 4C_{m\frac{1}{4}_u}\right)$$

$$C_l = C_{l_u}(1-\sigma-2\epsilon)$$

$$C_{m_{\frac{1}{4}}} = C_{m_{\frac{1}{4}_u}} (1-2\epsilon) + \frac{\sigma C_l}{4}$$

$$C_d = C_{d_u} (1-3\epsilon_{sb}-2\epsilon_{wb})$$

where

$$\sigma = \frac{\pi^2}{48} \left(\frac{c}{h}\right)^2$$

$$\epsilon = \epsilon_{sb} + \epsilon_{wb}$$

$$\epsilon_{sb} = \Lambda \sigma$$

$$\epsilon_{wb} = \frac{c}{h4} C_{d_u}$$

Model wake data was taken for steady state cases when the wake could be completely traversed. Pressures were acquired from a pitot-static probe which was connected to measure incompressible dynamic pressure through the wake. These pressure measurements were used to calculate drag coefficient using a form of the Jones equation derived from Schlichting (1979).

$$C_{dw} = \frac{2}{c} \int \sqrt{\frac{q_w}{q_\infty}} \left(1 - \sqrt{\frac{q_w}{q_\infty}}\right) dy$$

This usage assumes static pressure at the measurement site is the free-stream value. The integration was done automatically except the computer operator chose the end points of the integration from a plot of the wake survey displayed on the computer screen.

For pitch oscillation cases, model surface pressures were reduced to pressure coefficient form with subsequent integrations and angle of attack considerations giving lift, moment and pressure drag coefficients. There was no calibration available for unsteady model pitch conditions; therefore, the unsteady pressure data were not corrected for any possible effects due to time dependent pitching or solid tunnel walls. Also for these cases, the wind tunnel contraction pressures (used for steady state cases) could not be used to calculate instantaneous freestream conditions due to slow response. The tunnel conditions were obtained from a total pressure probe, and the average of opposing static taps in the test section entrance; thereby giving near instantaneous flow pressure conditions for the pitching frequencies used.

Test Matrix

The test was designed to study steady state and unsteady pitch oscillation data. Steady state data was acquired at Reynolds numbers of 0.75, 1, and 1.25 million with and without LEGR. Refer to the tabular data in Appendix B for the actual Reynolds number for each angle of attack for the steady state data. The angle of attack increment was two degrees when $-10° < \alpha < +10°$ or $+20° < \alpha < +40°$, and one degree when $+10° < \alpha < +20°$. Wake surveys were conducted to find total airfoil drag over an approximate angle of attack range of -10° to +10°. Unsteady data was taken for Reynolds numbers of 0.75, 1, and 1.25 million. A sine wave cam having an amplitude of ±5.5°, and arc-tangent wave cams having amplitudes of ±12.5° and 20° were used for pitch oscillations, and the mean angles for all these amplitudes were 0°, 7.5°, and 15°. For all these conditions, the frequencies were varied to 0.6, 1.2, and 1.8 Hz. All data points for the unsteady cases were acquired for both clean and LEGR cases.

Results and Discussion

The S824 airfoil model was tested under steady state and pitch oscillation conditions. A brief discussion of the results follows, including a comparison of experimental data and computational predictions, steady state results, and unsteady results.

Comparison With Theory

Comparisons were made between present wind tunnel steady state data and computed predictions made using the North Carolina State Airfoil Analysis Code. This analysis code has proven to be accurate for moderate angles of attack. The analysis was made with specifications set to allow free transition from laminar to turbulent flow, and the pressure distribution comparisons were matched to the same angle of attack as the wind tunnel cases.

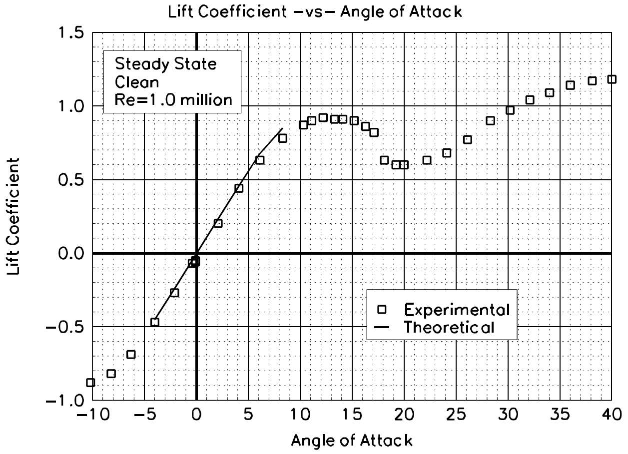

Figure 7. Comparison with theory, C_l vs α.

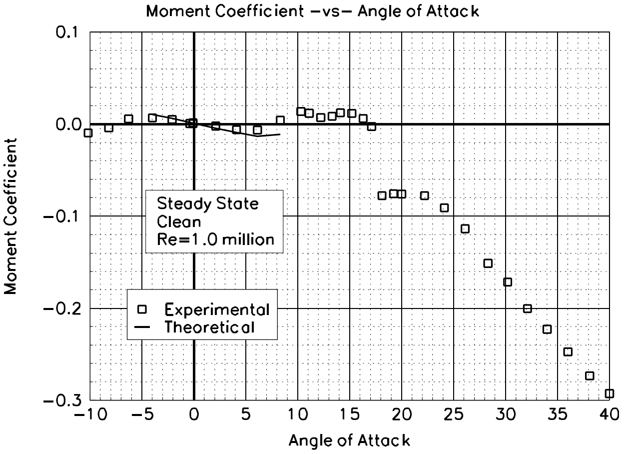

Figure 8. Comparison with theory, C_m vs α.

Figure 7 shows the lift coefficient versus angle of attack for the 1 million Reynolds number case. For moderate angles of attack, where the analysis code is valid, the comparison showed good agreement. The pitching moment about the quarter chord, figure 8, showed adequate agreement for angles of attack from -4° to +4°. The pressure distributions shown in figures 9 and 10 are for angles of attack of -0.1° and 8.3°, respectively, and include clean wind tunnel data as compared to computed free transition pressure

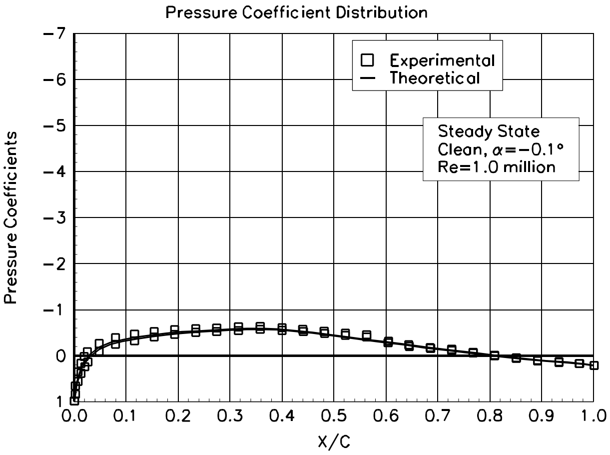

Figure 9. Comparison with theory, C_p vs x/c, α=-0.1°.

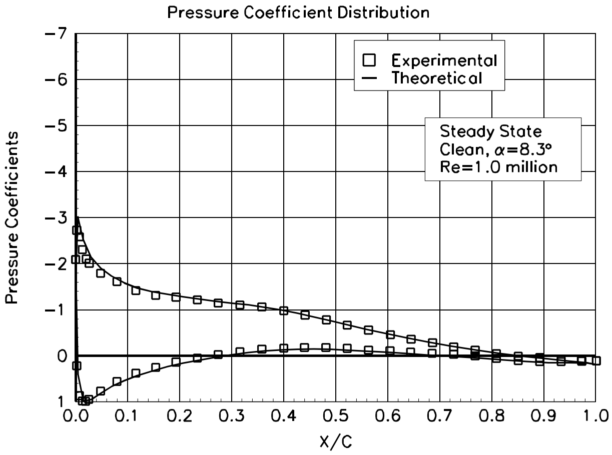

Figure 10. Comparison with theory, C_p vs x/c, α=8.3°.

distributions. For both angles of attack, there was correlation between the experimental and predicted values, although there seemed to be some discrepancy around the first 10% of the airfoil surface.

Steady State Data

The S824 airfoil model was tested at three Reynolds numbers at nominal angles of attack from -10° to +40°. Figures 11 and 12 show lift coefficients for all the test Reynolds numbers both for model clean and with LEGR applied, respectively. The maximum positive lift coefficient, found at 1.25 million Reynolds number, for the clean cases was about 0.94 and for the LEGR cases was about 0.81, a 14% reduction. The clean cases had a positive stall at 12.2° while the LEGR cases stalled at 13.3° angle of attack. The average lift curve slope through 0° angle of attack for clean data was about 0.112 and lower for the LEGR case at 0.100.

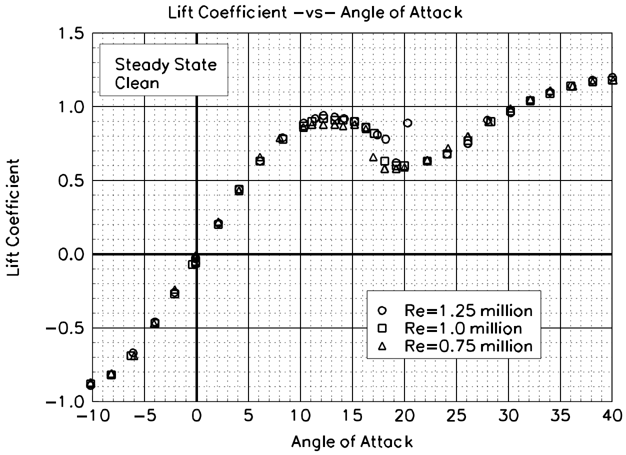

Figure 11. C_l vs α, clean.

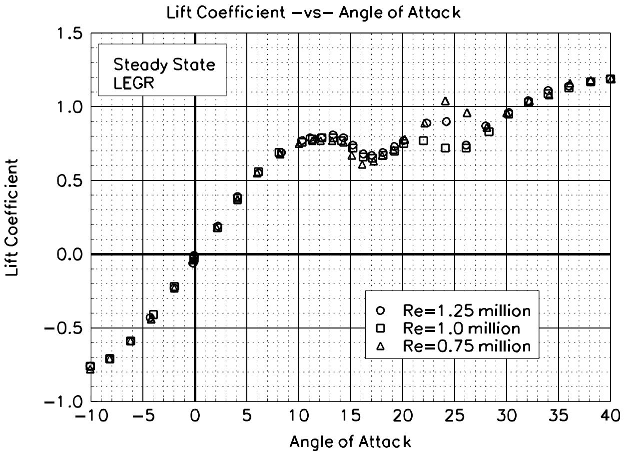

Figure 12. C_l vs α, LEGR, k/c=0.0019.

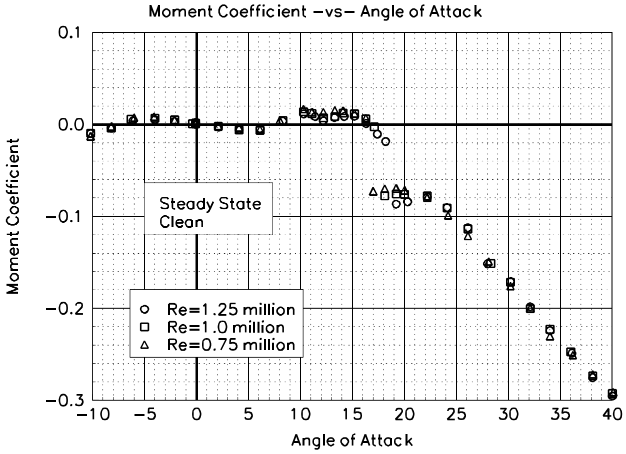

Figure 13. C_m vs α, clean.

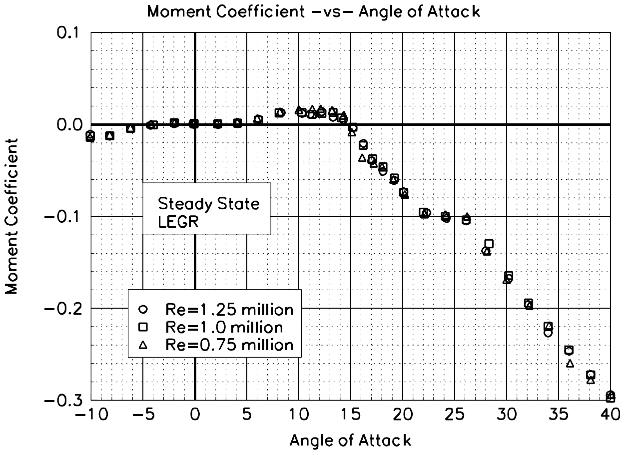

Figure 14. C_m vs α, LEGR, k/c=0.0019.

Figure 13 shows the pitching moment about the quarter chord for the clean cases and figure 14 shows the LEGR cases. Both curves follow the same trends except that between 16° and 24° angle of attack the clean pitching moment data showed a break that the LEGR data did not. As would be expected the pitching moment was nearly zero at zero degrees angle of attack which was expected because this was a symmetric airfoil section.

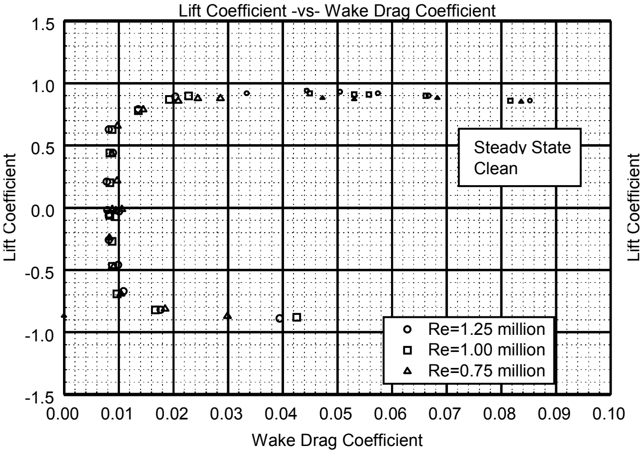

Figure 15. Clean, drag polar.

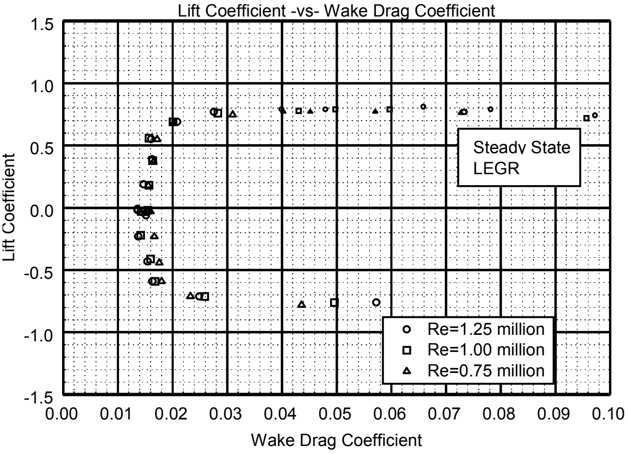

Figure 16. LEGR, drag polar.

Total wake drag data was obtained for both the clean and LEGR cases over an angle of attack range of -10° to +10°. A pitot-static probe was used to describe the wake profile. This method is reliable when there is relatively low turbulence in the wake flow; therefore, only moderate angles of attack have reliable total drag coefficient data. At angles of attack other than -10° to +10°, surface pressure data was integrated to give C_{dp} and is shown in the drag polars as small symbols. The model clean drag data is shown in figure 15 and the LEGR case is shown in figure 16. At 1.25 million Reynolds number, minimum drag coefficient for the clean cases was measured as 0.0079, and for LEGR as 0.0136; a 72% increase. The general effect of LEGR was to increase drag consistently through most angles of attack and narrow the drag bucket.

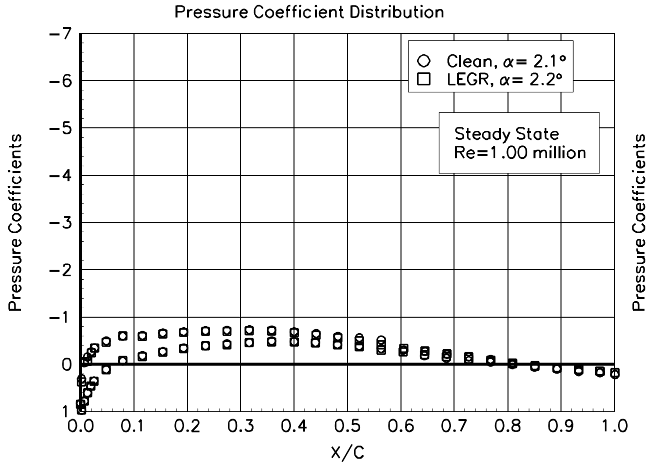

Figure 17. Pressure distribution, α=2.1°.

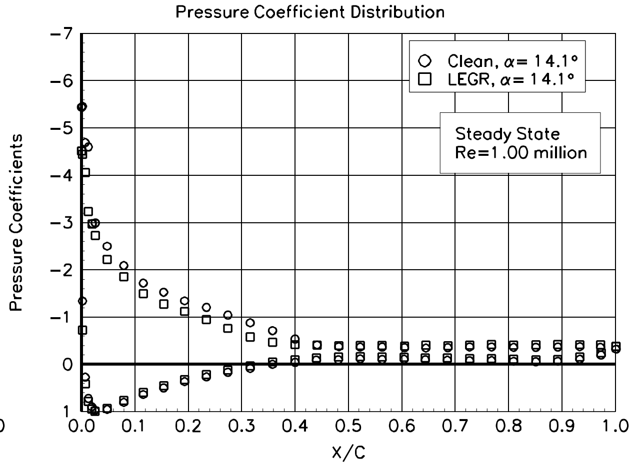

Figure 18. Pressure distribution, α=14.1°.

Two examples of the surface pressure distributions are shown in figures 17 and 18 for 2.1° and 14.1°, respectively, for 1 million Reynolds number. At the angles of attack close to zero degrees, the effect of LEGR did not appear to significantly affect the pressure distribution in comparison with the clean case distribution; however, there was a slight effect apparent in the lift coefficient with values of 0.18 for the LEGR case and 0.20 for the clean case at 2.1°. For the higher angle of attack case, figure 18, the effect of LEGR was to reduce the magnitude of the pressure peak from -5.5 to -4.5, increase the pressures on the upper (suction) surface over the forward 45% of the chord. The net effect was a reduction in lift coefficient from 0.91 to 0.77, a 15% decrease.

Unsteady Data

Unsteady experimental data were obtained for the S824 airfoil model undergoing sinusoidal and arc-tangential pitch oscillations. As mentioned earlier, no calibration was available for the unsteady oscillating model conditions; the steady state tunnel calibration was used to set the flow conditions while the model was stationary at its mean angle of attack. A comprehensive set of test conditions was used to describe unsteady behavior of the airfoil including: three angle of attack amplitudes and wave forms, ±5.5° sine, ±12.5° arc-tangent, and ±20° arc-tangent; three Reynolds numbers, 0.75, 1, and 1.25 million; three pitch oscillation frequencies, 0.6, 1.2, and 1.8 Hz; and three mean angles of attack, 0°, 7.5°, and 15°.

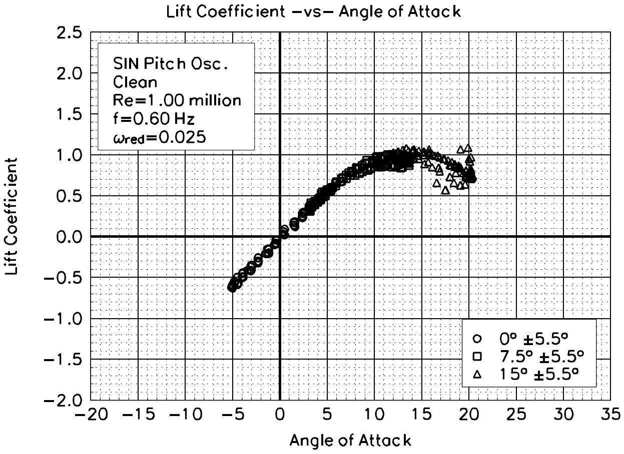

Figure 19. Clean, C_l vs α, ω_{red}=0.025, ±5.5° SIN.

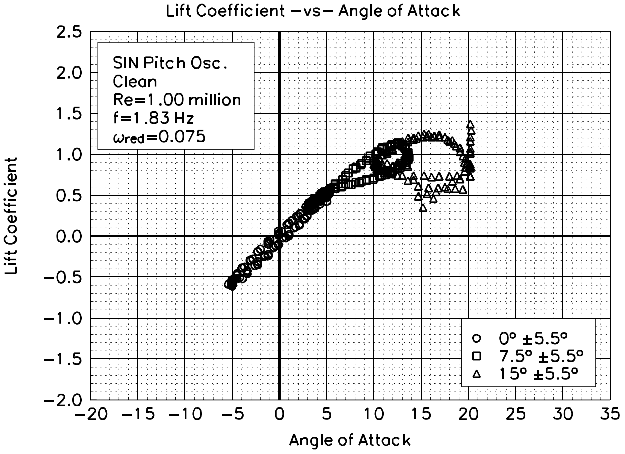

Figure 20. Clean, C_l vs α, ω_{red}=0.075, ±5.5° SIN.

Figure 19 shows the lift coefficient versus angle of attack for the ±5.5° amplitude sine model clean case, at reduced frequency of 0.025 and 1 million Reynolds number. Note that all three mean angles of attack are plotted on the same figure. The maximum pre-stall lift coefficient for this case was near 1.08 and occurred when the airfoil was traveling with the angle of attack increasing. In contrast, when the model was traveling through decreasing angles of attack, the stall recovery was delayed and a hysteresis behavior was exhibited in the lift coefficient that could be seen throughout all of the unsteady data. In order to obtain some measure of this hysteresis behavior, the lift coefficient on the "return" portion of the curve, at the angle of attack where maximum lift coefficient occurs, could be used. For the case discussed here, the "hysteresis" lift coefficient was 0.95, a 12% decrease from the 1.08 unsteady maximum value. In comparison, the steady state maximum lift coefficient was 0.92. At higher reduced frequency of 0.075, the hysteresis behavior was more pronounced as seen in figure 20. In addition to greater hysteresis, the maximum lift coefficient was increased to about 1.25, which was a 36% increase over the steady state value. The corresponding "hysteresis" lift coefficient was 0.59. This difference between steady state behavior and unsteady hysteresis behavior is a main reason that unsteady testing should be required for airfoils used in wind turbine applications.

The pitching moment in figures 21 and 22 corresponds to the same conditions as the two lift coefficient plots previously discussed. There was an indication that the hysteresis behavior was present but it was not as apparent as in the lift coefficient plots; but the higher reduced frequency case did show hysteresis more than the lower reduced frequency case. For reference, the steady state maximum lift occurred near 12° angle of attack and the steady state pitching moment at this maximum lift point was 0.0068. In comparison, when the airfoil was undergoing pitch oscillation for the lower frequency, pitching moment varied from -0.0146 to -0.0109 (at the angle of attack where unsteady maximum lift occurs), a large departure from the steady state value. Note the angle of attack where the maximum unsteady lift coefficient occurs does not necessarily show the "greatest" hysteresis behavior but does give a relative indication of the effect.

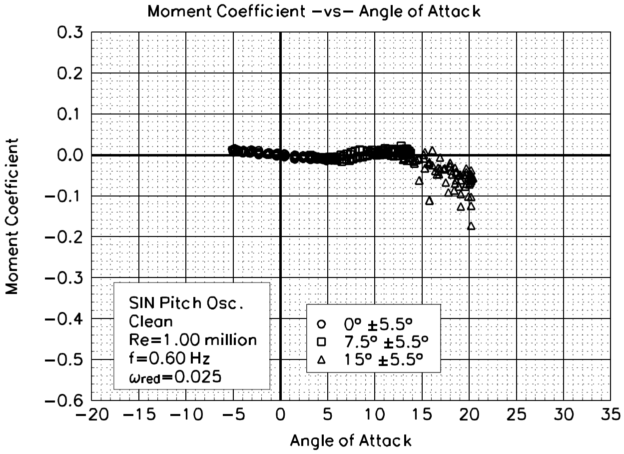

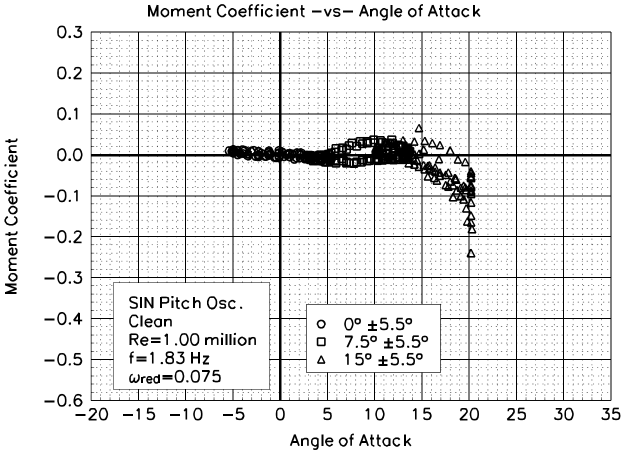

Figure 21. Clean, C_m vs α, ω_{red}=0.025, ±5.5° SIN. **Figure 22. Clean, C_m vs α, ω_{red}=0.075, ±5.5° SIN.**

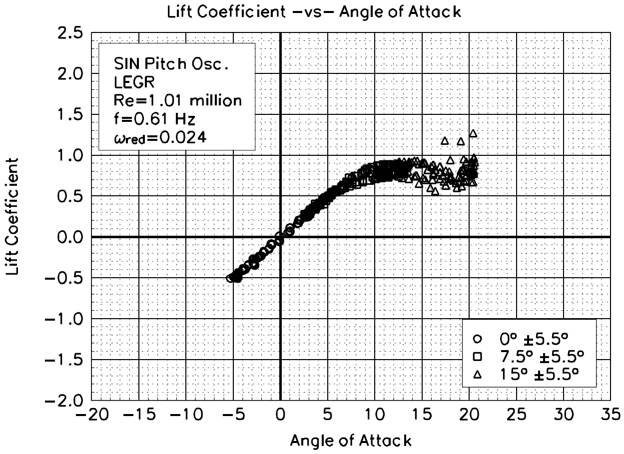

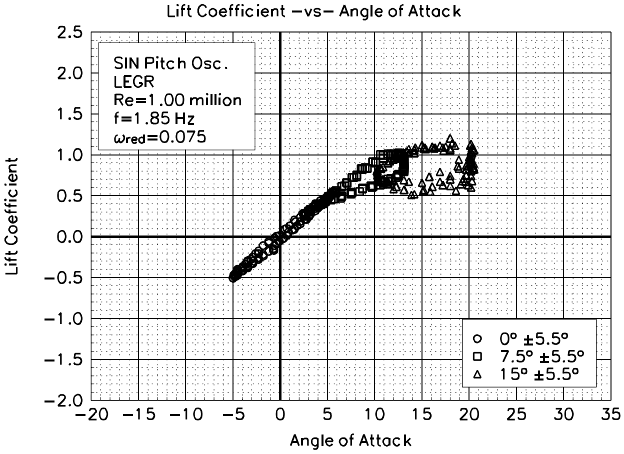

Figure 23. LEGR, C_l vs α, ω_{red}=0.024, ±5.5° SIN. **Figure 24. LEGR, C_l vs α, ω_{red}=0.075, ±5.5° SIN.**

In comparison to the clean data, the application of LEGR reduced the maximum lift coefficient in the 5.5° sinusoidal pitch oscillation cases. Lift coefficient versus angle of attack with LEGR applied is shown in figure 23 for the 0.024 reduced frequency case. The 0.075 reduced frequency case is in figure 24. Both correspond to the same run conditions which were described earlier for the clean cases. For the lower reduced frequency, the maximum unsteady lift coefficient was reduced to 0.93 from the corresponding clean case of 1.08, an 14% decrease. Hysteresis behavior was apparent at this frequency; the corresponding "hysteresis" lift coefficient was 0.74 when LEGR was applied. In contrast, the higher frequency LEGR case had a maximum lift coefficient of 1.12 while the model was increasing in angle of attack and the corresponding decreasing angle of attack lift coefficient was 0.57. In this case, the application of LEGR slightly reduced the hysteresis loop behavior for larger angles of attack in comparison with the clean case at the same run conditions, but the hysteresis persisted into lower angles of attack for the LEGR case.

The pitching moment coefficient shown in figure 25 is for 0.024 reduced frequency with LEGR applied. At the angle of unsteady maximum lift, the pitching moment ranged from -0.0172 to -0.0067, while the steady state LEGR pitching moment was 0.0127 at the steady state stall angle of attack (13.3°). The higher reduced frequency of 0.075 with LEGR application is shown in figure 26. As was seen with the lift coefficient, pitching moment hysteresis was more apparent at the higher reduced frequency than the corresponding low reduced frequency case. Unsteady maximum lift angle of attack for this reduced frequency occurred at 15.0° and the pitching moment ranged from -0.0404 to -0.0184 at that angle. Throughout the higher angle of attack range, the magnitude of the unsteady pitching moment can be very different than the steady state clean case (steady state pitching moment at maximum lift is 0.0127). It seems that if these differences are not taken into consideration, then they can have significant impact on the fatigue life predictions of a wind turbine system.

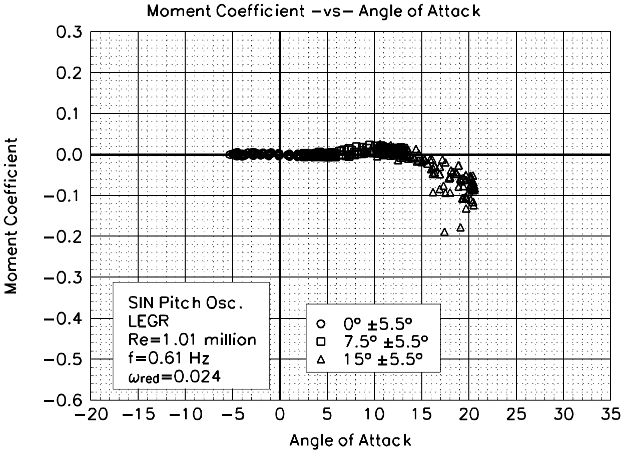

Figure 25. LEGR, C_m vs α, ω_{red}=0.024, ±5.5° SIN.

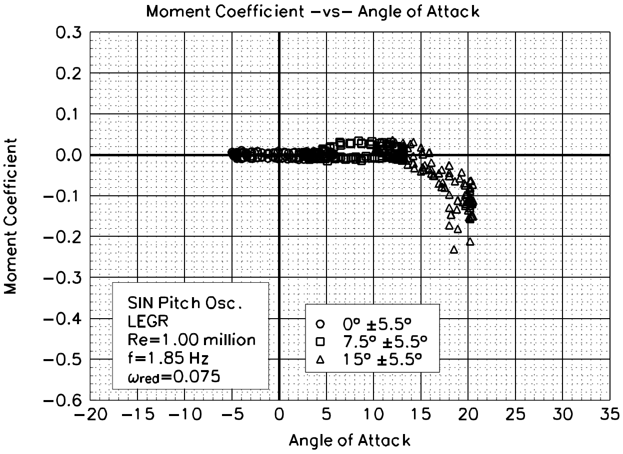

Figure 26. LEGR, C_m vs α, ω_{red}=0.075, ±5.5° SIN.

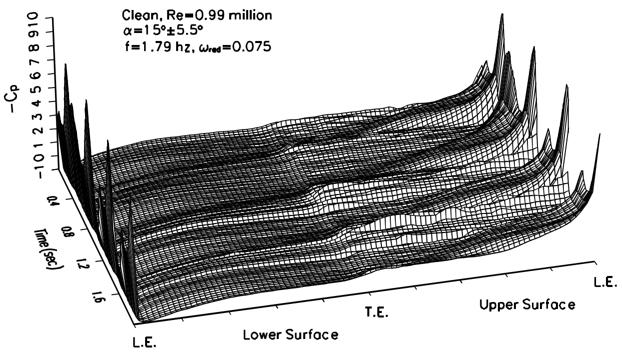

Figure 27. Unsteady pressure distribution, clean, ω_{red}=0.075, 15°±5.5°.

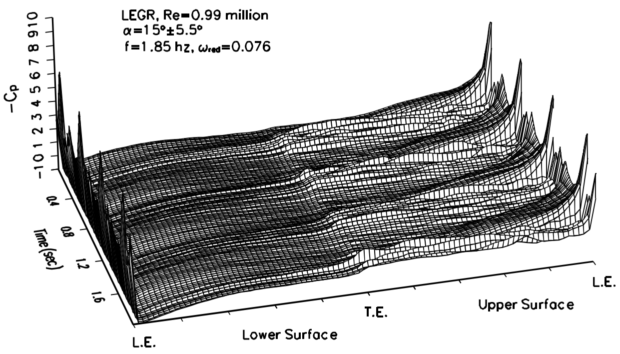

Figure 28. Unsteady pressure distribution, LEGR, ω_{red}=0.076, 15°±5.5°.

To examine the data closely two pressure distributions were plotted to compare the effects on the pressure distributions of adding LEGR to the model. The cases shown here are for the higher reduced frequency and a mean angle of attack of 15°. Figure 27 shows the clean case while figure 28 shows the LEGR case. For plotting clarity, the model pressures were "unwrapped" about the trailing edge. The upper surface pressures are depicted on the right of the surface plot, lower surface values on the left. The trailing edge is then at the midpoint of the x-axis with the leading edge at each extreme. Additionally, the pressure coefficients were linearly interpolated to make an evenly spaced grid. The time scale corresponds to angle of attack. In comparing the clean and the LEGR data the minimum pressure coefficient was -7 for the clean case and then the magnitude was increased to near -6 when LEGR was applied. Overall the magnitude of the pressure coefficients were more positive when the LEGR was applied. Separated flow is defined as the irregular, "rough" areas on the upper surface, that were more noticeable for the LEGR case than for the clean case.

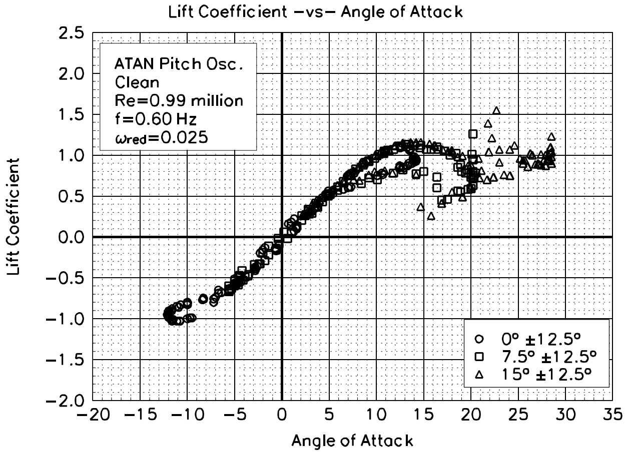

Figure 29. Clean, C_l vs α, ω_{red}=0.025, ±12.5° ATAN.

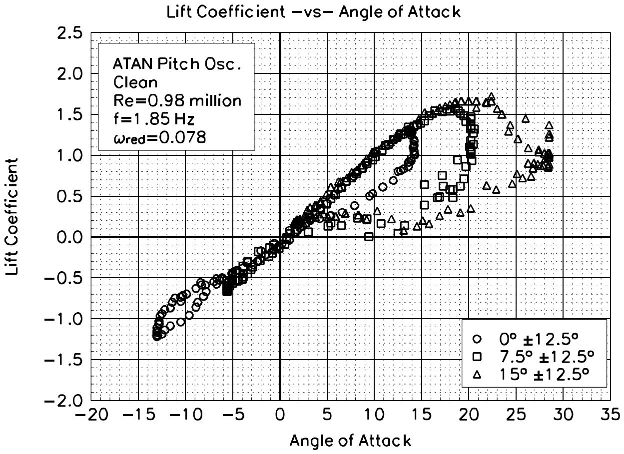

Figure 30. Clean, C_l vs α, ω_{red}=0.078, ±12.5° ATAN.

Figures 29 and 30 show the ±12.5° arc-tangent, unsteady, clean, lift coefficient for the reduced frequencies of 0.025 and 0.078, respectively. The maximum lift coefficient for the lower frequency was 1.16 and occurred, as expected, when the airfoil was traveling through increasing angle of attack. The "hysteresis" lift coefficient (at 14.7°) was 0.80. At the higher reduced frequency, the maximum lift coefficient occurred at a higher angle of attack, 20.0°, and was 1.66. The corresponding "hysteresis" lift coefficient was 0.35. The difference between the maximum lift coefficient and the "hysteresis" lift coefficient indicates a much greater hysteresis response than experienced for the lower reduced frequency. The steady state, clean, maximum lift coefficient was 0.92; therefore, the unsteady behavior created lift coefficients up to 80% higher than the steady state conditions.

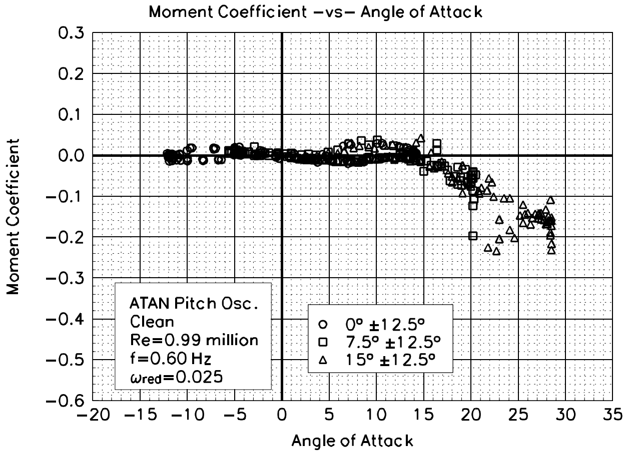

Figure 31. Clean, C_m vs α, ω_{red}=0.025, ±12.5° ATAN.

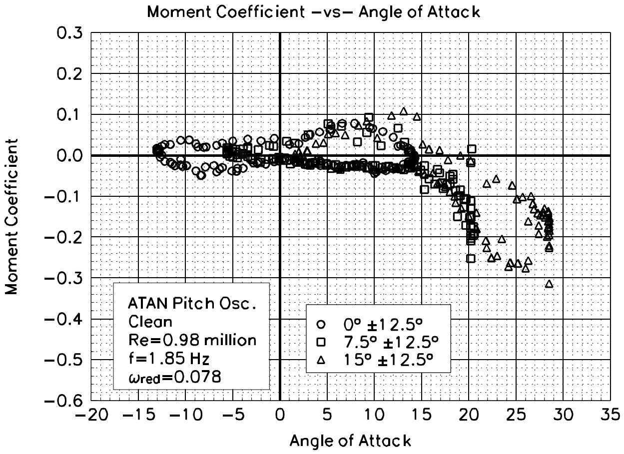

Figure 32. Clean, C_m vs α, ω_{red}=0.078, ±12.5° ATAN.

The quarter chord pitching moments having the same reduced frequencies as the lift coefficient cases are shown in figures 31 and 32. The hysteresis behavior observed in the lift coefficient plots was also reflected in this pitching moment data. Near the maximum lift angle, 14.7° for the lower frequency, the pitching moment coefficient ranged from -0.0163 to -0.0422; whereas the 0.078 reduced frequency case had maximum lift near 20.0° and pitching moment ranged from less than -0.1487 to -0.0138. In comparison, the steady state pitching moment was 0.0068 near the steady state maximum lift coefficient angle of attack of 12.2°. The higher reduced frequency showed large hysteresis loops for all three mean angles of attack.

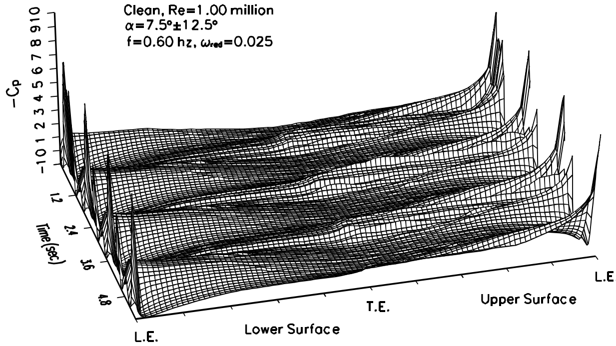

Figure 33. Unsteady pressure distribution, clean, ω_{red}=0.025, 7.5°±12.5°.

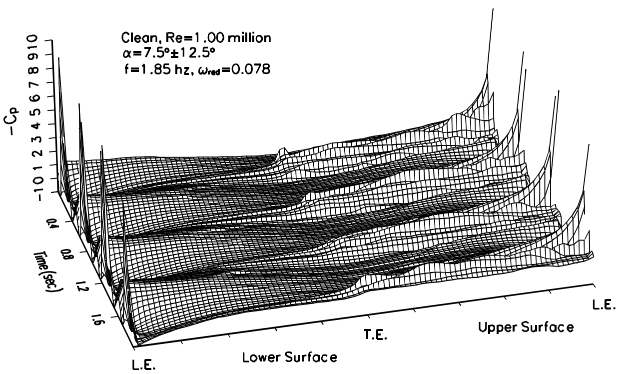

Figure 34. Unsteady pressure distribution, clean, ω_{red}=0.078, 7.5°±12.5°.

Figure 33 shows the lower reduced frequency clean pressure distributions for the ±7.5° mean case. The oscillation amplitude was such that the model traveled through negative angles of attack and this was reflected as the pressure increases on the lower surface. On the upper surface the pressures reached a minimum and then they dropped in magnitude as the model began to develop trailing edge stall. A secondary peak developed when the model traveled through decreasing angle of attack and the airflow began to reattach. Figure 34 shows the higher reduced frequency clean case for the same run conditions as previously discussed. Again the lower surface showed well behaved pressure decreases corresponding to when the model was traveling through negative angle of attack. The upper surface showed higher minimum pressures and the flow reattachment was reduced for decreasing angles of attack as compared to the lower frequency case.

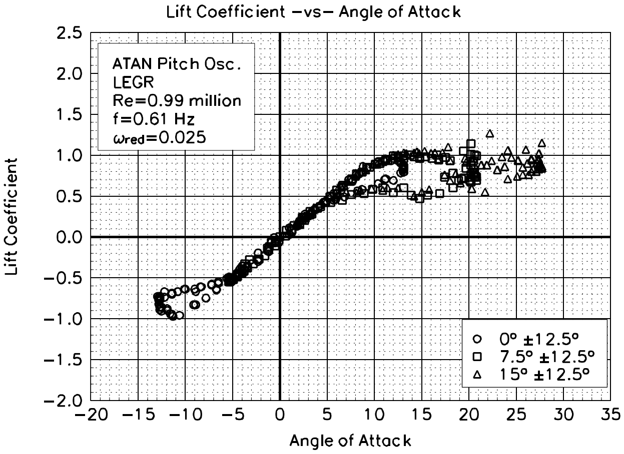

Figure 35. LEGR, C_l vs α, ω_{red}=0.025, ±12.5° ATAN.

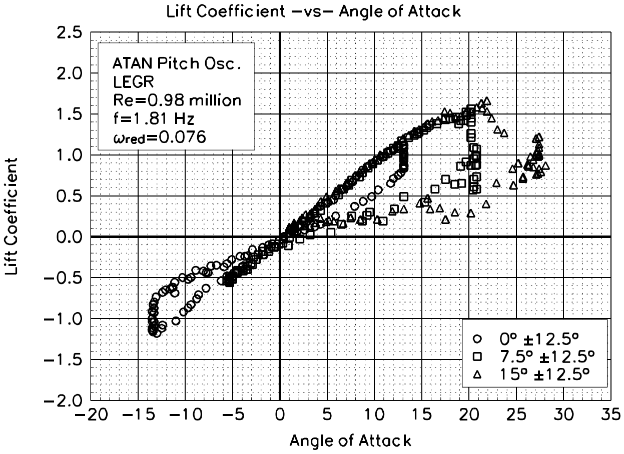

Figure 36. LEGR, C_l vs α, ω_{red}=0.076, ±12.5° ATAN.

The application of LEGR degraded the maximum lift performance of the airfoil undergoing the ±12.5° arc-tangent oscillation as would be expected from the results discussed previously. The LEGR lift coefficient data for reduced frequencies of 0.025 and 0.076 are shown in Figures 35 and 36, respectively. The maximum lift coefficient was reduced to 1.05 from 1.16 for the low frequency clean case. Although there was a reduction, this value was still higher than the LEGR steady state case which had a maximum lift coefficient of 0.79 at 13.3° angle of attack. The higher reduced frequency had a maximum lift coefficient of 1.53 which occurred near 17° angle of attack. The corresponding lift coefficient at 17° for the airfoil traveling with decreasing angle of attack was 0.21, an 86% reduction from the maximum.

Figures 37 and 38 show the corresponding pitching moment coefficients for the reduced frequencies of 0.025 and 0.076. For the 0.025 reduced frequency case, the pitching moment varied from -0.0342 to 0.0158 at 15.3° (where the maximum lift occurred). The hysteresis behavior was more pronounced for the higher reduced frequency case, where the range of pitching moments at the maximum lift angle of 17.4° was from -0.1083 to 0.0356. These values could then be compared to the steady state maximum lift LEGR pitching moment value of 0.0127.

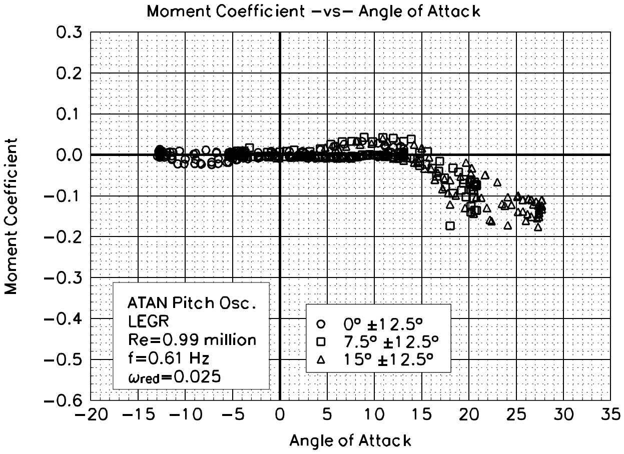

Figure 37. LEGR, C_m vs α, ω_{red}=0.025, ±12.5° ATAN.

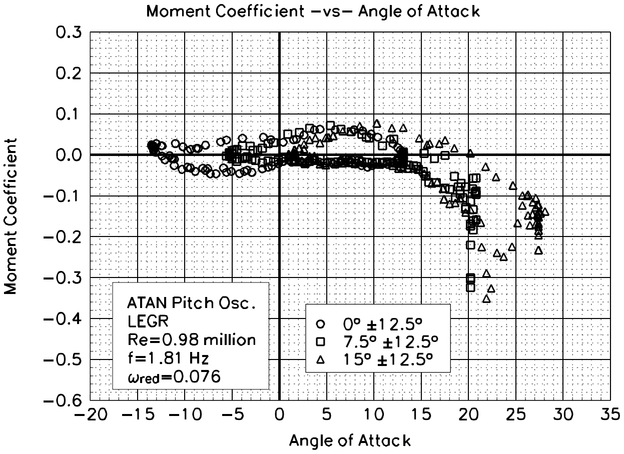

Figure 38. LEGR, C_m vs α, ω_{red}=0.076, ±12.5° ATAN.

Using the same run conditions as previously discussed, a ±20 arc-tangent oscillation wave form was used. Figures 39 and 40 show the corresponding clean, unsteady, lift coefficient for the reduced frequencies of 0.025 and 0.076, respectively. The maximum lift coefficient for the lower reduced frequency was 1.21 and occurred, at an angle of attack of 15.1°. Because of the large amplitude wave form, the model was traveling almost twice as fast as the previous ±12.5° wave form case when the model passed through the mean angle of attack. In addition, because of this wave form pattern, the model was moving at a faster rate through decreasing angles of attack than the increasing angles of attack. These two facts coupled together caused the hysteresis behavior to persist through the entire angle of attack range shown in the clean cases here. The low frequency "hysteresis" lift coefficient (at 15.1°) was 0.35. At the higher reduced frequency, the maximum lift coefficient occurred at a higher angle of attack, 18.2°, and was 1.75. The corresponding "hysteresis" lift coefficient was 0.43. As in the previous cases, a much greater hysteresis response occurred at the higher reduced frequency than was experienced for the lower reduced frequency.

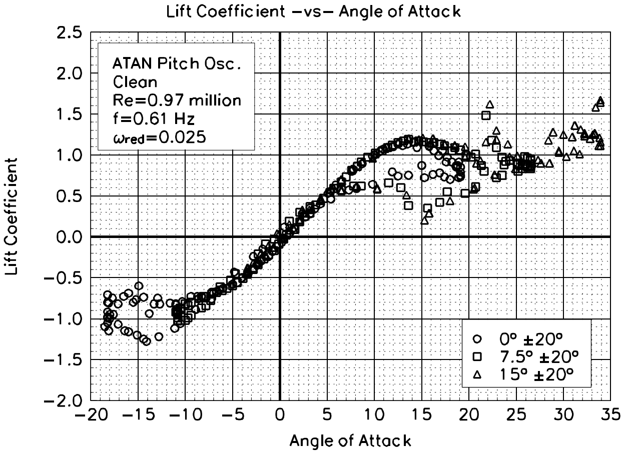

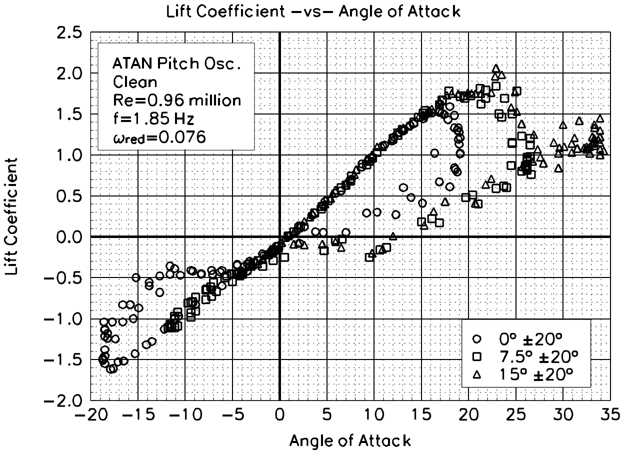

Figure 39. Clean, C_l vs α, ω_{red}=0.025, ±20° ATAN. Figure 40. Clean, C_l vs α, ω_{red}=0.076, ±20° ATAN.

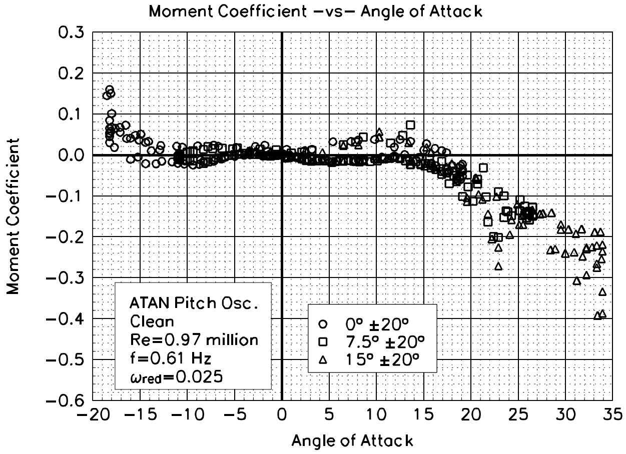

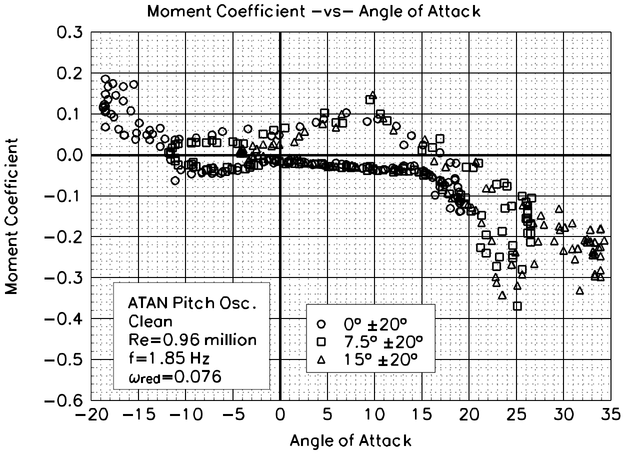

Figure 41. Clean, C_m vs α, ω_{red}=0.025, ±20° ATAN.

Figure 42. Clean, C_m vs α, ω_{red}=0.076, ±20° ATAN.

The quarter chord pitching moments having the same wave form and reduced frequencies as the lift coefficient cases above are shown in figures 41 and 42. The hysteresis behavior observed in the lift coefficient plots was also reflected in this pitching moment data. Near the maximum lift angle, 15.1° for the lower frequency, the pitching moment coefficient ranged from -0.0274 to 0.0182; whereas the 0.076 reduced frequency case had maximum lift near 18.2° and pitching moment ranged from -0.1051 to -0.0298. In comparison, the steady state pitching moment was 0.0068 near the steady state maximum lift coefficient angle of attack of 12.2°. The higher reduced frequency again showed large hysteresis loops for all three mean angles of attack where on the decreasing portion of the curve the pitching moment switched to positive for angle of attack less than 17°.

An unsteady pressure distribution for a ±20° arc-tangent low frequency case is shown in figure 43. This clean data set showed the upper (suction) surface had high magnitude peak pressures and highly separated flow while the airfoil traveled through positive angles of attack. The lower surface showed oscillatory pressure decreases as the airfoil traveled through negative angles of attack. The maximum negative angle of attack was less than the angle of attack for which the onset of stall occurred so the pressures on the lower surface showed less separation than did the upper surface.

The application of LEGR degraded the maximum lift performance of the airfoil for most cases tested in this study; however, at the highest reduced frequencies the maximum lift coefficient occurred for the LEGR cases. The LEGR lift coefficient data for reduced frequencies of 0.025 and 0.076 are shown in figures 44 and 45, respectively. The maximum lift coefficient was reduced to 1.11 from 1.21 for the low frequency

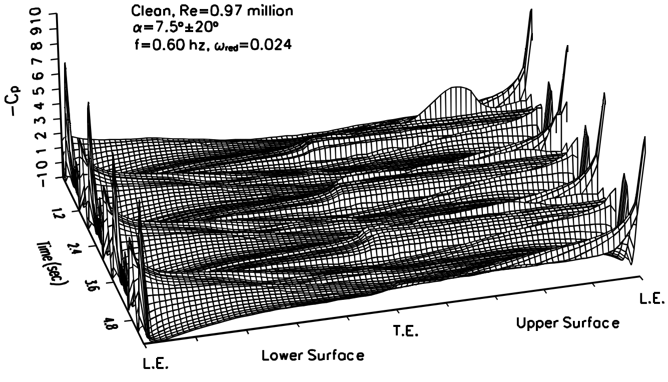

Figure 43. Unsteady pressure distribution, clean, ω_{red}=0.024, 7.5°±20°.

clean case. The higher reduced frequency had a maximum lift coefficient of 1.91 which occurred near 22.7° angle of attack. The corresponding maximum lift coefficient for the clean case was 1.75 this gave a 9% increase for the LEGR over the clean data.

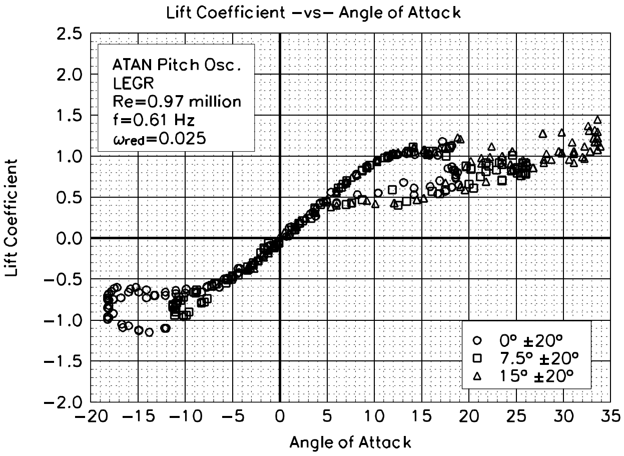

Figure 44. LEGR, C_l vs α, ω_{red}=0.025, ±20° ATAN.

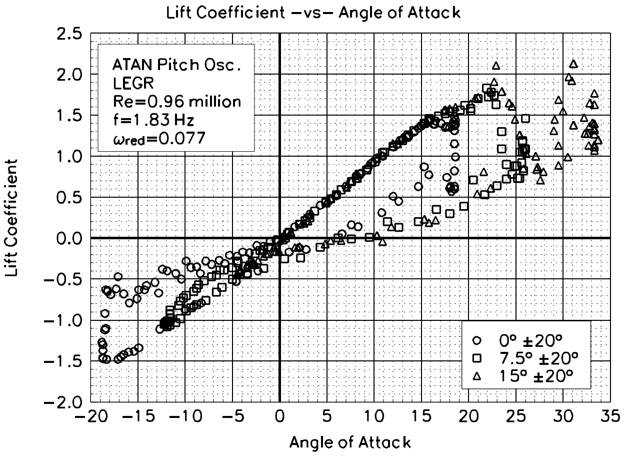

Figure 45. LEGR, C_l vs α, ω_{red}=0.077, ±20° ATAN.

Figures 46 and 47 show the corresponding pitching moment coefficients for the LEGR cases above. For the 0.025 reduced frequency case, the pitching moment varied from -0.0260 to 0.0447 at 14.1° (where the unsteady maximum lift occurred). And for the higher frequency case where the hysteresis behavior was more pronounced the range of pitching moments at the unsteady maximum lift angle of 22.7° was from less than -0.2875 to -0.0622. These values could then be compared to the corresponding steady state LEGR pitching moment value of 0.0127 that occurred at the same angle of attack as the steady state maximum lift coefficient.

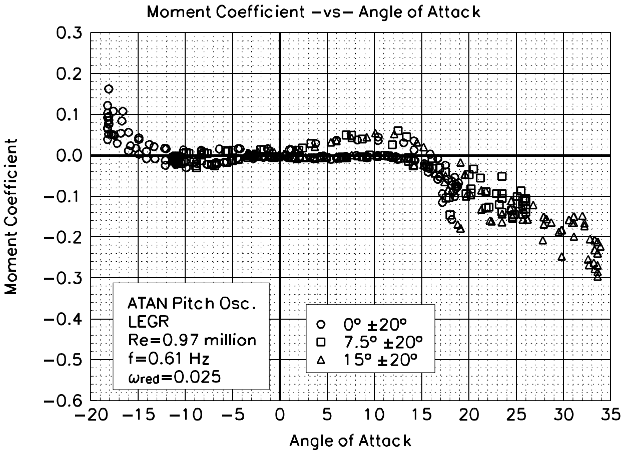

Figure 46. LEGR, C_m vs α, ω_{red}=0.025, ±20° ATAN.

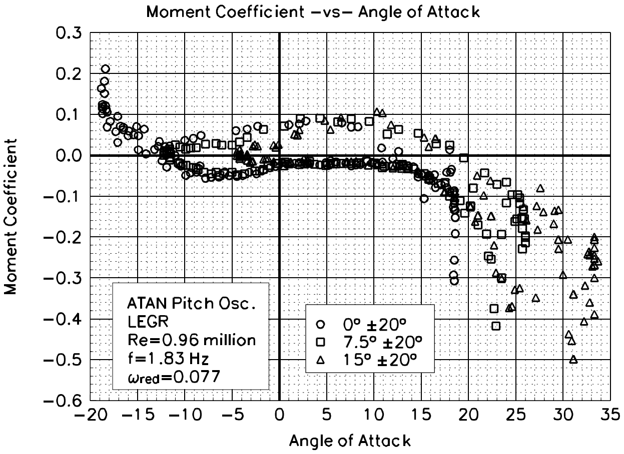

Figure 47. LEGR, C_m vs α, ω_{red}=0.077, ±20° ATAN.

Although not all the unsteady data was discussed here, the previous discussion included typical examples of the wind tunnel data. The remaining cases for the three oscillation wave forms and for all the Reynolds numbers is included in Appendix C.

Summary of Results

An S824 airfoil model was tested under steady state and pitch oscillation conditions. Baseline tests were made while the model was clean, and then corresponding tests were conducted with leading edge grit roughness (LEGR) applied.

A summary of the steady state aerodynamic parameters is shown in table 1. As observed, the application of LEGR reduced the maximum lift of the airfoil up to 14% and the minimum drag coefficient increased in some cases up to 79%. The angle of attack for which the maximum lift occurred was increased slightly when LEGR was applied up to 13.3° from the clean 12.2°. The zero lift pitching moment was near zero as would be expected for a symmetric airfoil section for which zero lift occurs at zero degrees angle of attack.

Table 1. S824 Steady State Parameters Summary.

Grit Pattern	Re x 10^{-6}	C_{lmax}	C_{dmin}	C_{mo}
Clean	0.75	0.88 @ 12.2°	0.0083	0.0005
LEGR	0.75	0.77 @ 13.2°	0.0149	0.0013
Clean	1.00	0.92 @ 12.2°	0.0083	0.0003
LEGR	1.00	0.79 @ 13.3°	0.0142	0.0004
Clean	1.25	0.94 @ 12.2°	0.0079	0.0000
LEGR	1.25	0.81 @ 13.3°	0.0136	0.0001

For all the clean pitch oscillation data, the ±5.5° sine, ±12.5° arc-tangent, and ±20° arc-tangent oscillations, some similar trends were found for each data set. For all cases, the unsteady test conditions and some parameters are in tables 2, 3, 4, 5, 6, and 7. Looking at the reduced frequency, which takes oscillation and tunnel speed into account, and comparing as this value was increased, it was observed that the maximum lift coefficient increased. The increase in maximum lift coefficient with reduced frequency was nearly linear for all of the test cases as shown in figures 48, 49 and 50. In addition, the hysteresis behavior became increasingly apparent with increased reduced frequency.

Table 2. S824, Unsteady, Clean, ±5.5° SIN.

ω_{red}	Re x 10^{-6}	f	C_{lmax}	α_{max}	$C_{l\ dec}$	$C_{m\ inc}$	$C_{m\ dec}$
0.033	0.75	0.59	1.09	14.5	0.95	-0.0193	0.0094
0.065	0.75	1.19	1.20	14.5	0.71	-0.0360	0.0255
0.101	0.75	1.85	1.29	16.4	0.48	-0.0501	-0.0555
0.025	1.00	0.60	1.08	13.4	0.96	-0.0146	-0.0109
0.050	1.00	1.21	1.15	14.3	0.82	-0.0225	-0.0180
0.075	1.00	1.83	1.25	15.8	0.59	-0.0341	-0.0255
0.020	1.25	0.61	1.10	15.3	0.97	-0.0263	0.0024
0.038	1.26	1.18	1.12	14.2	0.81	-0.0130	0.0276
0.059	1.26	1.83	1.23	15.3	0.81	-0.0371	0.0234

Table 3. S824, Unsteady, LEGR, ±5.5° SIN.

ω_{red}	Re x 10^{-6}	f	C_{lmax}	α_{max}	$C_{l\ dec}$	$C_{m\ inc}$	$C_{m\ dec}$
0.033	0.75	0.61	0.92	11.4	0.75	-0.0004	0.0137
0.065	0.75	1.19	0.99	11.4	0.68	-0.0060	0.0283
0.100	0.75	1.83	1.21	15.8	0.50	-0.0467	-0.0017
0.024	1.01	0.61	0.93	14.2	0.74	-0.0172	-0.0067
0.048	1.00	1.18	1.01	13.9	0.55	-0.0241	0.0252
0.075	1.00	1.85	1.12	15.0	0.57	-0.0404	0.0184
0.019	1.25	0.60	0.88	12.5	0.79	-0.0044	0.0113
0.039	1.25	1.19	0.94	12.0	0.74	-0.0087	0.0181
0.058	1.25	1.81	1.06	15.3	0.61	-0.0287	0.0116

Table 4. S824, Unsteady, Clean, ±12.5° ATAN.

ω_{red}	Re x 10^{-6}	f	C_{lmax}	α_{max}	$C_{l\ dec}$	$C_{m\ inc}$	$C_{m\ dec}$
0.033	0.75	0.60	1.21	15.0	0.36	-0.0315	-0.0186
0.067	0.74	1.19	1.57	20.3	0.87	-0.1339	-0.0488
0.103	0.74	1.83	1.80	20.4	0.81	-0.2880	-0.0889
0.025	0.99	0.60	1.16	14.7	0.80	-0.0163	-0.0422
0.050	0.98	1.19	1.43	15.6	0.37	-0.0535	-0.0086
0.078	0.98	1.85	1.66	20.0	0.35	-0.1487	-0.0138
0.020	1.23	0.60	1.12	14.3	0.83	-0.0061	-0.0196
0.040	1.23	1.19	1.33	15.5	0.54	-0.0373	-0.0068
0.061	1.22	1.81	1.51	18.0	0.37	-0.0782	-0.0048

Table 5. S824, Unsteady, LEGR, ±12.5° ATAN.

ω_{red}	Re x 10^{-6}	f	C_{lmax}	α_{max}	$C_{l\ dec}$	$C_{m\ inc}$	$C_{m\ dec}$
0.034	0.75	0.61	1.11	14.5	0.49	-0.0242	0.0147
0.067	0.74	1.21	1.45	18.0	0.30	-0.1113	0.0078
0.103	0.74	1.85	1.66	20.2	0.67	-0.3008	-0.0525
0.025	0.99	0.61	1.05	15.3	0.55	-0.0342	0.0158
0.051	0.98	1.21	1.27	15.6	0.53	-0.0541	-0.0073
0.076	0.98	1.81	1.53	17.4	0.21	-0.1083	0.0356
0.020	1.23	0.60	0.99	14.2	0.55	-0.0206	0.0294
0.040	1.23	1.21	1.20	15.3	0.35	-0.0420	0.0223
0.061	1.23	1.83	1.36	18.0	0.38	-0.0968	0.0235

Table 6. S824, Unsteady, Clean, ±20° ATAN.

ω_{red}	Re x 10^{-6}	f	C_{lmax}	α_{max}	$C_{l\ dec}$	$C_{m\ inc}$	$C_{m\ dec}$
0.033	0.73	0.61	1.27	14.1	0.14	-0.0317	0.0384
0.065	0.73	1.19	1.76	20.7	0.55	-0.1860	-0.0254
0.100	0.73	1.83	2.18	25.1	1.01	-0.3870	-0.1195
0.025	0.97	0.61	1.21	15.1	0.35	-0.0274	0.0182
0.049	0.96	1.19	1.51	18.6	0.51	-0.0902	-0.0355
0.076	0.96	1.85	1.75	18.2	0.43	-0.1051	-0.0298
0.020	1.21	0.61	1.18	14.7	0.62	-0.0171	0.0386
0.040	1.20	1.21	1.41	15.8	0.15	-0.0518	0.0396
0.061	1.20	1.85	1.62	17.7	0.42	-0.0741	-0.0140

Table 7. S824, Unsteady, LEGR, ±20° ATAN.

ω_{red}	Re x 10^{-6}	f	C_{lmax}	α_{max}	$C_{l\ dec}$	$C_{m\ inc}$	$C_{m\ dec}$
0.033	0.73	0.60	1.17	14.7	0.42	-0.0314	0.0377
0.067	0.73	1.21	1.58	19.8	0.33	-0.1130	0.0128
0.104	0.72	1.85	2.20	25.2	0.93	-0.3895	-0.1512
0.025	0.97	0.61	1.11	14.1	0.45	-0.0260	0.0447
0.049	0.97	1.18	1.41	18.0	0.45	-0.1051	-0.0068
0.077	0.96	1.83	1.91	22.7	0.61	-0.2875	-0.0622
0.020	1.21	0.61	1.04	15.6	0.56	-0.0218	0.0268
0.040	1.21	1.22	1.25	16.4	0.64	-0.0538	-0.0368
0.060	1.20	1.81	1.67	22.0	0.60	-0.3514	-0.0567

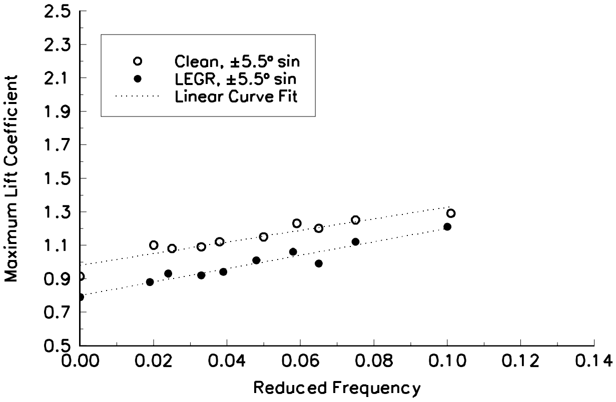

Figure 48. ±5.5° SIN, unsteady C_{lmax} vs ω_{red}.

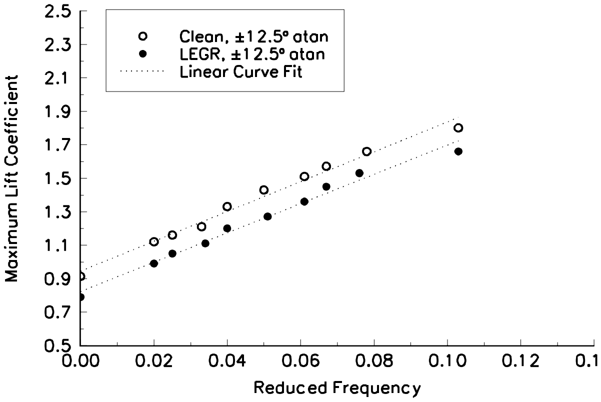

Figure 49. ±12.5° ATAN, unsteady C_{lmax} vs ω_{red}.

As expected, in most cases, the application of LEGR reduced the aerodynamic performance of the airfoil. The unsteady maximum lift coefficient was reduced from 6% to 20% for the ±5.5° sine case, from 7% to 12% for the ±12.5° arc-tangent case. Although, for the highest amplitude case the LEGR maximum lift coefficient was sometimes greater than the clean maximum lift coefficient, as seen from figure 50. At the higher reduced frequencies for this case the C_{lmax} became more scattered as compared to the smaller amplitude cases of ±5.5° and ±12.5° and this was reflected in the plots of the dynamic data for the ±20° case where the data was more scattered at the highest reduced frequencies than were the other two cases. As well as following the same trends as the clean, unsteady data discussed previously, the LEGR caused the hysteresis behavior to persist into lower angles of attack than did the clean cases. Overall, the unsteady wind tunnel data showed hysteresis behavior that became more apparent with increased, reduced frequency. The maximum unsteady lift coefficient was up to 57% higher for the ±5.5° sine case, up to 115% higher for the ±12.5° arc-tangent cases, and up to 200% higher for the ±20° arc-tangent case than the steady state maximum lift coefficient. In addition, variation in the quarter chord pitching moment coefficient could be an order of magnitude different than that indicated by steady state results. These findings indicate that it is very important to consider the unsteady loading that will occur in wind turbine operation because use of steady state results can greatly underestimate the forces.

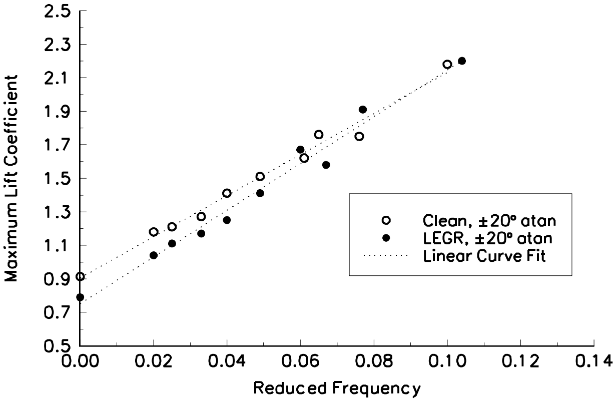

Figure 50. ±20° ATAN, unsteady C_{lmax} vs ω_{red}.

References

Pope, A.; Harper, J.J. (1966). *Low Speed Wind Tunnel Testing*. New York, NY: John Wiley & Sons, Inc.

Schlichting, H. (1979). *Boundary Layer Theory*. New York, NY: McGraw-Hill Inc.

Smetana, F., Summey, D. et-al. (1975) *Light Aircraft Lift, Drag, and Moment Prediction - a Review and Analysis*. North Carolina State University. NASA CR-2523.

Appendix A: Surface Pressure Tap Coordinates

List of Tables Page

Table A1. S824 Surface Pressure Taps, Non-Diminsional Coordinates

Tap Number	Chord Station	Ordinate
1	1.0010	--
2	0.9727	--
3	0.9331	--
4	0.8923	--
5	0.8505	--
6	0.8092	--
7	0.7677	--
8	0.7265	--
9	0.6851	--
10	0.6443	--
11	0.6038	--
12	0.5632	--
13	0.5222	--
14	0.4814	--
15	0.4405	--
16	0.3997	--
17	0.3581	--
18	0.3159	--
19	0.2741	--
20	0.2335	--
21	0.1931	--
22	0.1540	--
23	0.1158	--
24	0.0791	--
25	0.0480	--
26	0.0248	--
27	0.0188	--
28	0.0128	--
29	0.0072	--
30	0.0019	--
31	0.0000	--
32	0.0023	--
33	0.0072	--
34	0.0128	--
35	0.0198	--
36	0.0258	--

Table A1. S824 Surface Pressure Taps, Non-Diminsional Coordinates

Tap Number	Chord Station	Ordinate
37	0.0480	--
38	0.0794	--
39	0.1160	--
40	0.1541	--
41	0.1935	--
42	0.2341	--
43	0.2745	--
44	0.3161	--
45	0.3582	--
46	0.3998	--
47	0.4409	--
48	0.4818	--
49	0.5225	--
50	0.5633	--
51	0.6046	--
52	0.6447	--
53	0.6860	--
54	0.7271	--
55	0.7682	--
56	0.8091	--
57	0.8505	--
58	0.8918	--
59	0.9330	--
60	0.9724	--

End of Table A1

Appendix B: Steady State Data
Integrated Coefficients and Pressure Distributions

List of Tables page

List of Figures page

Table B1. S824, Clean, Re = 0.75 x 10^6

RUN	AOA	C_l	C_{dp}	$C_{m\frac{1}{4}}$	Re x 10^{-6}	C_{dw}
6	-10.2	-0.87	0.0219	-0.0131	0.75	0.0299
5	-8.2	-0.81	0.0139	-0.0024	0.75	0.0185
4	-6.0	-0.69	0.0064	0.0072	0.75	0.0104
3	-4.1	-0.47	0.0063	0.0082	0.76	0.0091
2	-2.1	-0.24	0.0040	0.0044	0.76	0.0083
1	-0.1	-0.01	0.0034	0.0005	0.76	0.0106
7	-0.1	-0.01	0.0035	0.0013	0.76	0.0088
33	-0.1	-0.02	0.0043	0.0026	0.75	0.0095
8	2.1	0.22	0.0033	-0.0018	0.75	0.0097
9	4.1	0.43	0.0050	-0.0034	0.75	0.0088
10	6.1	0.66	0.0066	-0.0058	0.75	0.0098
11	8.0	0.79	0.0101	0.0043	0.75	0.0145
12	10.3	0.86	0.0212	0.0164	0.75	0.0209
13	11.1	0.88	0.0305	0.0133	0.75	0.0245
14	12.2	0.88	0.0400	0.0131	0.75	0.0286
15	13.3	0.88	0.0473	0.0153	0.75	--
16	14.1	0.87	0.0531	0.0146	0.74	--
17	15.2	0.88	0.0683	0.0117	0.75	--
18	16.3	0.85	0.0837	0.0067	0.75	--
19	17.0	0.66	0.2591	-0.0729	0.76	--
20	18.1	0.58	0.2686	-0.0700	0.76	--
21	19.2	0.58	0.2842	-0.0697	0.77	--
22	20.0	0.59	0.3011	-0.0718	0.76	--
23	22.2	0.64	0.3484	-0.0798	0.75	--
24	24.2	0.72	0.4148	-0.0992	0.75	--
25	26.1	0.80	0.4886	-0.1214	0.74	--
26	28.1	0.90	0.5780	-0.1491	0.74	--
27	30.2	0.99	0.6729	-0.1760	0.74	--
28	32.1	1.05	0.7553	-0.2000	0.73	--
29	34.0	1.11	0.8496	-0.2304	0.73	--

Table B1. S824, Clean, Re = 0.75 x 10^6

RUN	AOA	C_l	C_{dp}	$C_{m¼}$	Re x 10^{-6}	C_{dw}
30	36.2	1.14	0.9358	-0.2510	0.73	--
31	38.1	1.17	1.0145	-0.2718	0.73	--
32	40.1	1.18	1.0932	-0.2912	0.72	--
End of Table B1						

Table B2. S824, Clean, Re = 1.0 x 10^6

RUN	AOA	C_l	C_{dp}	$C_{m¼}$	Re x 10^{-6}	C_{dw}
39	-10.2	-0.88	0.0226	-0.0098	1.00	0.0426
38	-8.2	-0.82	0.0115	-0.0043	1.00	0.0167
37	-6.3	-0.69	0.0072	0.0053	1.00	0.0097
36	-4.0	-0.47	0.0033	0.0066	1.00	0.0089
35	-2.1	-0.27	0.0021	0.0046	1.00	0.0088
66	-0.4	-0.07	0.0026	0.0005	1.00	0.0094
34	-0.1	-0.06	0.0022	0.0003	1.00	0.0084
40	-0.1	-0.05	0.0021	0.0011	1.00	0.0083
41	2.1	0.20	0.0046	-0.0024	1.01	0.0084
42	4.1	0.44	0.0061	-0.0063	1.01	0.0084
43	6.1	0.63	0.0092	-0.0067	1.01	0.0088
44	8.3	0.78	0.0149	0.0042	1.01	0.0136
45	10.3	0.87	0.0232	0.0134	1.01	0.0193
46	11.1	0.90	0.0297	0.0116	1.01	0.0228
47	12.2	0.92	0.0450	0.0068	1.00	--
48	13.3	0.91	0.0531	0.0082	1.01	--
49	14.1	0.91	0.0558	0.0121	1.01	--
50	15.2	0.90	0.0662	0.0114	1.00	--
51	16.3	0.86	0.0817	0.0057	1.00	--
52	17.1	0.82	0.1005	-0.0029	1.00	--
53	18.1	0.63	0.2773	-0.0781	1.01	--
54	19.2	0.60	0.2911	-0.0759	1.01	--
55	20.0	0.60	0.3048	-0.0762	1.01	--
56	22.2	0.63	0.3449	-0.0780	1.01	--
57	24.1	0.68	0.3982	-0.0912	1.00	--
58	26.1	0.77	0.4725	-0.1139	0.99	--
59	28.3	0.90	0.5838	-0.1514	0.99	--
60	30.2	0.97	0.6588	-0.1717	0.98	--
61	32.1	1.04	0.7547	-0.2006	0.99	--
62	34.0	1.09	0.8362	-0.2229	0.98	--

Table B2. S824, Clean, Re = 1.0 x 10^6

RUN	AOA	C_l	C_{dp}	$C_{m¼}$	Re x 10^{-6}	C_{dw}
63	36.0	1.14	0.9266	-0.2476	0.98	--
64	38.1	1.17	1.0188	-0.2736	0.97	--
65	40.0	1.18	1.0914	-0.2928	0.96	--

End of Table B2

Table B3. S824, Clean, Re = 1.25 x 10^6

RUN	AOA	C_l	C_{dp}	$C_{m1/4}$	Re x 10^{-6}	C_{dw}
492	-10.2	-0.89	0.0167	-0.0102	1.25	0.0395
491	-8.2	-0.82	0.0089	-0.0042	1.25	0.0177
490	-6.1	-0.67	0.0040	0.0037	1.25	0.0109
489	-4.0	-0.46	0.0028	0.0048	1.25	0.0099
488	-2.1	-0.26	0.0018	0.0029	1.25	0.0082
487	-0.1	-0.06	0.0022	0.0015	1.25	0.0082
493	-0.1	-0.02	0.0018	0.0009	1.26	0.0080
519	-0.1	-0.03	0.0025	0.0000	1.26	0.0101
494	2.1	0.21	0.0039	-0.0032	1.25	0.0079
495	4.1	0.44	0.0053	-0.0058	1.25	0.0090
496	6.1	0.63	0.0085	-0.0051	1.25	0.0082
497	8.3	0.79	0.0146	0.0032	1.25	0.0136
498	10.3	0.89	0.0231	0.0112	1.25	0.0204
499	11.4	0.92	0.0335	0.0082	1.25	--
500	12.2	0.94	0.0445	0.0036	1.25	--
501	13.3	0.93	0.0506	0.0071	1.25	--
502	14.2	0.92	0.0575	0.0083	1.25	--
503	15.2	0.90	0.0668	0.0086	1.26	--
504	16.3	0.86	0.0853	0.0008	1.25	--
505	17.4	0.81	0.1117	-0.0109	1.25	--
506	18.2	0.78	0.1317	-0.0188	1.26	--
507	19.2	0.62	0.2987	-0.0868	1.23	--
508	20.3	0.89	0.2923	-0.0843	1.27	--
509	22.2	0.63	0.3454	-0.0790	1.25	--
510	24.1	0.68	0.3965	-0.0906	1.25	--
511	26.1	0.75	0.4666	-0.1127	1.24	--
512	28.0	0.91	0.5800	-0.1517	1.24	--
513	30.2	0.96	0.6576	-0.1711	1.23	--
514	32.1	1.04	0.7501	-0.1985	1.23	--
515	34.0	1.10	0.8380	-0.2243	1.21	--

Table B3. S824, Clean, Re = 1.25 x 10^6

RUN	AOA	C_l	C_{dp}	$C_{m¼}$	Re x 10^{-6}	C_{dw}
516	36.1	1.14	0.9305	-0.2490	1.19	--
517	38.1	1.18	1.0246	-0.2754	1.17	--
518	40.0	1.20	1.1024	-0.2955	1.16	--

End of Table B3

Table B4. S824, LEGR, Re = 0.75 x 10^6

RUN	AOA	C_l	C_{dp}	$C_{m¼}$	Re x 10^{-6}	C_{dw}
366	-10.1	-0.78	0.0297	-0.0141	0.75	0.0436
365	-8.2	-0.71	0.0181	-0.0115	0.75	0.0233
364	-6.2	-0.59	0.0131	-0.0039	0.75	0.0180
363	-4.2	-0.44	0.0086	0.0005	0.75	0.0176
362	-2.0	-0.23	0.0061	0.0016	0.75	0.0167
361	-0.1	-0.03	0.0066	0.0013	0.75	0.0155
367	-0.1	-0.03	0.0054	0.0016	0.74	0.0160
393	-0.1	-0.04	0.0062	0.0017	0.74	0.0149
368	2.1	0.18	0.0068	0.0017	0.75	0.0156
369	4.1	0.37	0.0093	0.0026	0.75	0.0165
370	6.0	0.55	0.0121	0.0066	0.75	0.0172
371	8.2	0.68	0.0207	0.0136	0.74	0.0202
372	10.0	0.75	0.0301	0.0158	0.75	0.0310
373	11.3	0.77	0.0403	0.0166	0.74	--
374	12.1	0.77	0.0452	0.0169	0.74	--
375	13.2	0.77	0.0571	0.0151	0.75	--
376	14.3	0.76	0.0727	0.0097	0.75	--
377	15.1	0.67	0.1024	-0.0083	0.75	--
378	16.1	0.61	0.1553	-0.0363	0.75	--
379	17.2	0.63	0.1805	-0.0424	0.76	--
380	18.0	0.67	0.1985	-0.0460	0.76	--
381	19.1	0.71	0.2359	-0.0599	0.76	--
382	20.2	0.78	0.2840	-0.0763	0.76	--
383	22.1	0.89	0.3632	-0.0976	0.76	--
384	24.1	1.04	0.4233	-0.0982	0.76	--
385	26.2	0.96	0.4744	-0.1002	0.75	--
386	28.1	0.86	0.5507	-0.1380	0.75	--
387	30.0	0.96	0.6497	-0.1689	0.74	--
388	32.2	1.04	0.7471	-0.1971	0.74	--
389	34.1	1.08	0.8269	-0.2186	0.74	--

Table B4. S824, LEGR, Re = 0.75 x 10^6

RUN	AOA	C_l	C_{dp}	$C_{m¼}$	Re x 10^{-6}	C_{dw}
390	36.1	1.16	0.9469	-0.2597	0.73	--
391	38.1	1.18	1.0230	-0.2776	0.73	--
392	40.1	1.19	1.0951	-0.2939	0.73	--

End of Table B4

Table B5. S824, LEGR, Re = 1.0 x 10^6

RUN	AOA	C_l	C_{dp}	$C_{m1/4}$	Re x 10^{-6}	C_{dw}
399	-10.1	-0.76	0.0300	-0.0129	1.00	0.0496
398	-8.2	-0.71	0.0177	-0.0125	1.00	0.0259
397	-6.2	-0.59	0.0125	-0.0047	1.00	0.0168
396	-4.0	-0.41	0.0082	-0.0008	1.00	0.0160
395	-2.0	-0.22	0.0062	0.0017	1.00	0.0142
394	-0.1	-0.02	0.0059	0.0008	1.00	0.0155
400	-0.1	-0.03	0.0060	0.0007	1.01	0.0150
426	-0.1	-0.03	0.0057	0.0004	1.00	0.0143
401	2.2	0.18	0.0076	0.0005	1.00	0.0157
402	4.1	0.38	0.0100	0.0012	1.01	0.0164
403	6.1	0.56	0.0136	0.0045	1.01	0.0157
404	8.1	0.69	0.0191	0.0123	1.01	0.0201
405	10.3	0.76	0.0343	0.0127	1.00	0.0283
406	11.3	0.78	0.0431	0.0106	1.00	--
407	12.2	0.79	0.0498	0.0117	1.00	--
408	13.3	0.79	0.0597	0.0127	1.00	--
409	14.1	0.77	0.0733	0.0067	1.00	--
410	15.2	0.72	0.0957	-0.0032	1.00	--
411	16.2	0.66	0.1348	-0.0232	1.01	--
412	17.1	0.65	0.1708	-0.0376	1.00	--
413	18.1	0.67	0.1982	-0.0466	1.01	--
414	19.2	0.70	0.2343	-0.0585	1.00	--
415	20.1	0.75	0.2766	-0.0740	1.00	--
416	22.0	0.77	0.3515	-0.0957	1.01	--
417	24.1	0.72	0.3948	-0.1002	1.00	--
418	26.1	0.72	0.4377	-0.1040	0.99	--
419	28.3	0.83	0.5355	-0.1299	1.01	--
420	30.2	0.95	0.6416	-0.1645	0.99	--
421	32.1	1.03	0.7411	-0.1942	1.00	--
422	34.0	1.09	0.8274	-0.2198	0.98	--

Table B5. S824, LEGR, Re = 1.0 x 10^6

RUN	AOA	C_l	C_{dp}	$C_{m¼}$	Re x 10^{-6}	C_{dw}
423	36.0	1.13	0.9185	-0.2455	0.98	--
424	38.1	1.17	1.0126	-0.2724	0.96	--
425	40.0	1.19	1.0997	-0.2977	0.98	--

End of Table B5

Table B6. S824, LEGR, Re = 1.25 x 10^6

RUN	AOA	C_l	C_{dp}	$C_{m¼}$	Re x 10^{-6}	C_{dw}
432	-10.1	-0.76	0.0314	-0.0108	1.25	0.0573
431	-8.2	-0.71	0.0177	-0.0129	1.25	0.0249
430	-6.2	-0.59	0.0128	-0.0051	1.25	0.0164
429	-4.3	-0.43	0.0081	-0.0012	1.25	0.0155
428	-2.0	-0.23	0.0060	0.0008	1.25	0.0138
459	-0.2	-0.06	0.0054	0.0004	1.25	0.0152
427	-0.1	-0.02	0.0051	0.0007	1.25	0.0137
433	-0.1	-0.01	0.0056	0.0001	1.25	0.0136
434	2.2	0.19	0.0074	-0.0003	1.25	0.0147
435	4.1	0.39	0.0100	0.0007	1.26	0.0163
436	6.1	0.55	0.0137	0.0055	1.25	0.0161
437	8.3	0.69	0.0207	0.0125	1.25	0.0209
438	10.3	0.77	0.0339	0.0117	1.25	0.0276
439	11.1	0.79	0.0400	0.0109	1.25	--
440	12.2	0.79	0.0480	0.0137	1.25	--
441	13.3	0.81	0.0659	0.0074	1.25	--
442	14.3	0.79	0.0782	0.0048	1.25	--
443	15.2	0.74	0.0973	-0.0040	1.25	--
444	16.2	0.68	0.1334	-0.0209	1.25	--
445	17.0	0.67	0.1721	-0.0399	1.25	--
446	18.1	0.69	0.2045	-0.0515	1.26	--
447	19.2	0.73	0.2346	-0.0611	1.26	--
448	20.1	0.77	0.2719	-0.0735	1.25	--
449	22.3	0.89	0.3606	-0.0961	1.26	--
450	24.2	0.90	0.4169	-0.1025	1.25	--
451	26.1	0.74	0.4431	-0.1050	1.25	--
452	28.0	0.87	0.5467	-0.1376	1.24	--
453	30.2	0.96	0.6460	-0.1677	1.24	--
454	32.1	1.04	0.7427	-0.1962	1.23	--
455	34.0	1.11	0.8418	-0.2269	1.21	--

Table B6. S824, LEGR, Re = 1.25 x 10^6

RUN	AOA	C_l	C_{dp}	$C_{m¼}$	Re x 10^{-6}	C_{dw}
456	36.0	1.14	0.9213	-0.2467	1.20	--
457	38.1	1.17	1.0129	-0.2721	1.18	--
458	40.0	1.19	1.0928	-0.2940	1.16	--

End of Table B6

S824

Pressure Distributions, Steady State, Re = 0.75 million

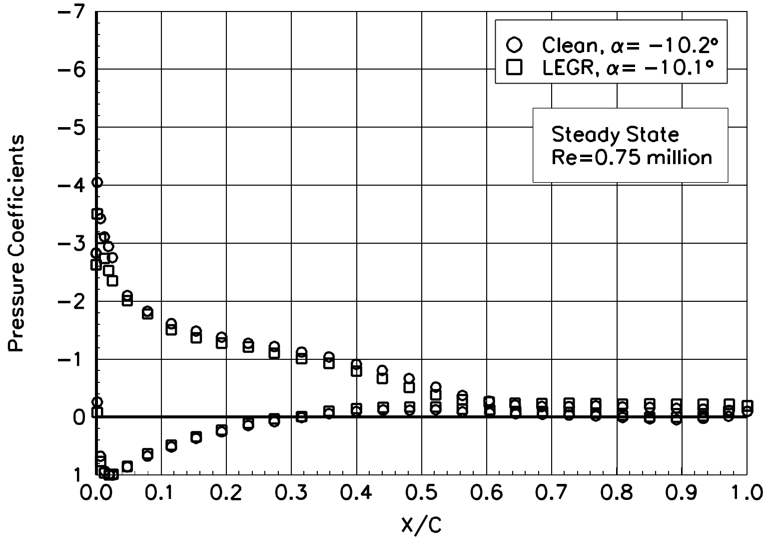

Figure 1. α = -10.2°

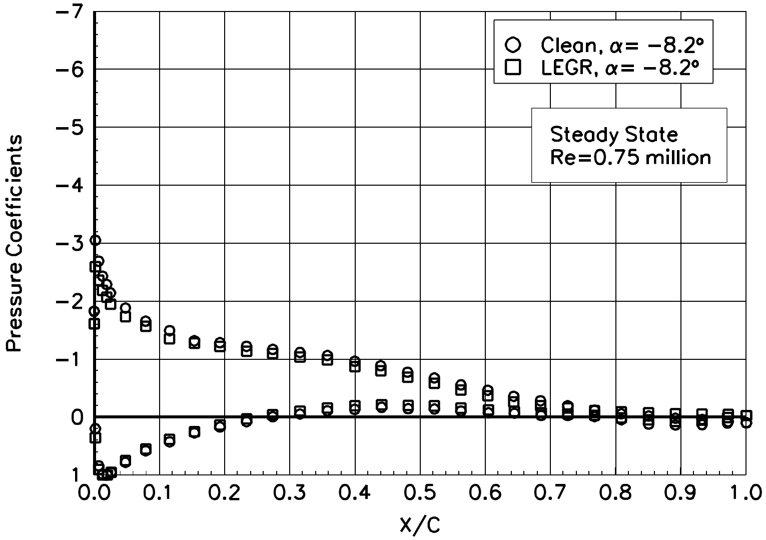

Figure 2. α = -8.2°

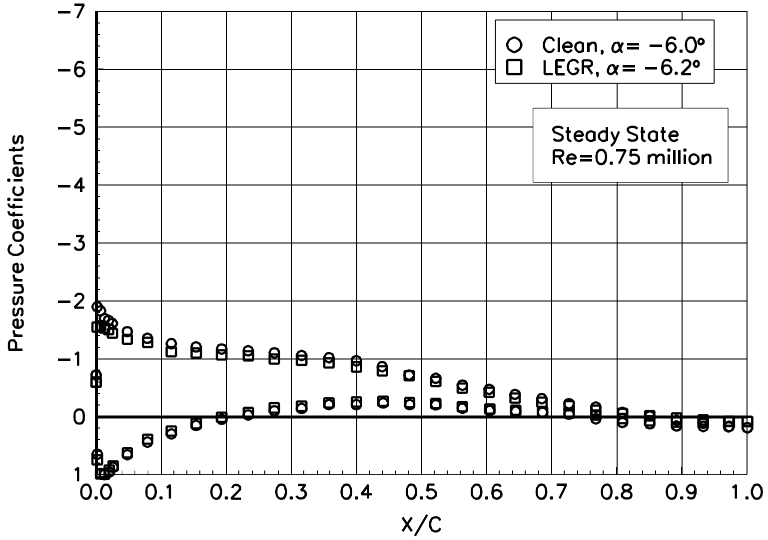

Figure 3. α = -6.0°

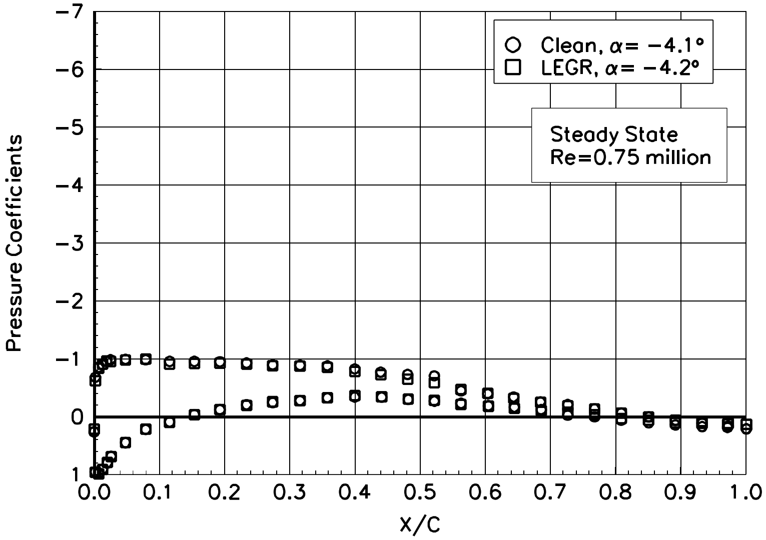

Figure 4. α = -4.1°

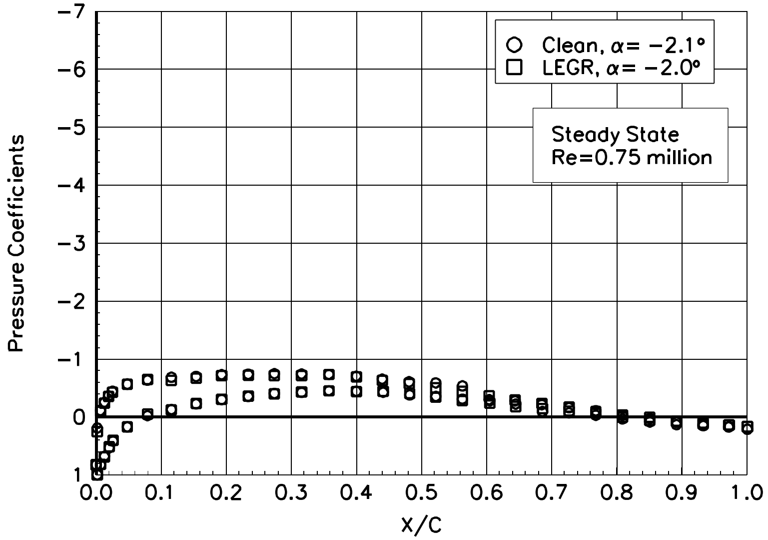

Figure 5. α = -2.1°

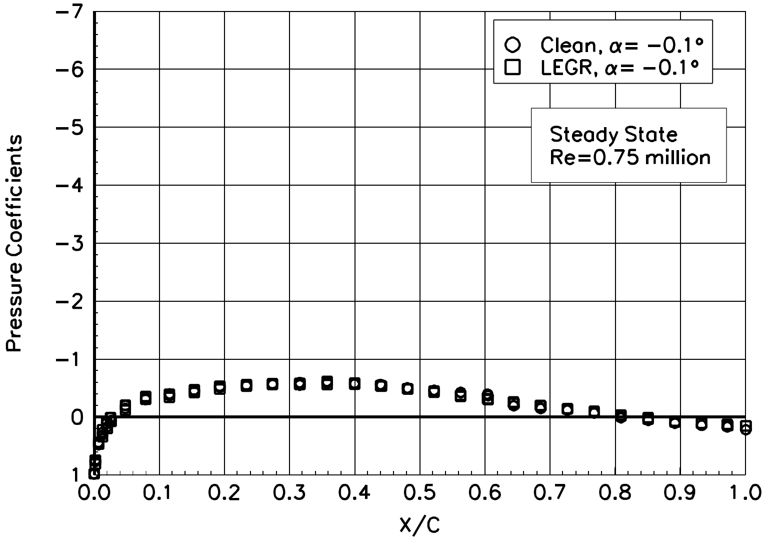

Figure 6. α = -0.1°

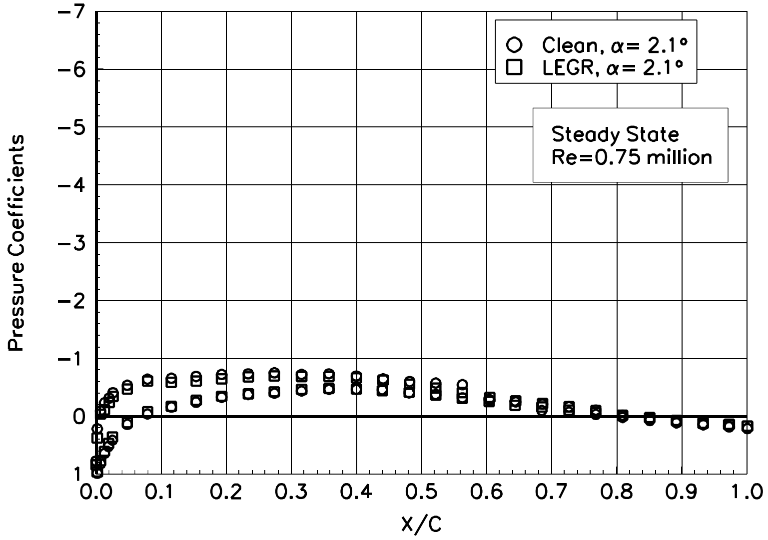

Figure 7. α = 2.1°

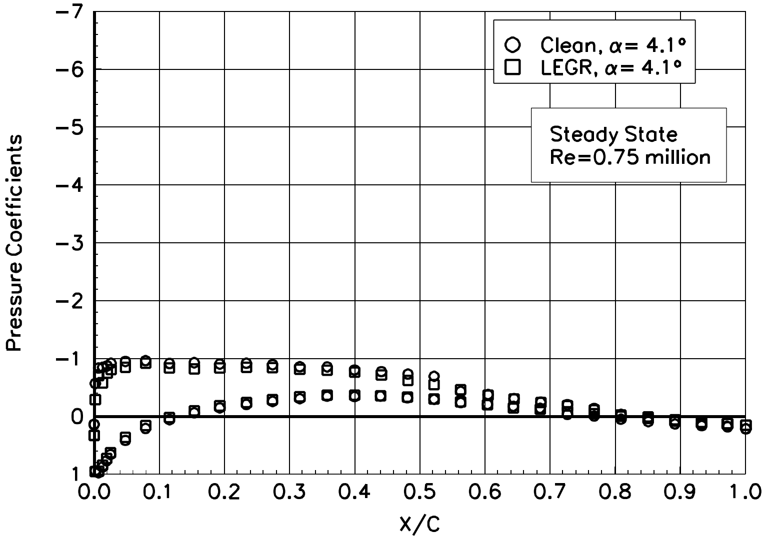

Figure 8. α = 4.1°

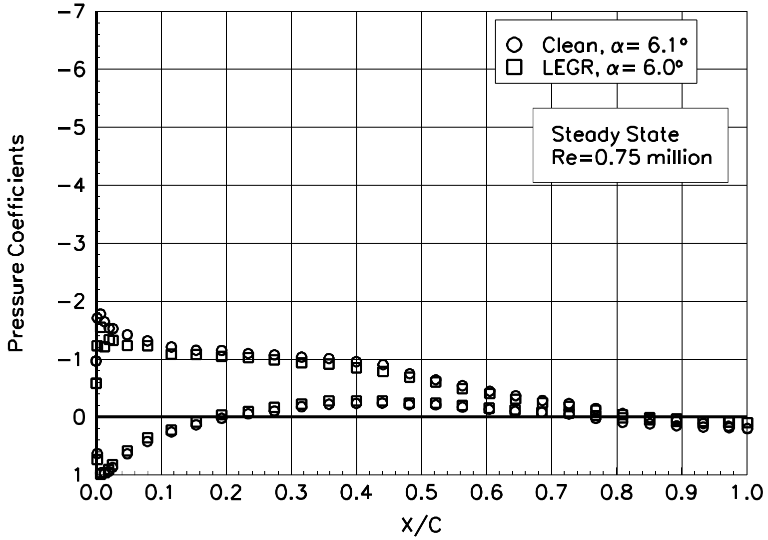

Figure 9. α = 6.1°

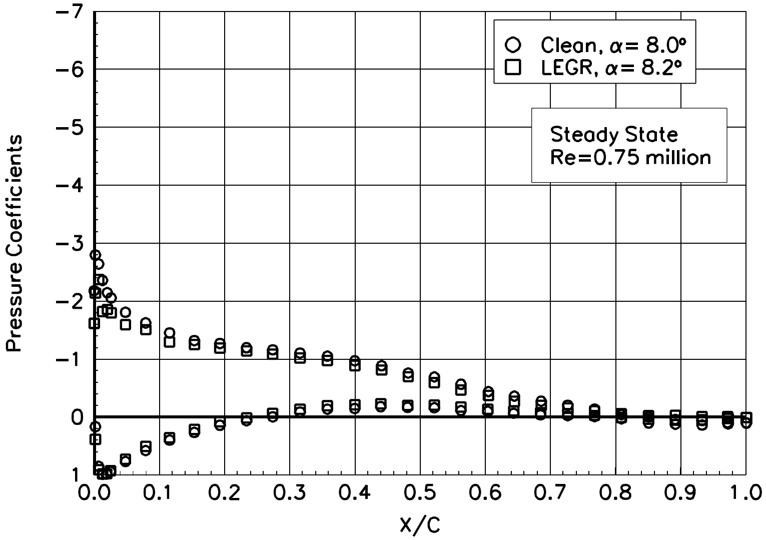

Figure 10. α = 8.0°

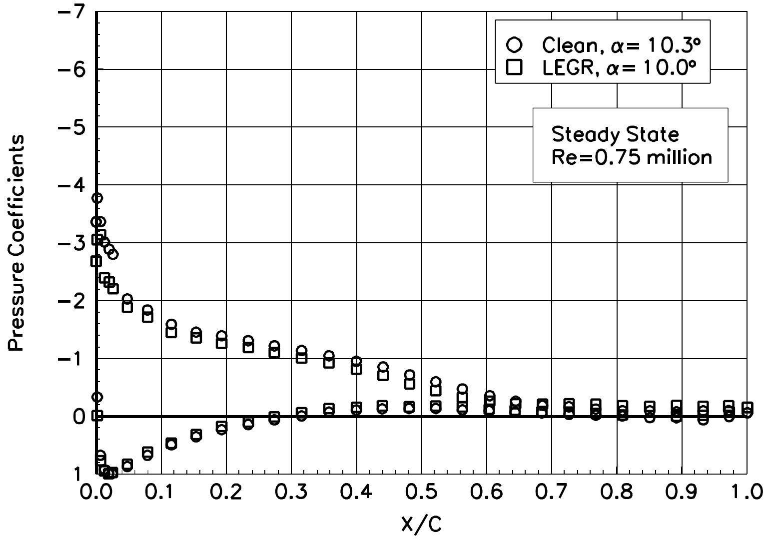

Figure 11. α = 10.3°

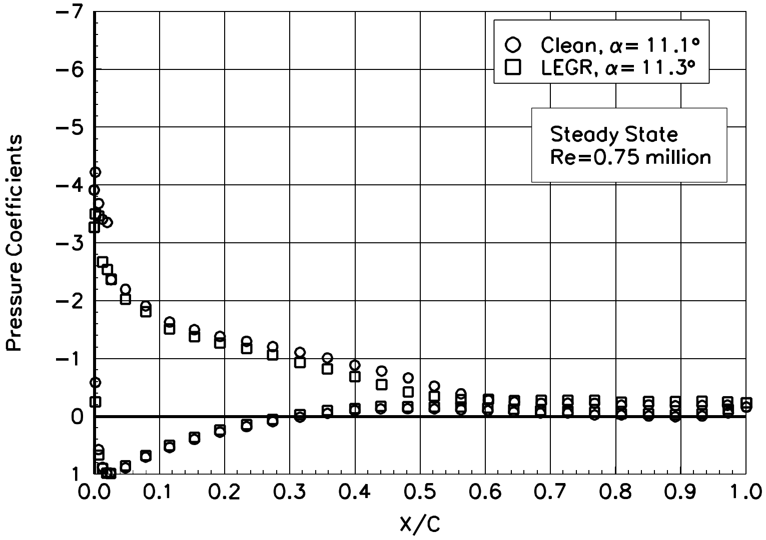

Figure 12. α = 11.1°

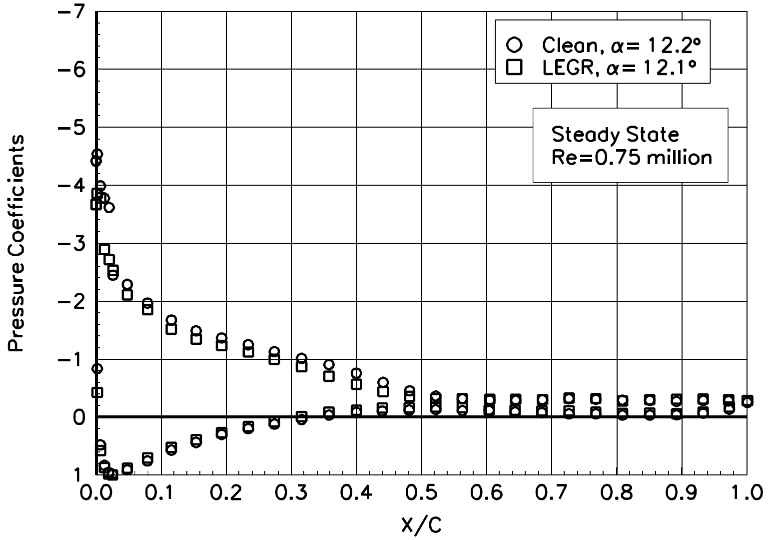

Figure 13. α = 12.2°

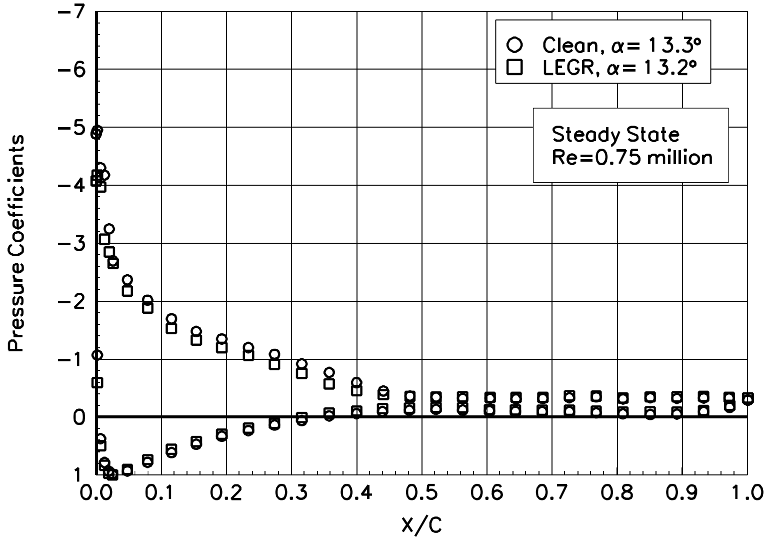

Figure 14. α = 13.3°

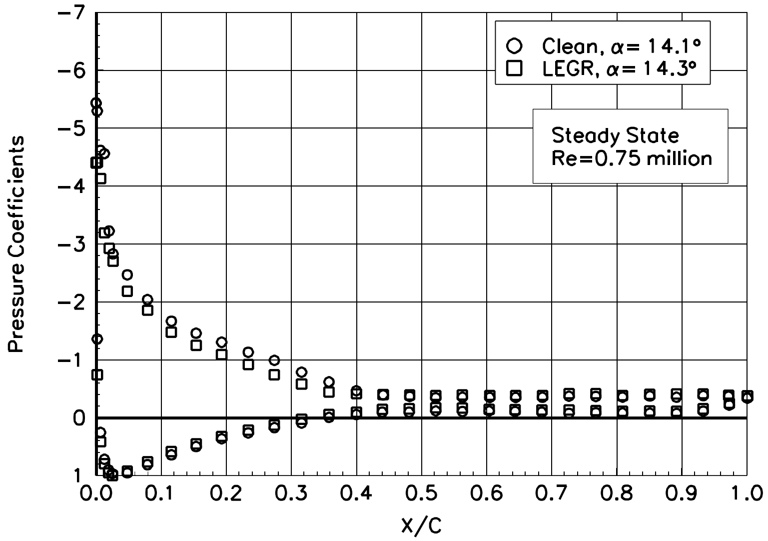

Figure 15. α = 14.1°

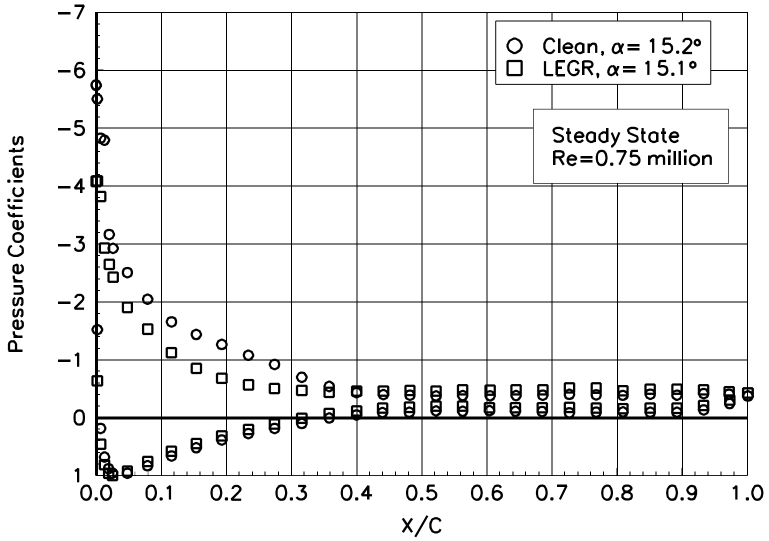

Figure 16. α = 15.2°

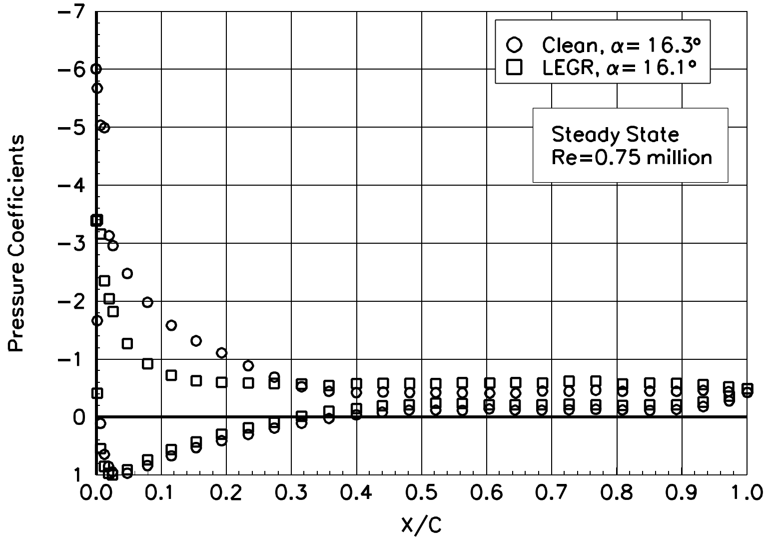

Figure 17. α = 16.3°

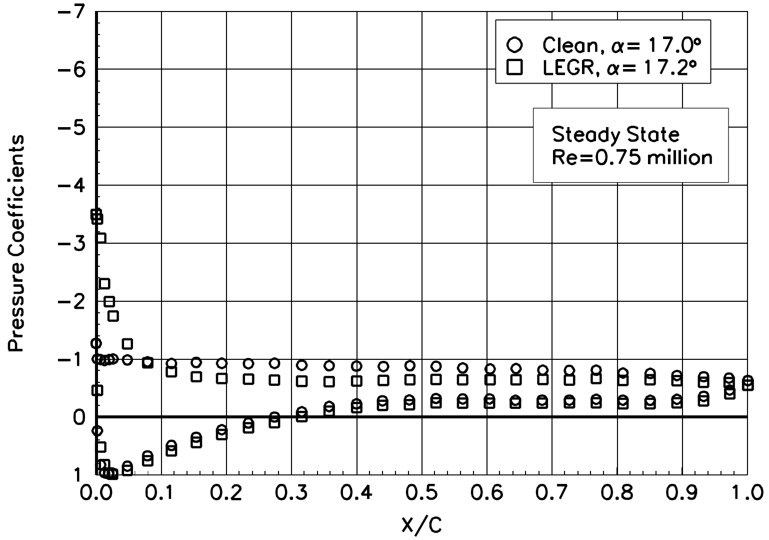

Figure 18. α = 17.0°

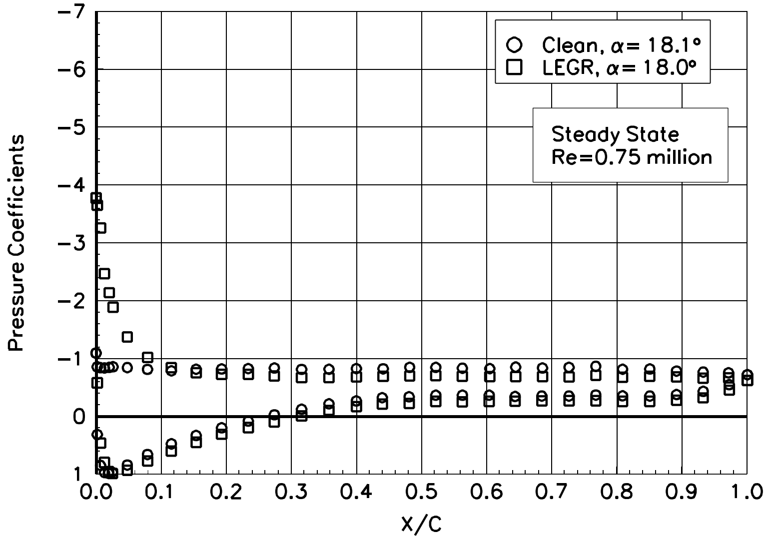

Figure 19. α = 18.1°

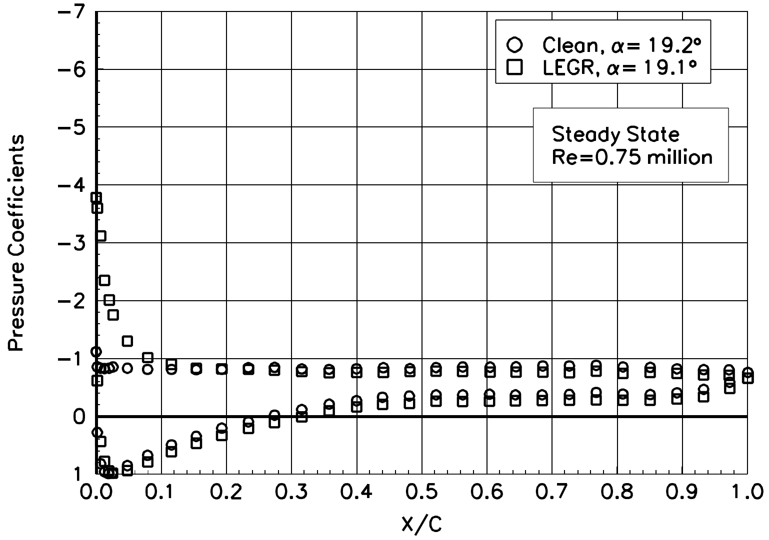

Figure 20. α = 19.2°

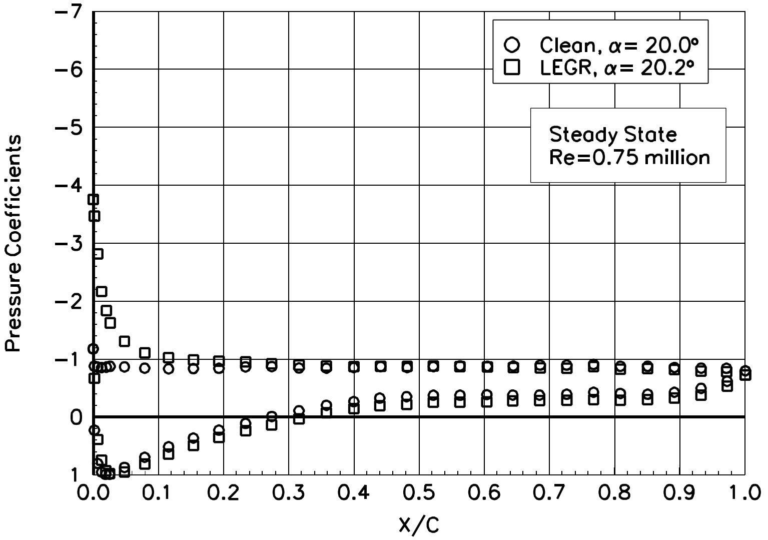

Figure 21. α = 20.0°

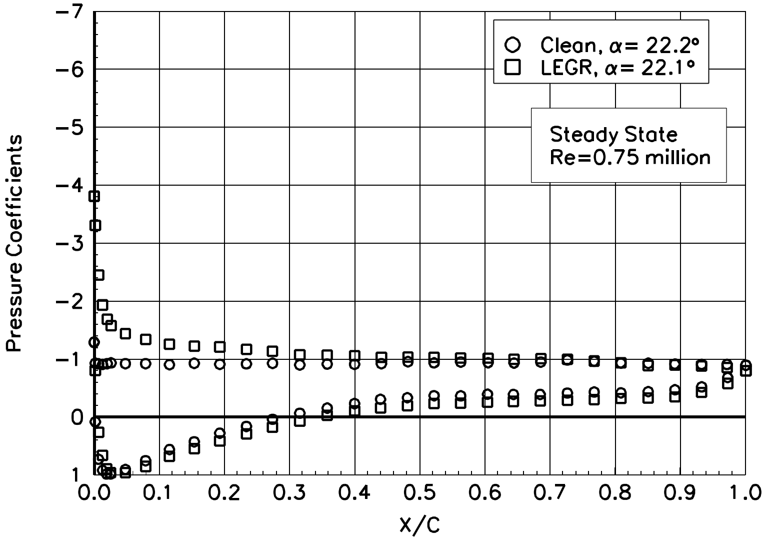

Figure 22. α = 22.2°

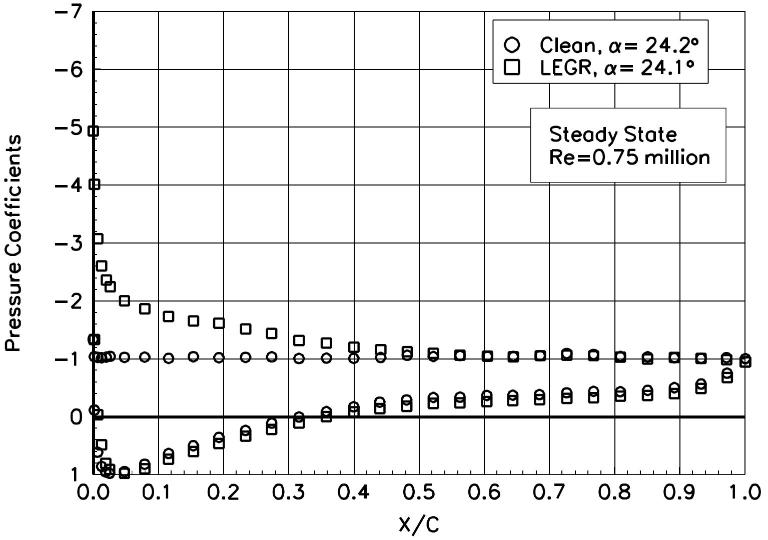

Figure 23. α = 24.2°

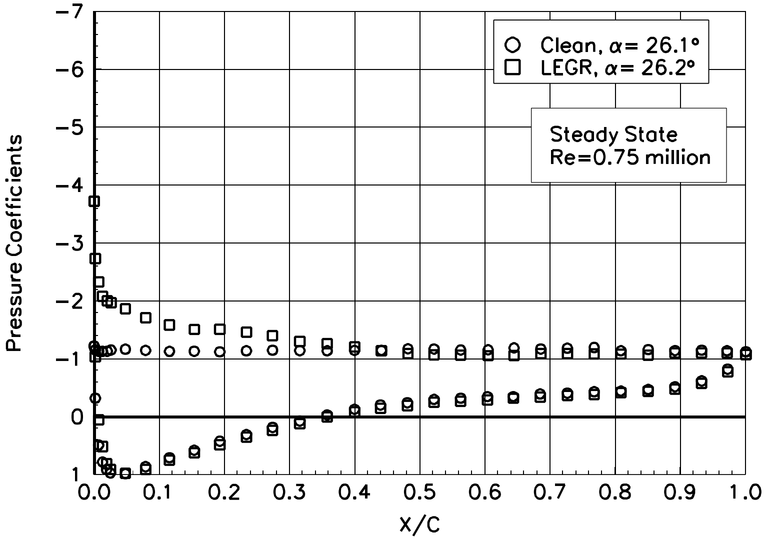

Figure 24. α = 26.1°

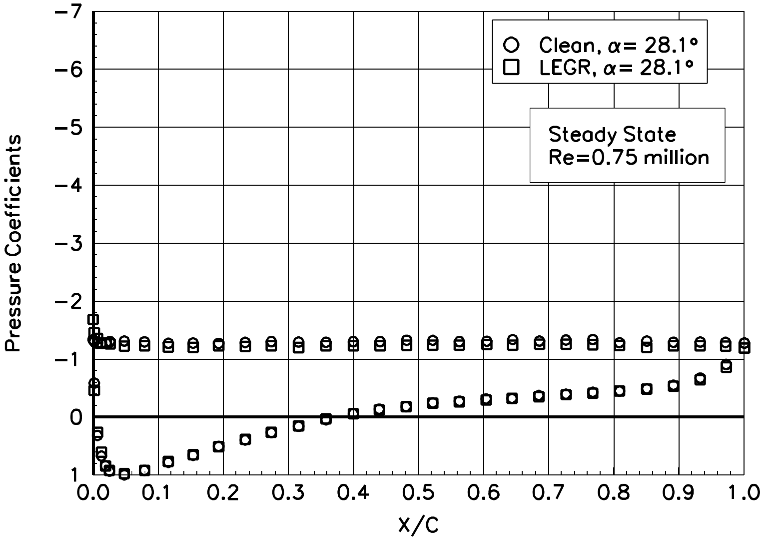

Figure 25. α = 28.1°

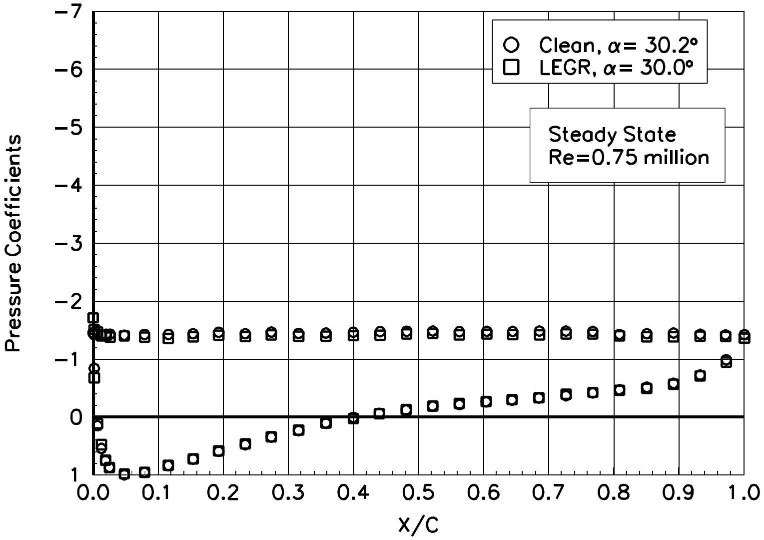

Figure 26. α = 30.2°

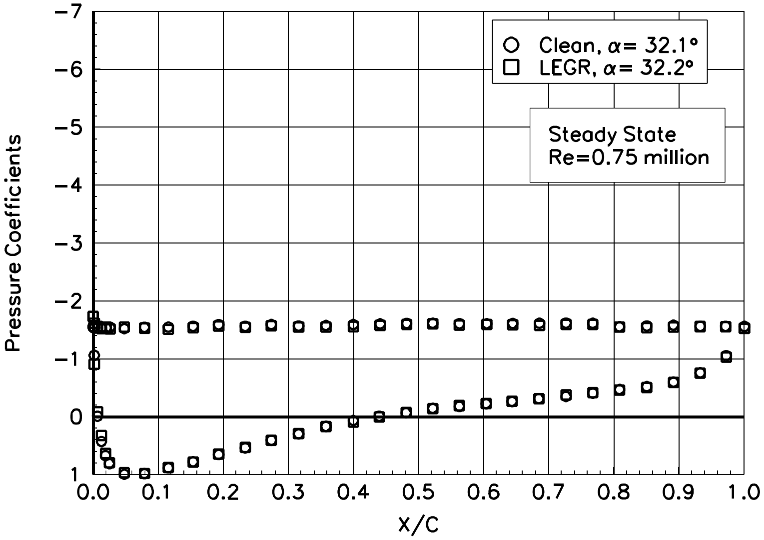

Figure 27. α = 32.1°

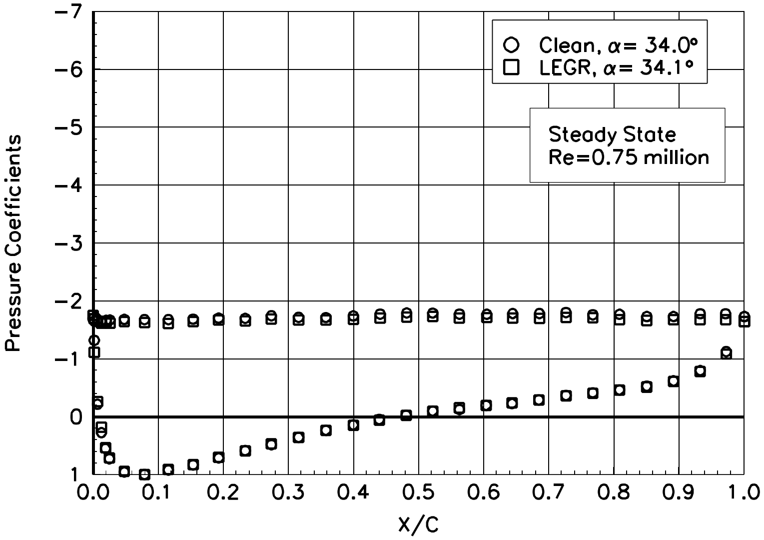

Figure 28. α = 34.0°

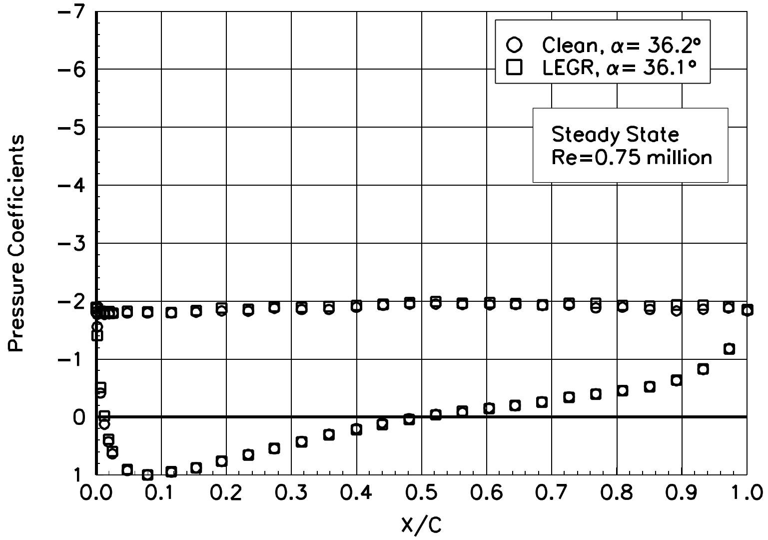

Figure 29. α = 36.2°

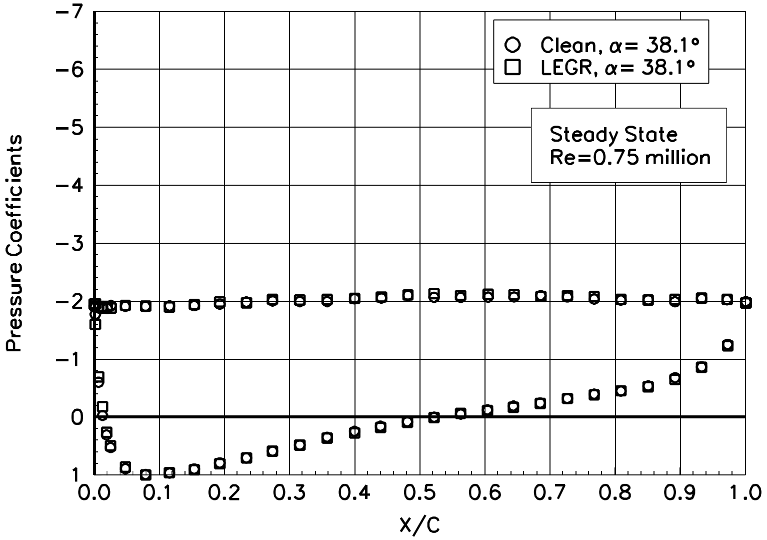

Figure 30. α = 38.1°

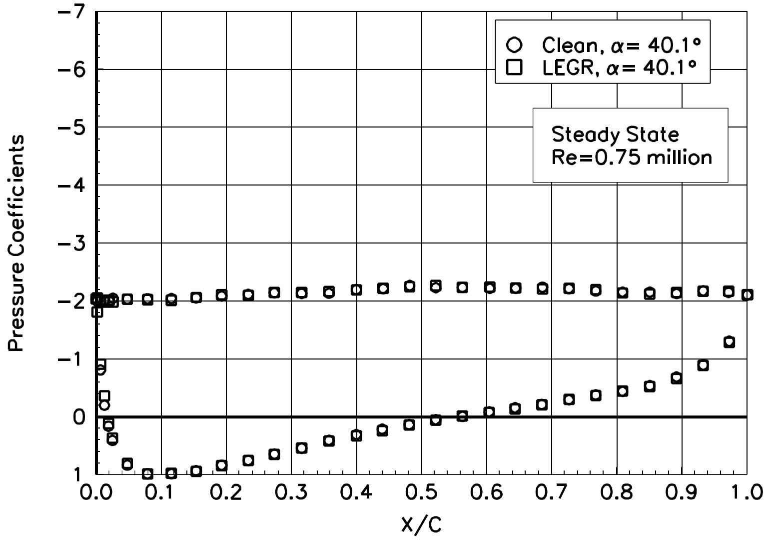

Figure 31. α = 40.1°

S824

Pressure Distributions, Steady State, Re = 1 million

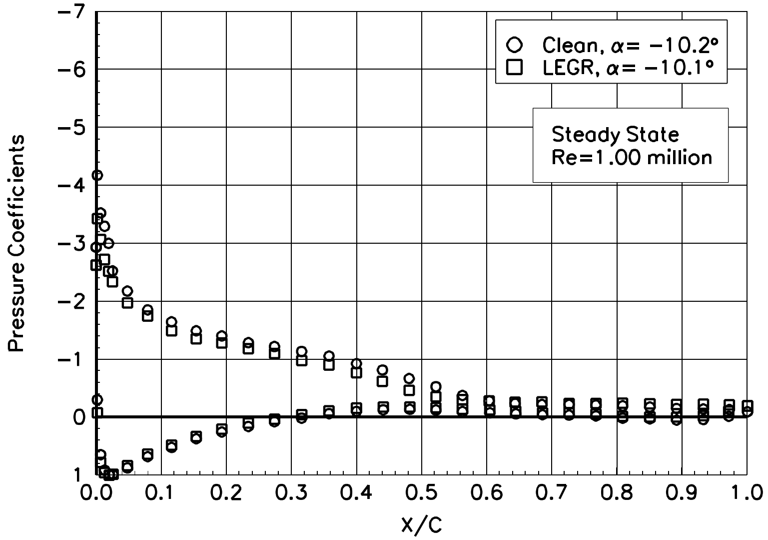

Figure 32. α = -10.2°

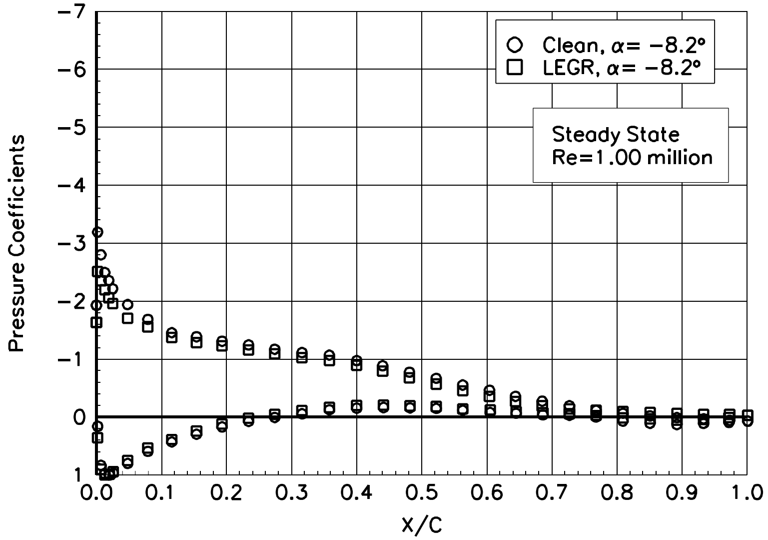

Figure 33. α = -8.2°

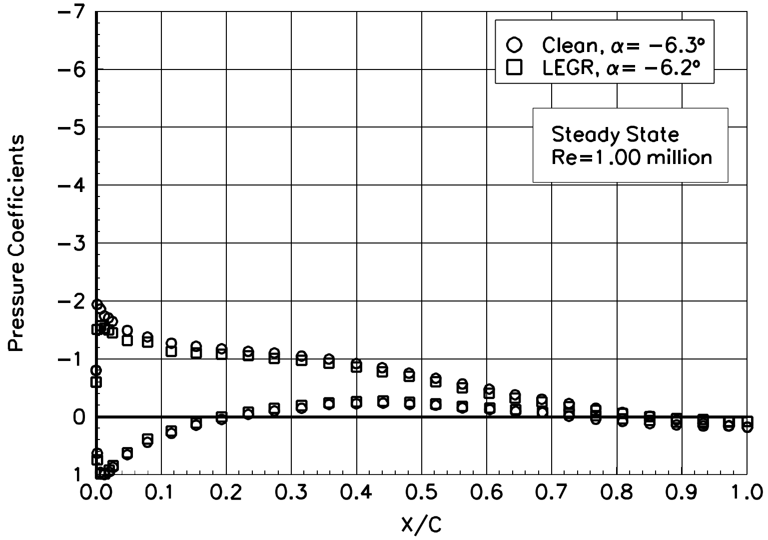

Figure 34. α = -6.3°

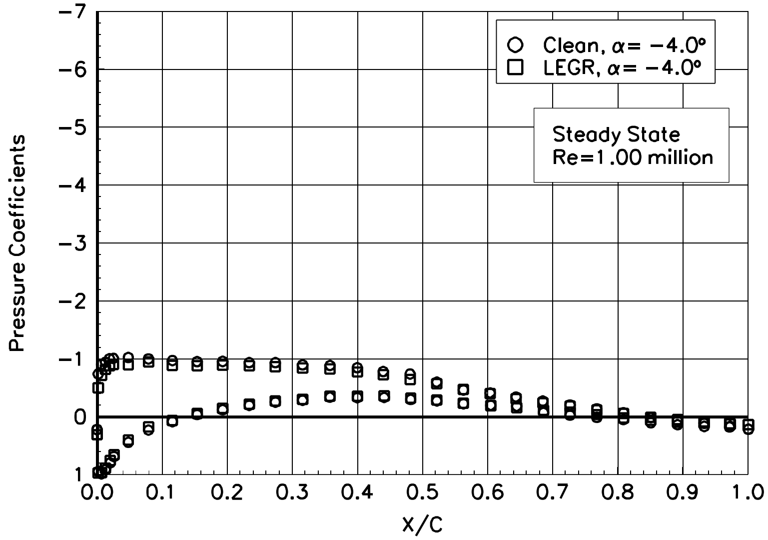

Figure 35. α = -4.0°

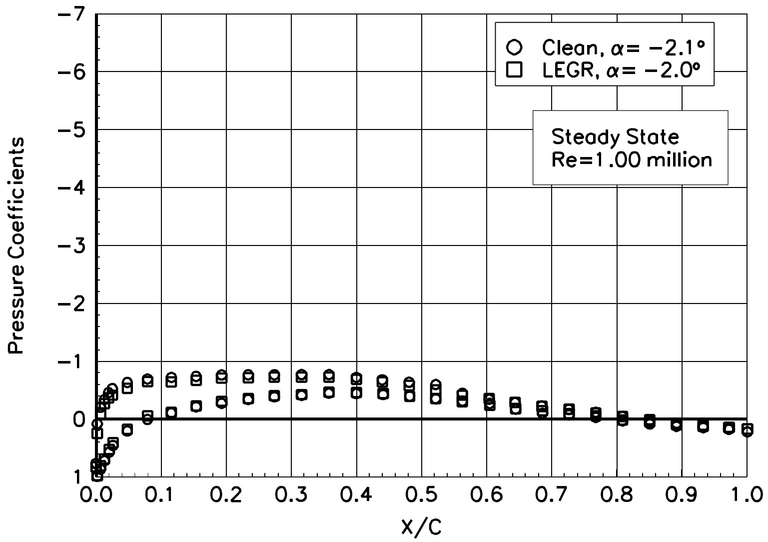

Figure 36. α = -2.1°

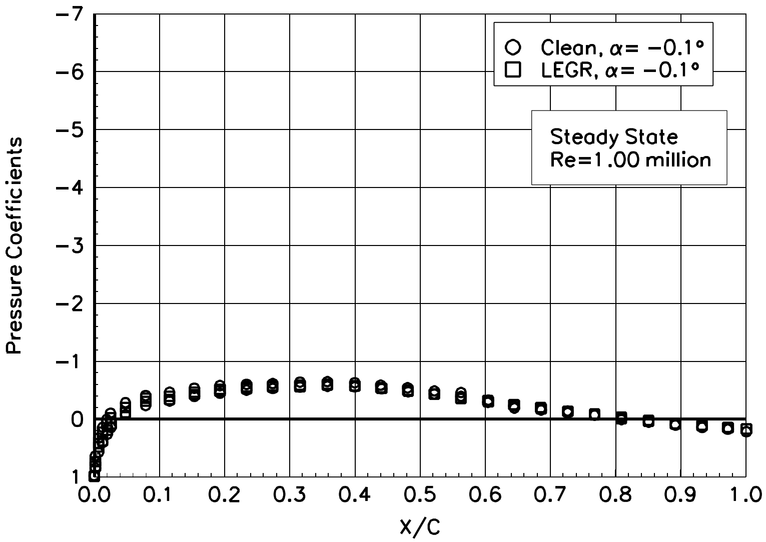

Figure 37. α = -0.1°

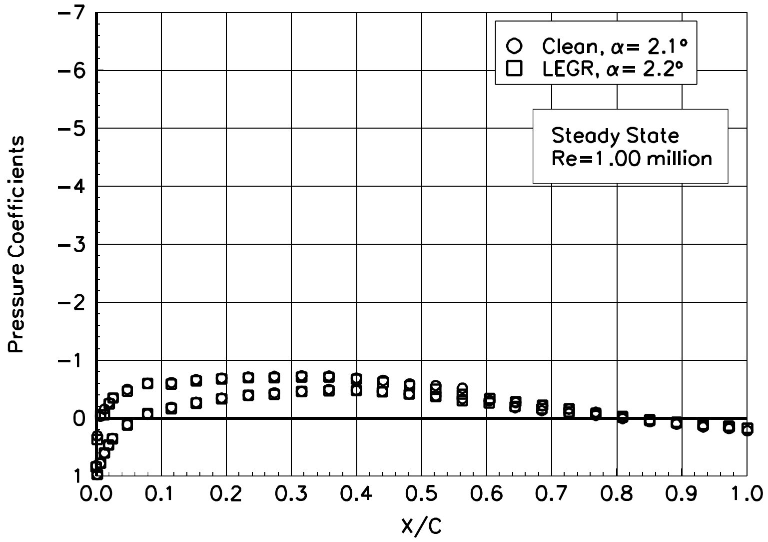

Figure 38. α = 2.1°

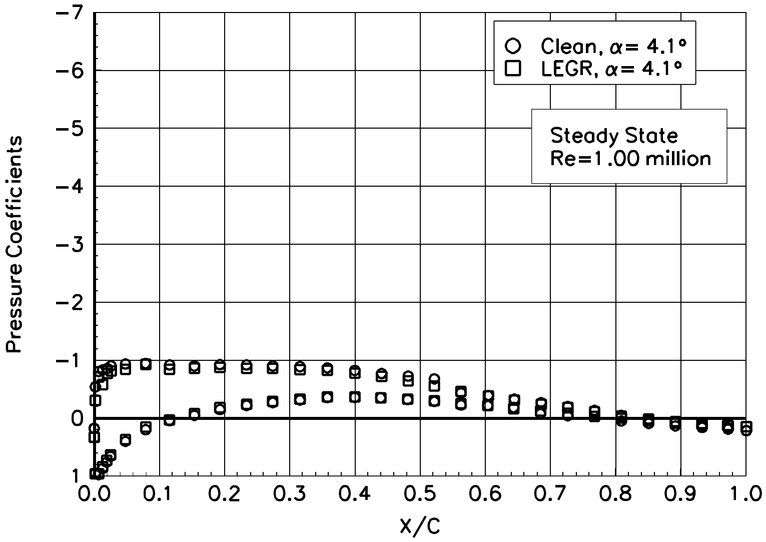

Figure 39. α = 4.1°

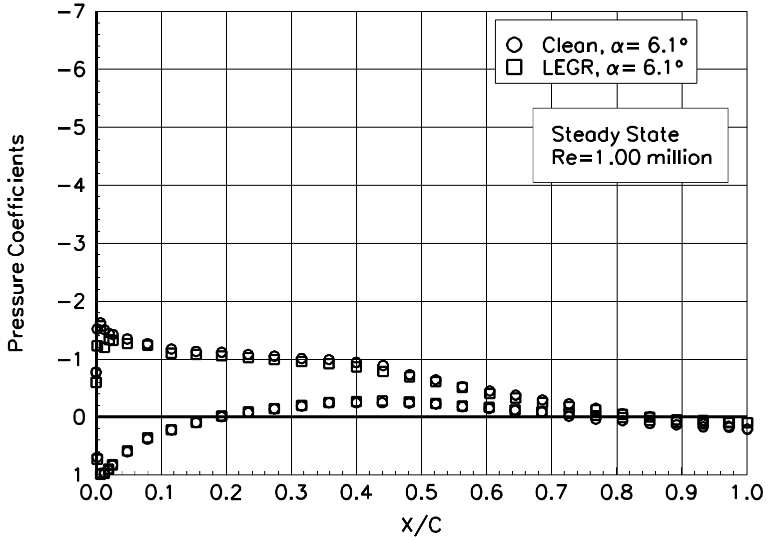

Figure 40. α = 6.1°

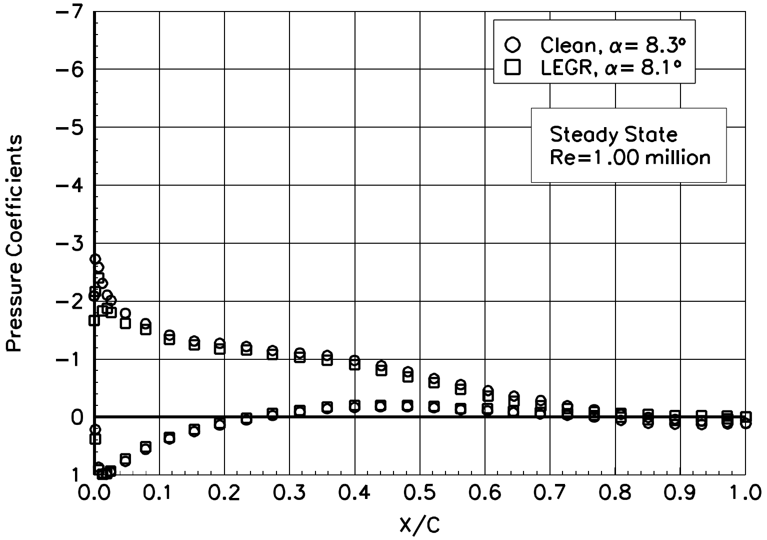

Figure 41. α = 8.3°

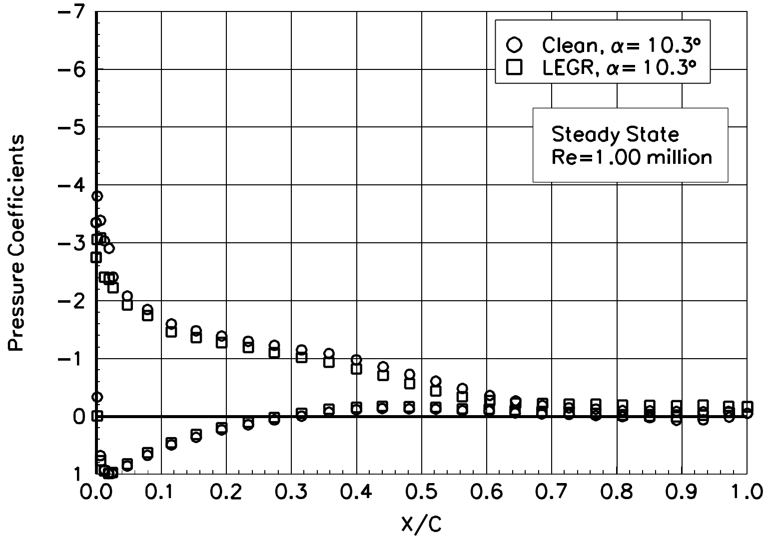

Figure 42. α = 10.3°

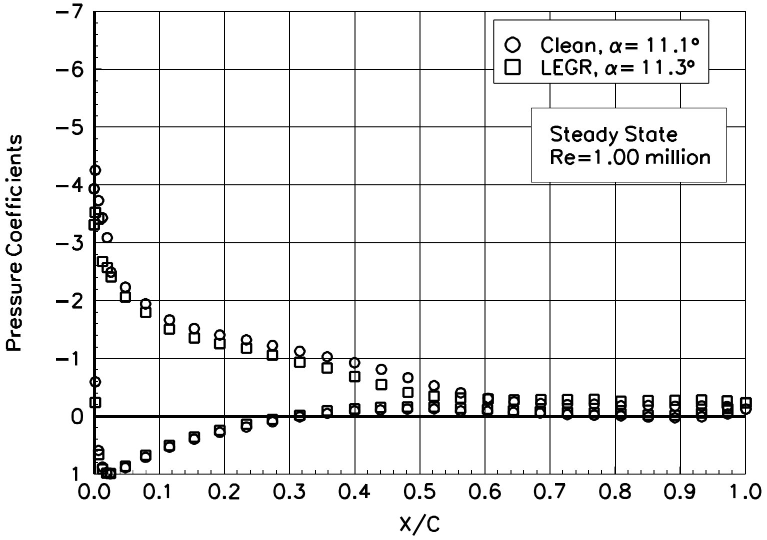

Figure 43. α = 11.1°

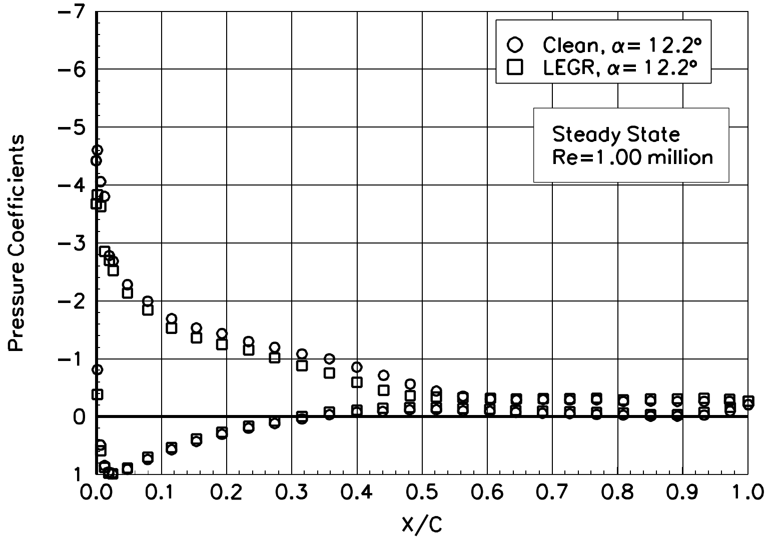

Figure 44. α = 12.2°

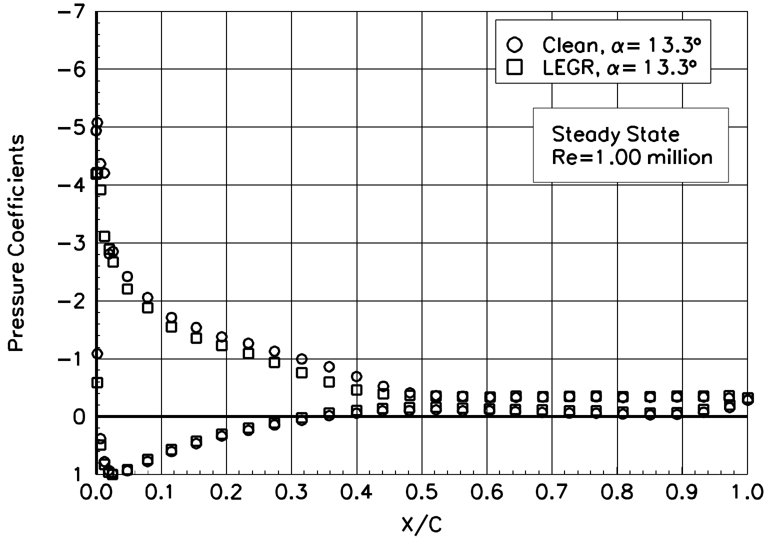

Figure 45. α = 13.3°

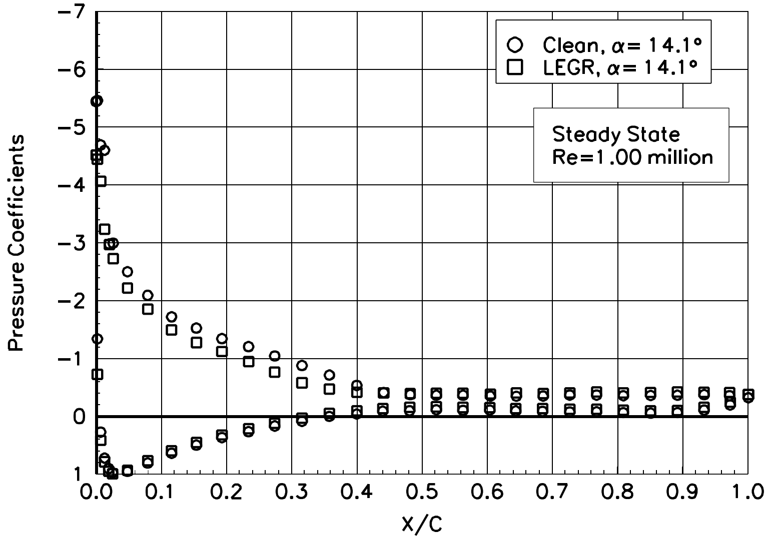

Figure 46. α = 14.1°

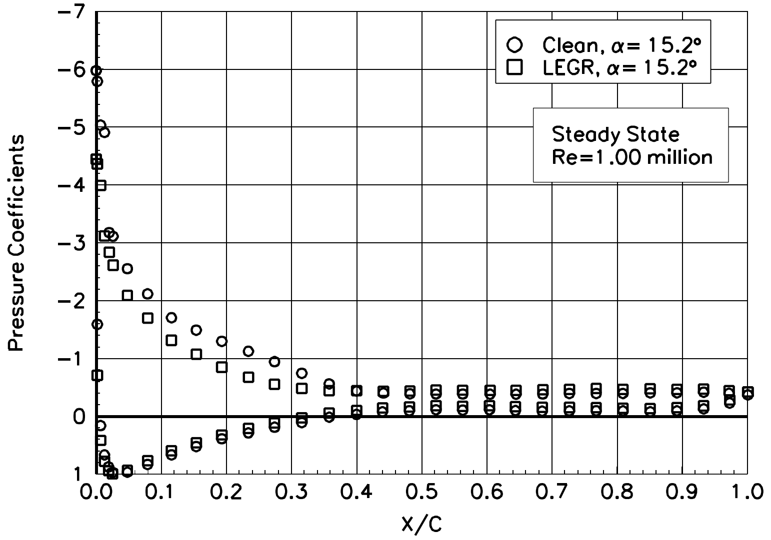

Figure 47. α = 15.2°

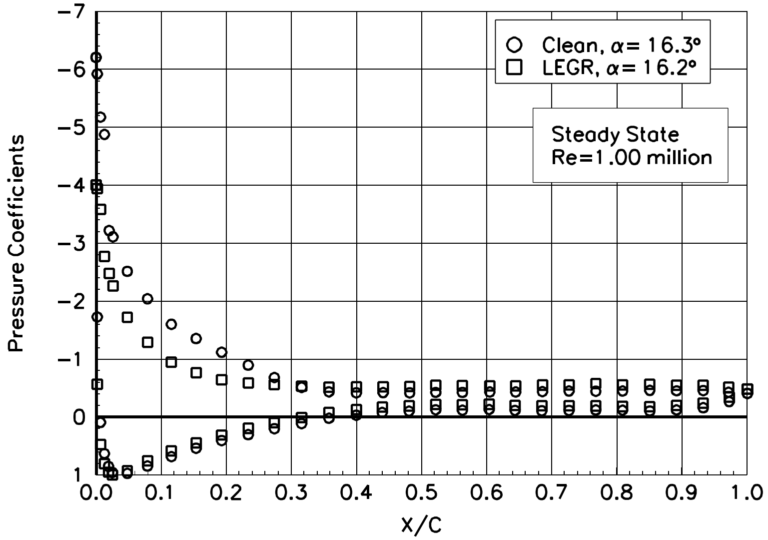

Figure 48. α = 16.3°

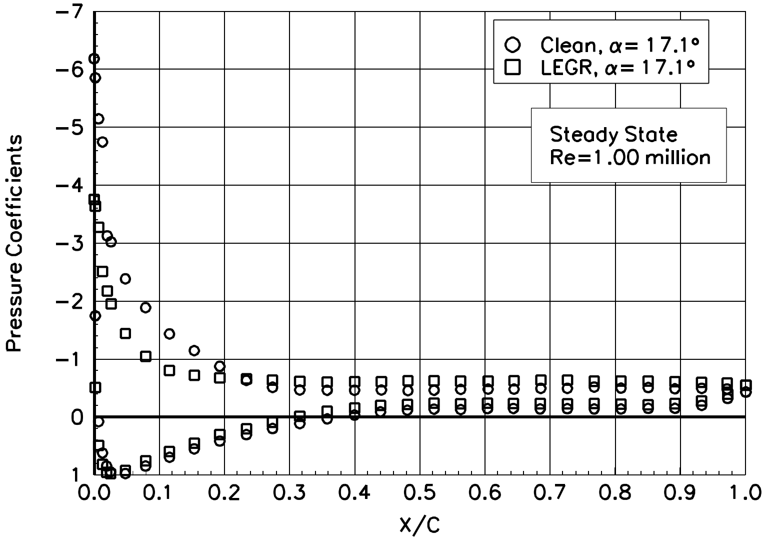

Figure 49. α = 17.1°

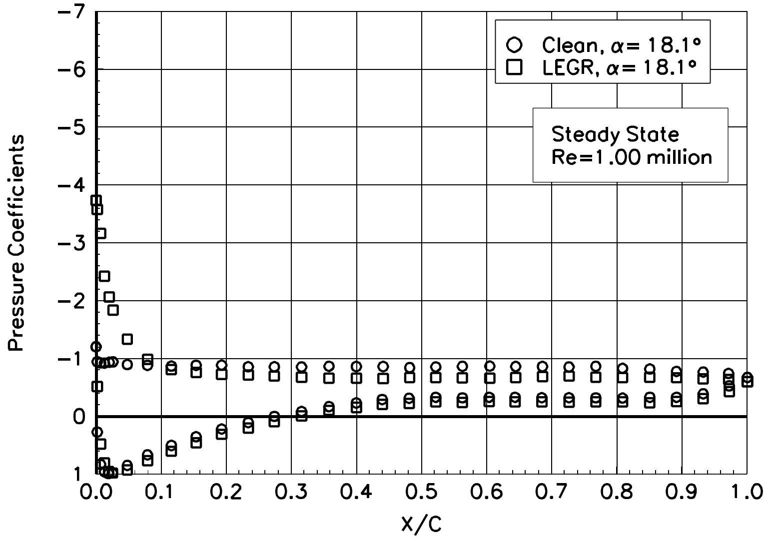

Figure 50. α = 18.1°

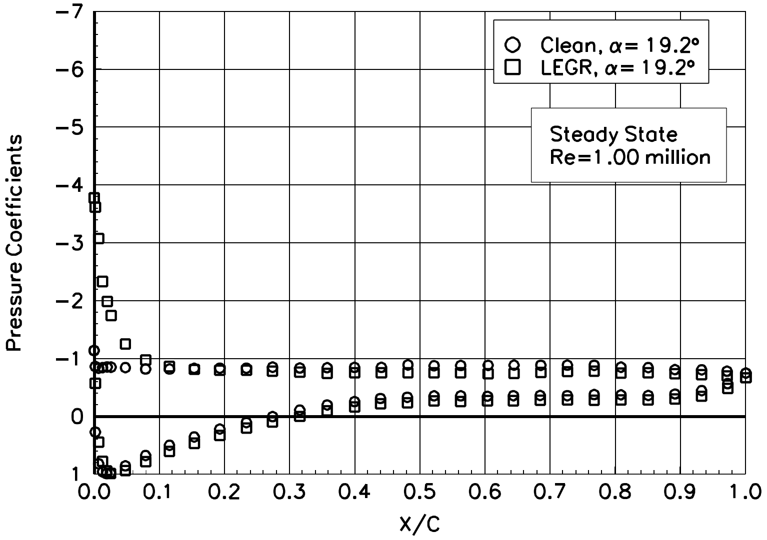

Figure 51. α = 19.2°

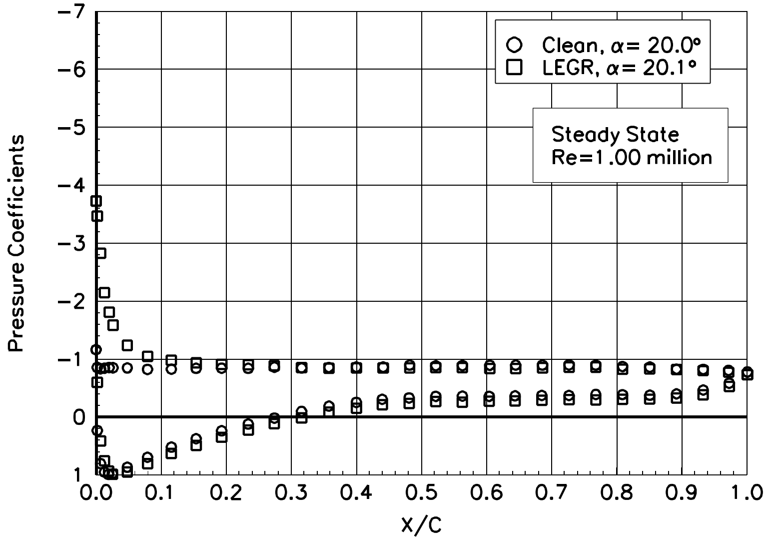

Figure 52. α = 20.0°

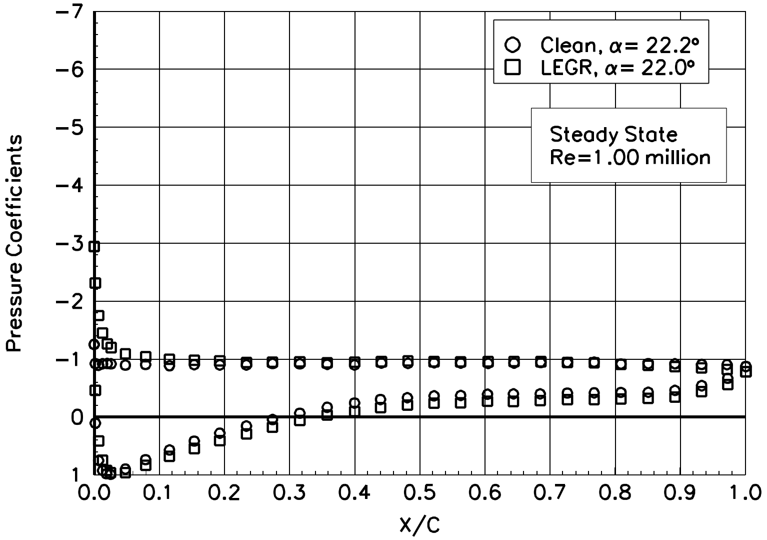

Figure 53. α = 22.2°

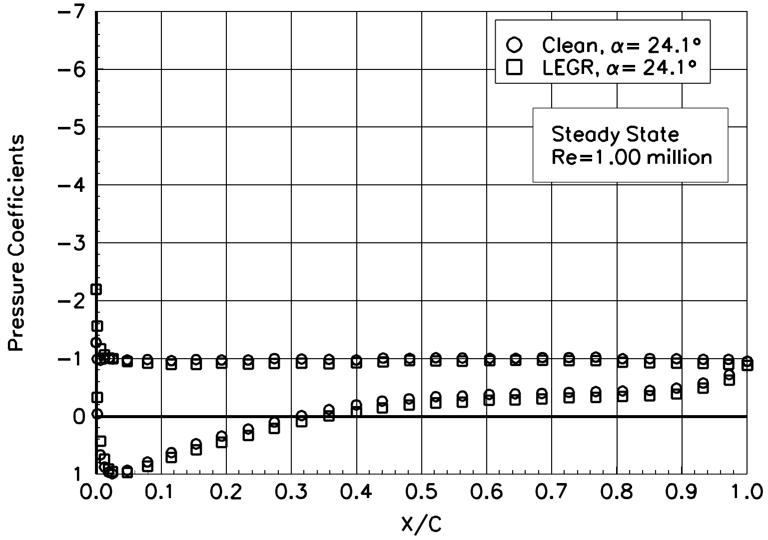

Figure 54. α = 24.1°

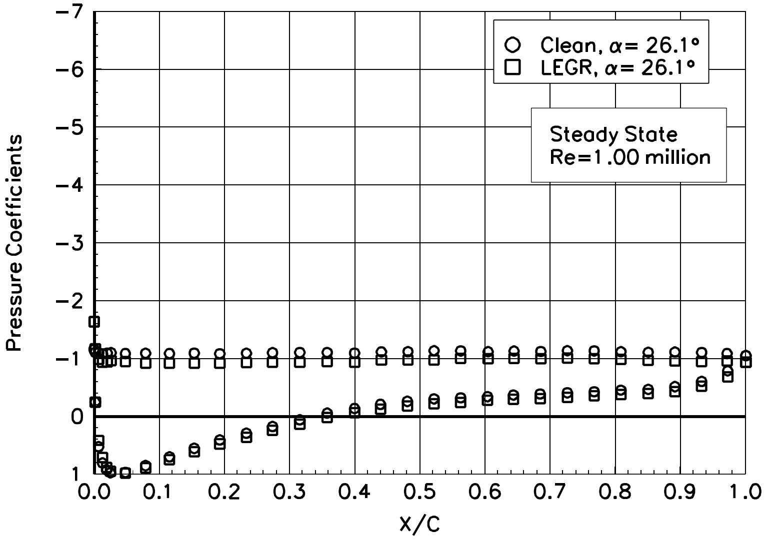

Figure 55. α = 26.1°

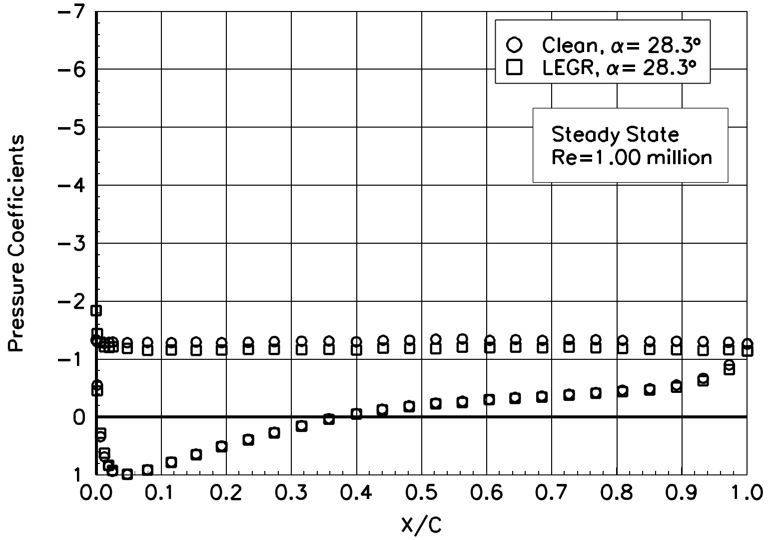

Figure 56. α = 28.3°

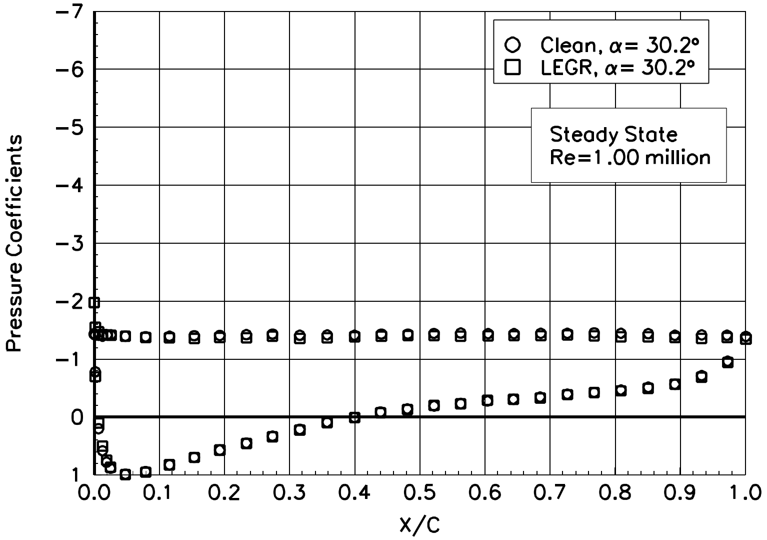

Figure 57. α = 30.2°

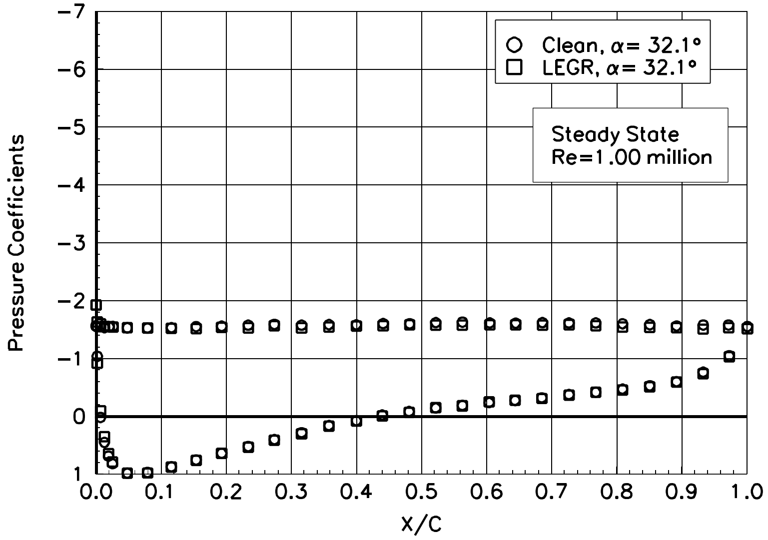

Figure 58. α = 32.1°

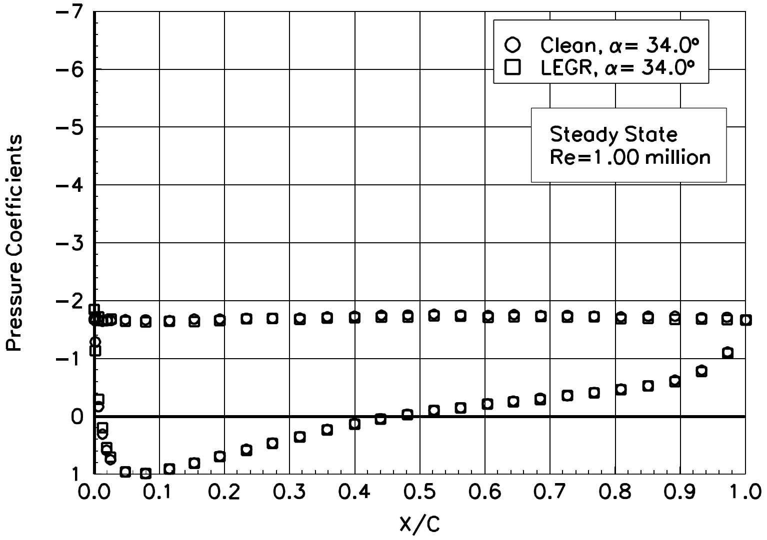

Figure 59. α = 34.0°

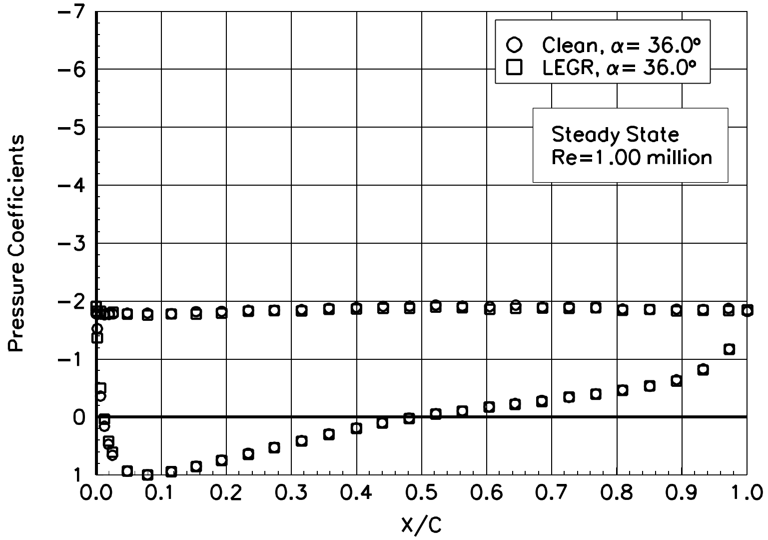

Figure 60. α = 36.0°

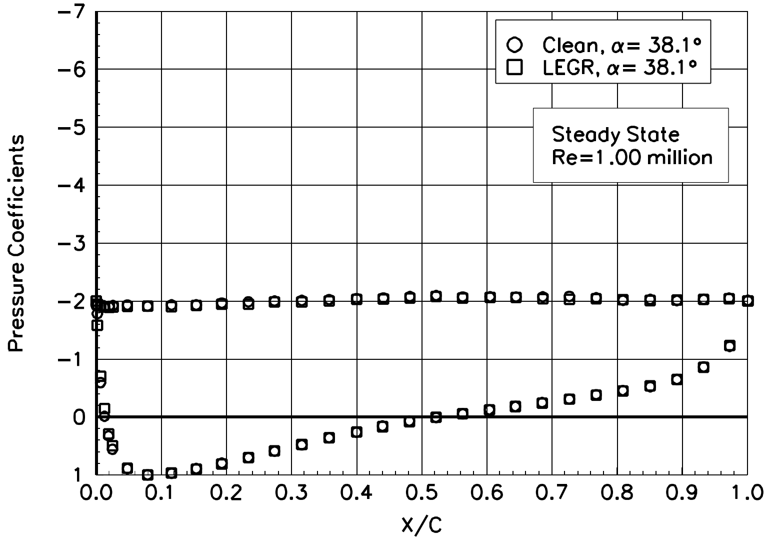

Figure 61. α = 38.1°

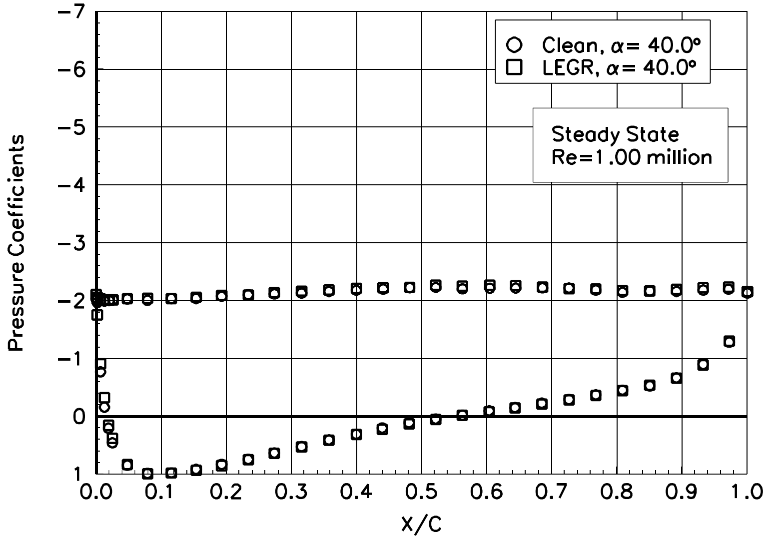

Figure 62. α = 40.0°

S824

Pressure Distributions, Steady State, Re = 1.25 million

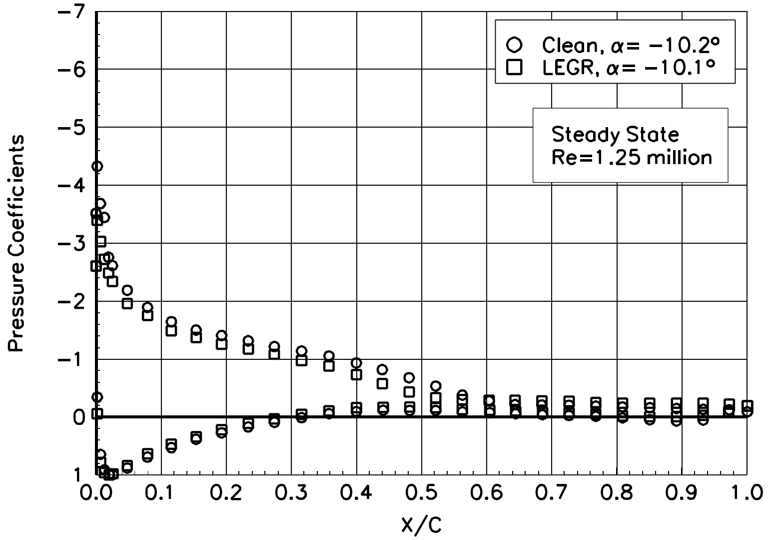

Figure 63. α = -10.2°

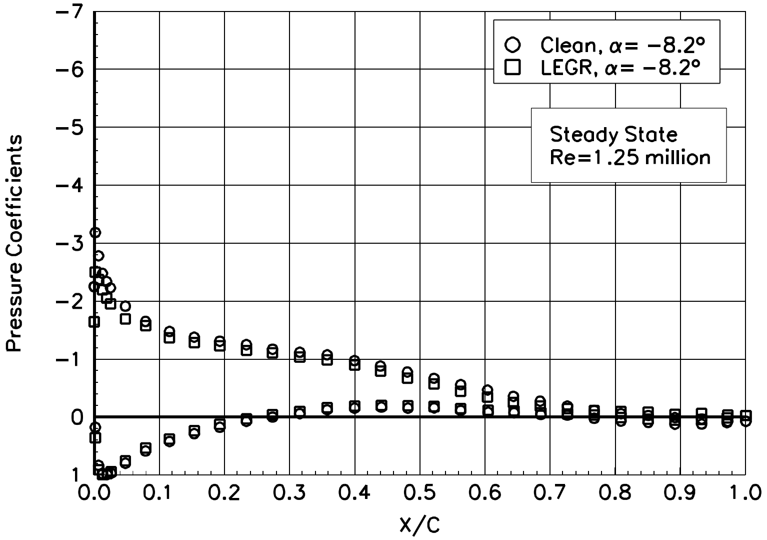

Figure 64. α = -8.2°

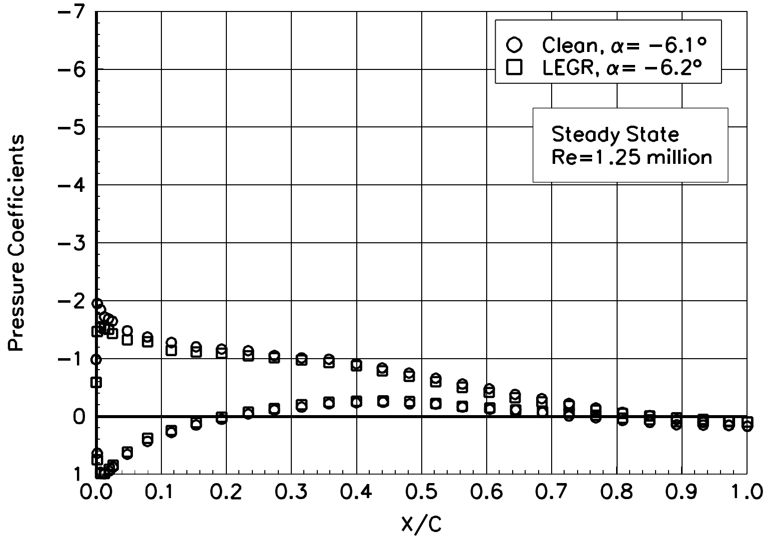

Figure 65. α = -6.1°

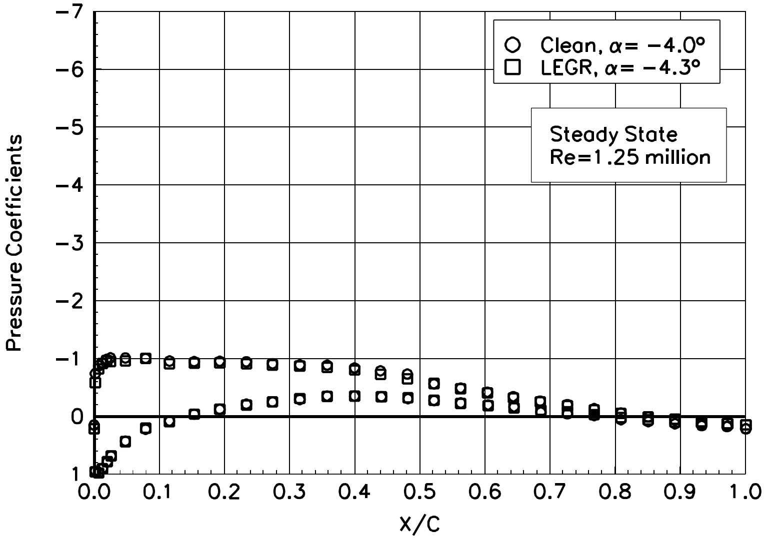

Figure 66. α = -4.0°

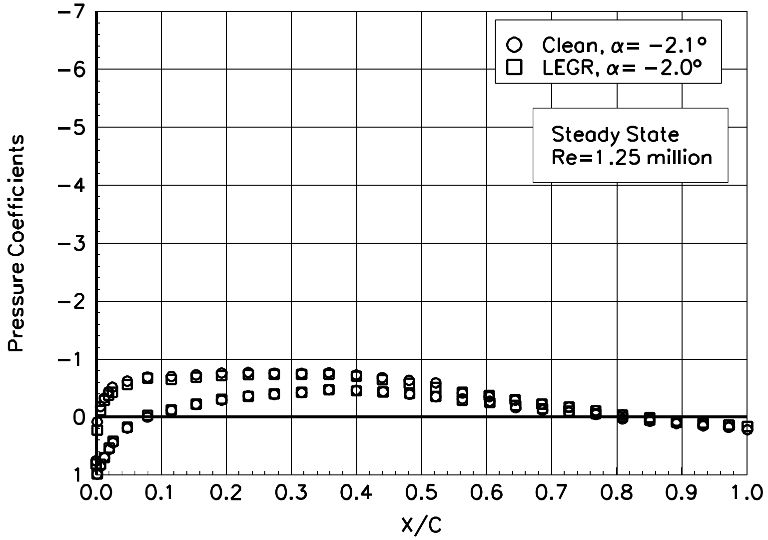

Figure 67. α = -2.1°

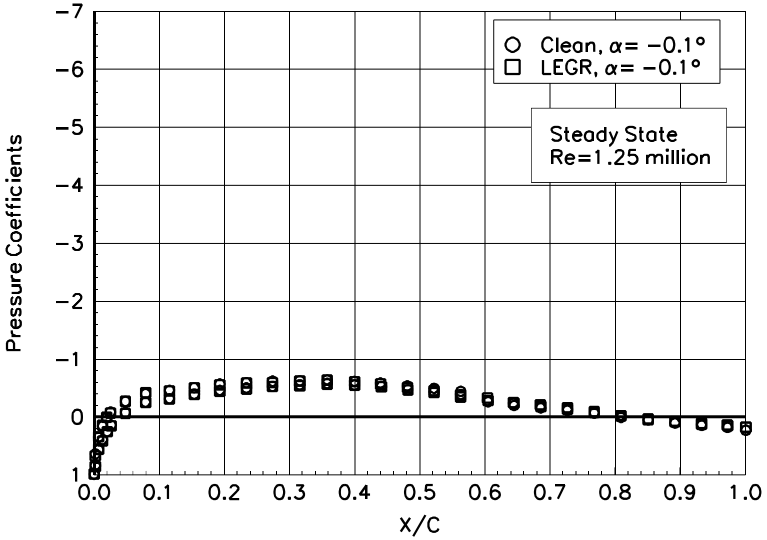

Figure 68. α = -0.1°

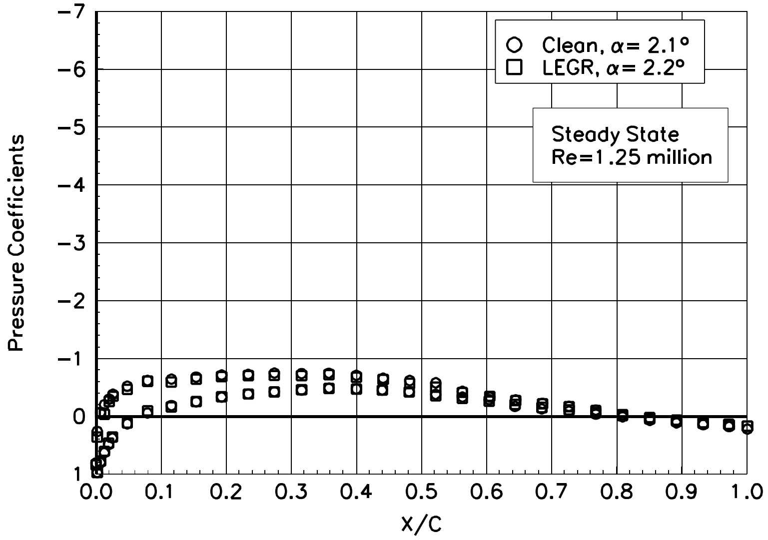

Figure 69. α = 2.1°

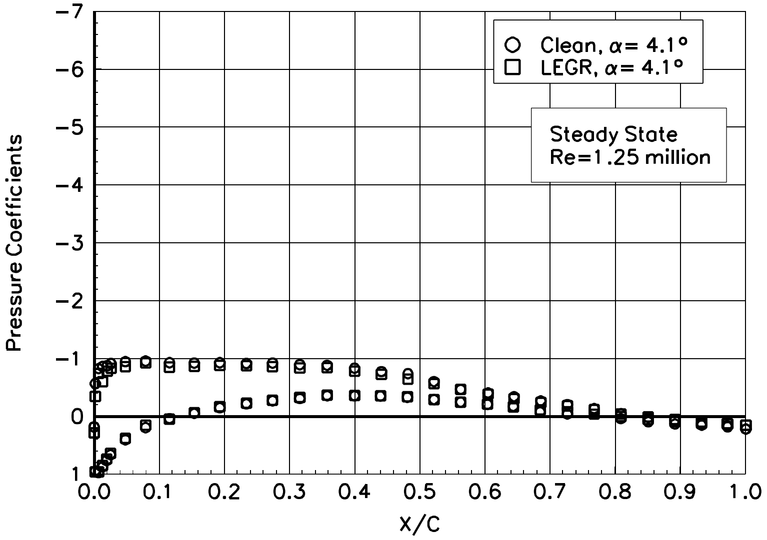

Figure 70. α = 4.1°

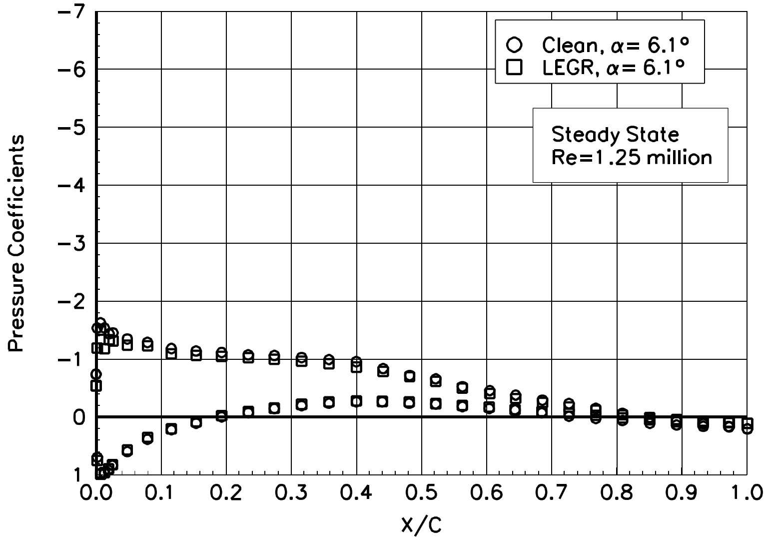

Figure 71. α = 6.1°

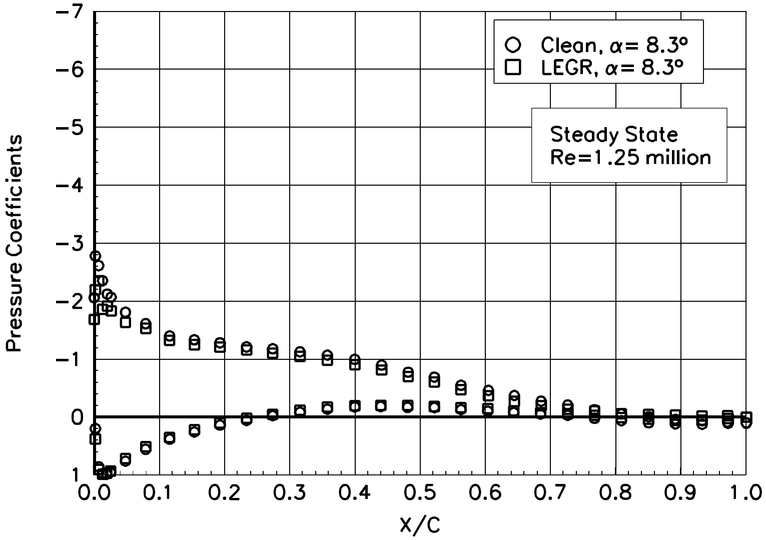

Figure 72. α = 8.3°

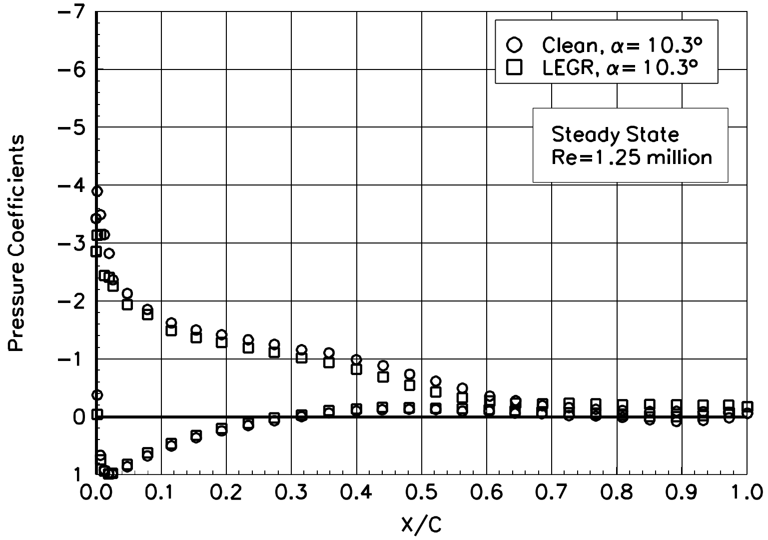

Figure 73. α = 10.3°

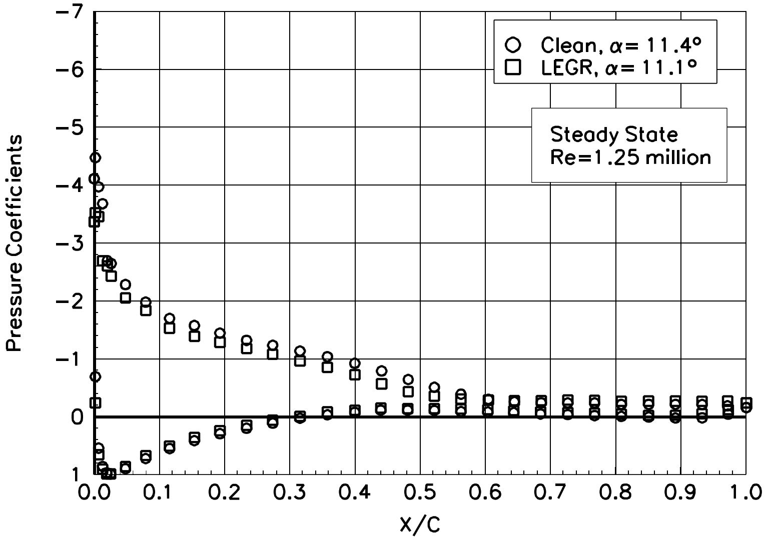

Figure 74. α = 11.4°

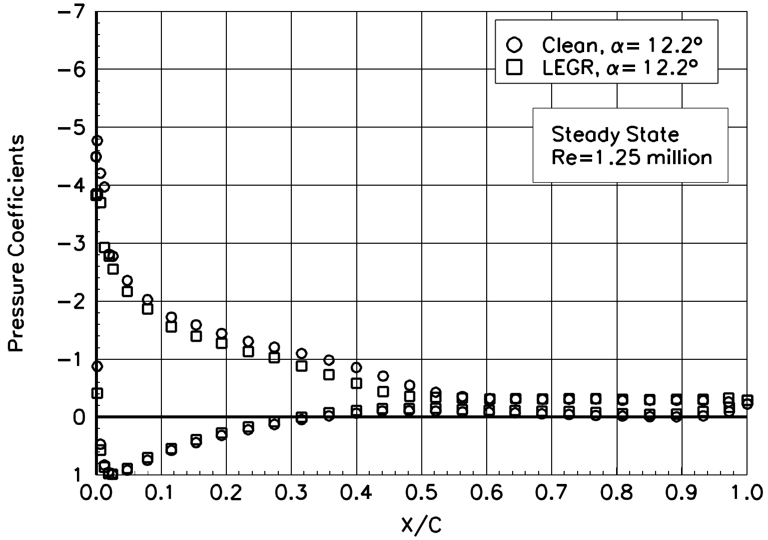

Figure 75. α = 12.2°

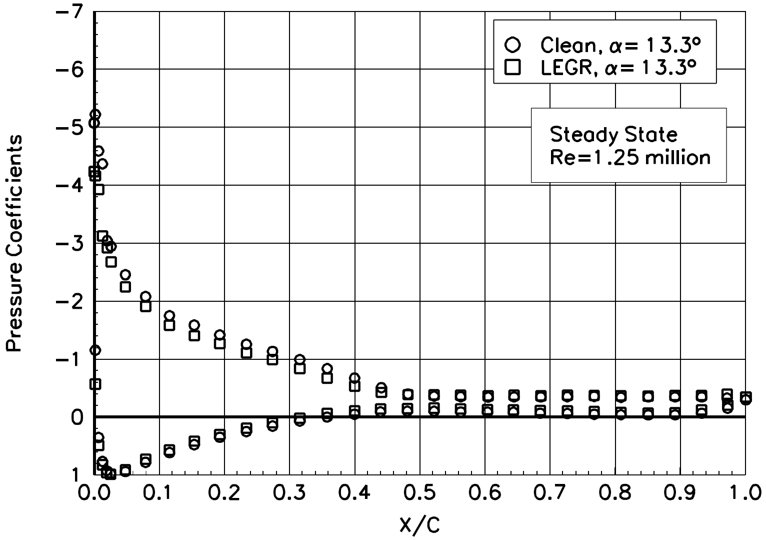

Figure 76. α = 13.3°

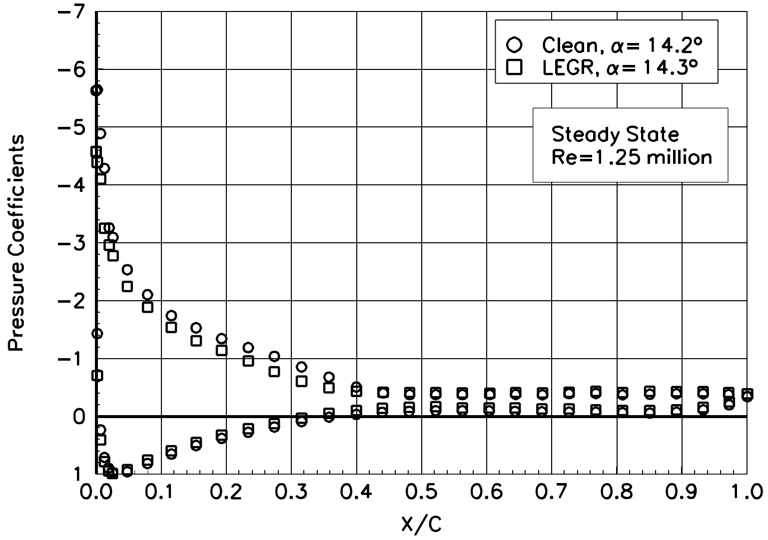

Figure 77. α = 14.2°

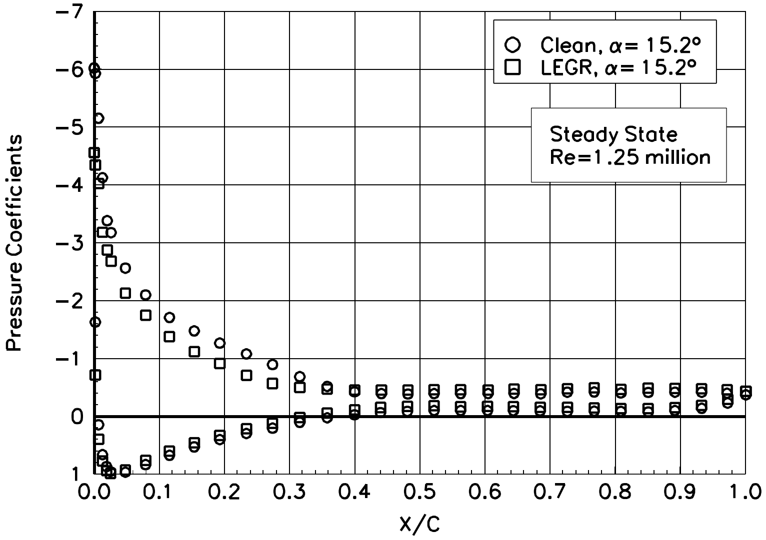

Figure 78. α = 15.2°

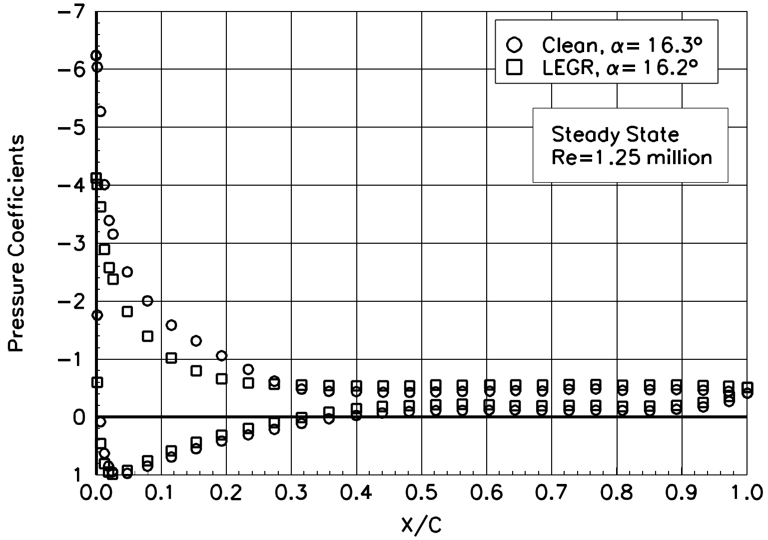

Figure 79. α = 16.3°

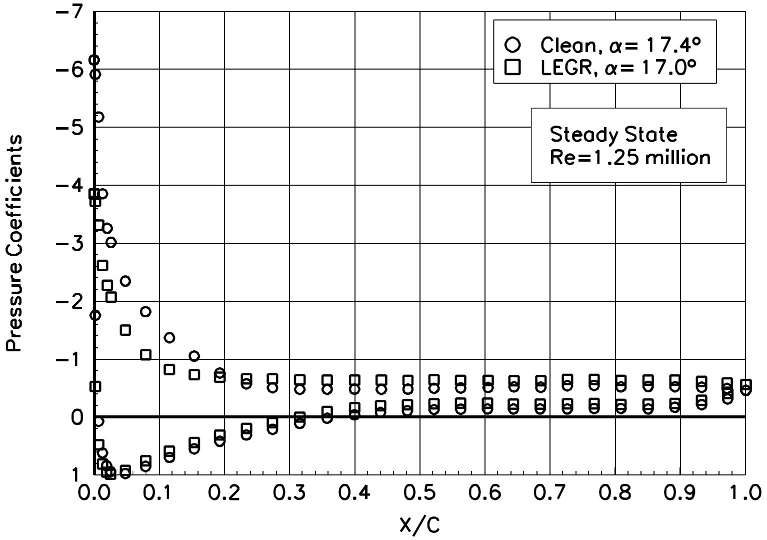

Figure 80. α = 17.4°

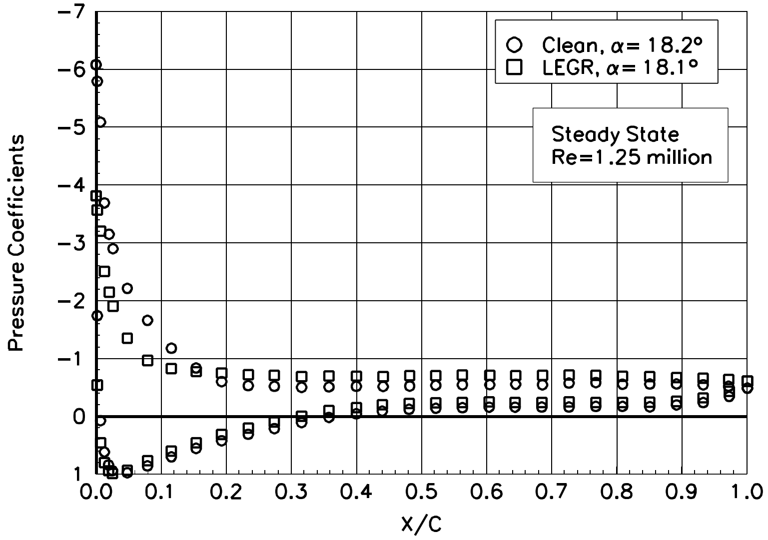

Figure 81. α = 18.2°

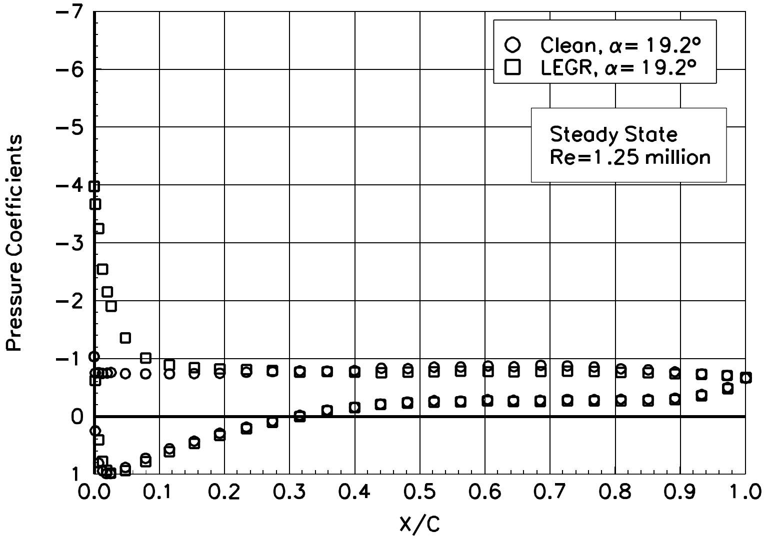

Figure 82. α = 19.2°

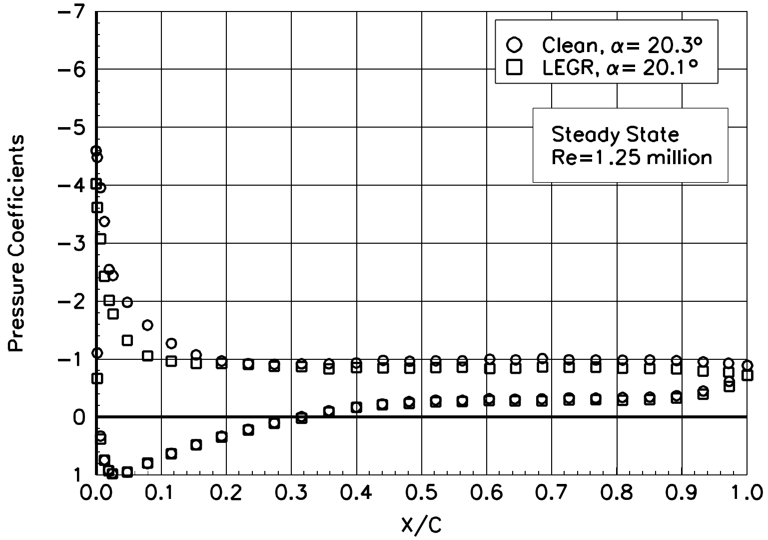

Figure 83. α = 20.3°

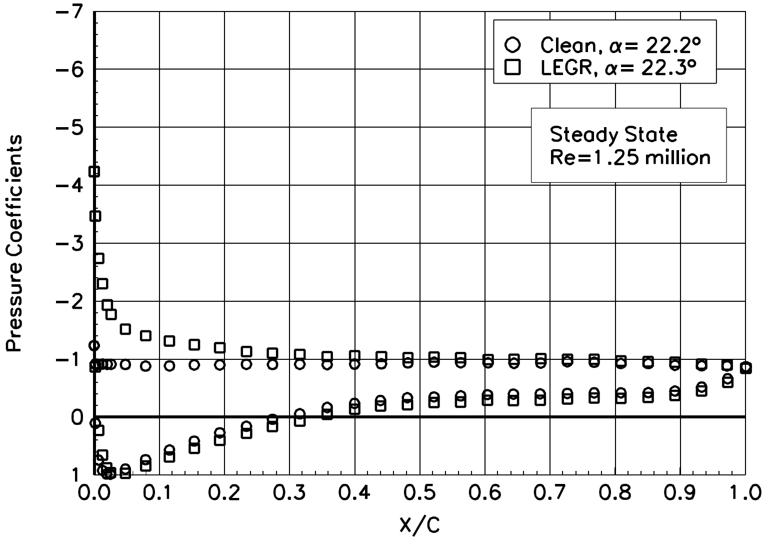

Figure 84. α = 22.2°

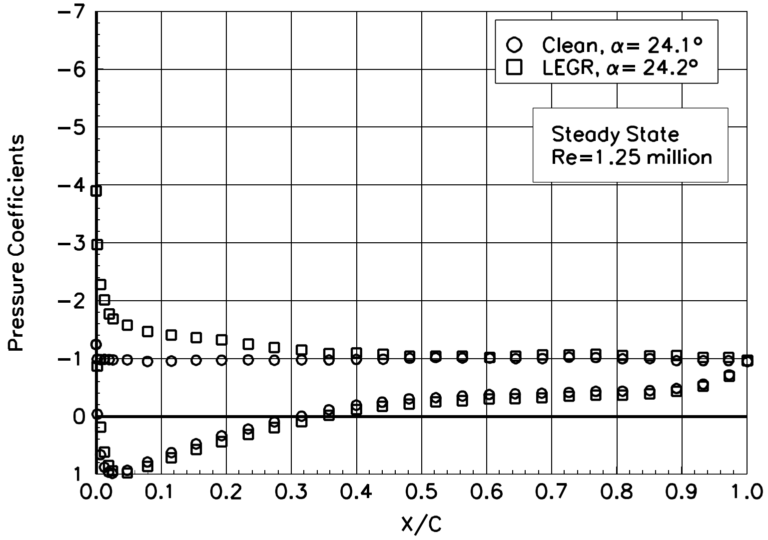

Figure 85. α = 24.1°

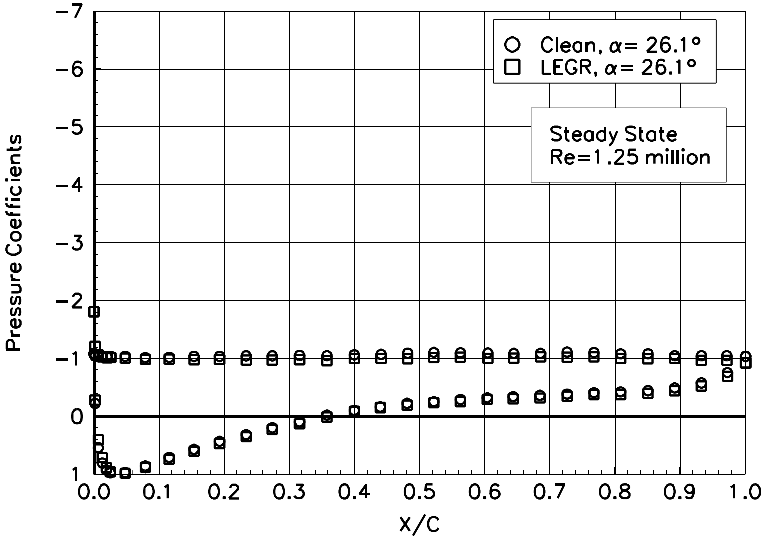

Figure 86. α = 26.1°

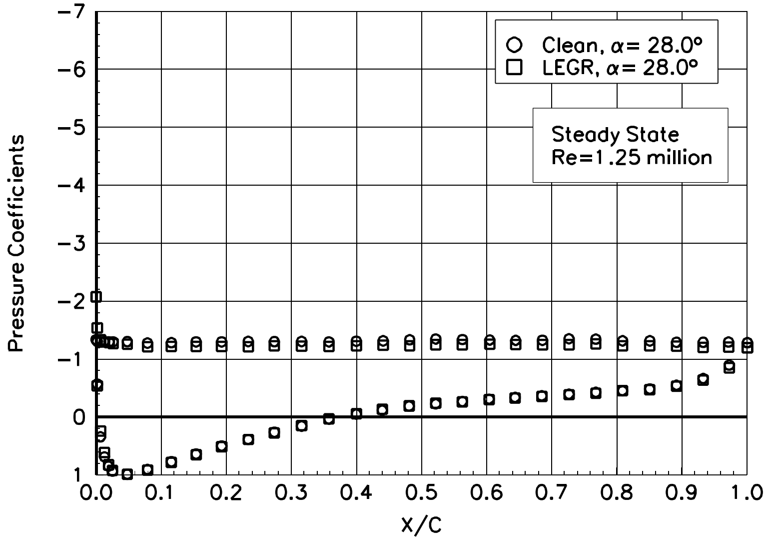

Figure 87. α = 28.0°

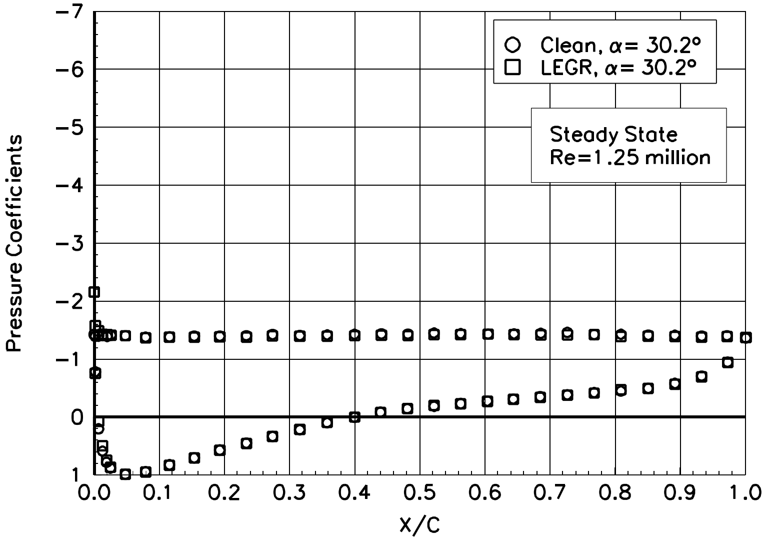

Figure 88. α = 30.2°

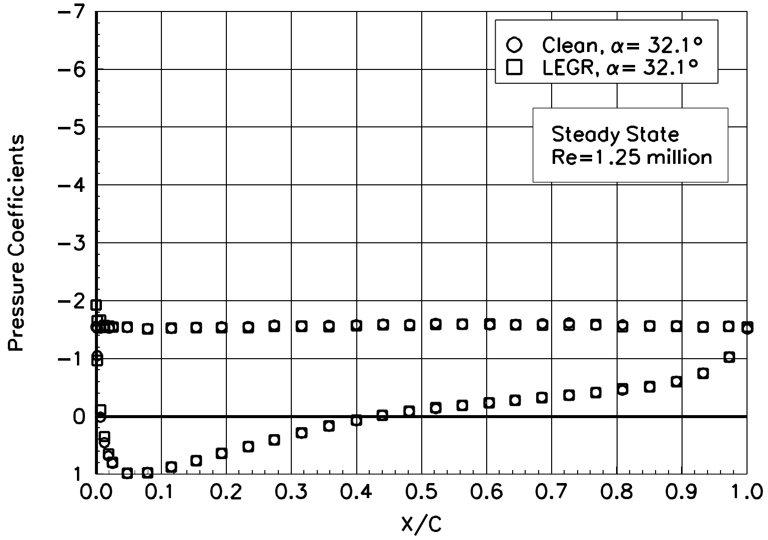

Figure 89. α = 32.1°

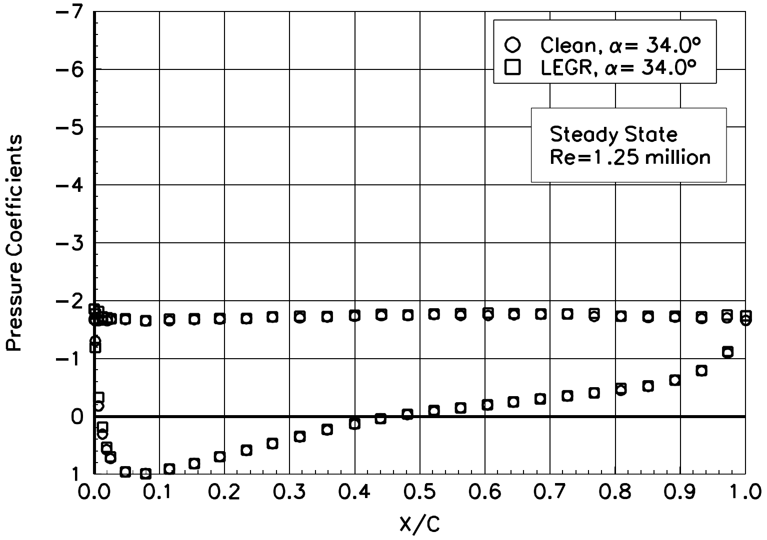

Figure 90. α = 34.0°

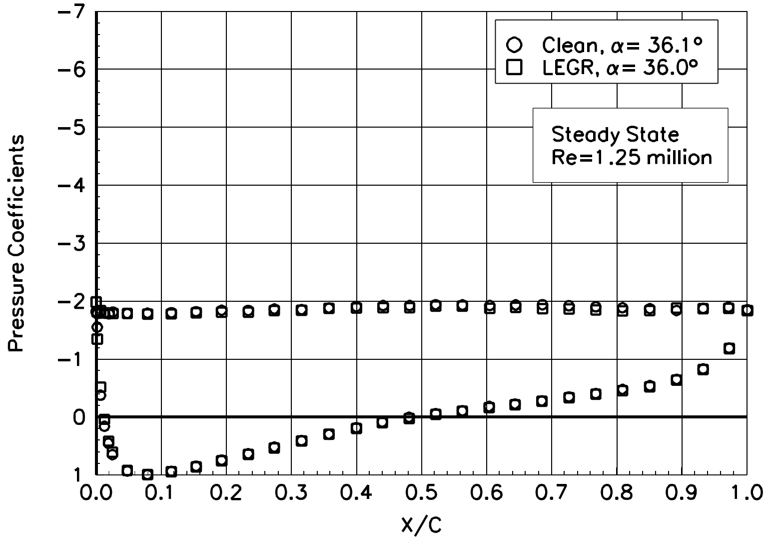

Figure 91. α = 36.1°

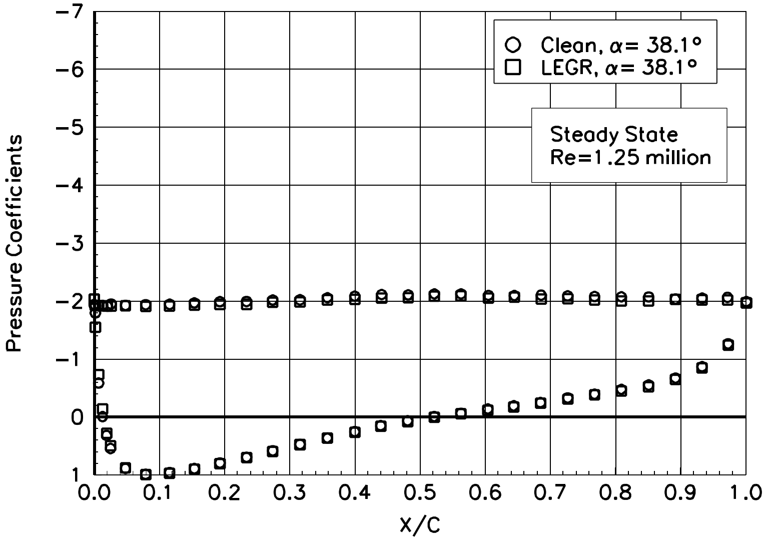

Figure 92. α = 38.1°

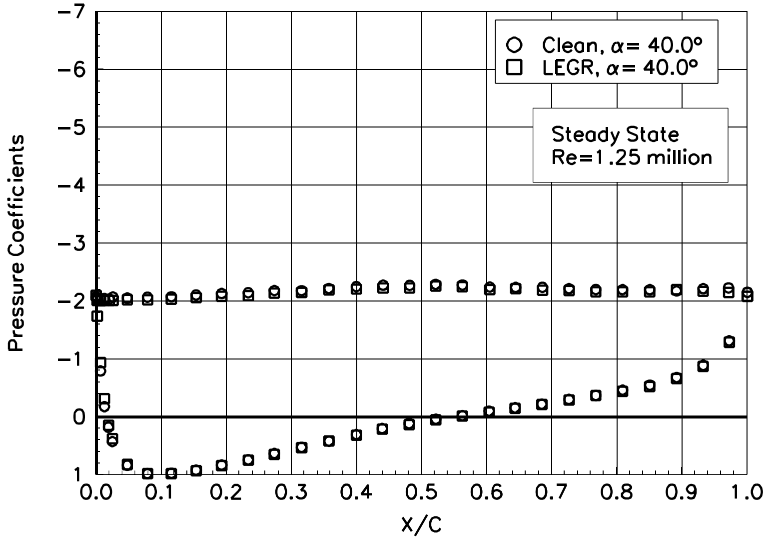

Figure 93. α = 40.0°

Appendix C: Unsteady Integrated Coefficients

List of Figures page

Unsteady Airfoil Characteristics

±5.5° Sine, Re = 0.75 million

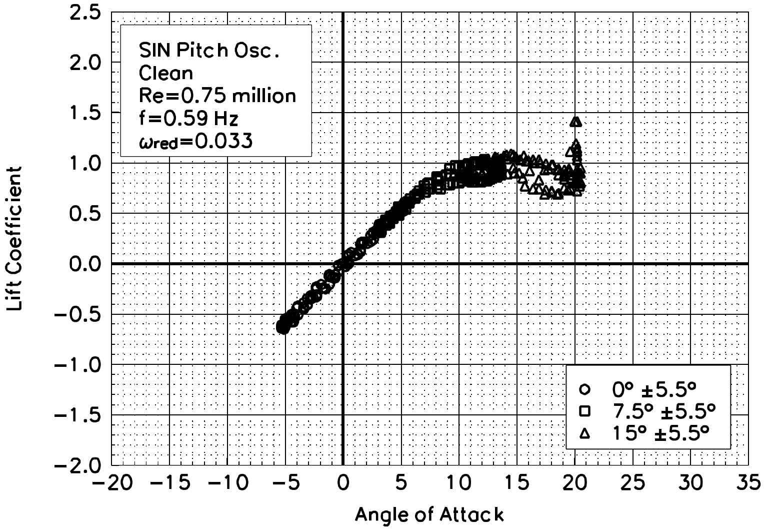

Figure C1. Lift coefficient vs α.

S824
Clean
Re=0.75 million
$\omega_{reduced}$=0.033

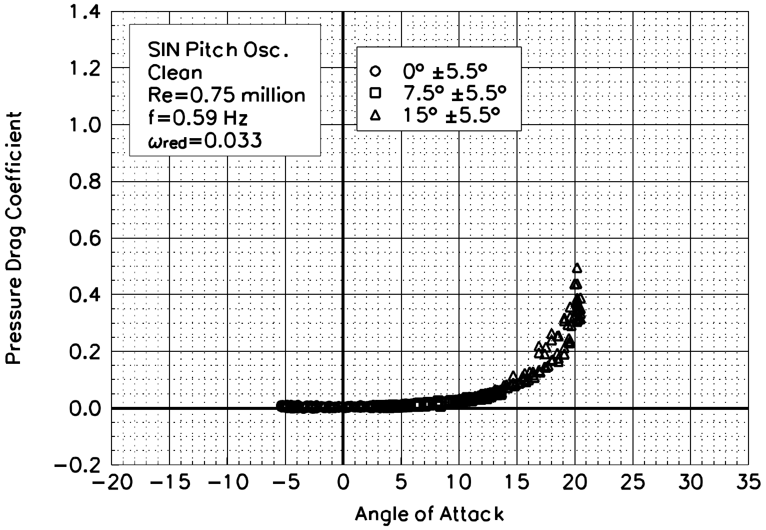

Figure C2. Pressure drag coefficient vs α.

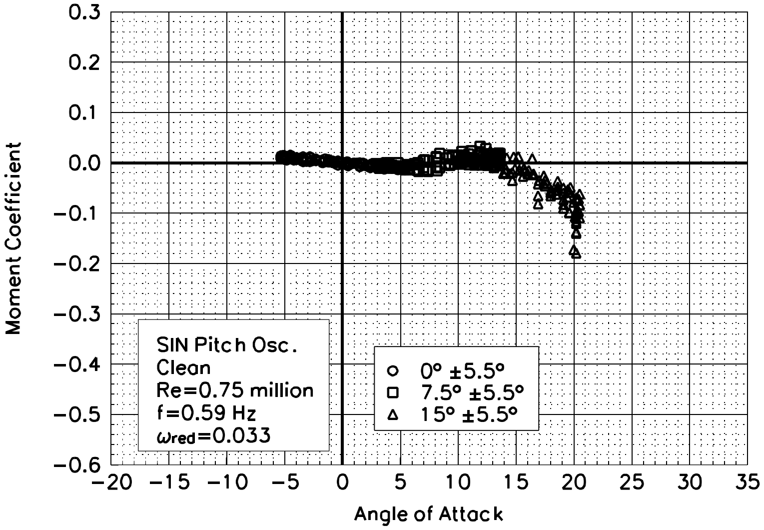

Figure C3. Moment coefficient vs α.

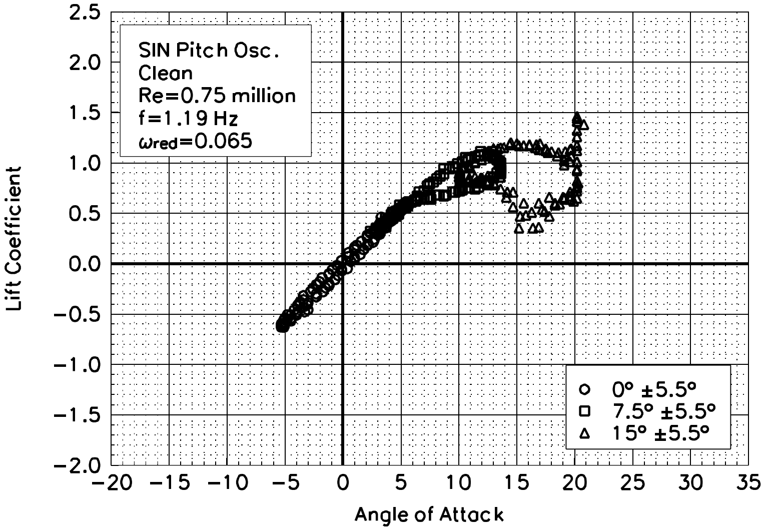

Figure C4. Lift coefficient vs α.

S824
Clean
Re=0.75 million
$\omega_{reduced}$=0.065

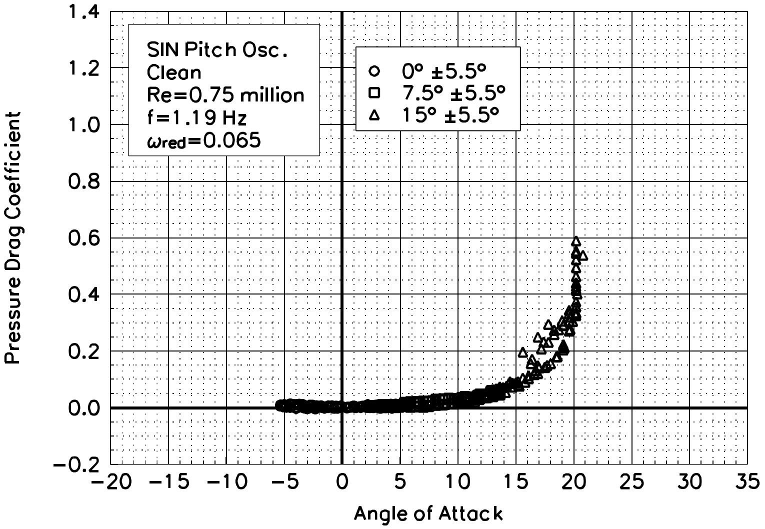

Figure C5. Pressure drag coefficient vs α.

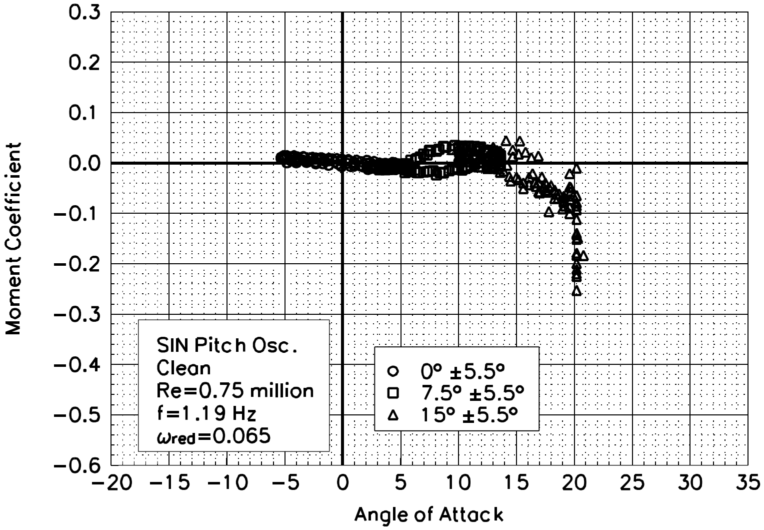

Figure C6. Moment coefficient vs α.

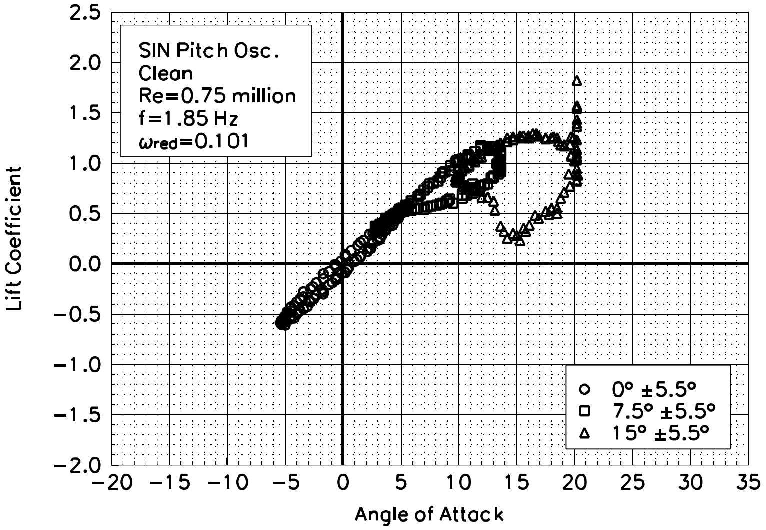

Figure C7. Lift coefficient vs α.

S824

Clean

Re=0.75 million

$\omega_{reduced}$=0.101

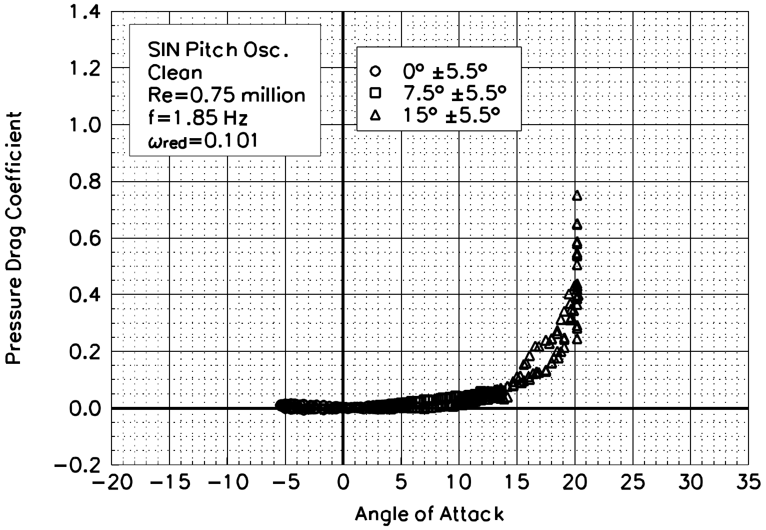

Figure C8. Pressure drag coefficient vs α.

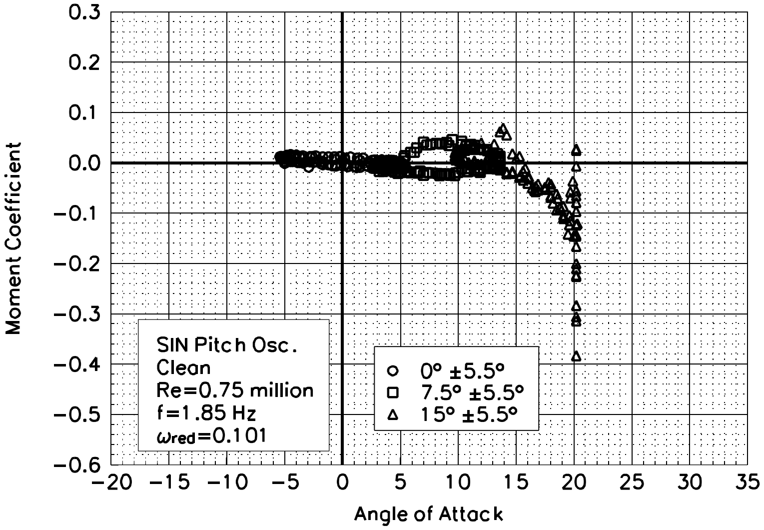

Figure C9. Moment coefficient vs α.

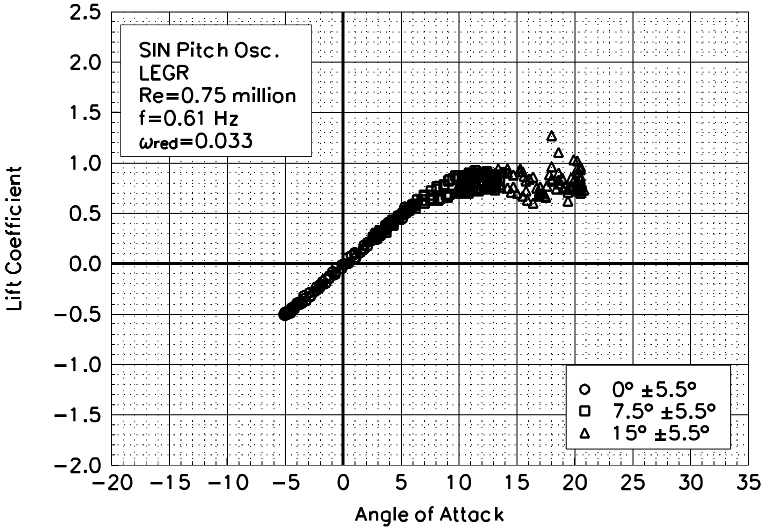

Figure C10. Lift coefficient vs α.

S824
LEGR
Re=0.75 million
$\omega_{reduced}$=0.033

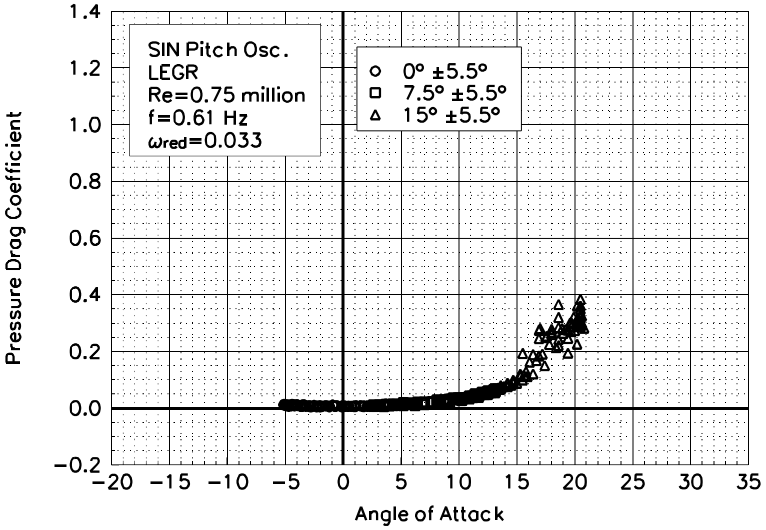

Figure C11. Pressure drag coefficient vs α.

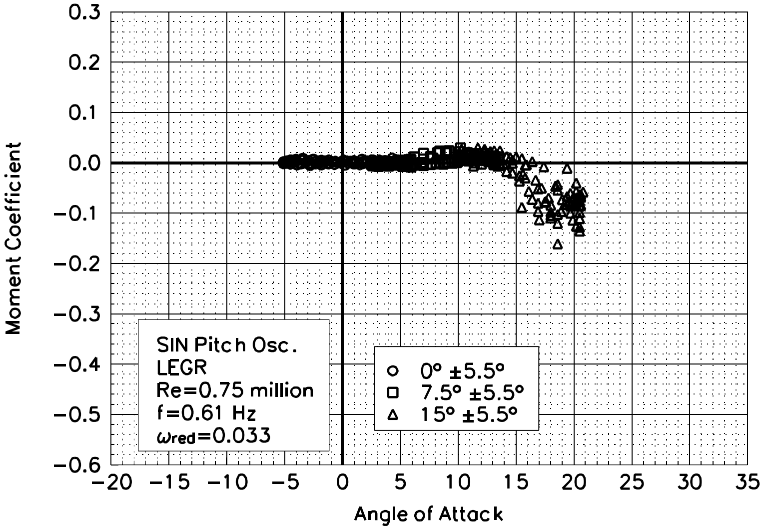

Figure C12. Moment coefficient vs α.

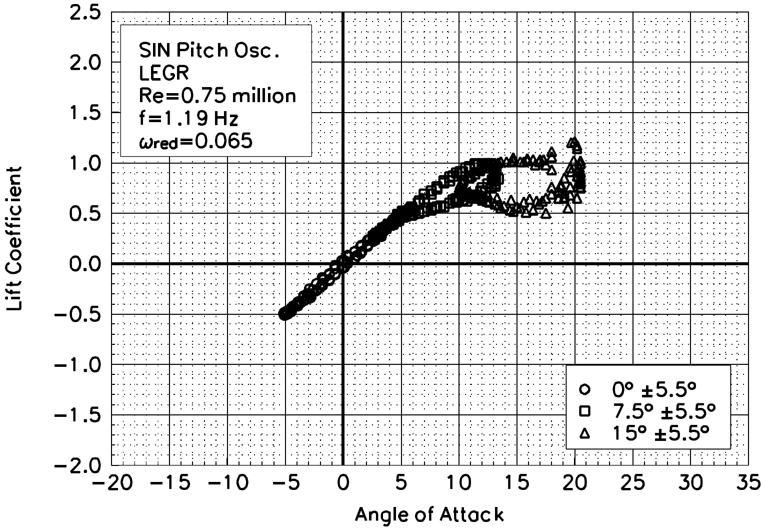

Figure C13. Lift coefficient vs α.

S824
LEGR
Re=0.75 million
$\omega_{reduced}$=0.065

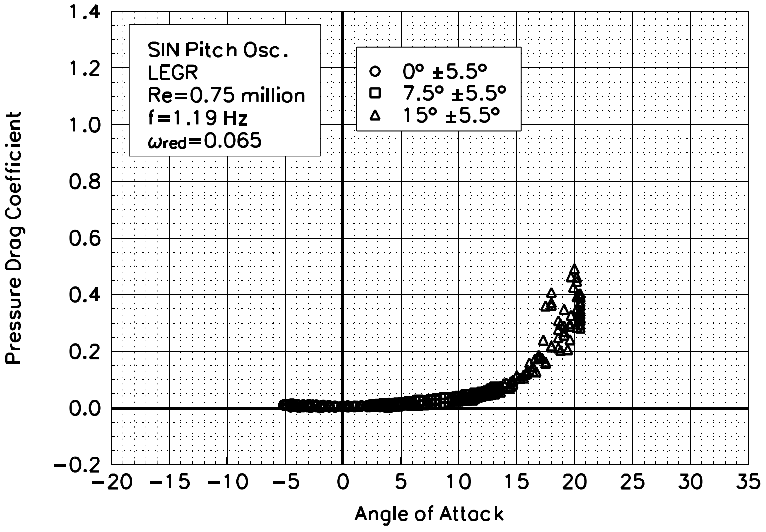

Figure C14. Pressure drag coefficient vs α.

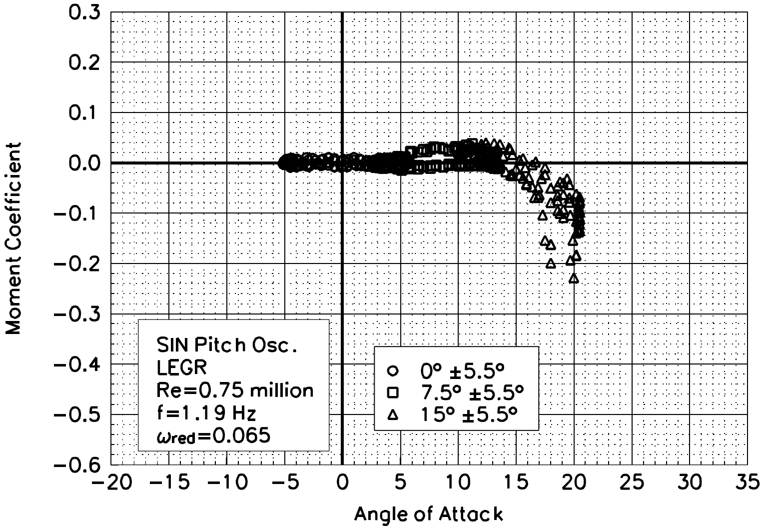

Figure C15. Moment coefficient vs α.

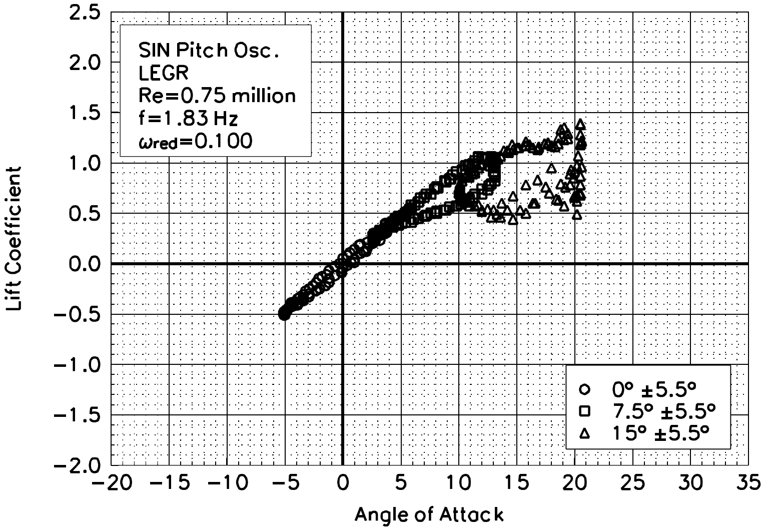

Figure C16. Lift coefficient vs α.

S824
LEGR
Re=0.75 million
$\omega_{reduced}$=0.100

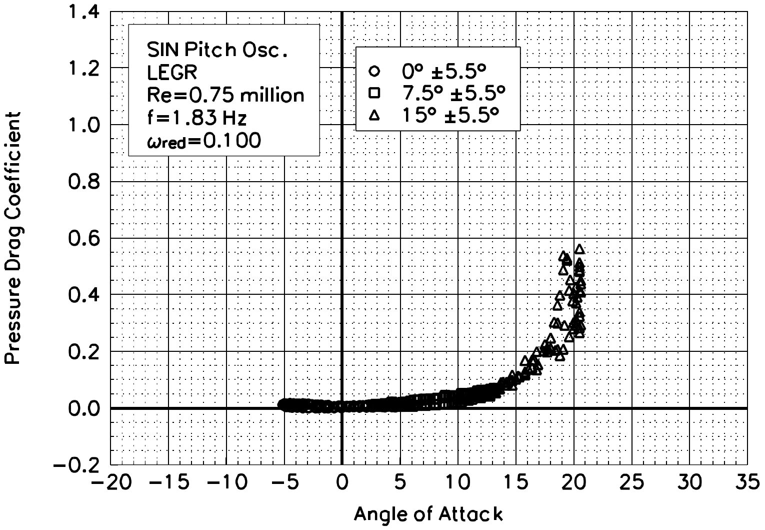

Figure C17. Pressure drag coefficient vs α.

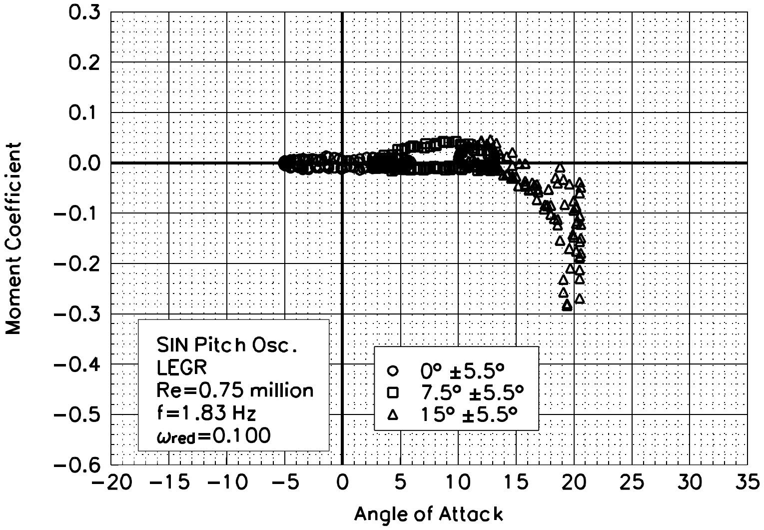

Figure C18. Moment coefficient vs α.

Unsteady Airfoil Characteristics

±5.5° Sine, Re = 1 million

S824
Clean
Re=1.00 million
$\omega_{reduced}$=0.025

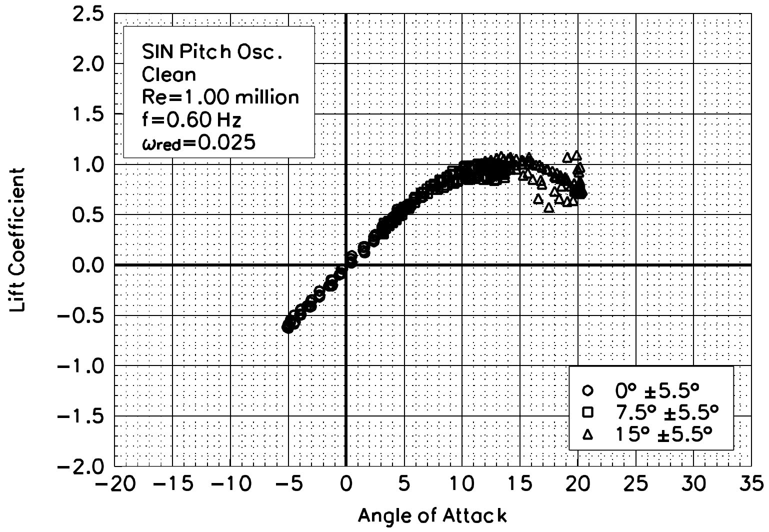

Figure C19. Lift coefficient vs α.

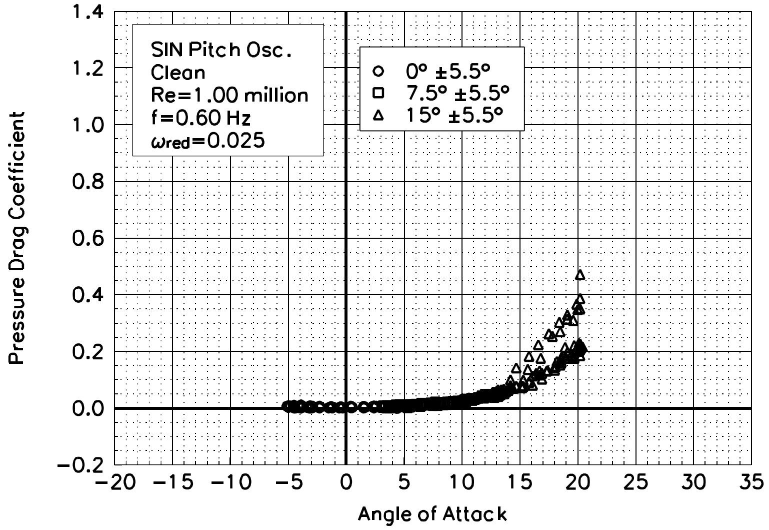

Figure C20. Pressure drag coefficient vs α.

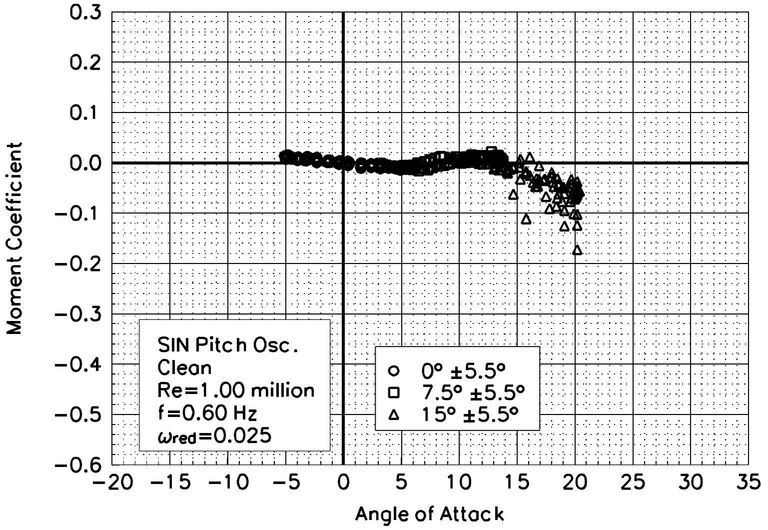

Figure C21. Moment coefficient vs α.

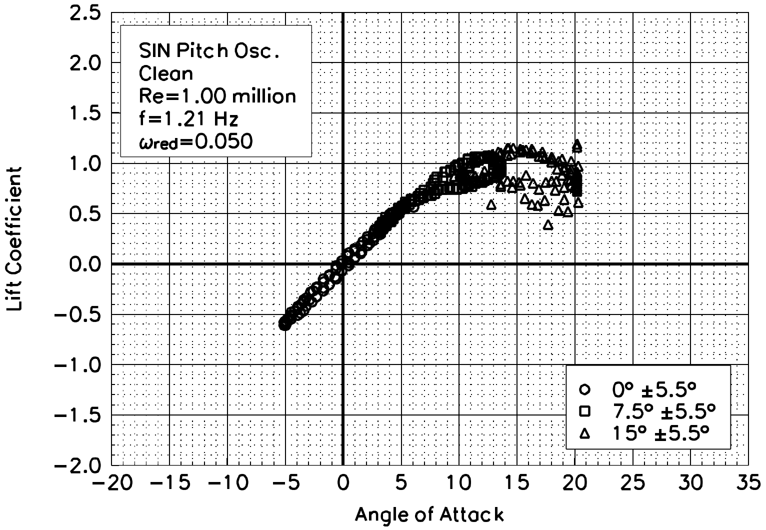

Figure C22. Lift coefficient vs α.

S824
Clean
Re=1.00 million
$\omega_{reduced}$=0.050

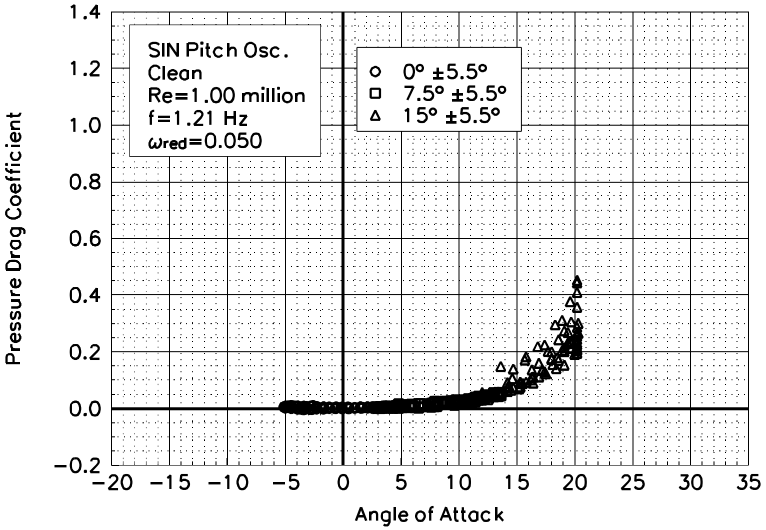

Figure C23. Pressure drag coefficient vs α.

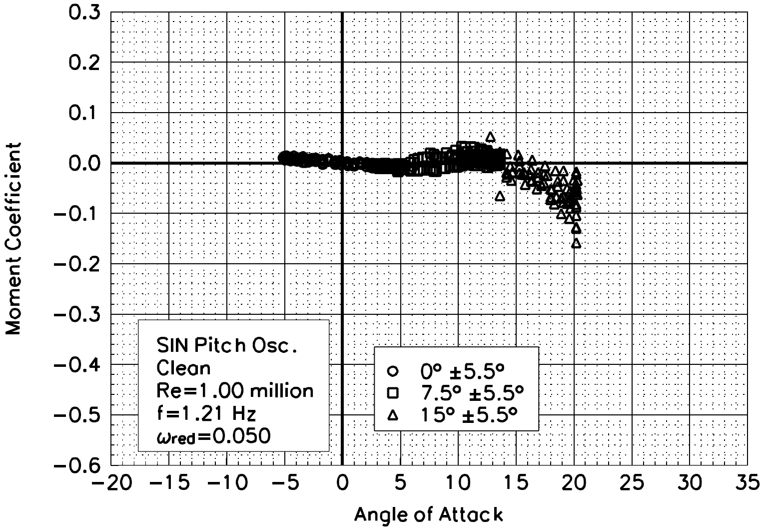

Figure C24. Moment coefficient vs α.

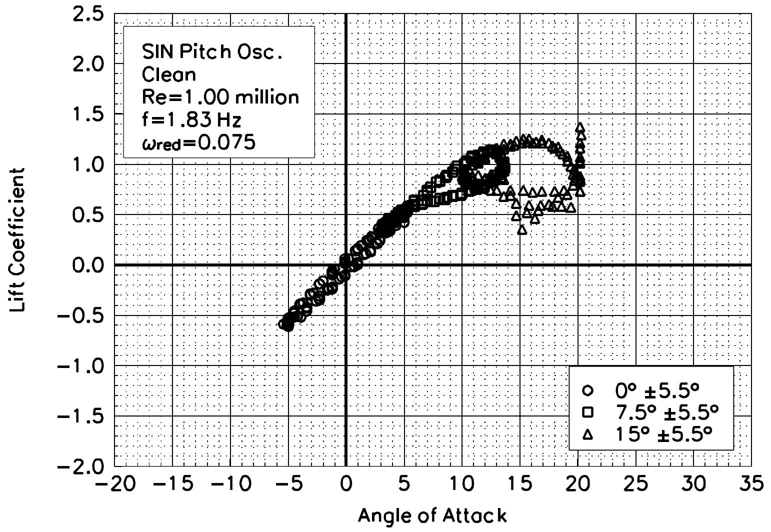

Figure C25. Lift coefficient vs α.

S824
Clean
Re=1.00 million
$\omega_{reduced}$=0.075

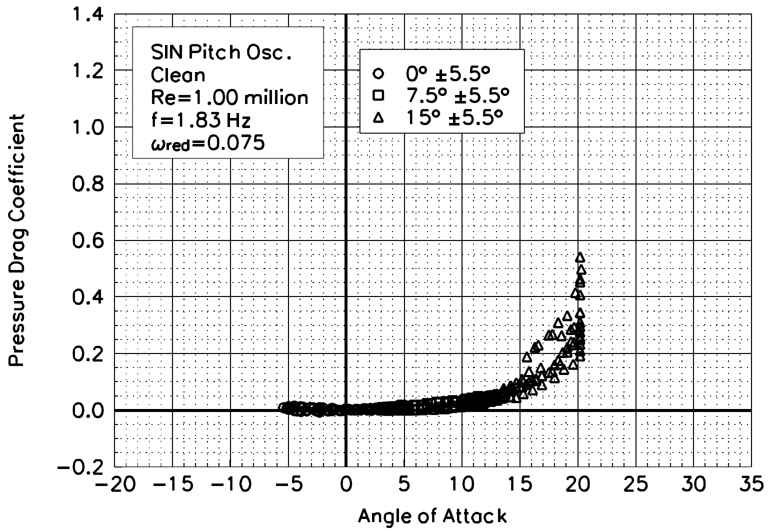

Figure C26. Pressure drag coefficient vs α.

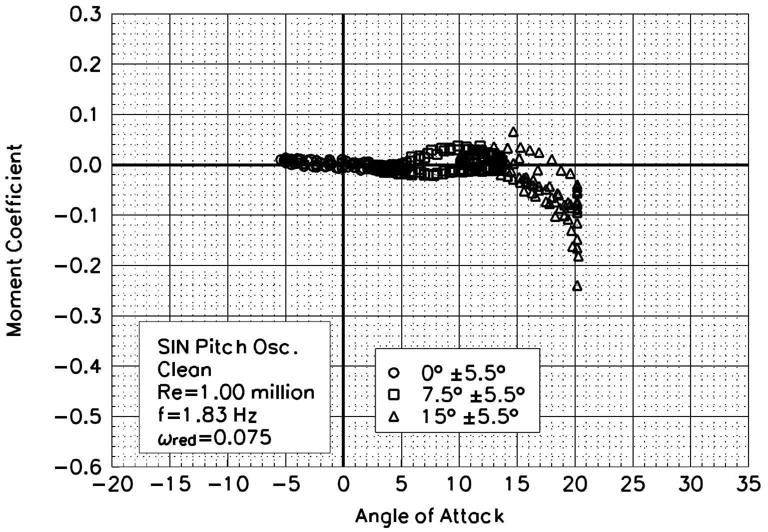

Figure C27. Moment coefficient vs α.

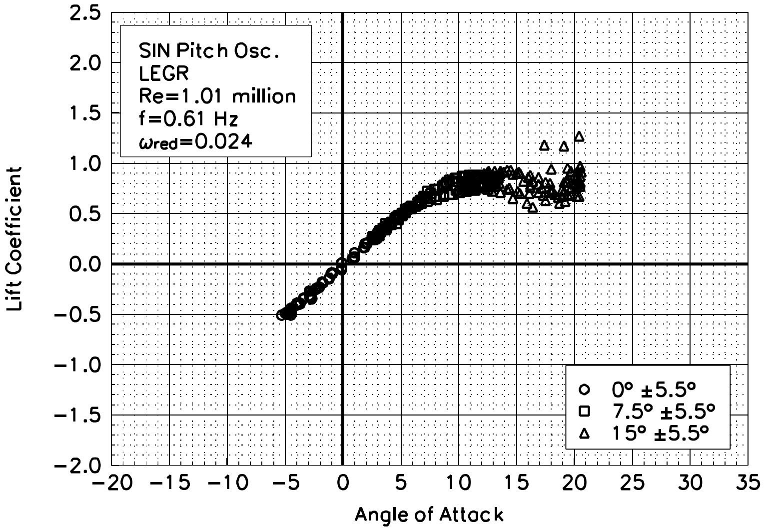

Figure C28. Lift coefficient vs α.

S824
LEGR
Re=1.01 million
$\omega_{reduced}$=0.024

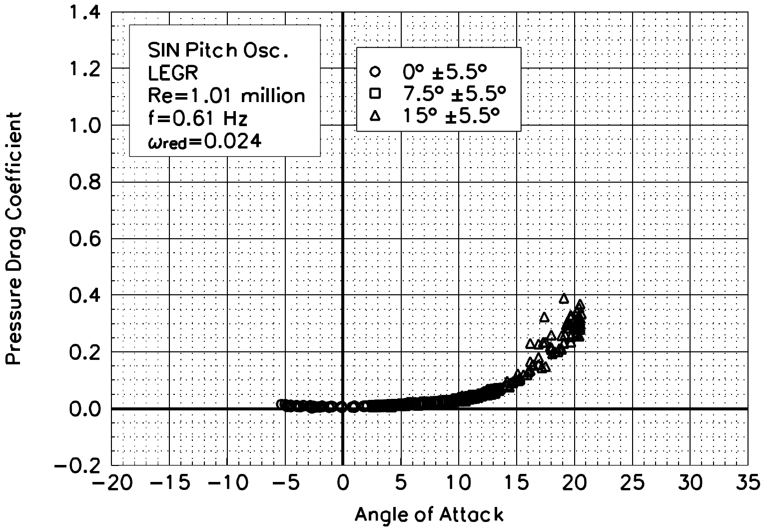

Figure C29. Pressure drag coefficient vs α.

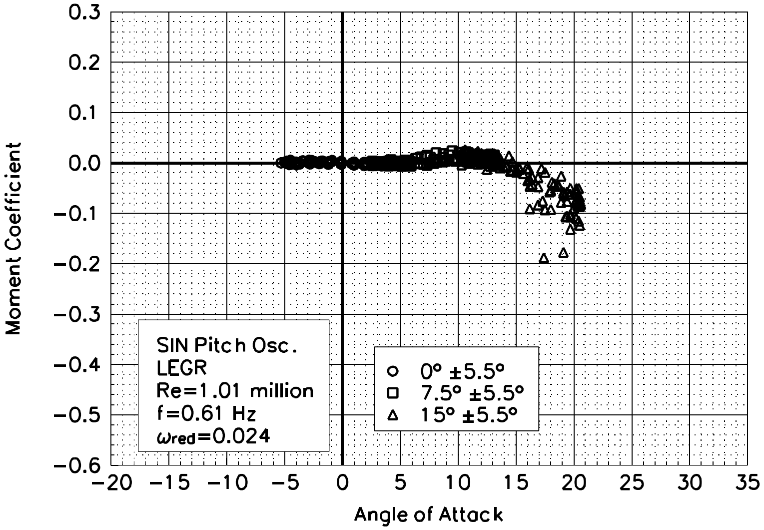

Figure C30. Moment coefficient vs α.

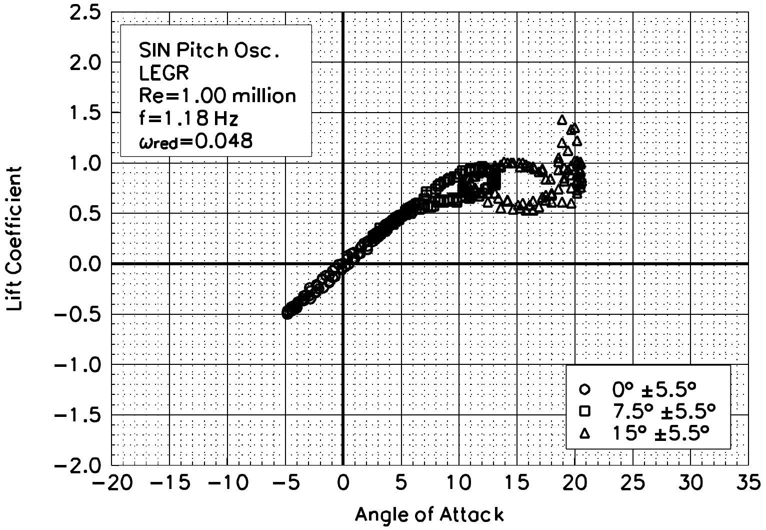

Figure C31. Lift coefficient vs α.

S824
LEGR
Re=1.00 million
$\omega_{reduced}$=0.048

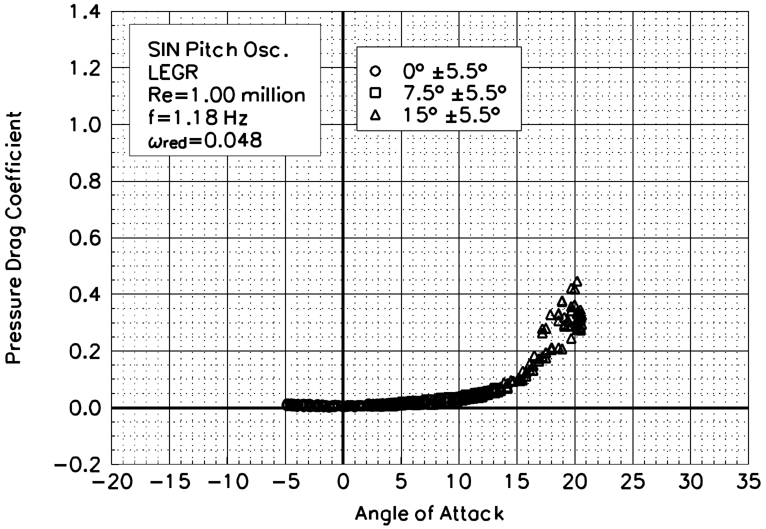

Figure C32. Pressure drag coefficient vs α.

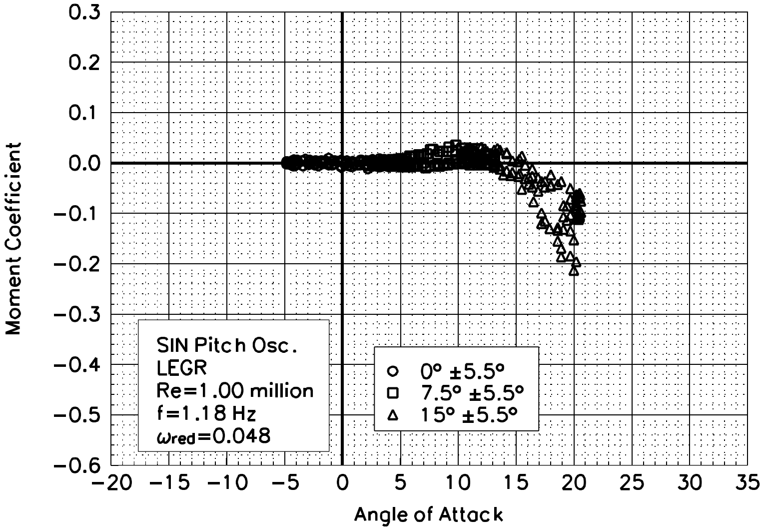

Figure C33. Moment coefficient vs α.

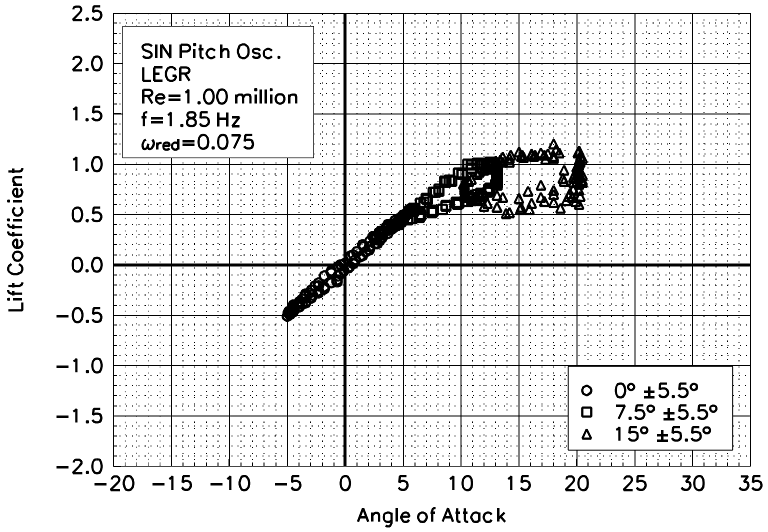

Figure C34. Lift coefficient vs α.

S824
LEGR
Re=1.00 million
$\omega_{reduced}$=0.075

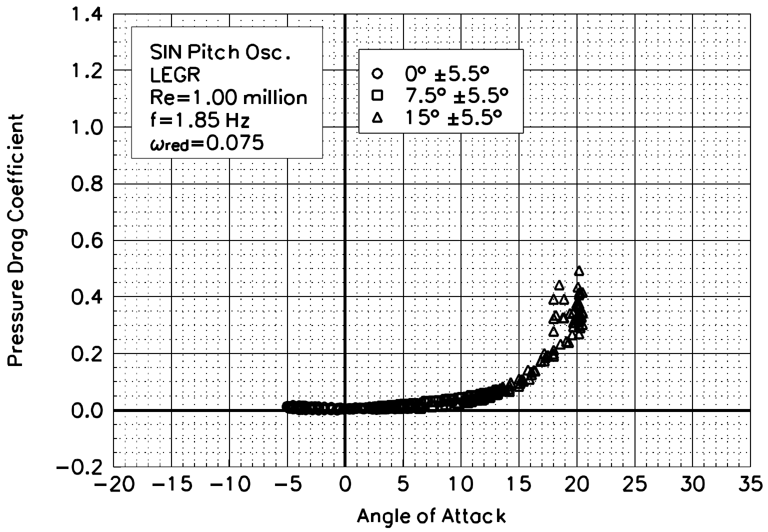

Figure C35. Pressure drag coefficient vs α.

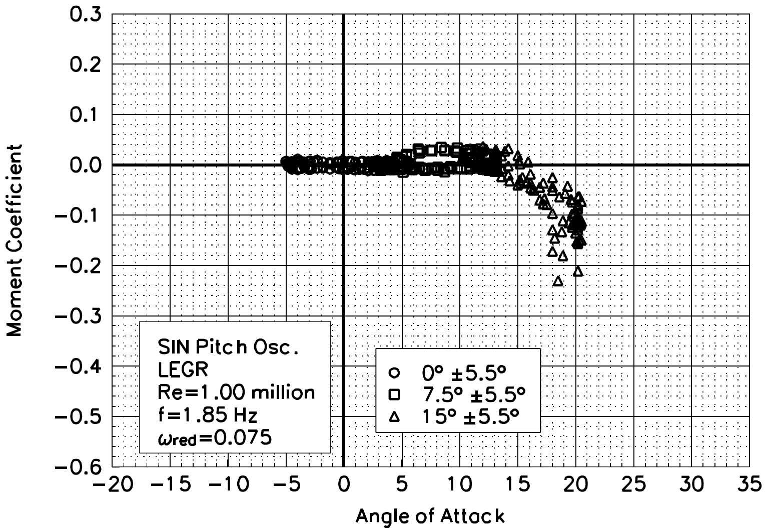

Figure C36. Moment coefficient vs α.

Unsteady Airfoil Characteristics

±5.5° Sine, Re= 1.25 million

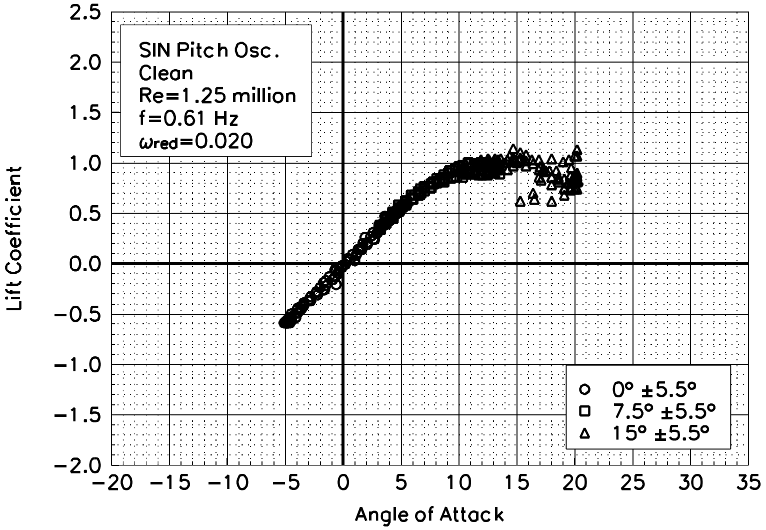

Figure C37. Lift coefficient vs α.

S824
Clean
Re=1.25 million
$\omega_{reduced}$=0.020

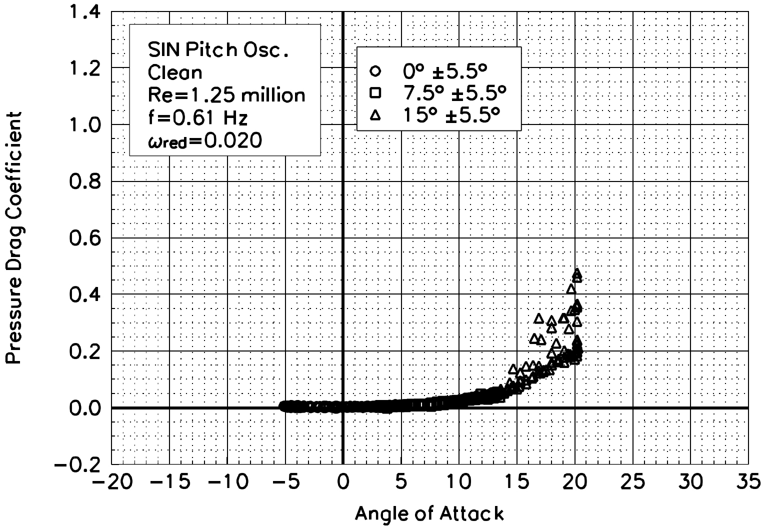

Figure C38. Pressure drag coefficient vs α.

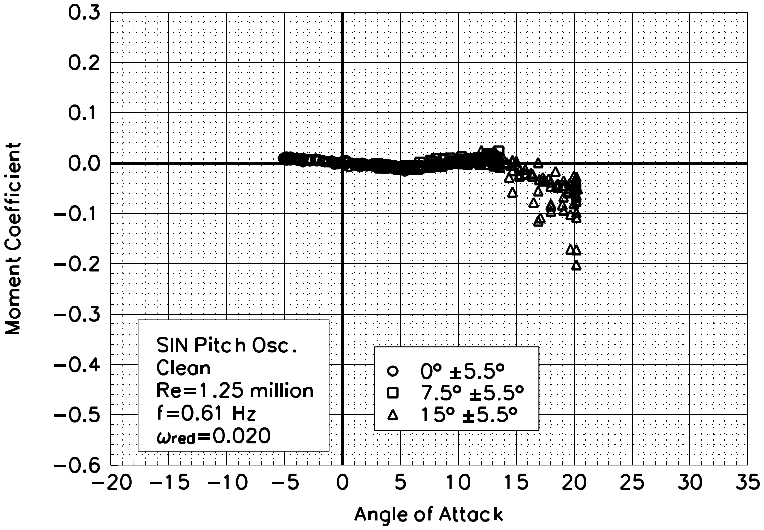

Figure C39. Moment coefficient vs α.

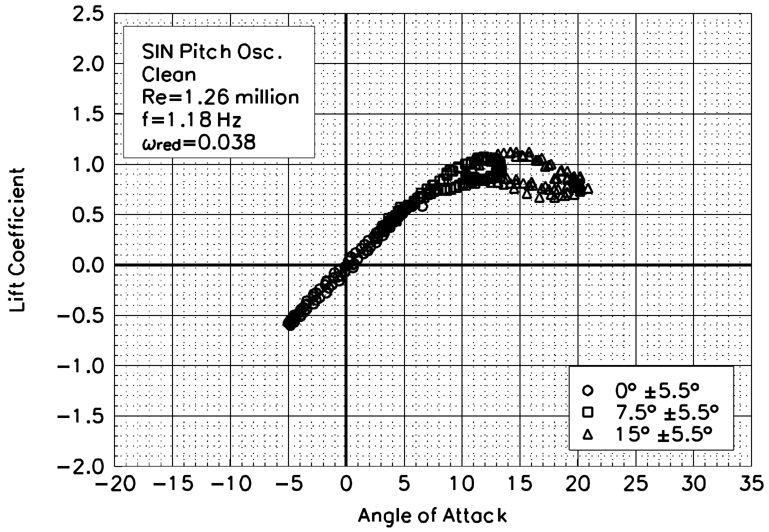

Figure C40. Lift coefficient vs α.

S824
Clean
Re=1.26 million
$\omega_{reduced}$=0.038

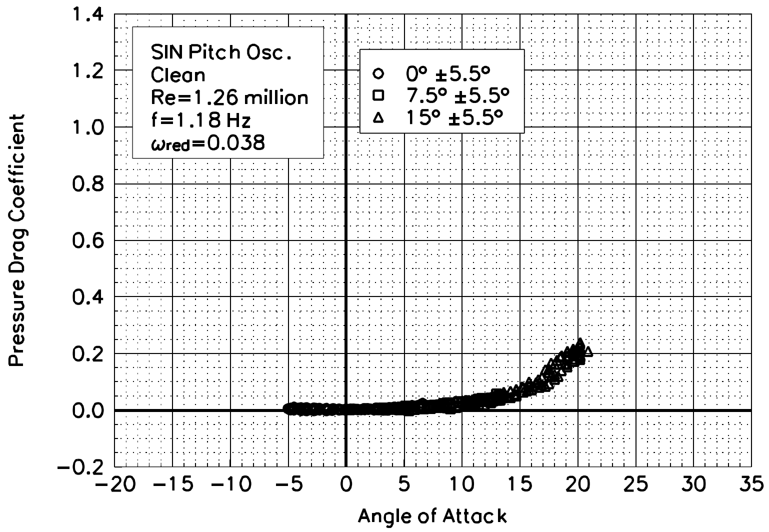

Figure C41. Pressure drag coefficient vs α.

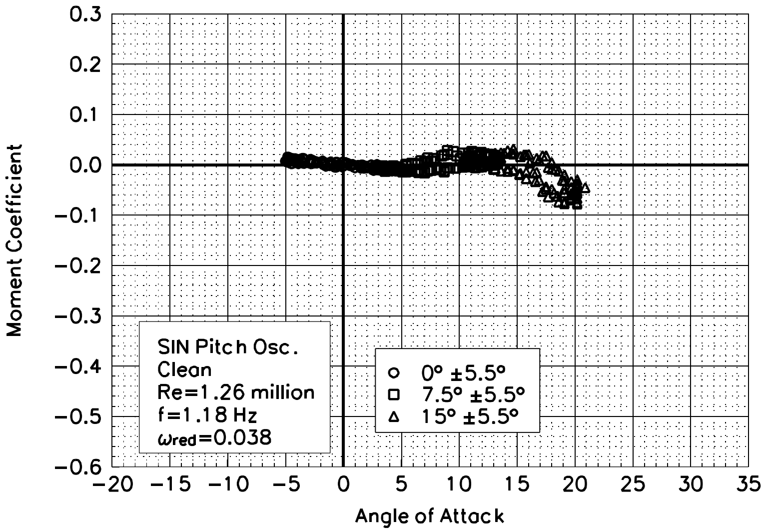

Figure C42. Moment coefficient vs α.

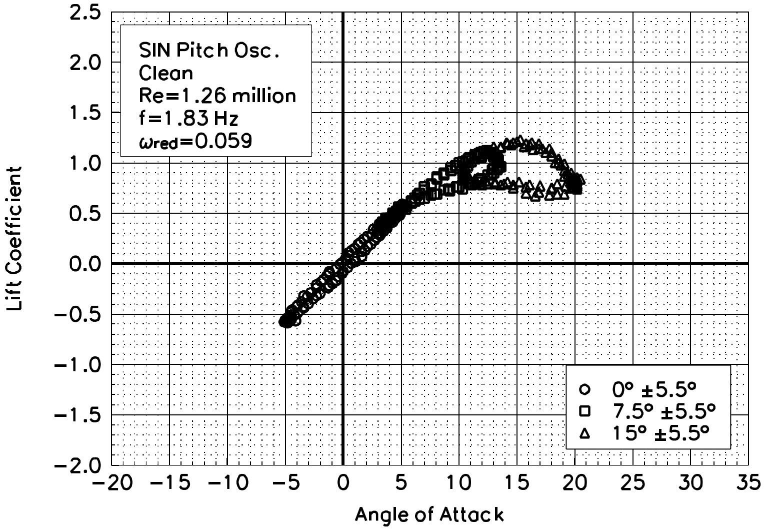

Figure C43. Lift coefficient vs α.

S824
Clean
Re=1.26 million
$\omega_{reduced}$=0.059

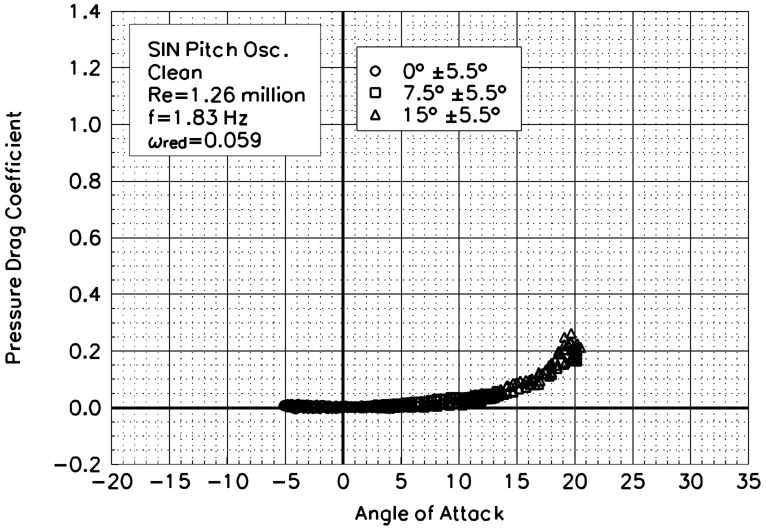

Figure C44. Pressure drag coefficient vs α.

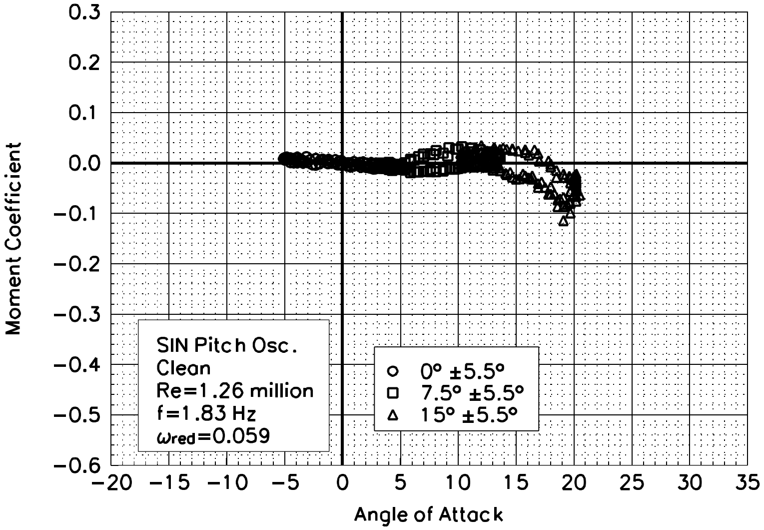

Figure C45. Moment coefficient vs α.

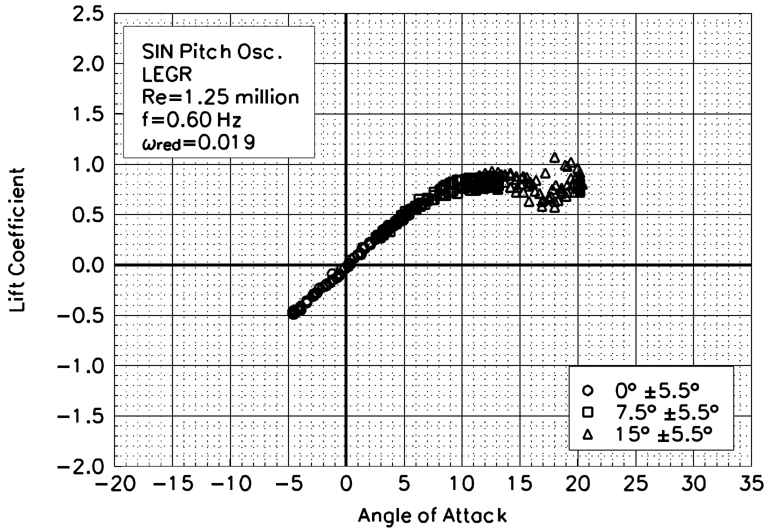

Figure C46. Lift coefficient vs α.

S824

LEGR

Re=1.25 million

$\omega_{reduced}$=0.019

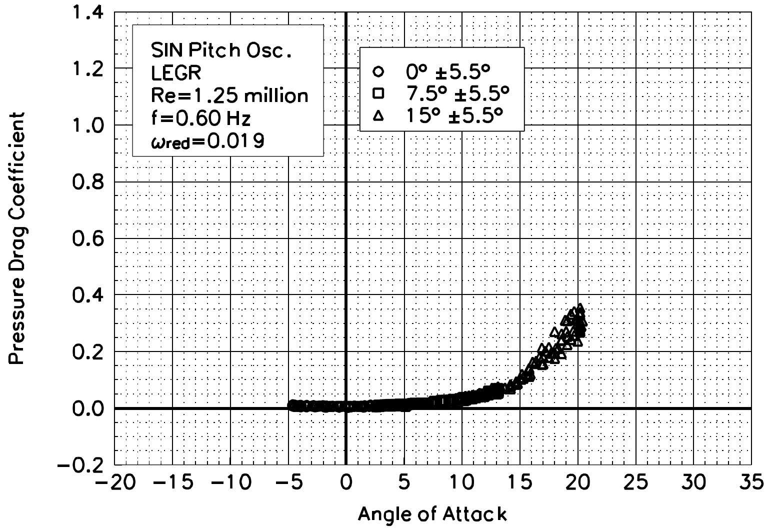

Figure C47. Pressure drag coefficient vs α.

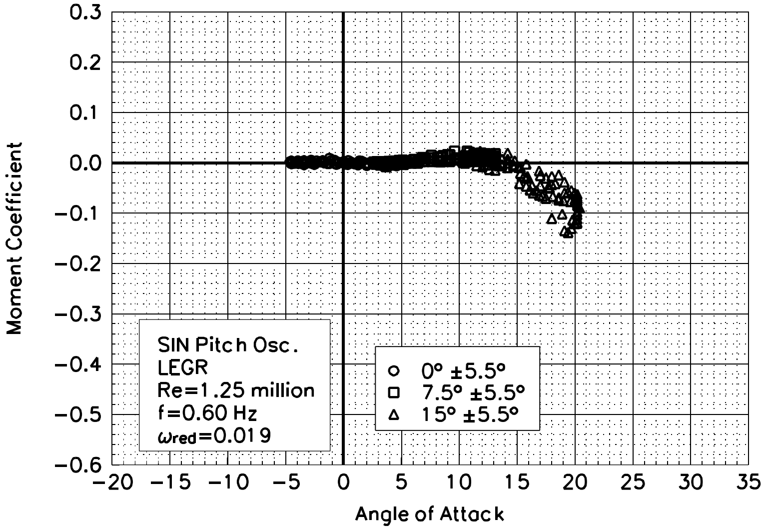

Figure C48. Moment coefficient vs α.

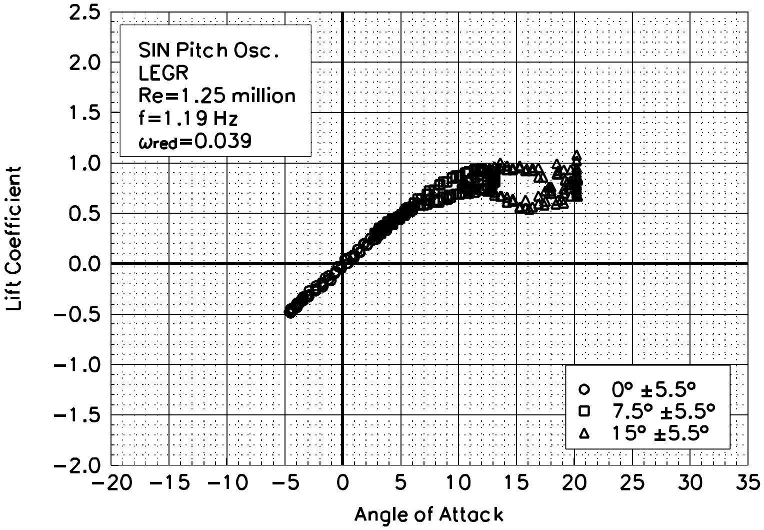

Figure C49. Lift coefficient vs α.

S824

LEGR

Re=1.25 million

$\omega_{reduced}$=0.039

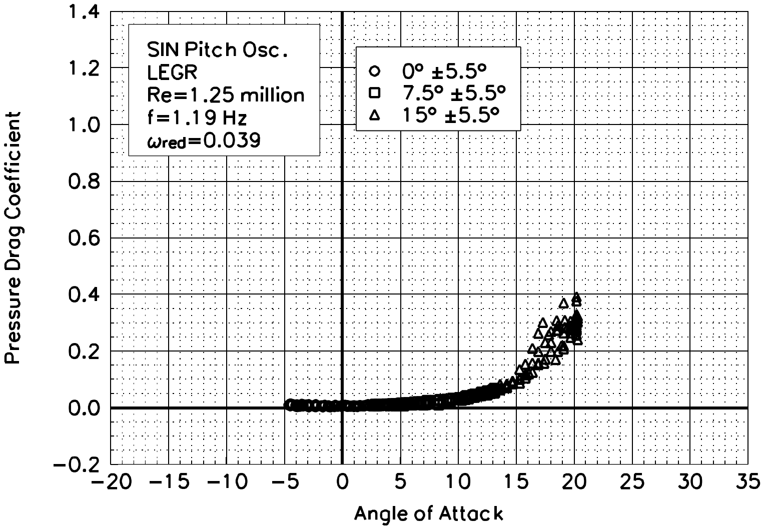

Figure C50. Pressure drag coefficient vs α.

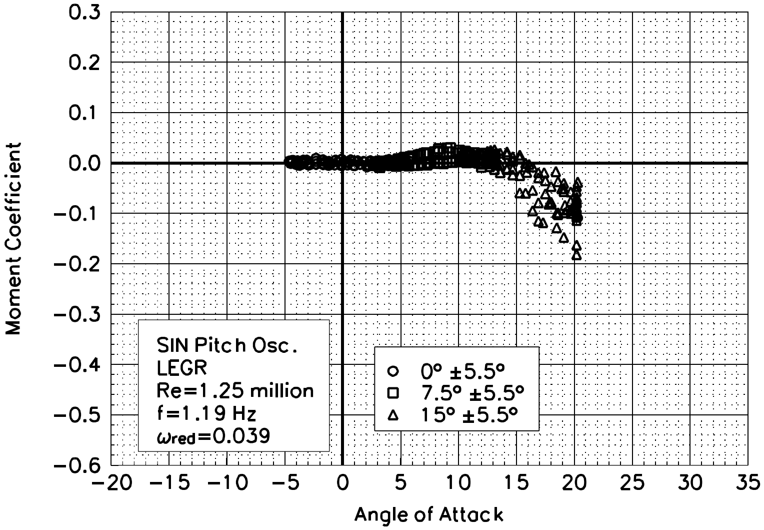

Figure C51. Moment coefficient vs α.

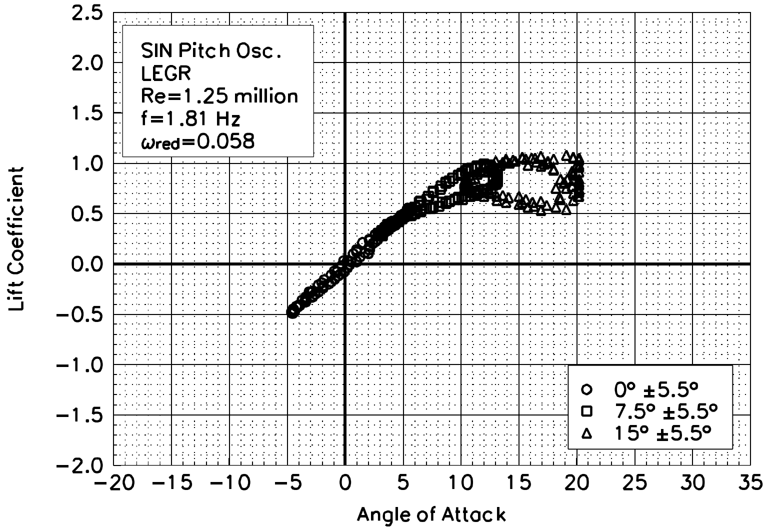

Figure C52. Lift coefficient vs α.

S824
LEGR
Re=1.25 million
$\omega_{reduced}$=0.058

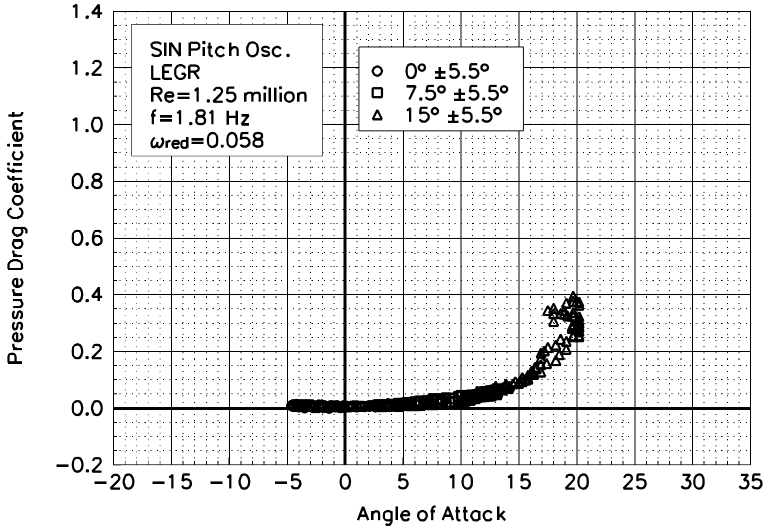

Figure C53. Pressure drag coefficient vs α.

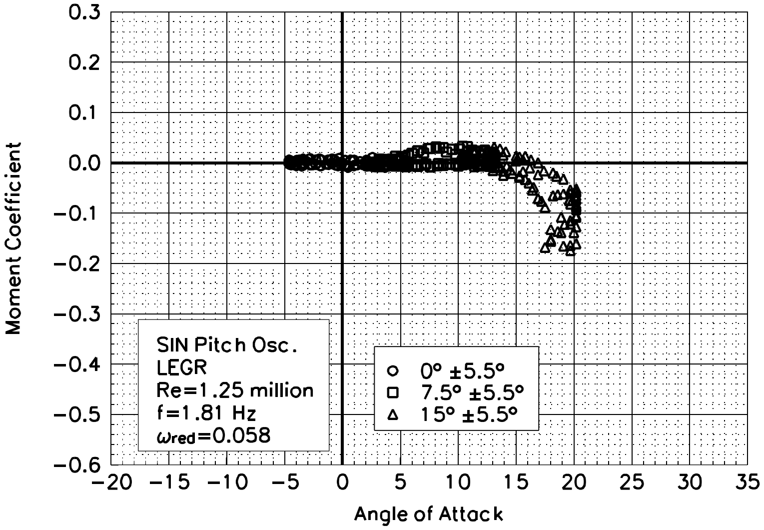

Figure C54. Moment coefficient vs α.

Unsteady Airfoil Characteristics

±12.5◦ Arc-Tangent, Re = 0.75 million

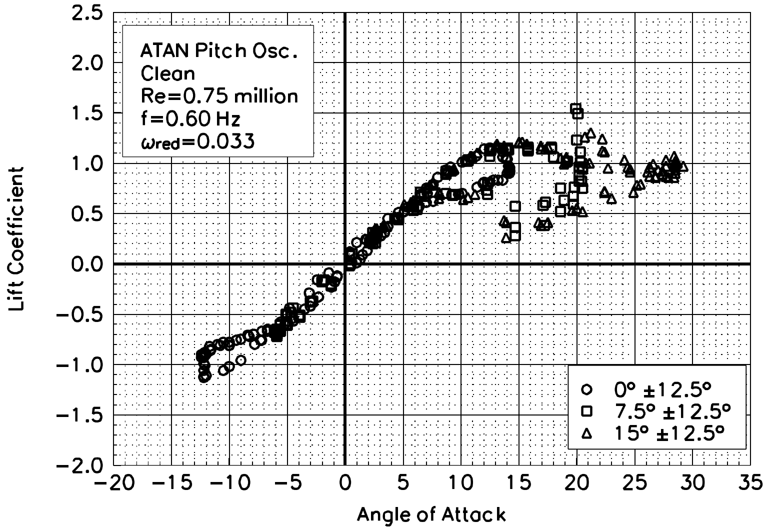

Figure C55. Lift coefficient vs α.

S824
Clean
Re=0.75 million
$\omega_{reduced}$=0.033

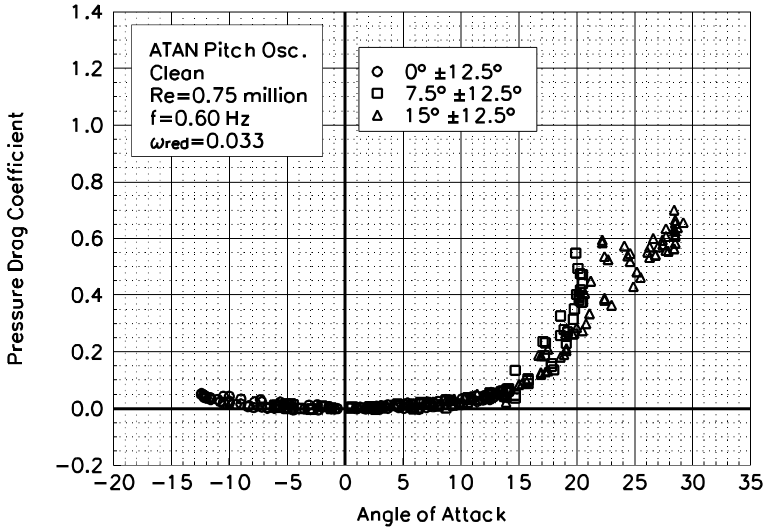

Figure C56. Pressure drag coefficient vs α.

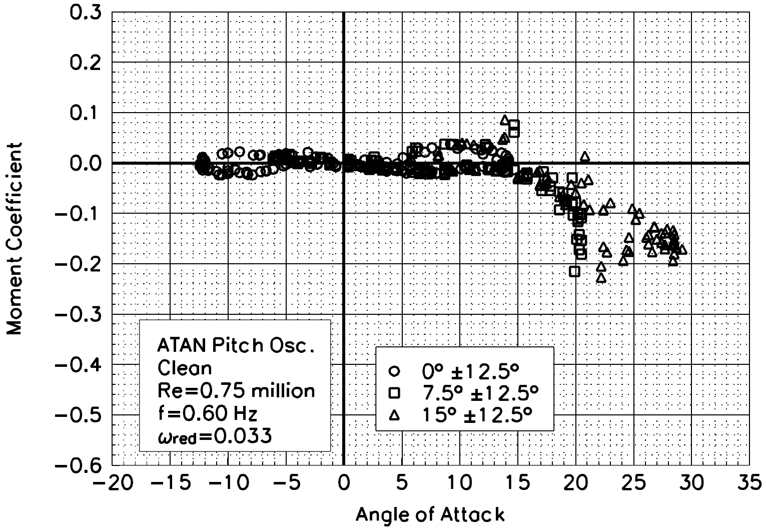

Figure C57. Moment coefficient vs α.

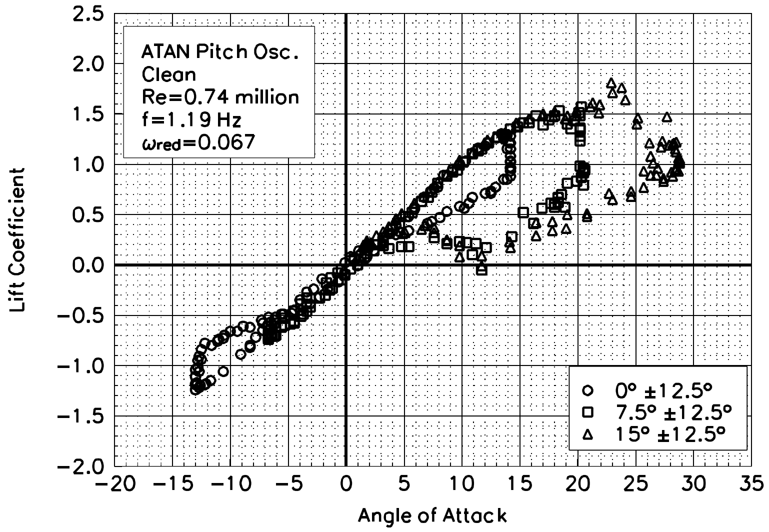

Figure C58. Lift coefficient vs α.

S824
Clean
Re=0.74 million
$\omega_{reduced}$=0.067

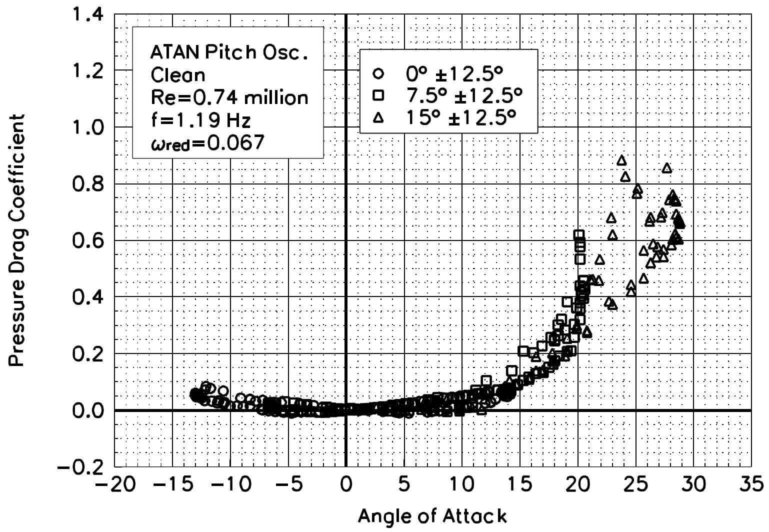

Figure C59. Pressure drag coefficient vs α.

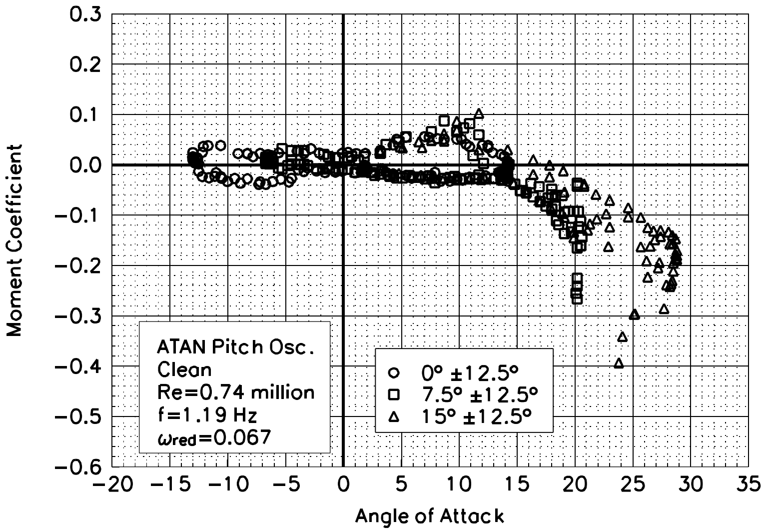

Figure C60. Moment coefficient vs α.

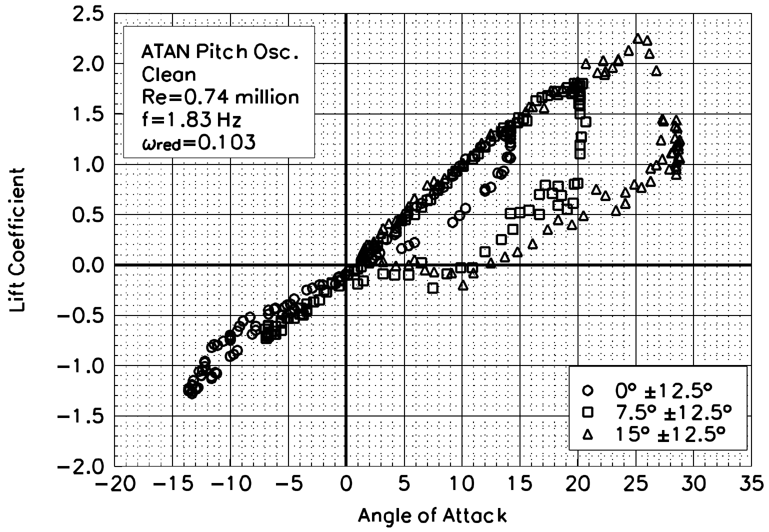

Figure C61. Lift coefficient vs α.

S824
Clean
Re=0.74 million
$\omega_{reduced}$=0.103

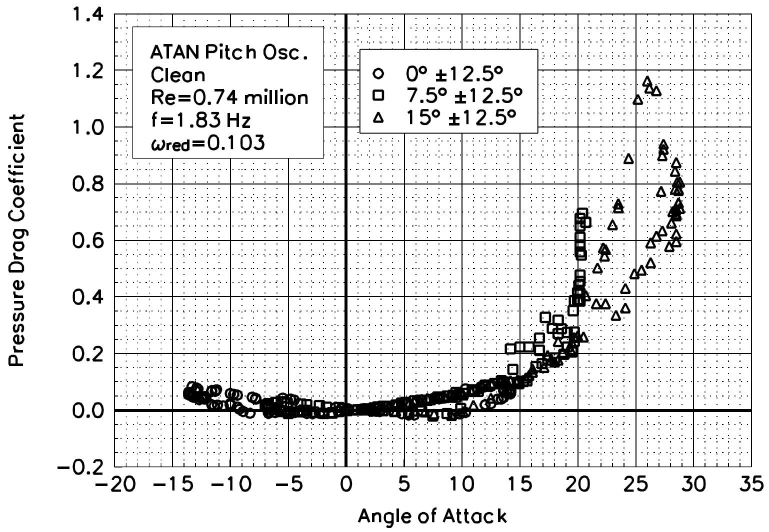

Figure C62. Pressure drag coefficient vs α.

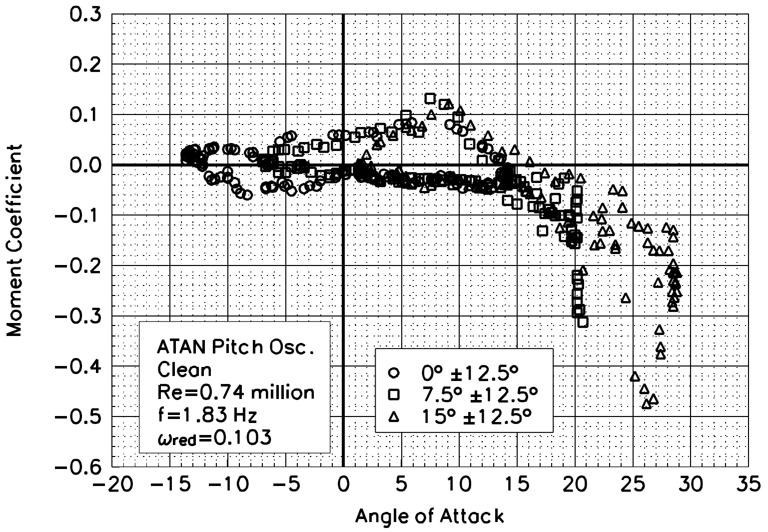

Figure C63. Moment coefficient vs α.

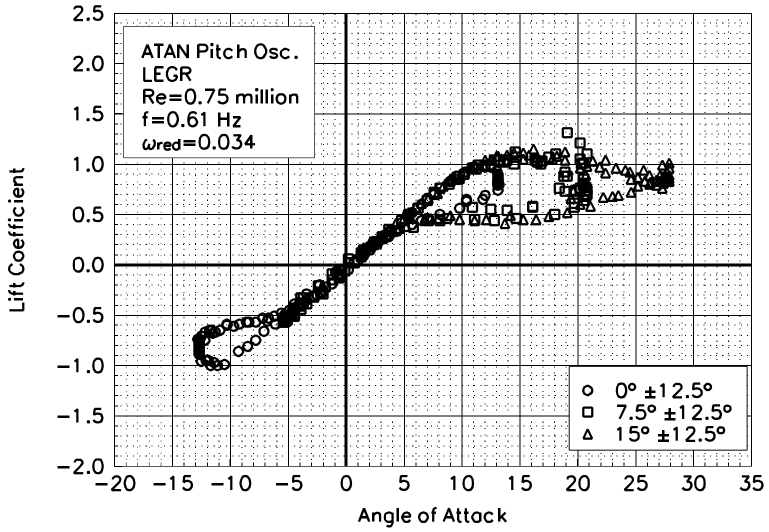

Figure C64. Lift coefficient vs α.

S824
LEGR
Re=0.75 million
$\omega_{reduced}$=0.034

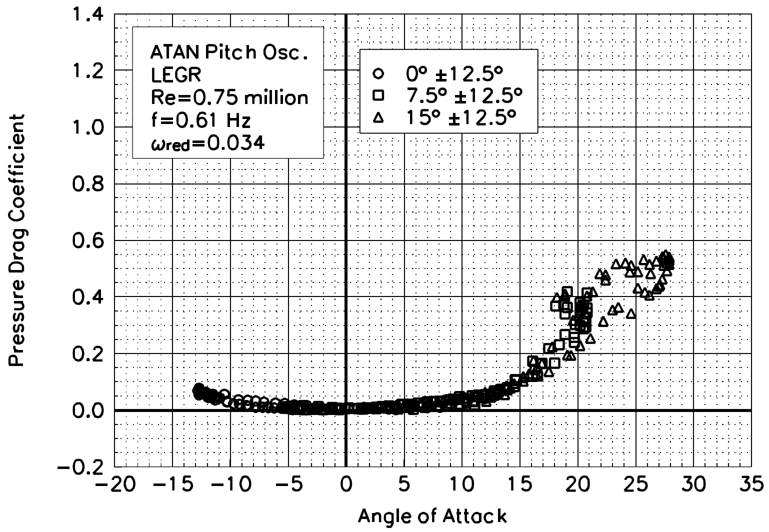

Figure C65. Pressure drag coefficient vs α.

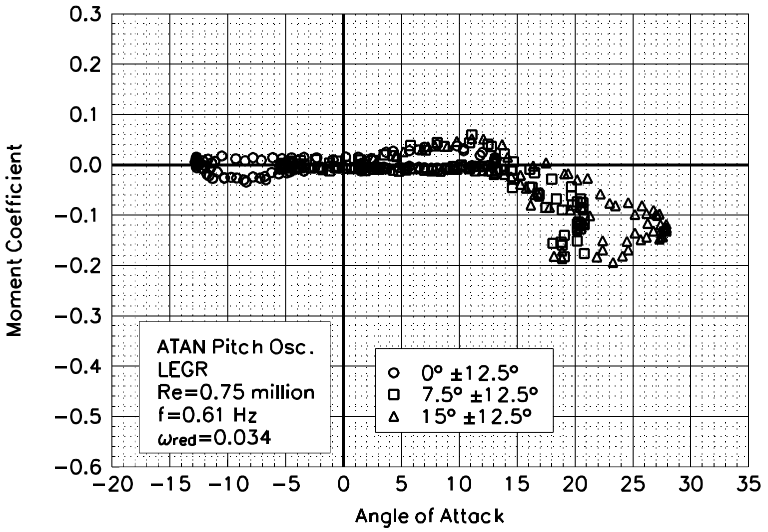

Figure C66. Moment coefficient vs α.

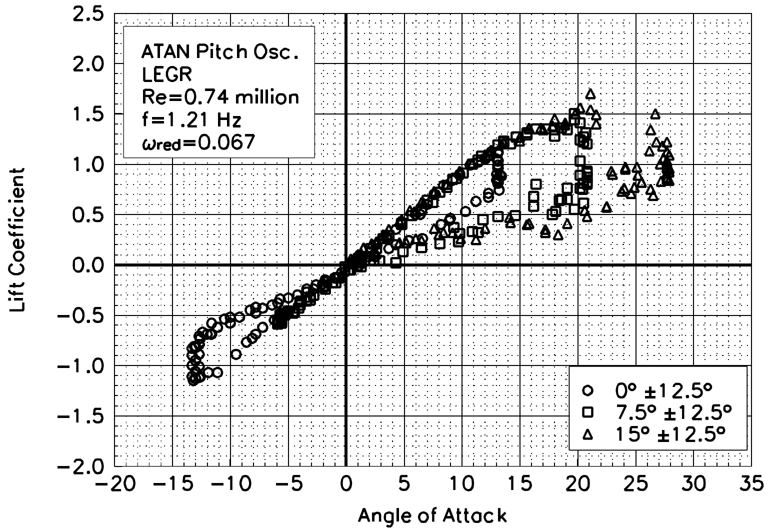

Figure C67. Lift coefficient vs α.

S824

LEGR

Re=0.74 million

$\omega_{reduced}$=0.067

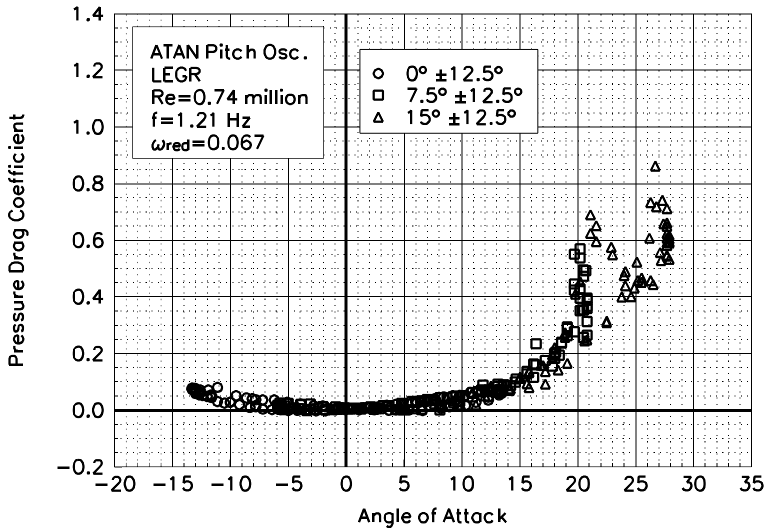

Figure C68. Pressure drag coefficient vs α.

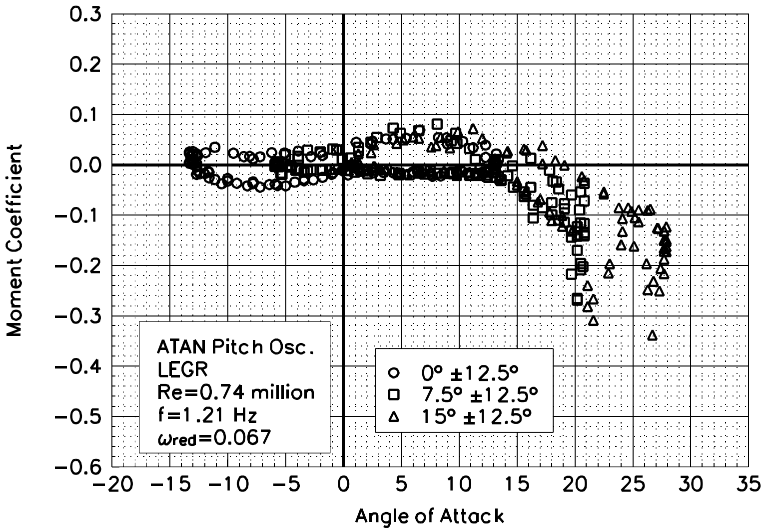

Figure C69. Moment coefficient vs α.

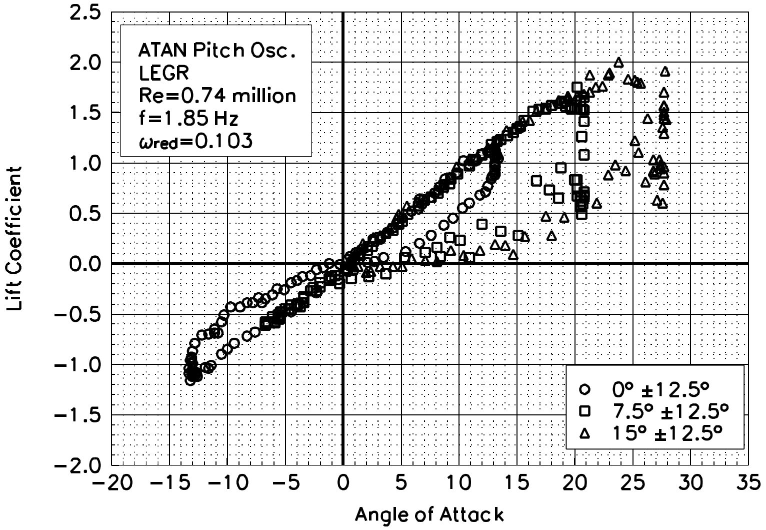

Figure C70. Lift coefficient vs α.

S824
LEGR
Re=0.74 million
$\omega_{reduced}$=0.103

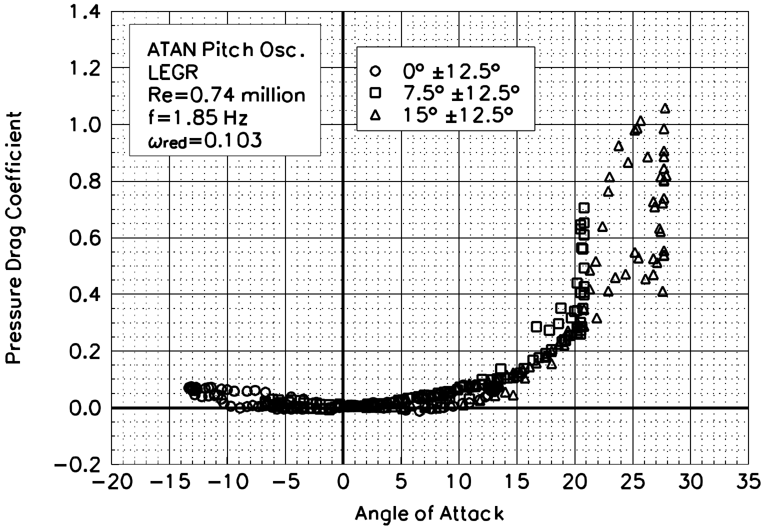

Figure C71. Pressure drag coefficient vs α.

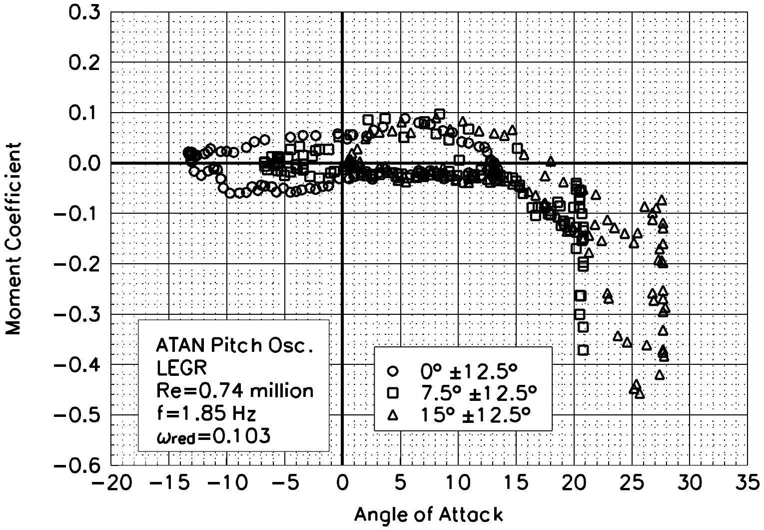

Figure C72. Moment coefficient vs α.

Unsteady Airfoil Characteristics

±12.5° Arc-Tangent, Re = 1.0 million

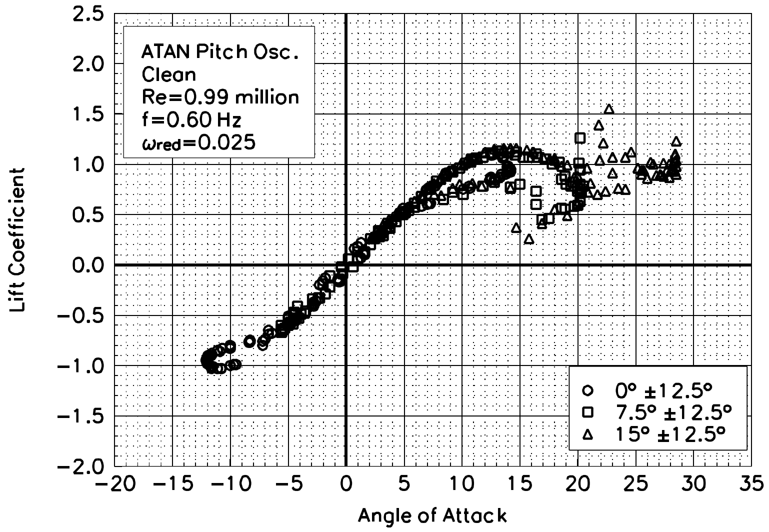

Figure C73. Lift coefficient vs α.

S824
Clean
Re=0.99 million
$\omega_{reduced}$=0.025

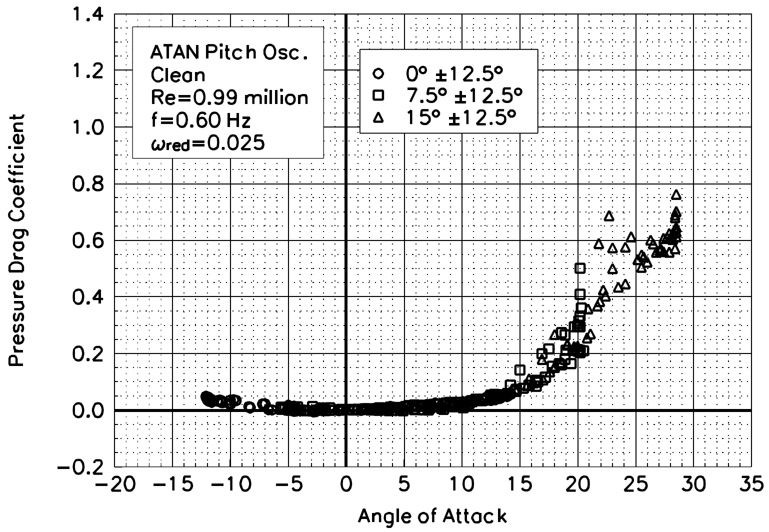

Figure C74. Pressure drag coefficient vs α.

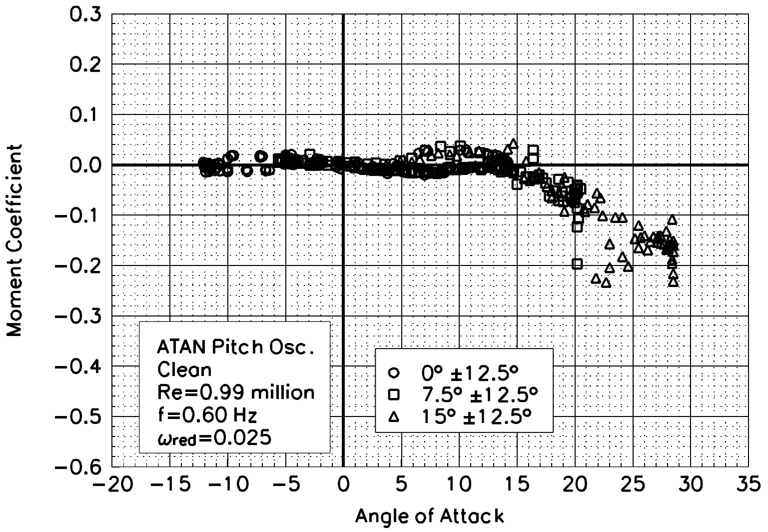

Figure C75. Moment coefficient vs α.

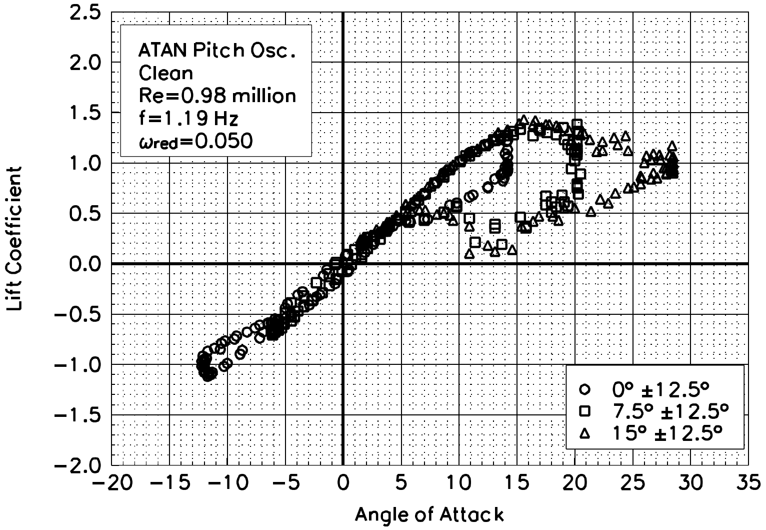

Figure C76. Lift coefficient vs α.

S824
Clean
Re=0.98 million
$\omega_{reduced}$=0.050

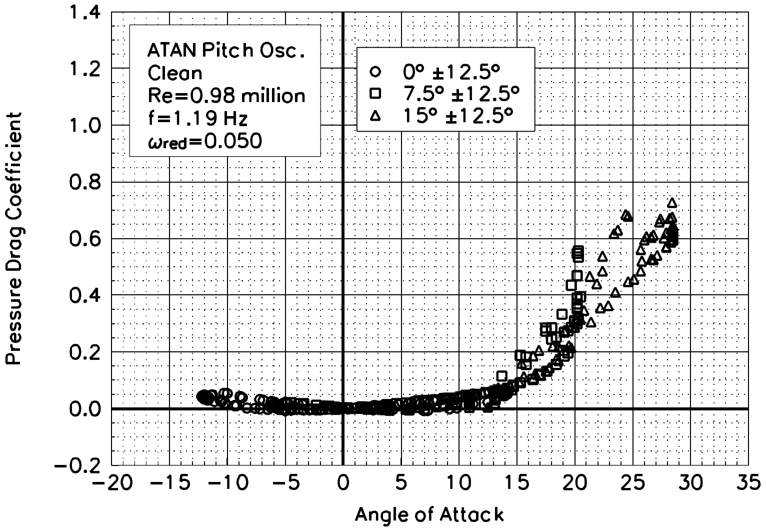

Figure C77. Pressure drag coefficient vs α.

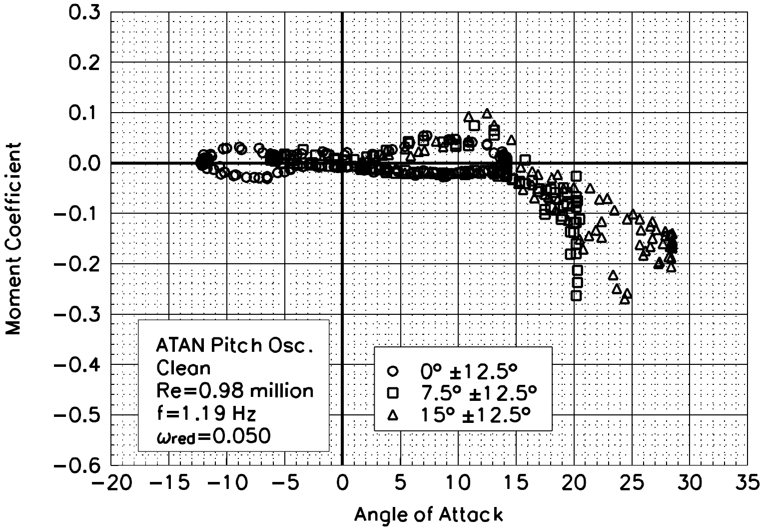

Figure C78. Moment coefficient vs α.

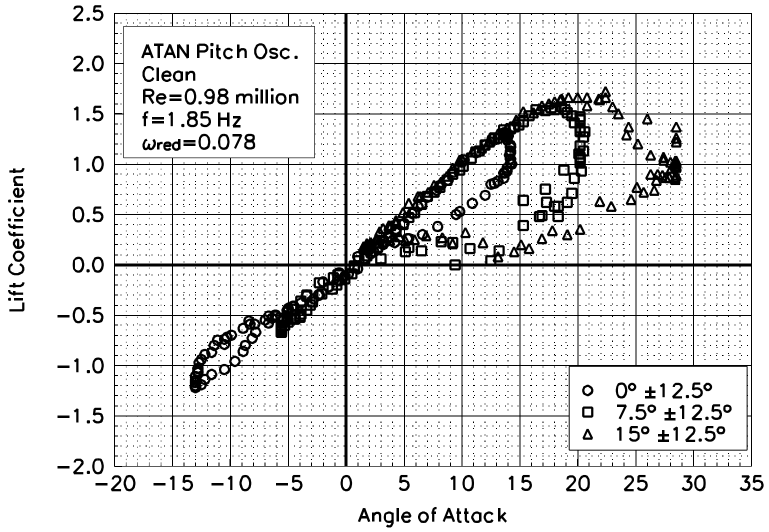

Figure C79. Lift coefficient vs α.

S824
Clean
Re=0.98 million
$\omega_{reduced}$=0.078

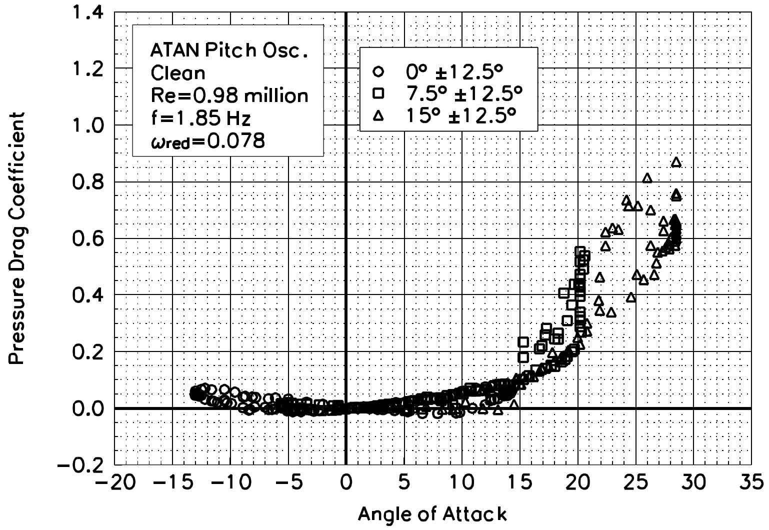

Figure C80. Pressure drag coefficient vs α.

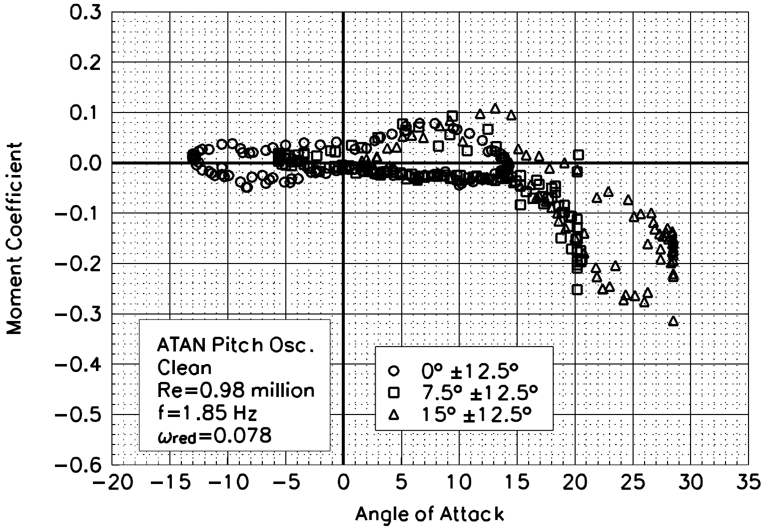

Figure C81. Moment coefficient vs α.

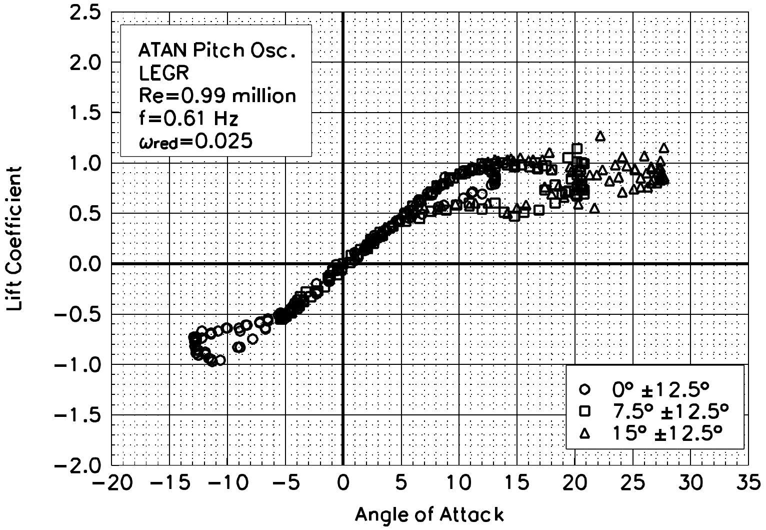

Figure C82. Lift coefficient vs α.

S824
LEGR
Re=0.99 million
$\omega_{reduced}$=0.025

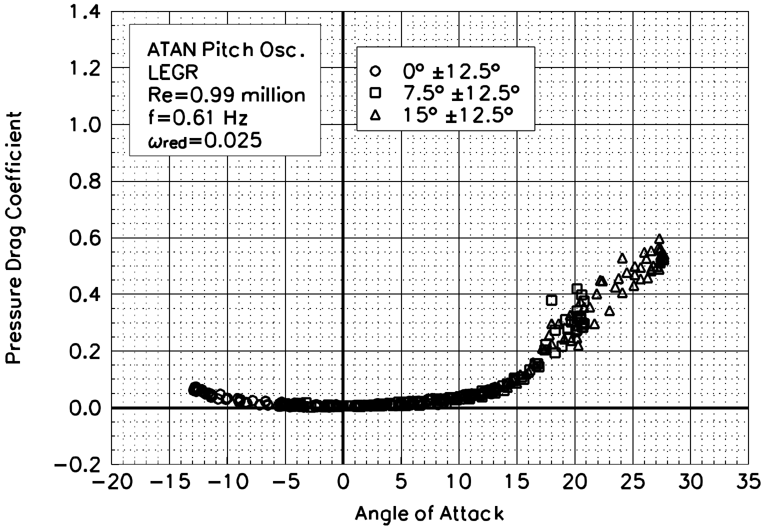

Figure C83. Pressure drag coefficient vs α.

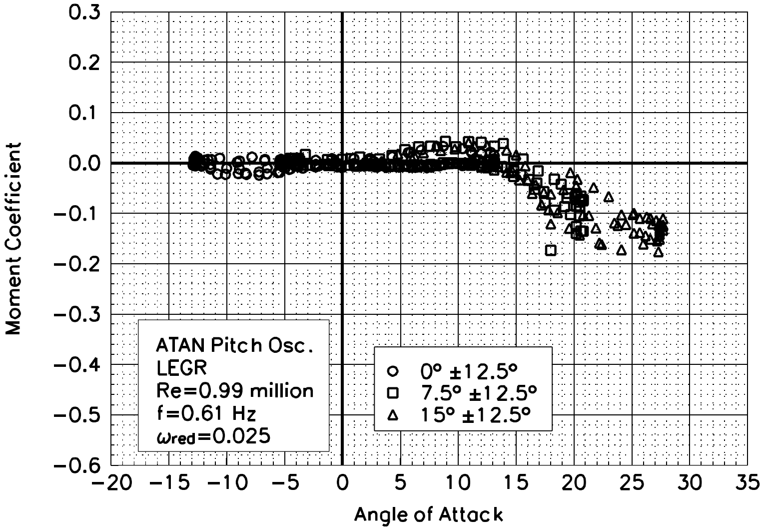

Figure C84. Moment coefficient vs α.

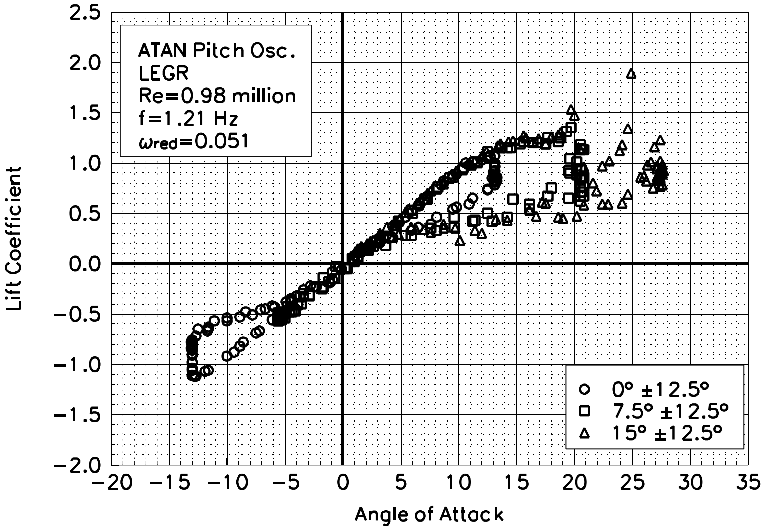

Figure C85. Lift coefficient vs α.

S824
LEGR
Re=0.98 million
$\omega_{reduced}$=0.051

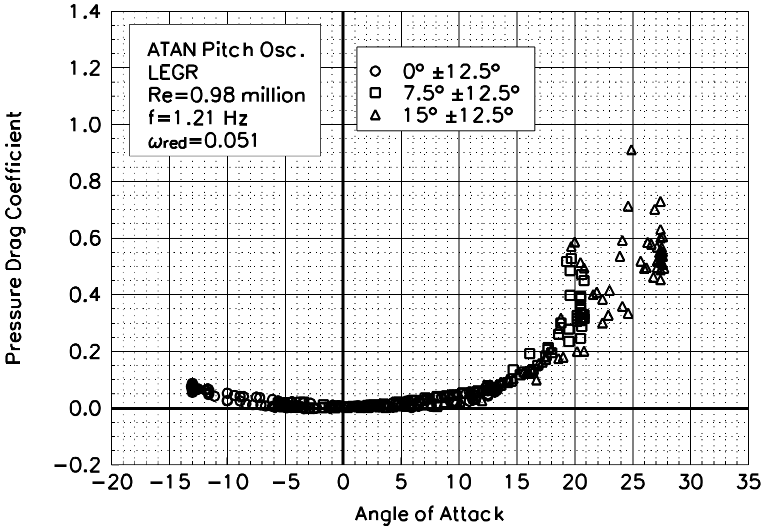

Figure C86. Pressure drag coefficient vs α.

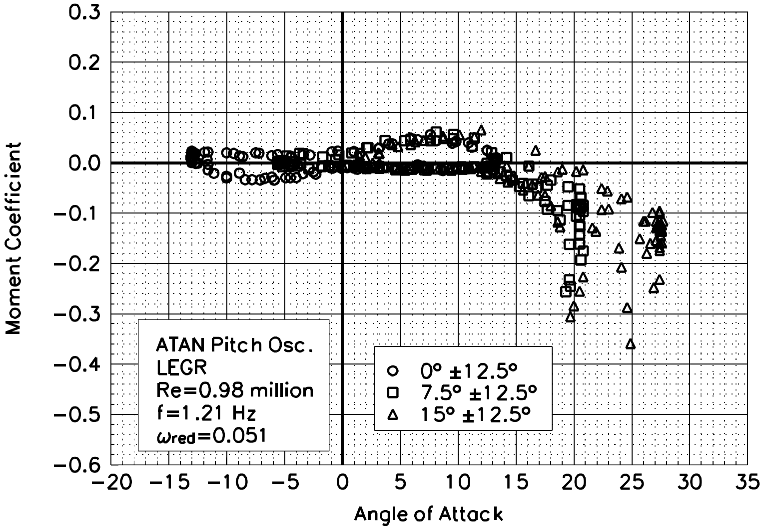

Figure C87. Moment coefficient vs α.

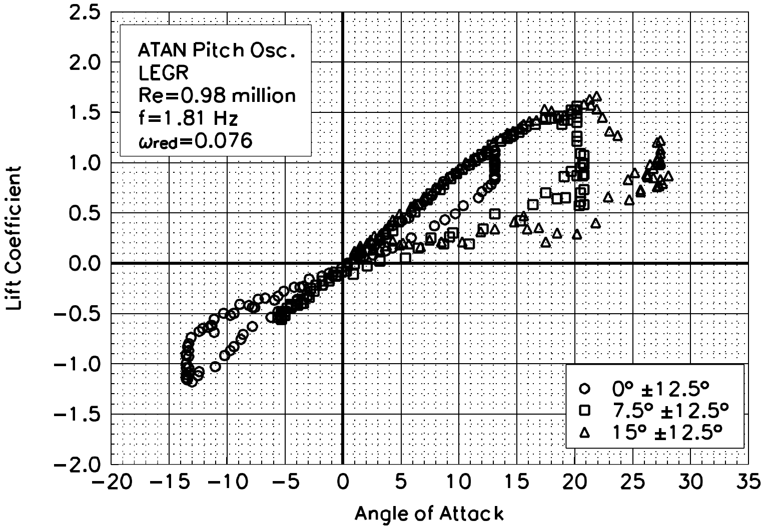

Figure C88. Lift coefficient vs α.

S824

LEGR

Re=0.98 million

$\omega_{reduced}$=0.076

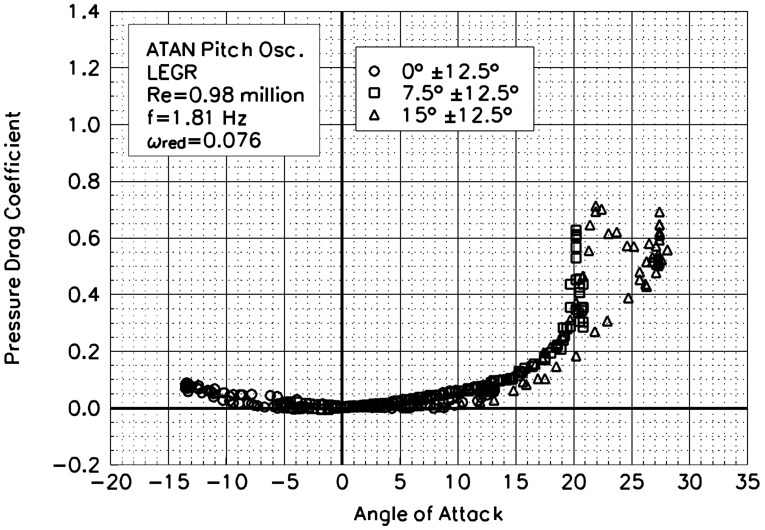

Figure C89. Pressure drag coefficient vs α.

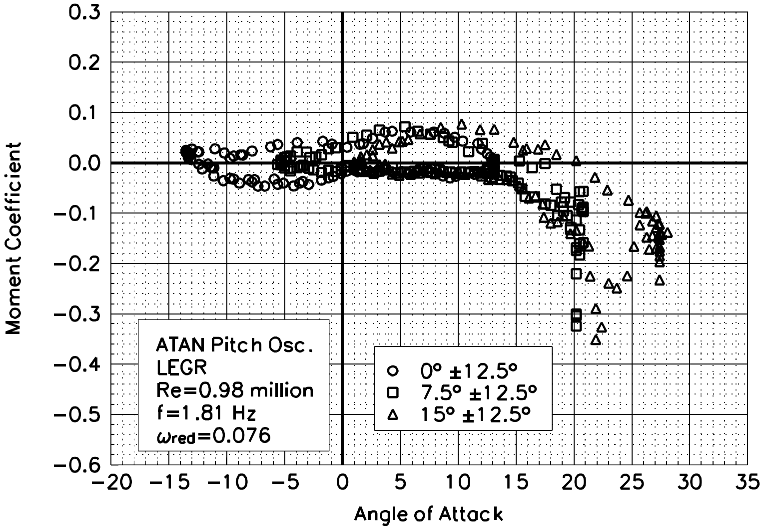

Figure C90. Moment coefficient vs α.

Unsteady Airfoil Characteristics

±12.5° Arc-Tangent, Re = 1.25 million

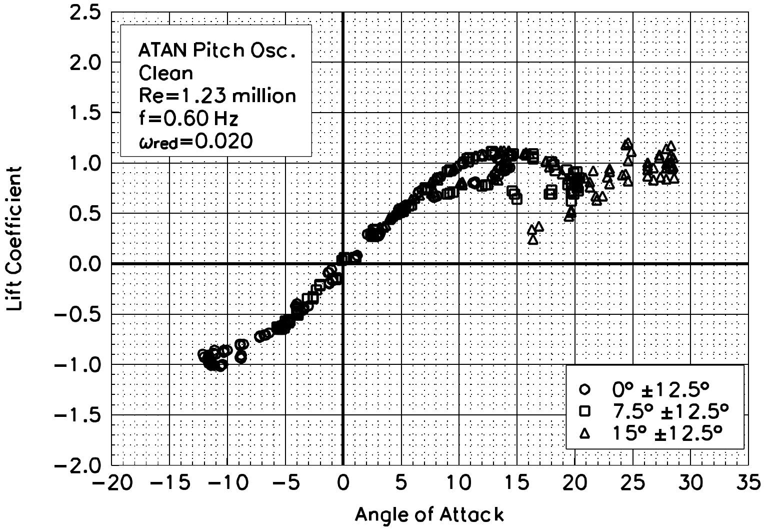

Figure C91. Lift coefficient vs α.

S824
Clean
Re=1.23 million
$\omega_{reduced}$=0.020

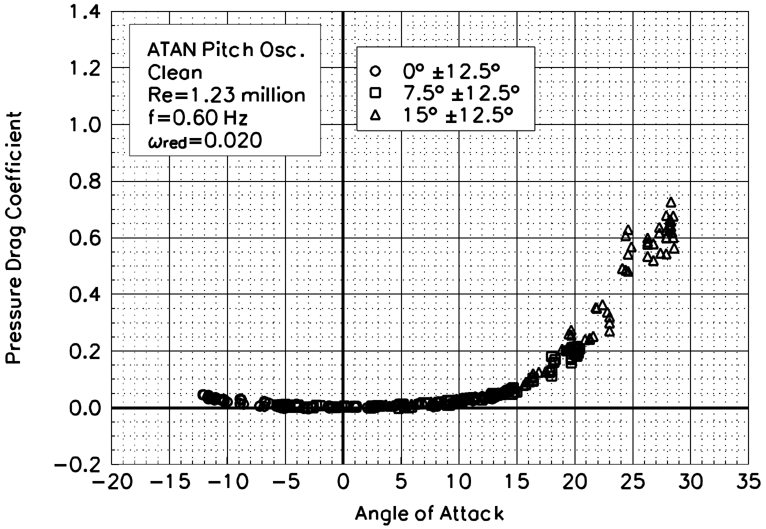

Figure C92. Pressure drag coefficient vs α.

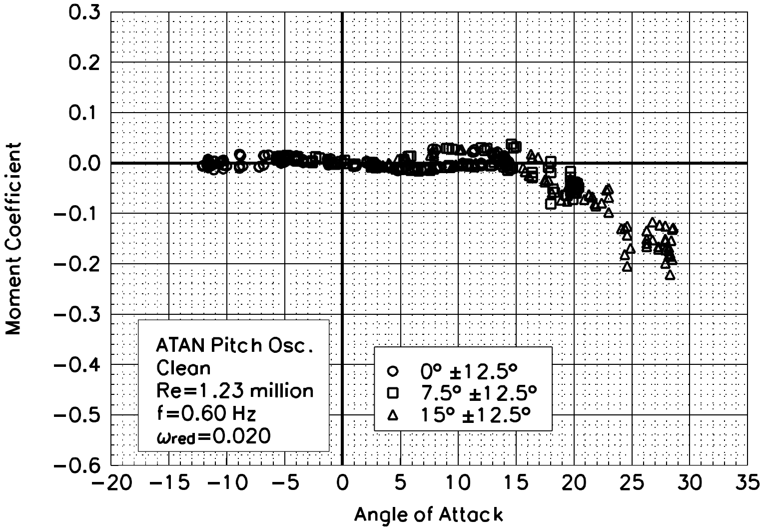

Figure C93. Moment coefficient vs α.

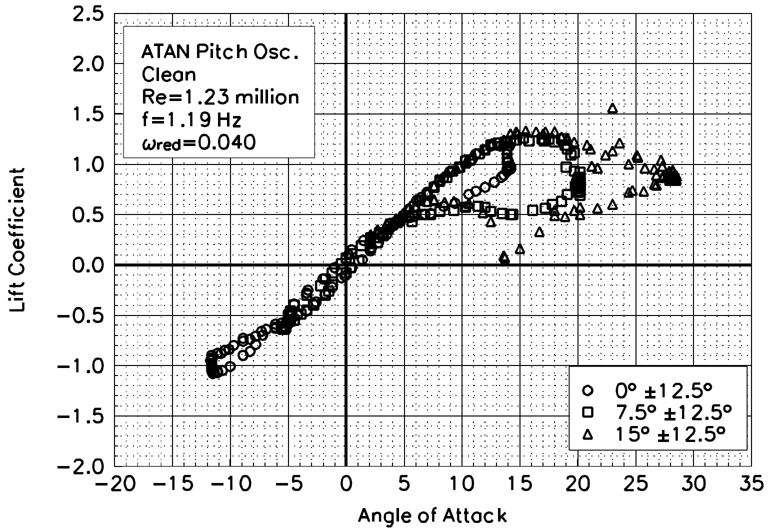

Figure C94. Lift coefficient vs α.

S824
Clean
Re=1.23 million
$\omega_{reduced}$=0.040

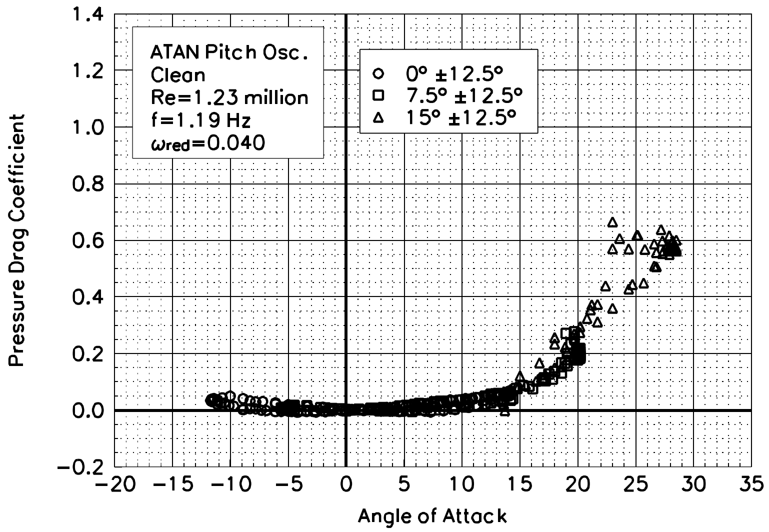

Figure C95. Pressure drag coefficient vs α.

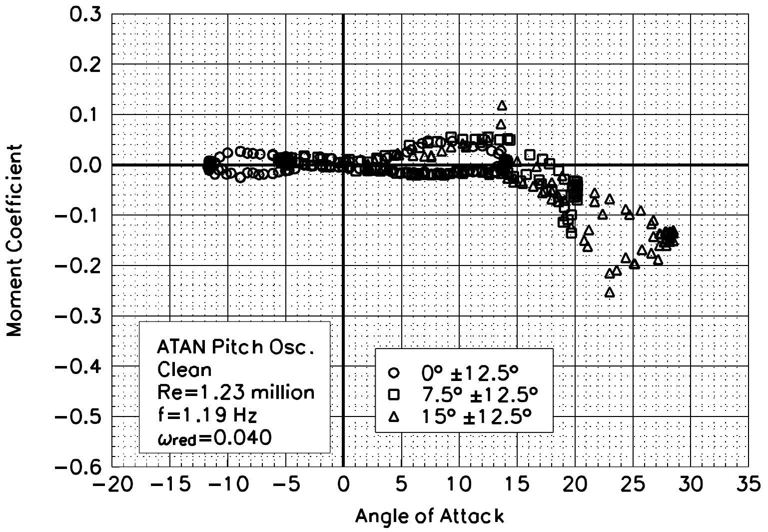

Figure C96. Moment coefficient vs α.

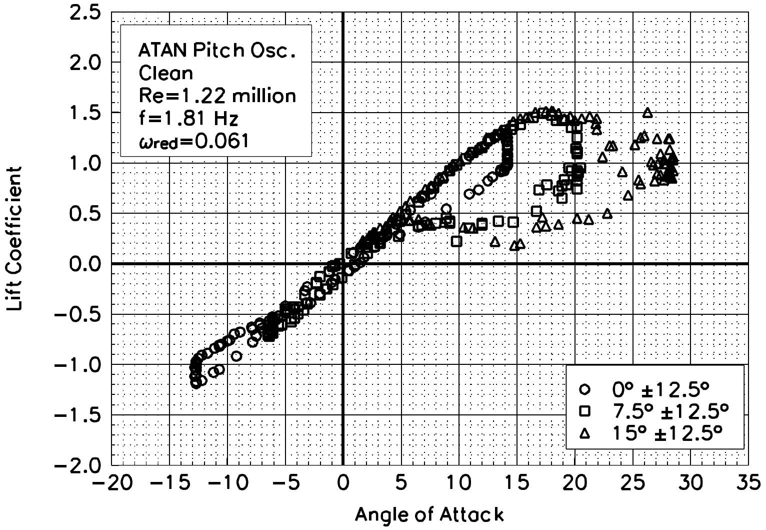

Figure C97. Lift coefficient vs α.

S824
Clean
Re=1.22 million
$\omega_{reduced}$=0.061

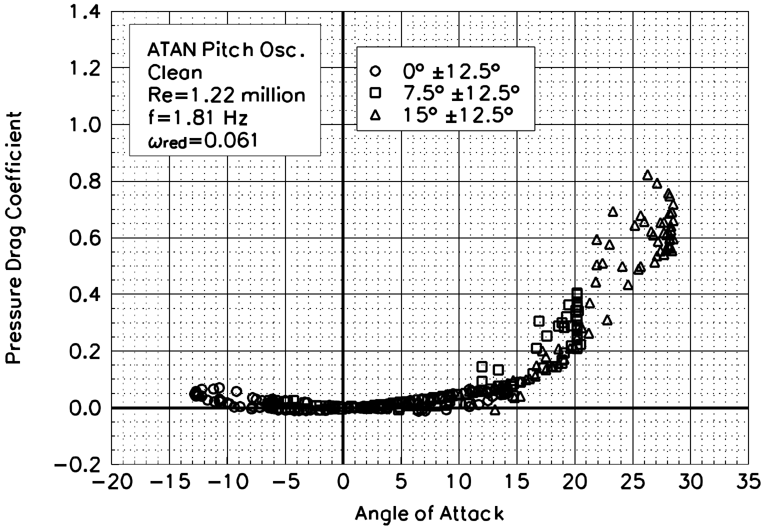

Figure C98. Pressure drag coefficient vs α.

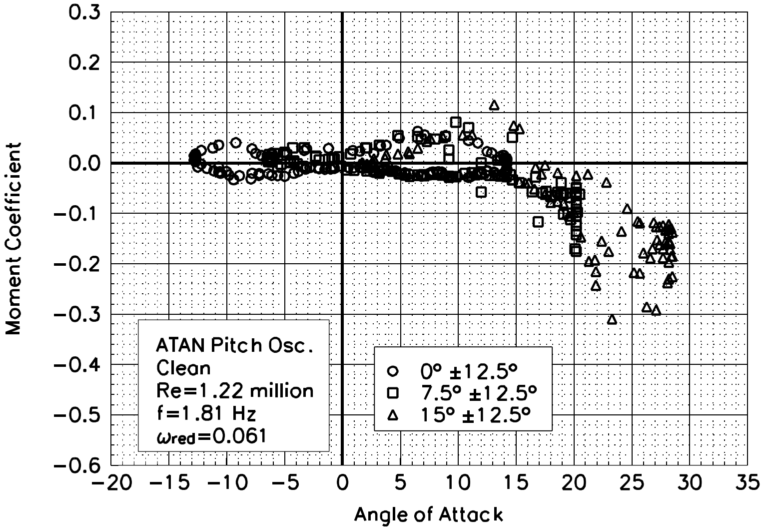

Figure C99. Moment coefficient vs α.

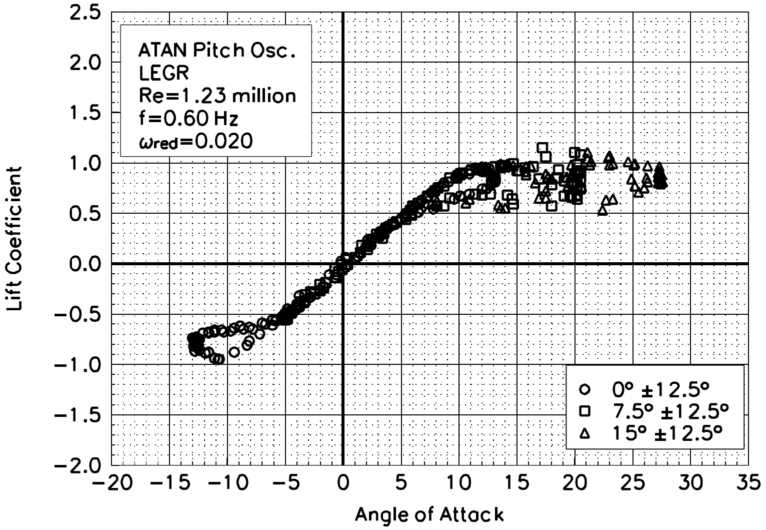

Figure C100. Lift coefficient vs α.

S824
LEGR
Re=1.23 million
$\omega_{reduced}$=0.020

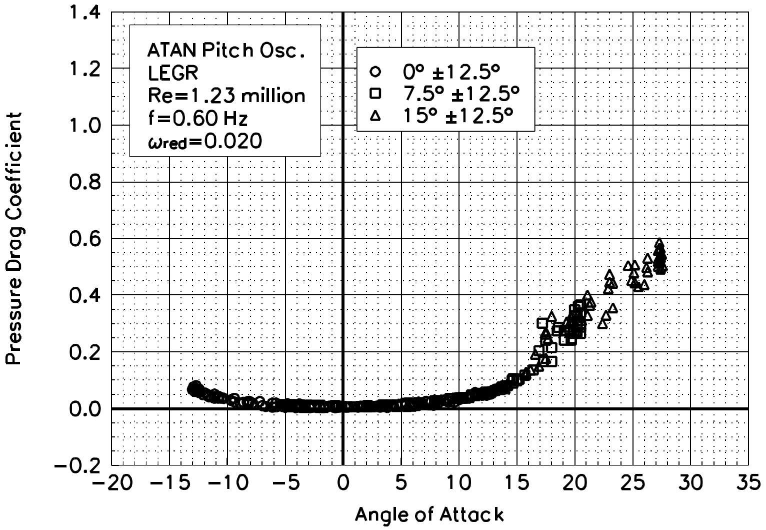

Figure C101. Pressure drag coefficient vs α.

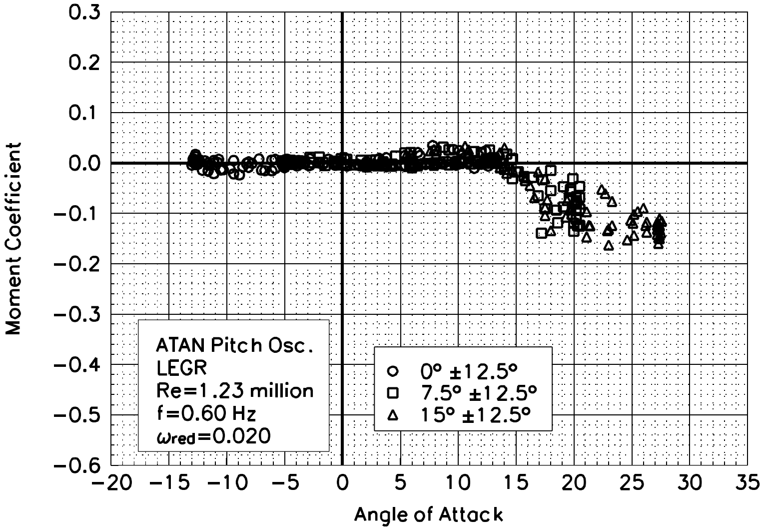

Figure C102. Moment coefficient vs α.

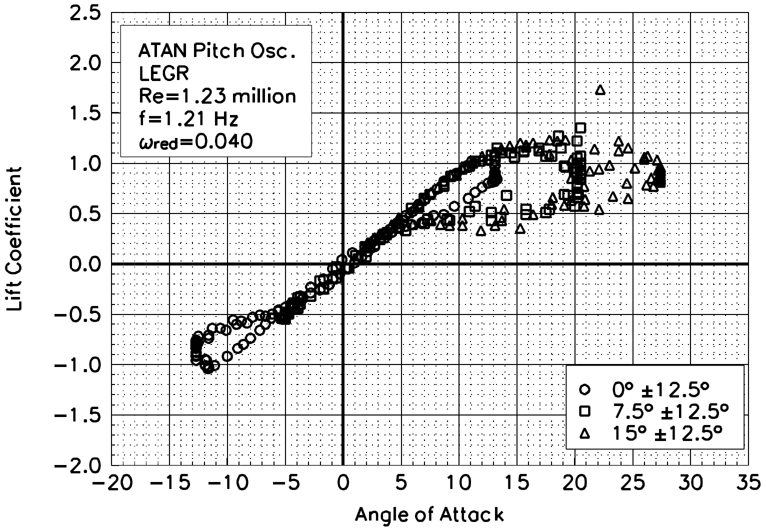

Figure C103. Lift coefficient vs α.

S824
LEGR
Re=1.23 million
$\omega_{reduced}$=0.040

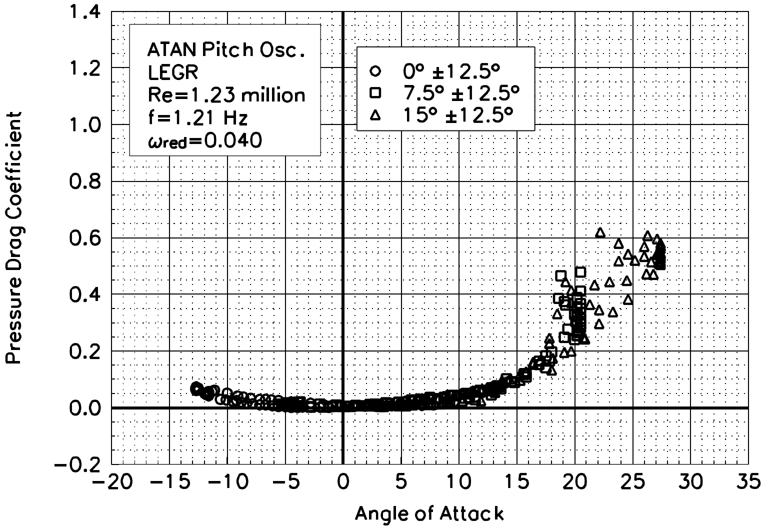

Figure C104. Pressure drag coefficient vs α.

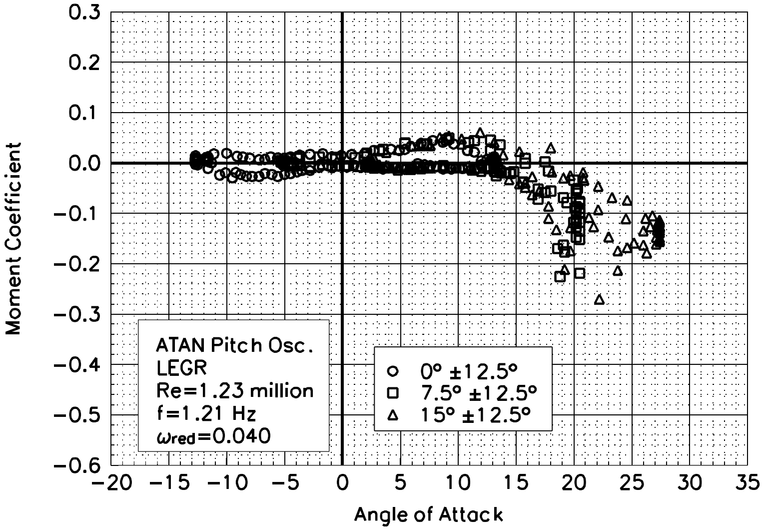

Figure C105. Moment coefficient vs α.

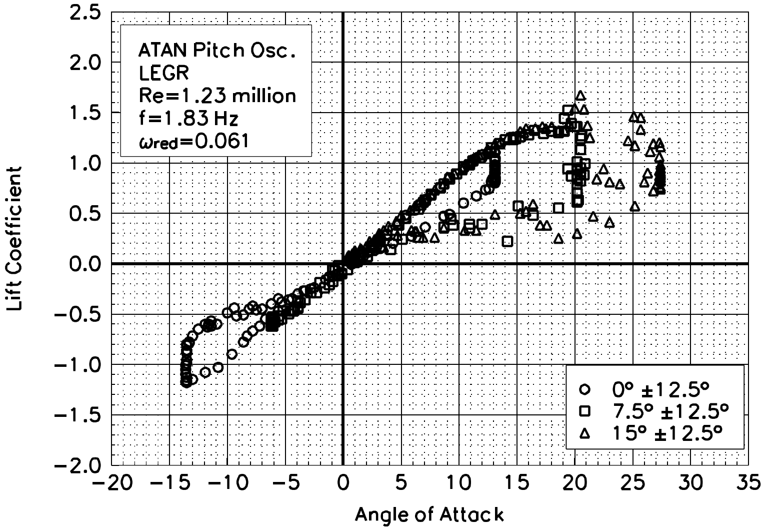

Figure C106. Lift coefficient vs α.

S824
LEGR
Re=1.23 million
$\omega_{reduced}$=0.061

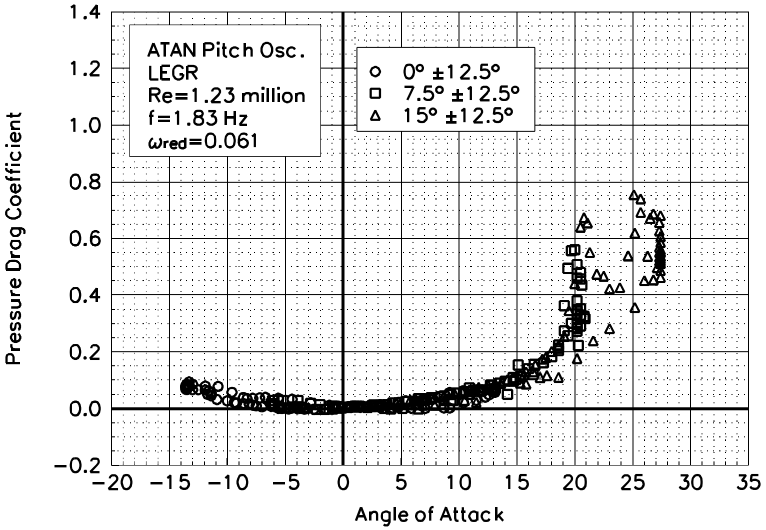

Figure C107. Pressure drag coefficient vs α.

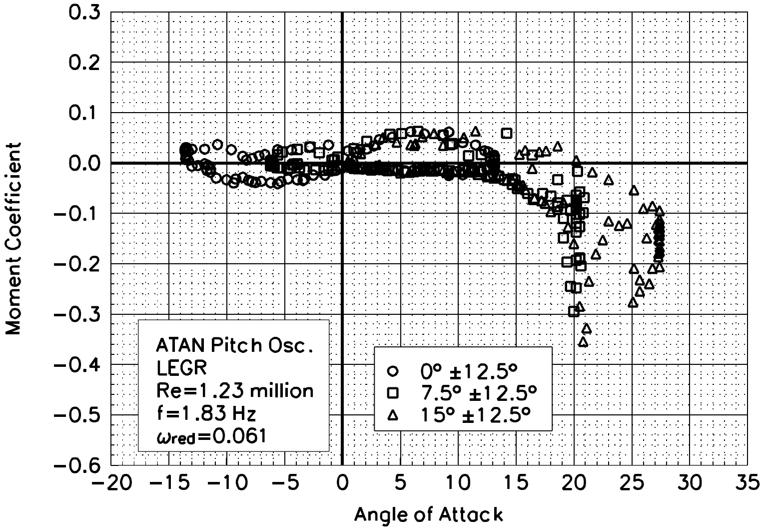

Figure C108. Moment coefficient vs α.

Unsteady Airfoil Characteristics

±20° Arc-Tangent, Re = 0.75 million

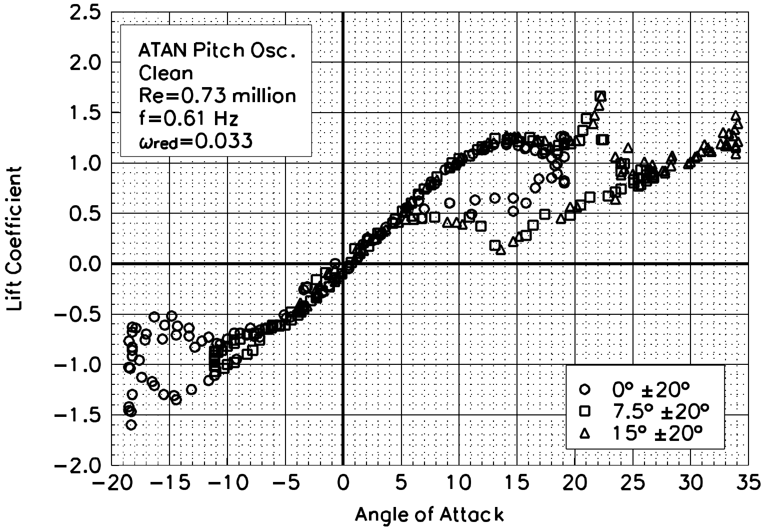

S824
Clean
Re=0.73 million
$\omega_{reduced}$=0.033

Figure C109. Lift coefficient vs α.

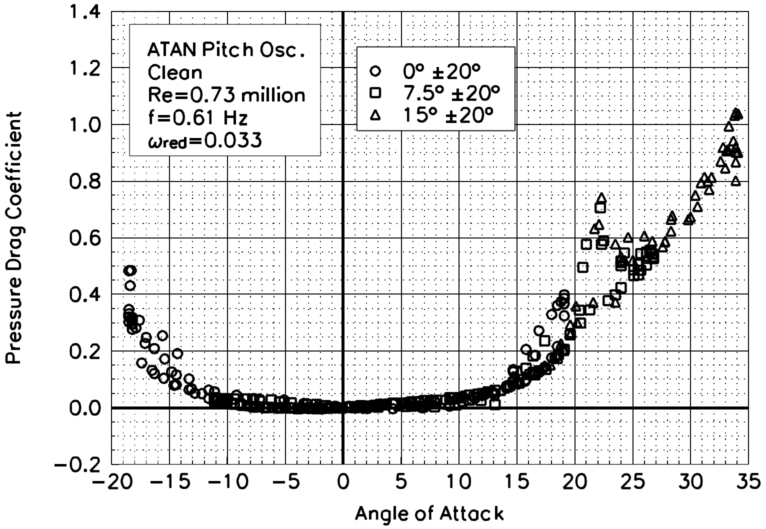

Figure C110. Pressure drag coefficient vs α.

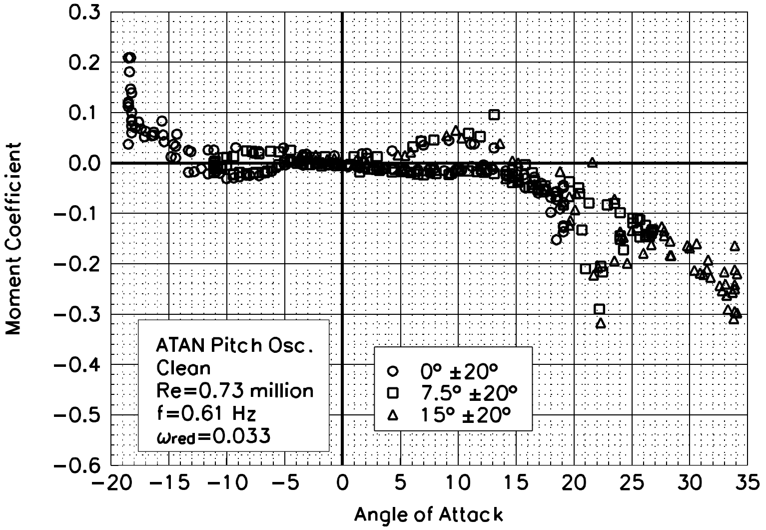

Figure C111. Moment coefficient vs α.

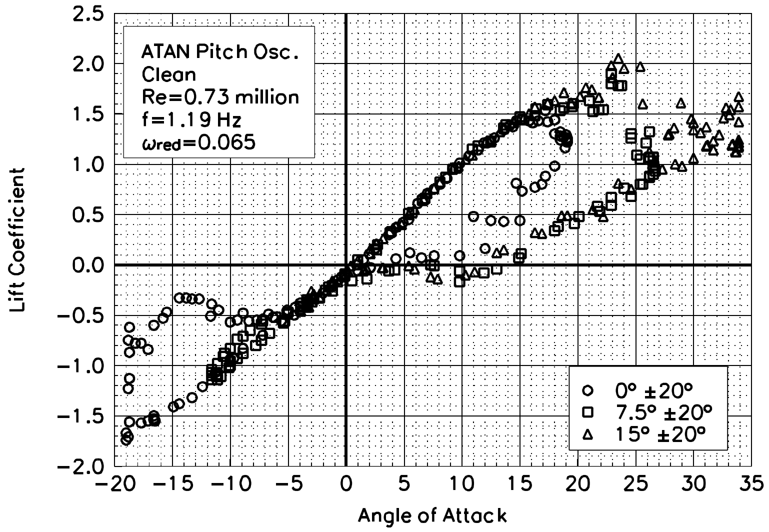

Figure C112. Lift coefficient vs α.

S824
Clean
Re=0.73 million
$\omega_{reduced}$=0.065

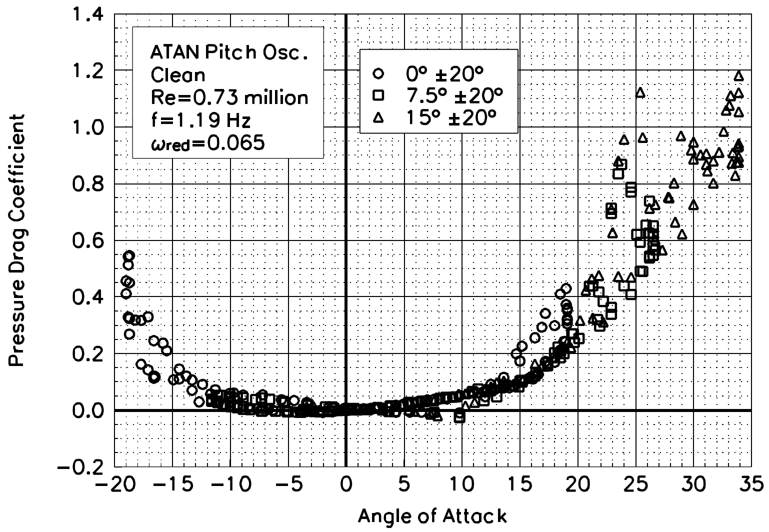

Figure C113. Pressure drag coefficient vs α.

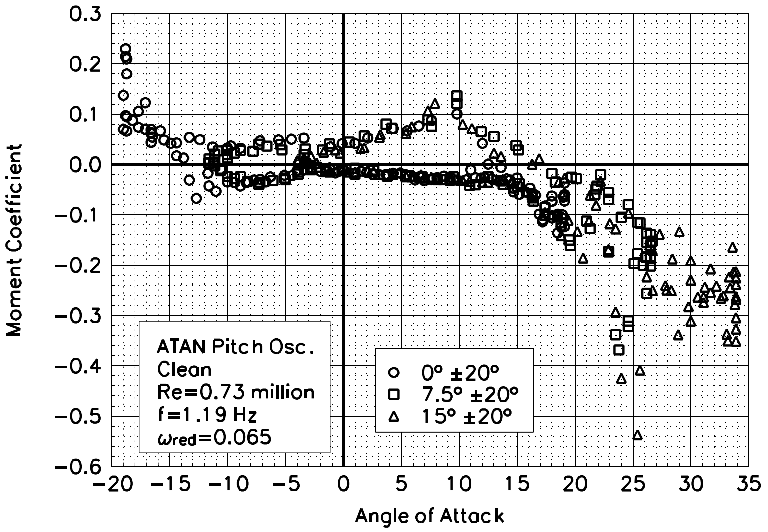

Figure C114. Moment coefficient vs α.

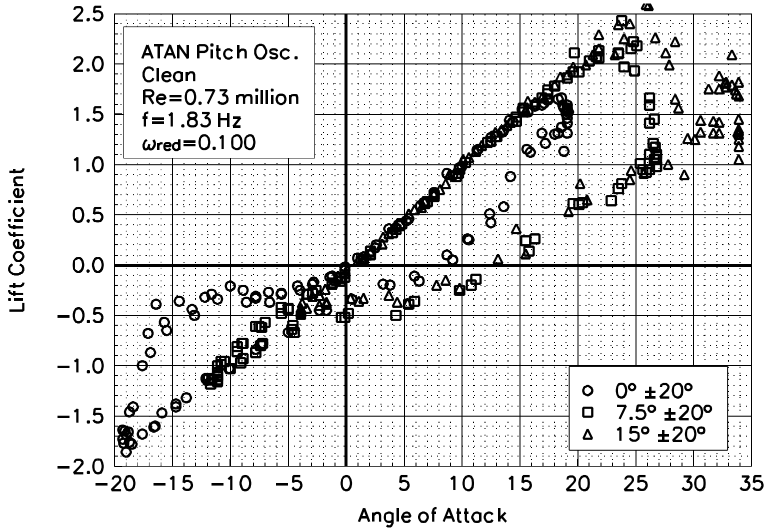

Figure C115. Lift coefficient vs α.

S824
Clean
Re=0.73 million
$\omega_{reduced}$=0.100

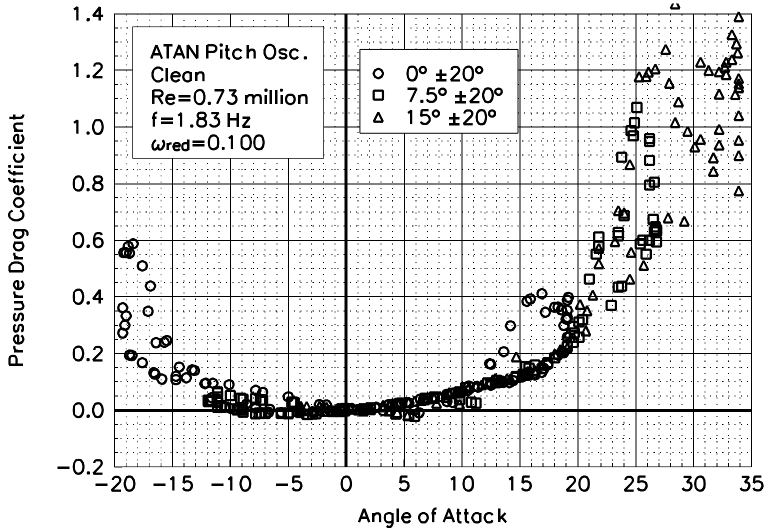

Figure C116. Pressure drag coefficient vs α.

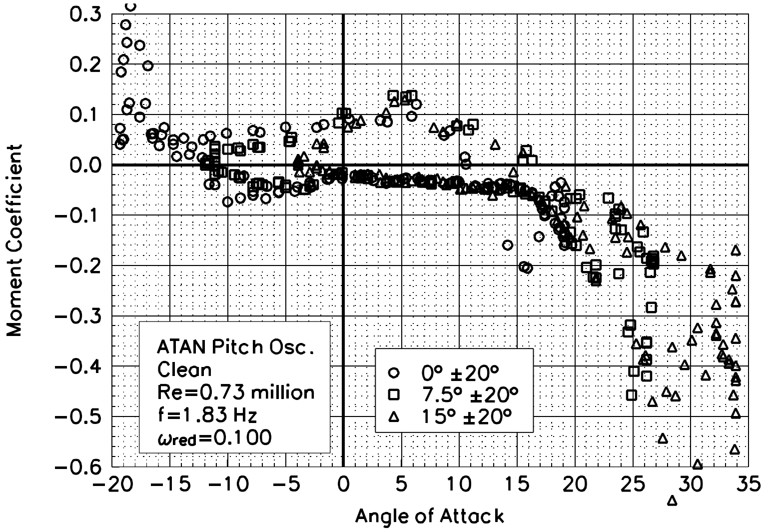

Figure C117. Moment coefficient vs α.

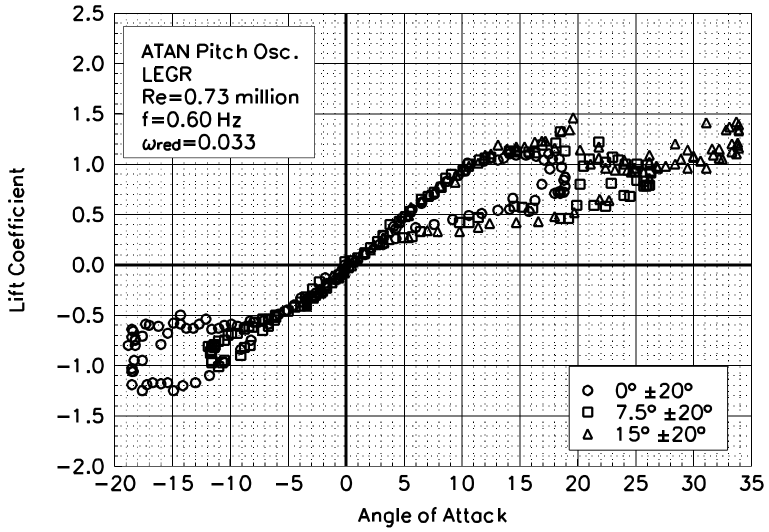

Figure C118. Lift coefficient vs α.

S824
LEGR
Re=0.73 million
$\omega_{reduced}$=0.033

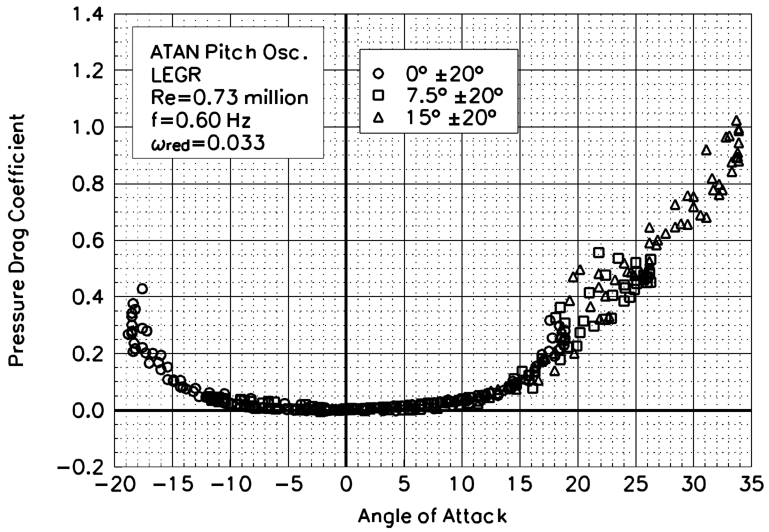

Figure C119. Pressure drag coefficient vs α.

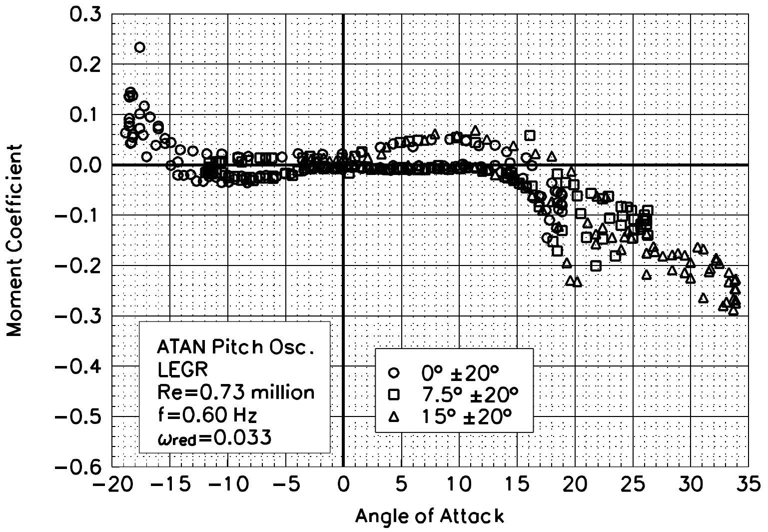

Figure C120. Moment coefficient vs α.

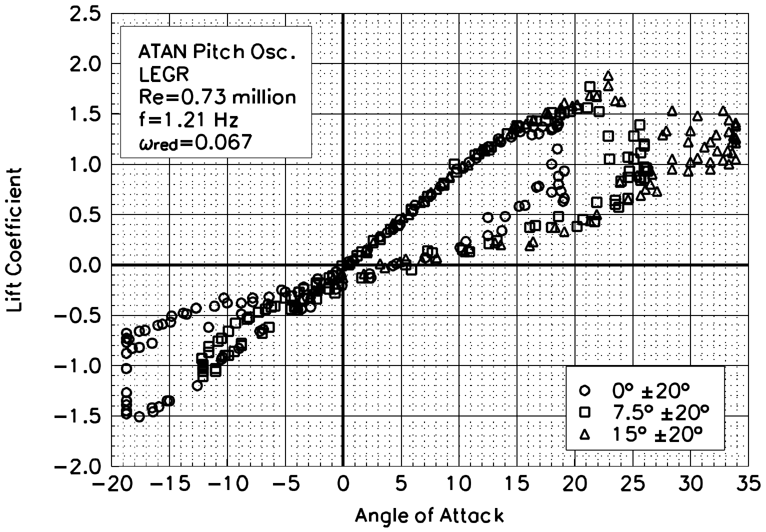

Figure C121. Lift coefficient vs α.

S824
LEGR
Re=0.73 million
$\omega_{reduced}$=0.067

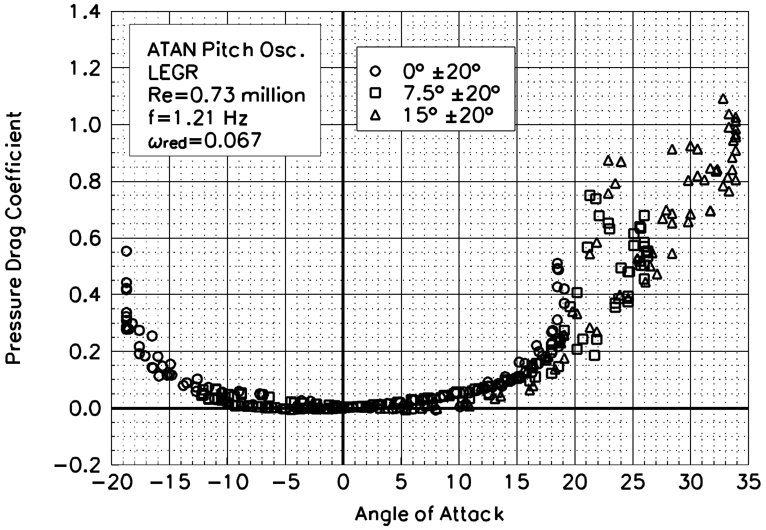

Figure C122. Pressure drag coefficient vs α.

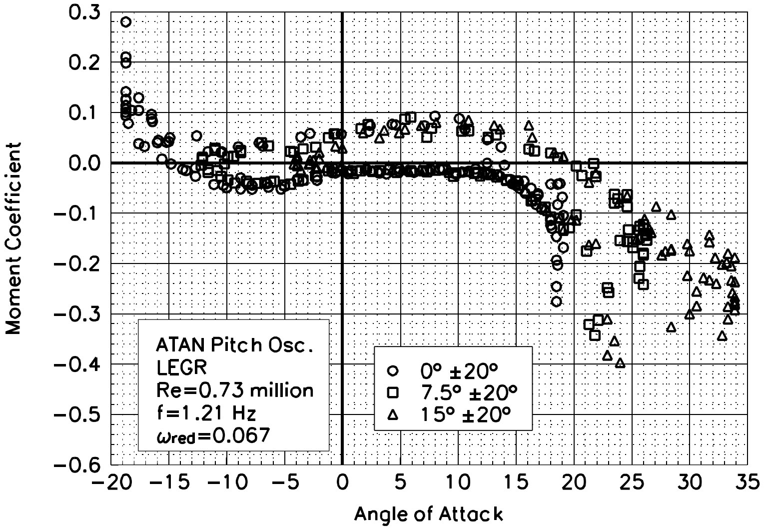

Figure C123. Moment coefficient vs α.

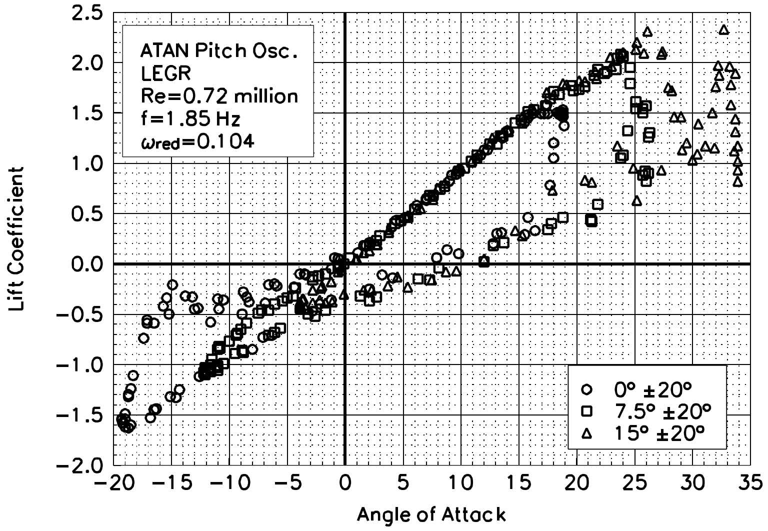

Figure C124. Lift coefficient vs α.

S824
LEGR
Re=0.72 million
$\omega_{reduced}$=0.104

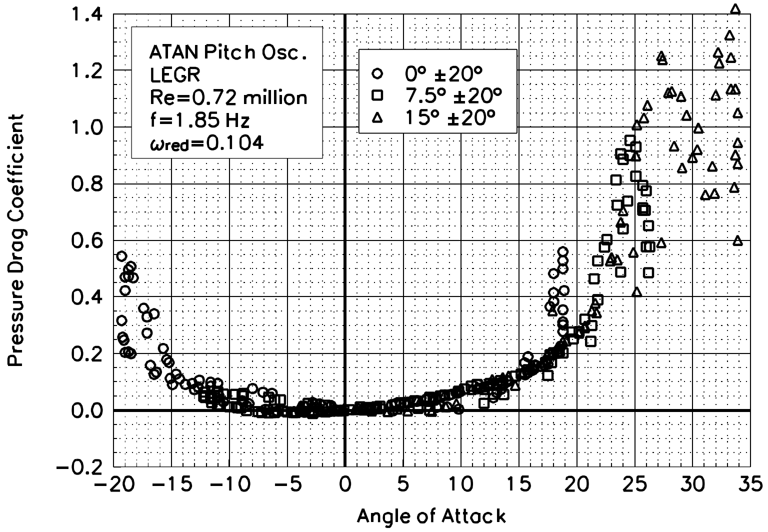

Figure C125. Pressure drag coefficient vs α.

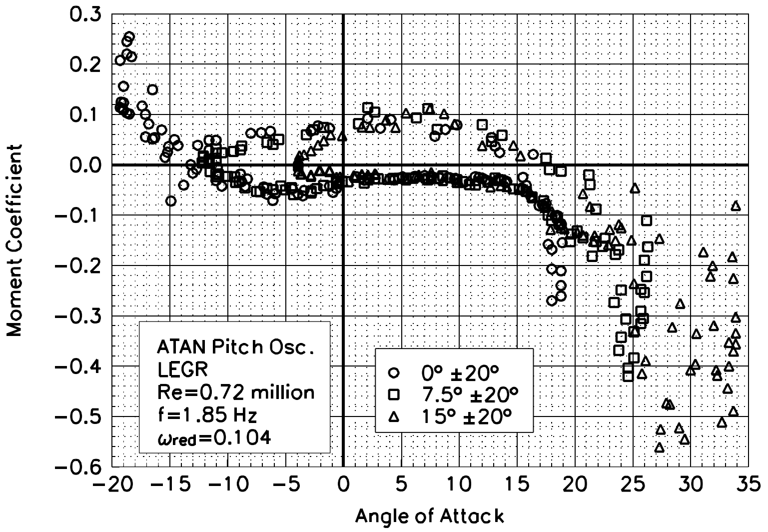

Figure C126. Moment coefficient vs α.

Unsteady Airfoil Characteristics

±20° Arc-Tangent, Re = 1.0 million

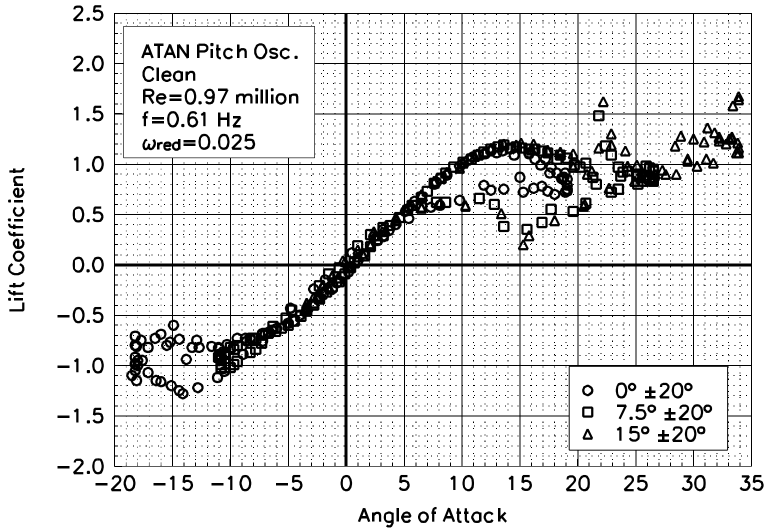

Figure C127. Lift coefficient vs α.

S824
Clean
Re=0.97 million
$\omega_{reduced}$=0.025

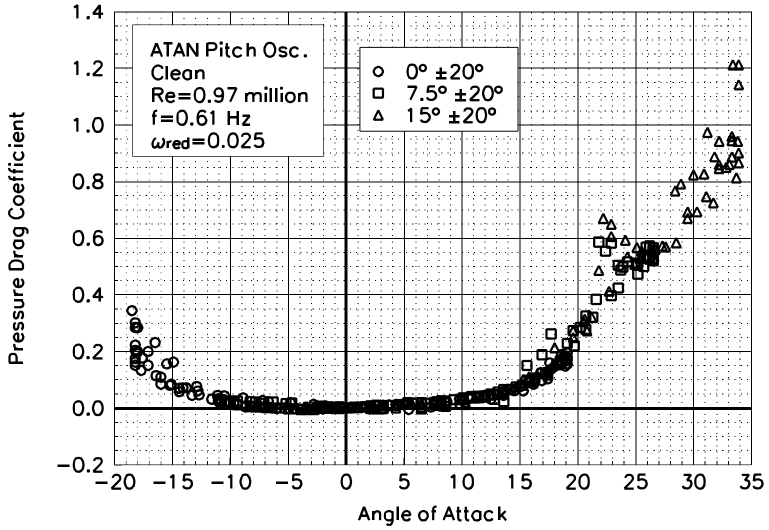

Figure C128. Pressure drag coefficient vs α.

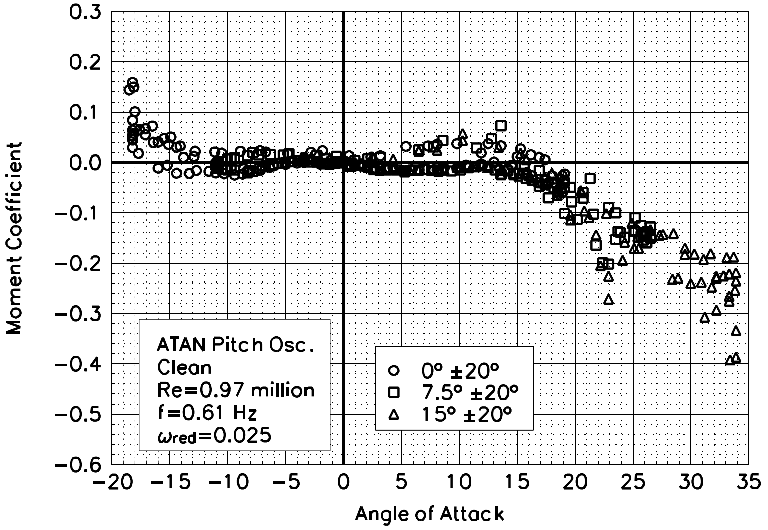

Figure C129. Moment coefficient vs α.

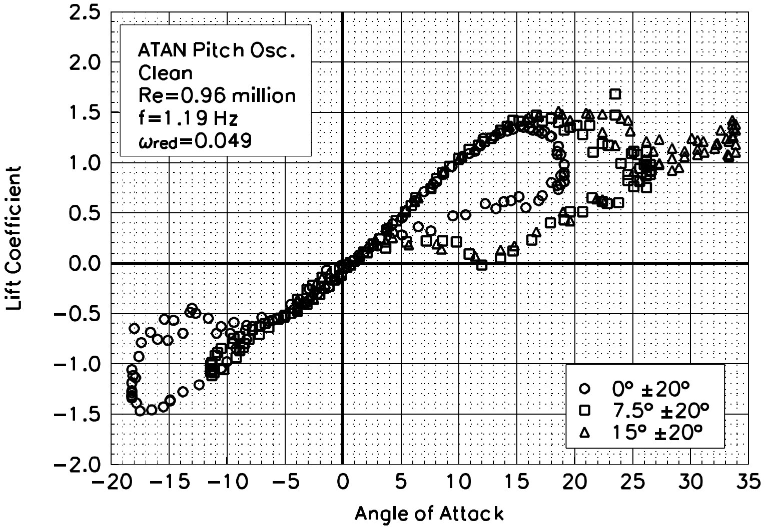

Figure C130. Lift coefficient vs α.

S824
Clean
Re=0.96 million
$\omega_{reduced}$=0.049

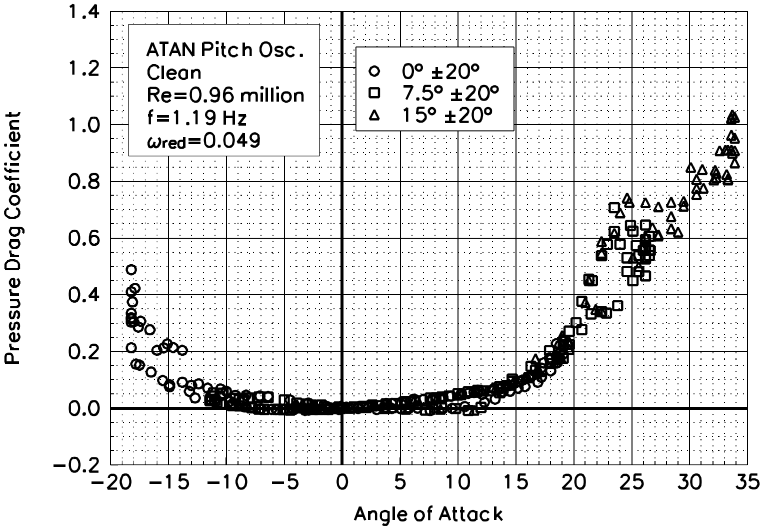

Figure C131. Pressure drag coefficient vs α.

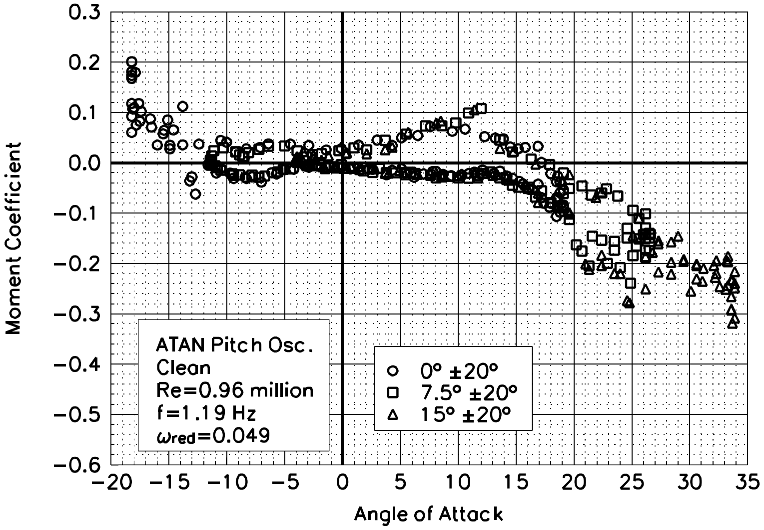

Figure C132. Moment coefficient vs α.

S824
Clean
Re=0.96 million
$\omega_{reduced}$=0.076

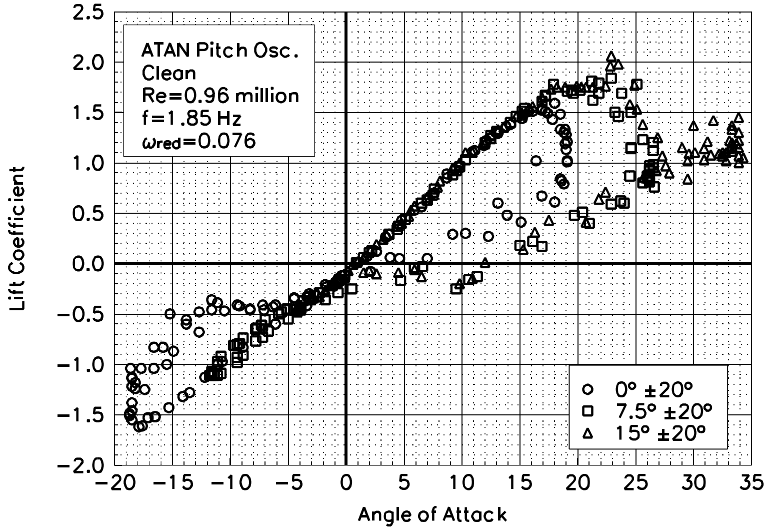

Figure C133. Lift coefficient vs α.

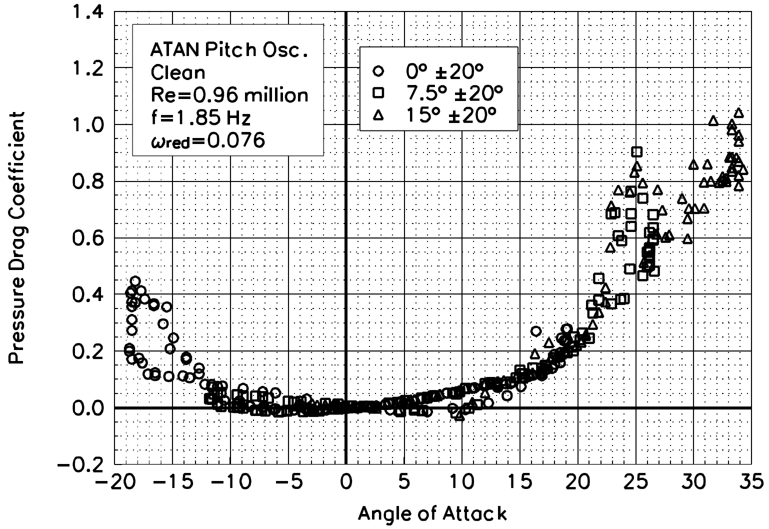

Figure C134. Pressure drag coefficient vs α.

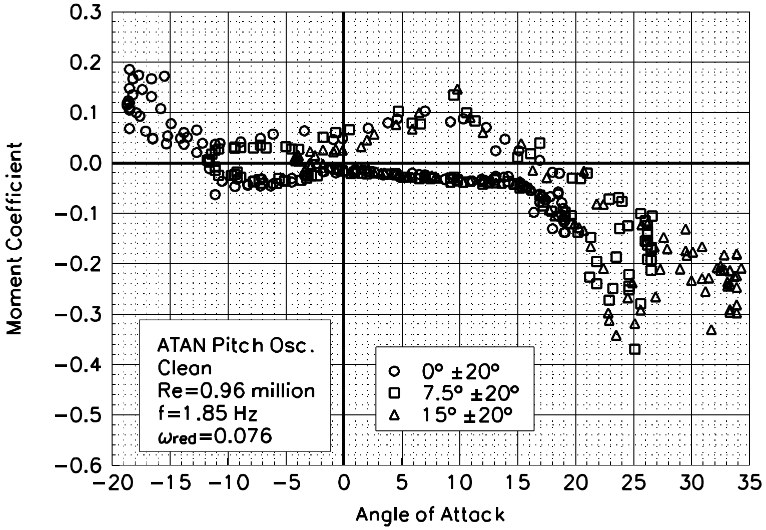

Figure C135. Moment coefficient vs α.

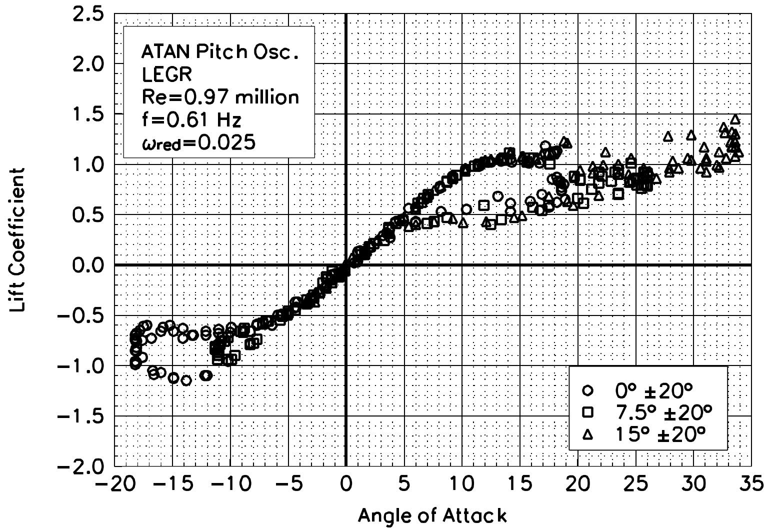

Figure C136. Lift coefficient vs α.

S824
LEGR
Re=0.97 million
$\omega_{reduced}$=0.025

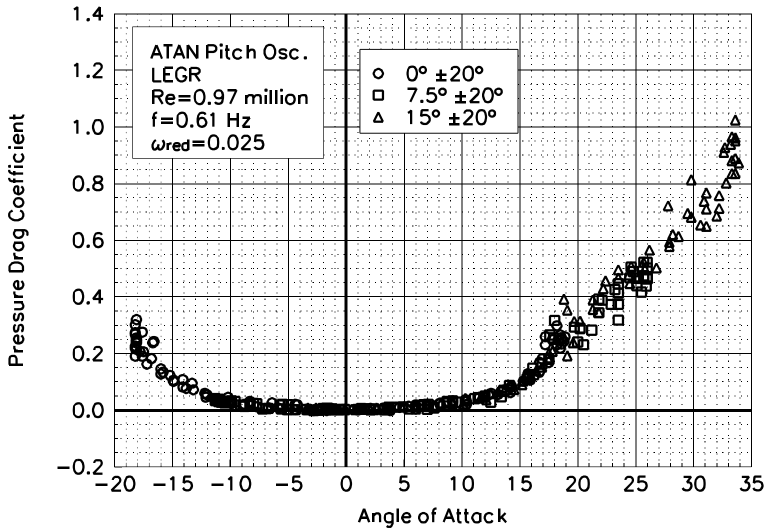

Figure C137. Pressure drag coefficient vs α.

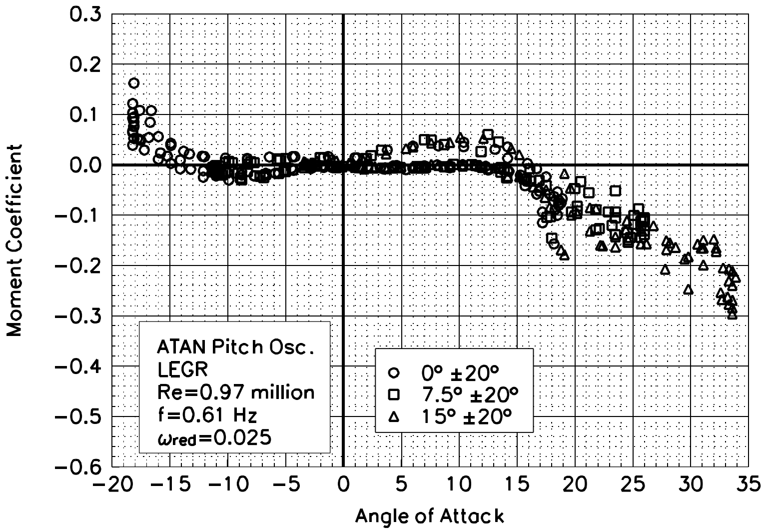

Figure C138. Moment coefficient vs α.

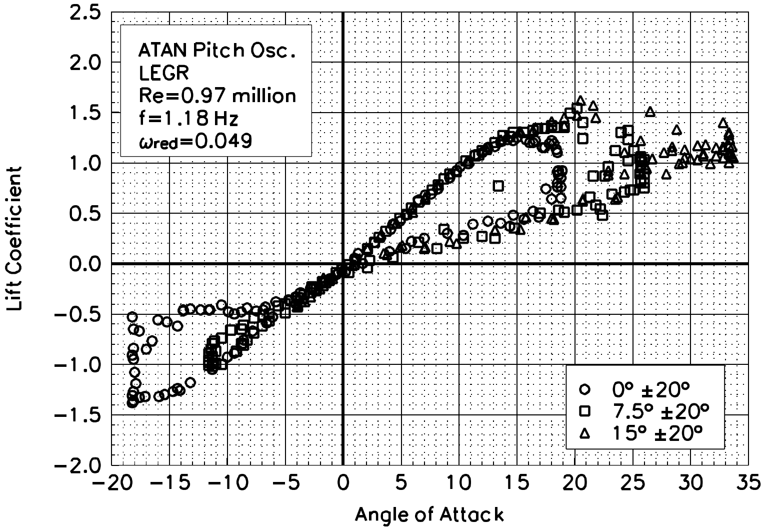

Figure C139. Lift coefficient vs α.

S824
LEGR
Re=0.97 million
$\omega_{reduced}$=0.049

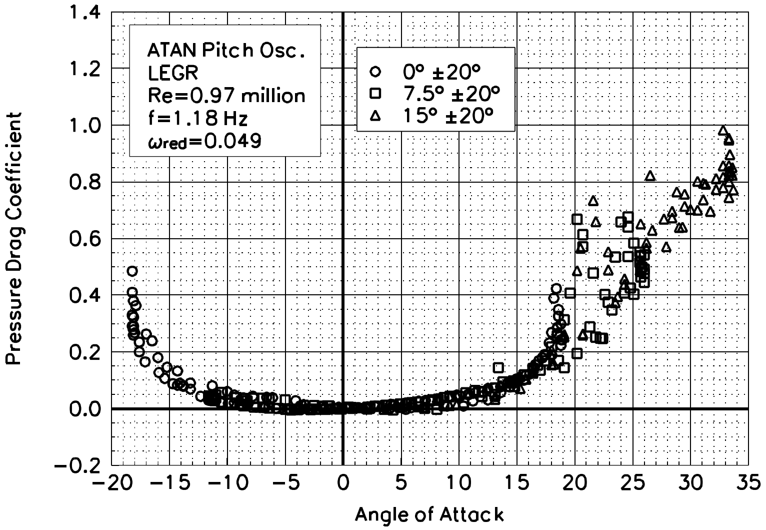

Figure C140. Pressure drag coefficient vs α.

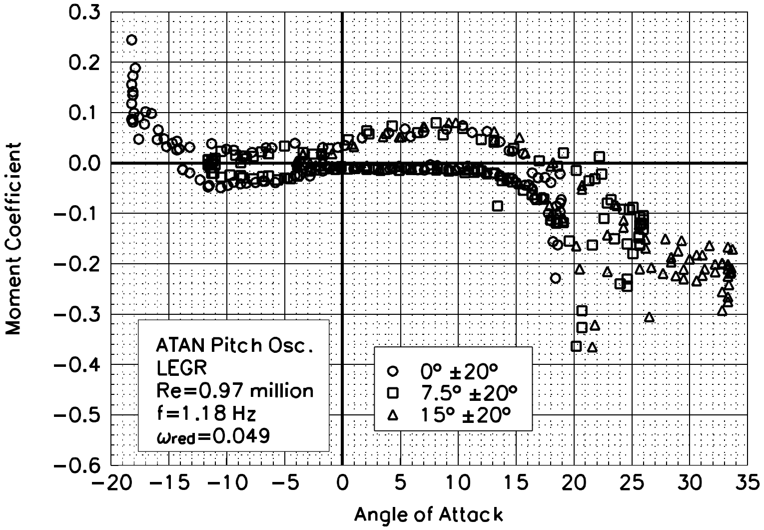

Figure C141. Moment coefficient vs α.

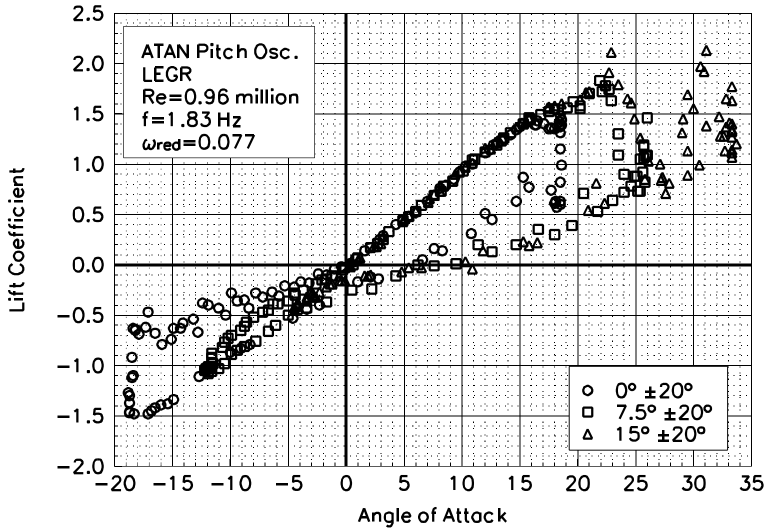

Figure C142. Lift coefficient vs α.

S824

LEGR

Re=0.96 million

$\omega_{reduced}$=0.077

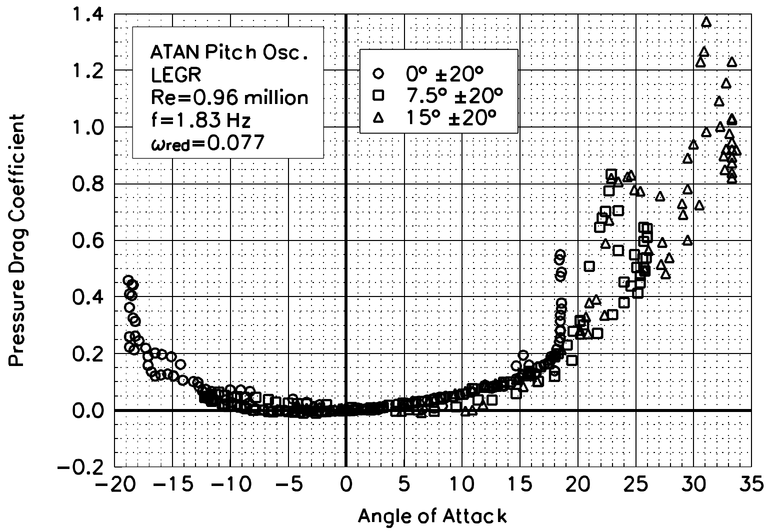

Figure C143. Pressure drag coefficient vs α.

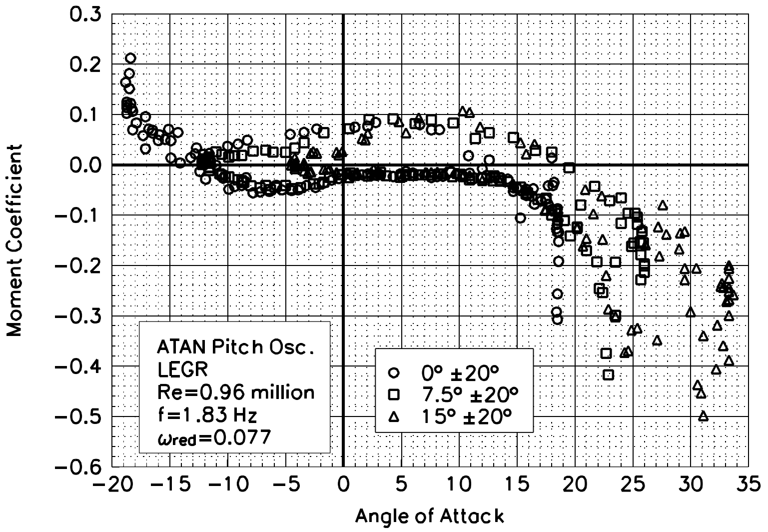

Figure C144. Moment coefficient vs α.

Unsteady Airfoil Characteristics

±20° Arc-Tangent, Re = 1.25 million

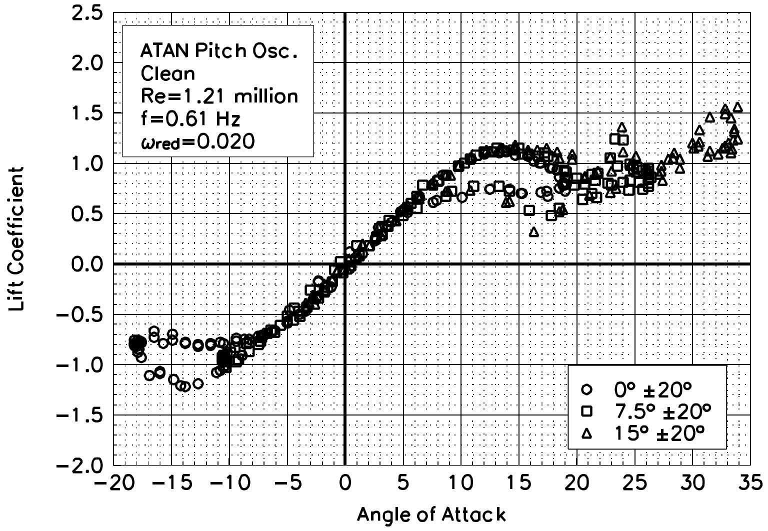

Figure C145. Lift coefficient vs α.

S824
Clean
Re=1.21 million
$\omega_{\mathrm{reduced}}$=0.020

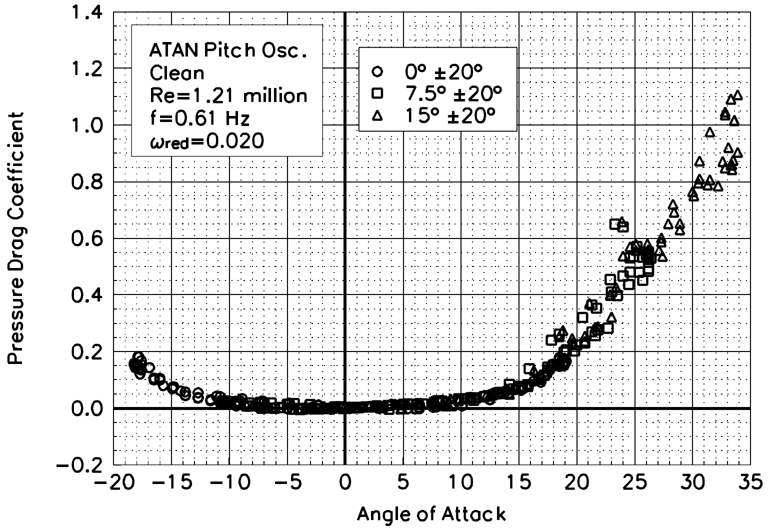

Figure C146. Pressure drag coefficient vs α.

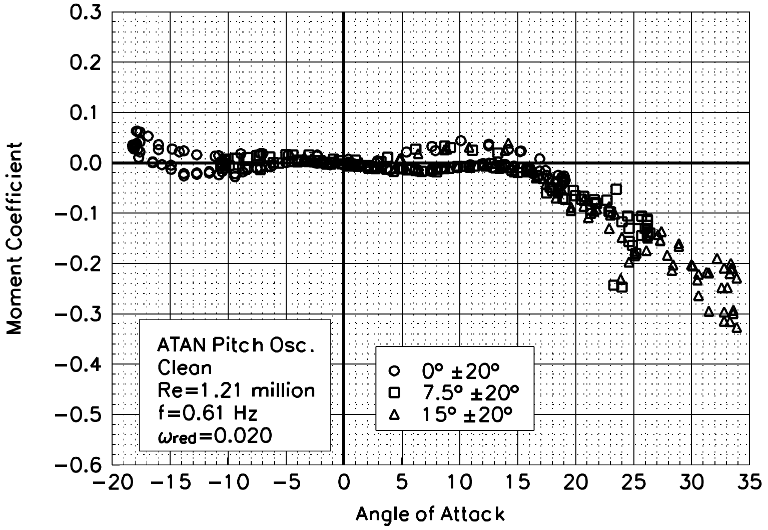

Figure C147. Moment coefficient vs α.

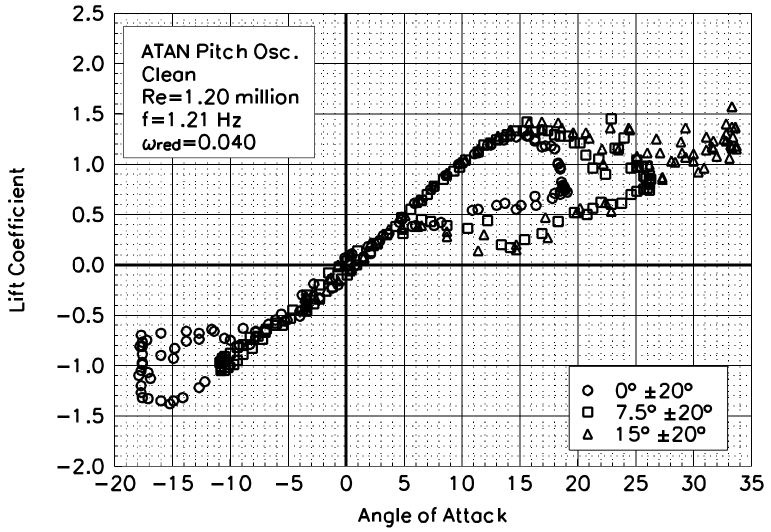

Figure C148. Lift coefficient vs α.

S824
Clean
Re=1.20 million
$\omega_{reduced}$=0.040

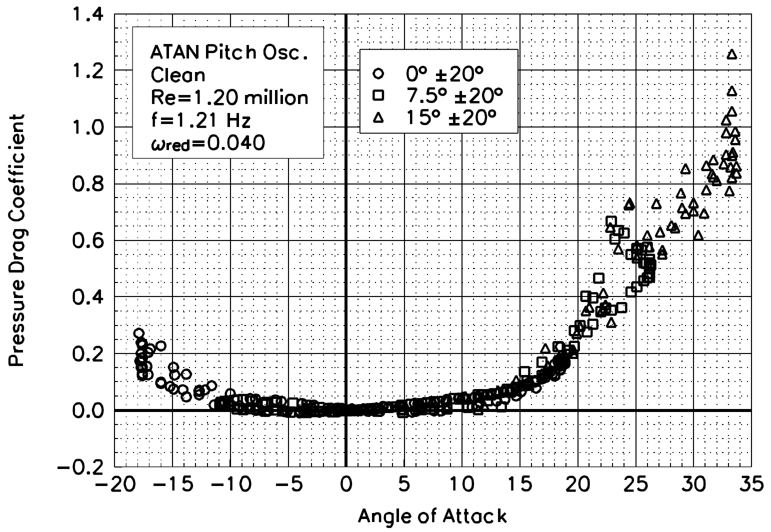

Figure C149. Pressure drag coefficient vs α.

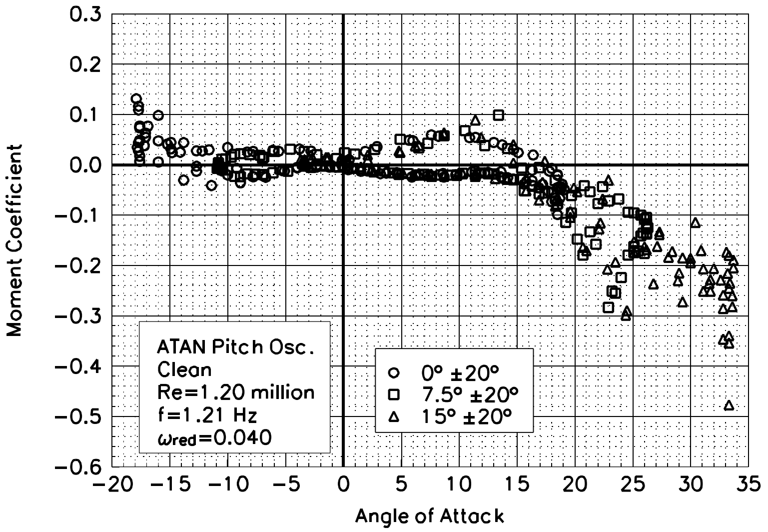

Figure C150. Moment coefficient vs α.

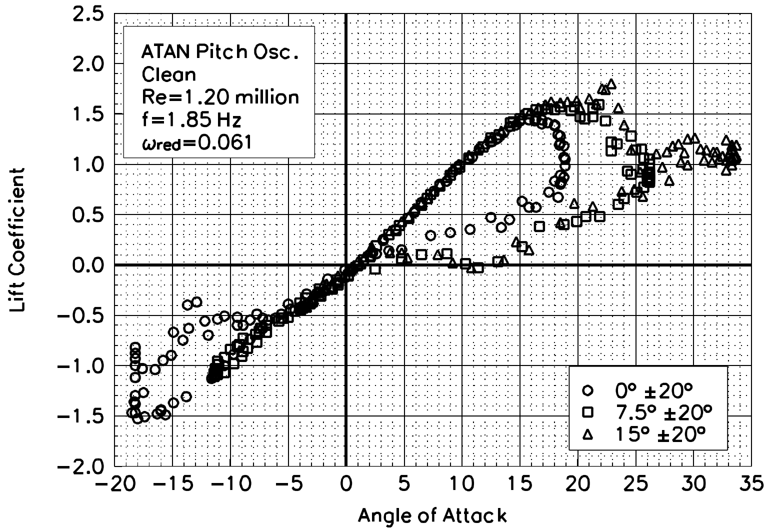

Figure C151. Lift coefficient vs α.

S824
Clean
Re=1.20 million
$\omega_{reduced}$=0.061

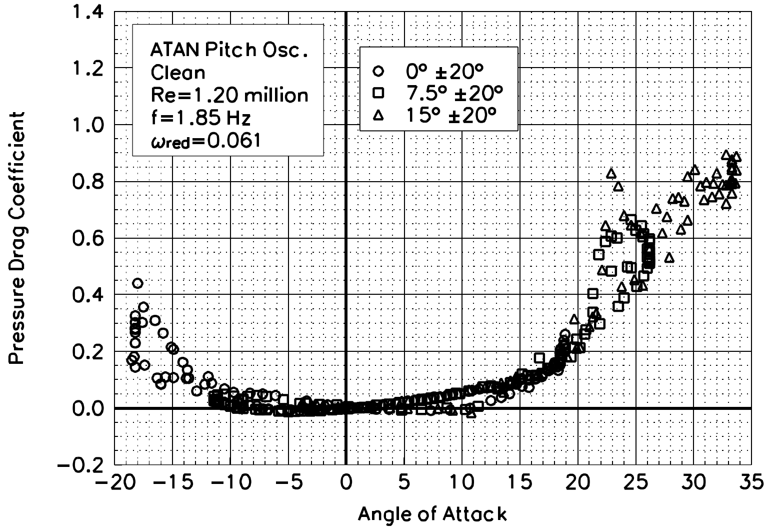

Figure C152. Pressure drag coefficient vs α.

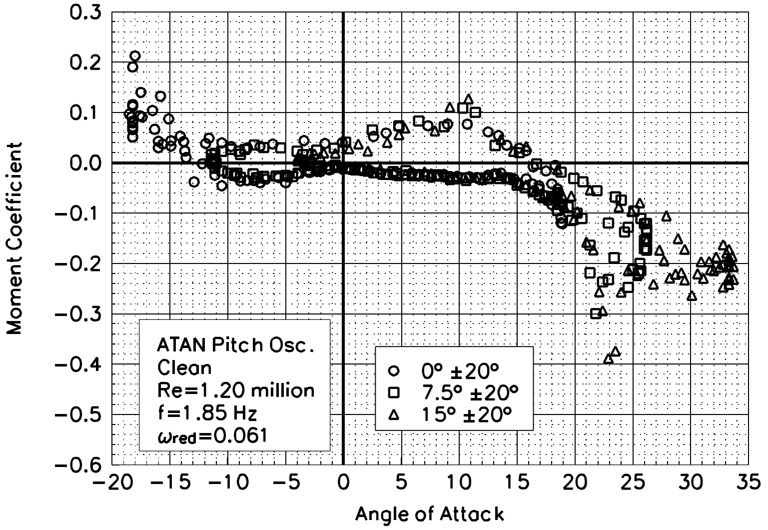

Figure C153. Moment coefficient vs α.

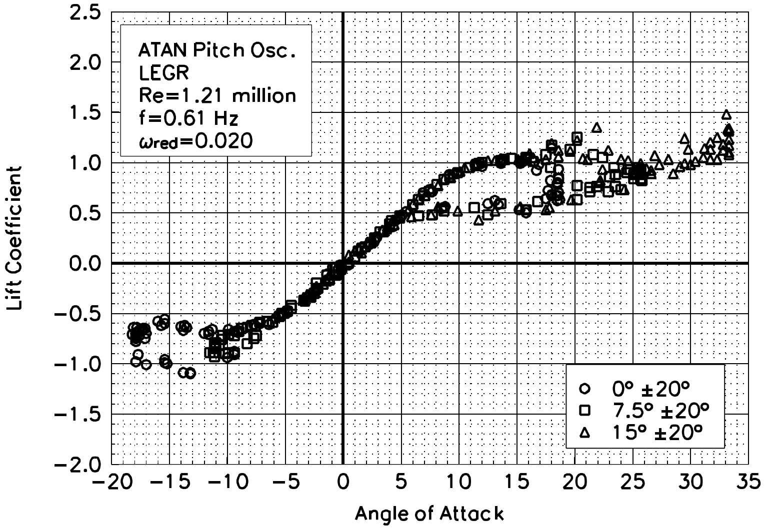

Figure C154. Lift coefficient vs α.

S824
LEGR
Re=1.21 million
$\omega_{reduced}$=0.020

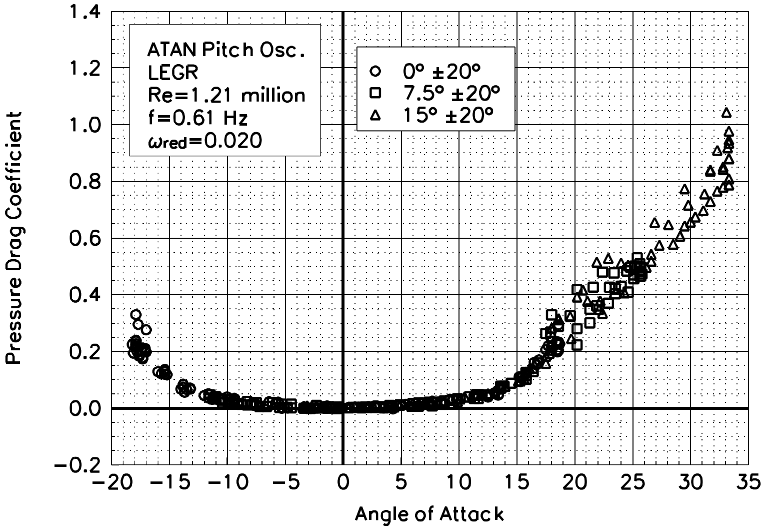

Figure C155. Pressure drag coefficient vs α.

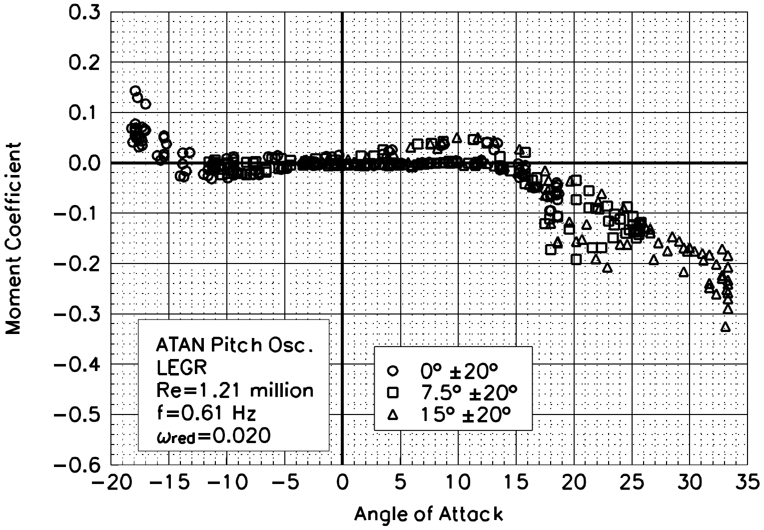

Figure C156. Moment coefficient vs α.

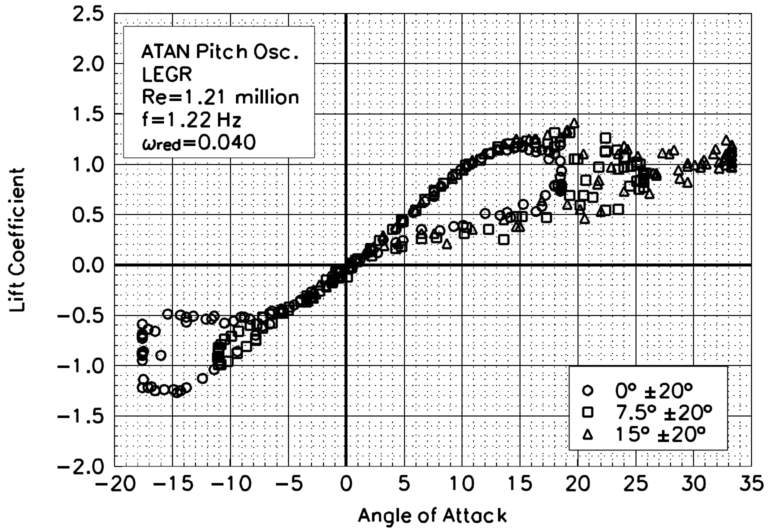

Figure C157. Lift coefficient vs α.

S824
LEGR
Re=1.21 million
$\omega_{reduced}$=0.040

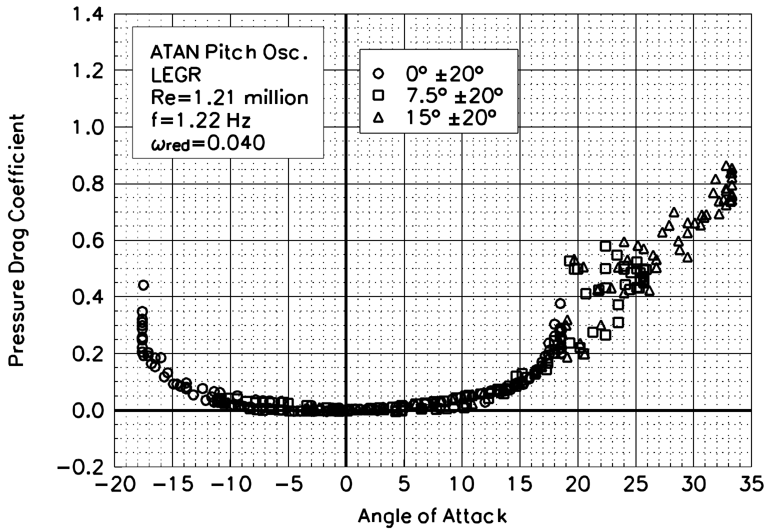

Figure C158. Pressure drag coefficient vs α.

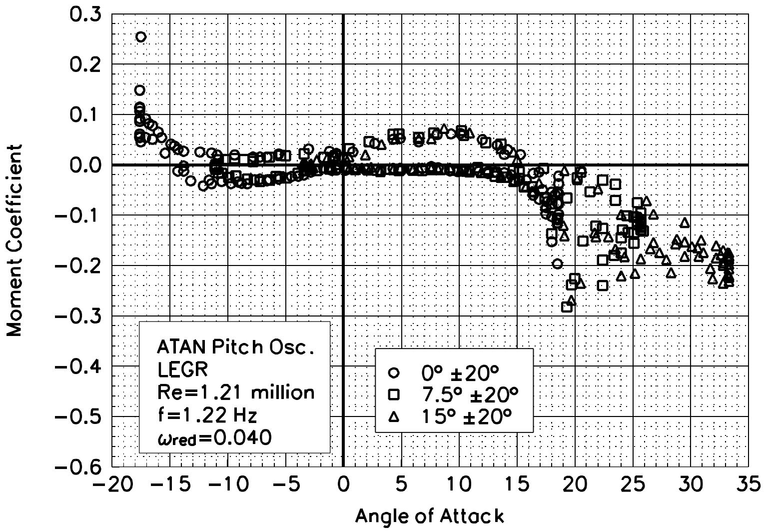

Figure C159. Moment coefficient vs α.

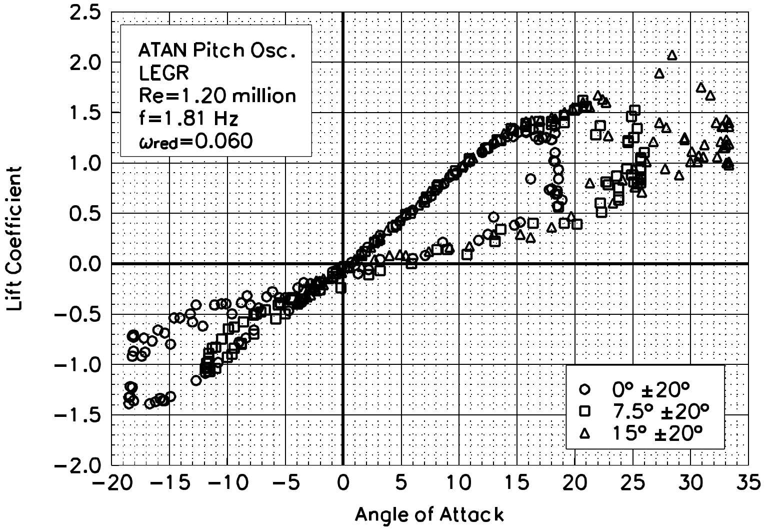

Figure C160. Lift coefficient vs α.

S824
LEGR
Re=1.20 million
$\omega_{reduced}$=0.060

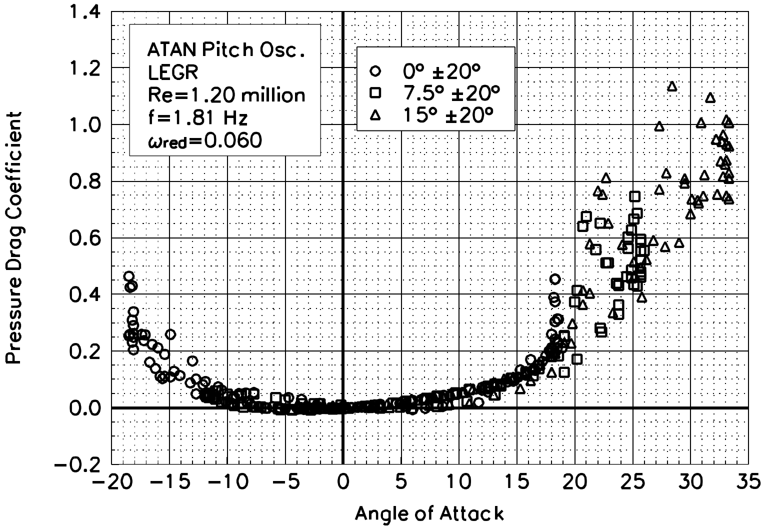

Figure C161. Pressure drag coefficient vs α.

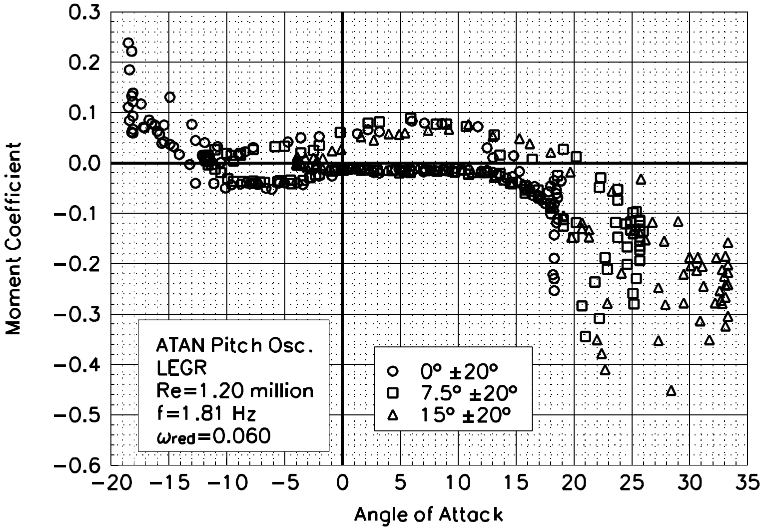

Figure C162. Moment coefficient vs α.